

TECHNISCHE UNIVERSITÄT MÜNCHEN  
Fakultät für Chemie  
Lehrstuhl I für Technische Chemie

# Modeling and CFD simulation of viscoelastic single and multiphase flows

Florian Habla

Vollständiger Abdruck der von der Fakultät für Chemie der Technischen Universität München  
zur Erlangung des akademischen Grades eines

Doktor-Ingenieurs (Dr.-Ing.)

genehmigten Dissertation.

Vorsitzender: Univ.-Prof. Dr. Thomas Brück

Prüfer der Dissertation:

1. Univ.-Prof. Dr.-Ing. Kai-Olaf Hinrichsen
2. Univ.-Prof. Dr.-Ing. Harald Klein
3. Univ.-Prof. Dr. Ville R. I. Kaila

Die Dissertation wurde am 12.11.2014 bei der Technischen Universität München eingereicht  
und durch die Fakultät für Chemie am 24.03.2015 angenommen.



*Das höchste Ziel im Seinsmodus ist tieferes Wissen, im Habenmodus mehr Wissen.*

Erich Fromm

*Als ein Universum von Mitteln kann die Technik ebenso die Schwäche wie die Macht des Menschen vermehren. Auf der gegenwärtigen Stufe ist er vielleicht ohnmächtiger als je zuvor gegenüber seinem eigenen Apparat.*

Herbert Marcuse

*Try not to become a person of success, but try instead to become a person of value.*

Albert Einstein



# Acknowledgements

Foremost, I would like to express my sincere appreciation to Prof. Dr.-Ing. Kai-Olaf Hinrichsen for giving me the opportunity to work in his group on a tremendously interesting topic and for the persistent encouragement, support and help he gave me in all stages of my Phd. I would like to thank him for giving me an initial direction for my research, but always leaving me with the freedom to work in my own fields of interest.

I am indebted to Laura Dietsche, who initiated the research in the field of viscoelastic multiphase flows, for without her this thesis would have never materialized. I would like to offer my special thanks to her for being an invaluable mentor and for the fruitful discussions we had throughout my Phd. I am deeply grateful that she gave me the opportunity to come to New Jersey, USA, where I had the pleasure to assist Tony Neubauer in the experiments on droplet breakup, and to come to Midland, USA, afterwards, where we had the possibility to collaborate together.

I would like to express my special appreciation to Joe Dooley, who encouraged me to investigate the issue of frame invariance in single-screw extrusion. I would like to thank him for the support he gave me during this research, the helpful comments and the hard questions he raised. I still admire his immense knowledge.

I would like to gratefully thank Miguel Nóbrega for inviting me to the University of Minho, Portugal, where we had prosperous discussions and after that started to work together on the modeling of calibrators. Miguel has an admirable enthusiasm and a broad knowledge in the field of polymer processing besides being a very warm-hearted person.

The study on frame invariance would never have taken such a shape without the generous help of Olaf Kintzel, who was willing to help by giving the mathematical proof for it. Olaf has an almost unprecedented scientific diligence.

I am grateful to the students I supervised during my Phd study: Nicolas Kohler, Stefanie Neuner, Alexander Woitalka, Matthias Steib, Johanna Hable, Chris Schüler, Andreas Prams, Andreas Obermeier, Stephan Obermeier, Fabian Rosner, Fei Ren, Peter Lorenz, Johannes Haßlberger, Christian Waas, Franziska Eschbach, Junrui Zhao, Ming Wei Tan, Emanuel Trunzer, Nicola Hupp, Konstantin Grambow, Lennart Densky and Max Maier. They contributed a lot to the quality and extent of this work and I shared many enjoyable and invaluable helpful discussions with them.

I would like to thank my colleague Matthias Fichtl for he was unrelentingly willing to help me with fixing hardware issues of my computer and the local computing cluster.

I am grateful to Heidi Holweck not only for her administrative support, but particularly for her kindness and friendship.

Above all - although I know words cannot express my true feelings - I owe my eternal gratitude to my family and friends not just for being part of this wonderful life but rather a very important reason.

# Contents

Acknowledgements	E
Contents	G
List of Figures	K
List of Tables	Q
1 Introduction	1
1.1 Background . . . . .	1
1.2 Objectives . . . . .	4
1.A Literature . . . . .	6
2 Theory	7
2.1 Viscoelasticity . . . . .	7
2.1.1 Linear viscoelasticity . . . . .	7
2.1.2 Non-linear viscoelasticity . . . . .	12
2.1.3 Temperature dependencies . . . . .	16
2.1.4 Constitutive equations . . . . .	18
2.2 Conservation laws . . . . .	21
2.3 Finite volume method . . . . .	23
2.3.1 Discretization of the solution domain . . . . .	23
2.3.2 Equation discretization . . . . .	24
2.3.3 Boundary and initial conditions . . . . .	27
2.3.4 Solution of sets of linear equations . . . . .	27
2.A Literature . . . . .	29
2.B Nomenclature . . . . .	30
3 Semi-implicit stress formulation for viscoelastic models: Application to three-dimensional contraction flows	35
3.1 Introduction . . . . .	35
3.2 Governing equations and numerical method . . . . .	36
3.2.1 Governing equations . . . . .	36
3.2.2 Numerical method . . . . .	37
3.2.3 Numerical algorithm . . . . .	41
3.3 Results . . . . .	42
3.3.1 Planar contraction . . . . .	42
3.3.2 Square-square contraction . . . . .	49
3.4 Conclusions . . . . .	54
3.A Literature . . . . .	55
3.B Nomenclature . . . . .	58

## Contents

3.C	Summary . . . . .	62
3.D	Author contribution . . . . .	62
3.E	Copyright permission . . . . .	62
4	Numerical simulation of the viscoelastic flow in a three-dimensional lid-driven cavity using the log-conformation reformulation in OpenFOAM® . . . . .	64
4.1	Introduction . . . . .	64
4.2	Mathematical background . . . . .	66
4.2.1	Governing equations . . . . .	66
4.2.2	Log-conformation approach . . . . .	67
4.3	Numerical method . . . . .	69
4.3.1	Discretization schemes . . . . .	69
4.3.2	Momentum equation discretization . . . . .	70
4.3.3	Flux formulation and pressure equation . . . . .	71
4.3.4	Constitutive equation discretization . . . . .	72
4.3.5	Solution algorithm . . . . .	72
4.4	Results and Discussion . . . . .	75
4.4.1	Startup Poiseuille flow . . . . .	75
4.4.2	Cavity flow . . . . .	78
4.5	Summary . . . . .	106
4.A	Literature . . . . .	107
4.B	Nomenclature . . . . .	110
4.C	Summary . . . . .	115
4.D	Author contribution . . . . .	115
4.E	Copyright permission . . . . .	115
5	Development of a methodology for numerical simulation of non-isothermal viscoelastic fluid flows with application to axisymmetric 4:1 contraction flows . . . . .	117
5.1	Introduction . . . . .	117
5.2	Methodology . . . . .	118
5.2.1	Conservation and constitutive equation . . . . .	118
5.2.2	Thermodynamical modeling . . . . .	119
5.2.3	Discretization and numerical algorithm . . . . .	121
5.3	Results and discussion . . . . .	123
5.3.1	Validation of the extrapolation method . . . . .	123
5.3.2	Results for the axisymmetric 4:1 contraction flow . . . . .	127
5.4	Conclusion . . . . .	146
5.A	Literature . . . . .	148
5.B	Nomenclature . . . . .	151
5.C	Summary . . . . .	155
5.D	Author contribution . . . . .	155



Contents

5.E	Copyright permission . . . . .	155
6	Modeling and Simulation of Conditionally Volume Averaged Viscoelastic Two-Phase Flows	157
6.1	Introduction . . . . .	157
6.2	Mathematical formulation . . . . .	159
6.2.1	Conditional Averaging . . . . .	159
6.2.2	Conservation equations . . . . .	162
6.2.3	Viscoelastic Two-Phase Flow Closure . . . . .	165
6.3	Numerical implementation . . . . .	171
6.3.1	Pressure reformulation . . . . .	171
6.3.2	Phase fraction equation reformulation . . . . .	172
6.3.3	Phase-intensive Momentum and Constitutive Equation . . . . .	173
6.3.4	Stabilization using the Both Sides Diffusion . . . . .	175
6.3.5	Summary of the model . . . . .	175
6.3.6	Numerical discretization . . . . .	175
6.3.7	Iterative procedure . . . . .	176
6.4	Results and Discussion . . . . .	177
6.4.1	Single Phase Flow . . . . .	177
6.4.2	Shear-flow parallel to a planar interface . . . . .	179
6.4.3	Pressure jump across a cylindrical interface due to surface tension . . . . .	181
6.4.4	Mesh convergence study: Poiseuille Two-Phase Flow . . . . .	184
6.5	Conclusions . . . . .	189
6.A	Literature . . . . .	191
6.B	Nomenclature . . . . .	194
6.C	Summary . . . . .	199
6.D	Author contribution . . . . .	199
6.E	Copyright permission . . . . .	199
7	An Improved Conditionally Volume Averaged Viscoelastic Two-Phase Model for Simulation of Transient Droplet Deformations under Simple Shear	201
7.1	Introduction . . . . .	201
7.2	Theory . . . . .	202
7.2.1	Conditional volume averaged viscoelastic two-phase model . . . . .	202
7.2.2	Numerical reformulation . . . . .	204
7.2.3	Intermediate Step . . . . .	205
7.2.4	Numerical Discretization and Algorithm . . . . .	206
7.3	Results and Discussion . . . . .	208
7.3.1	Validation of Advection Scheme . . . . .	208
7.3.2	Droplet deformation . . . . .	211
7.4	Summary . . . . .	224
7.A	Literature . . . . .	225

## Contents

7.B	Nomenclature . . . . .	227
7.C	Summary . . . . .	231
7.D	Author contribution . . . . .	231
7.E	Copyright permission . . . . .	231
8	CFD Analysis of the Frame Invariance of the Melt Temperature Rise in a Single-Screw Extruder . . . . .	233
8.1	Introduction . . . . .	233
8.2	Theory . . . . .	234
8.2.1	Viscous dissipation . . . . .	234
8.2.2	Conservation laws . . . . .	235
8.2.3	Single-screw extruder modeling . . . . .	236
8.2.4	Fluid rheology . . . . .	237
8.2.5	Numerical methodology . . . . .	237
8.3	Results and discussion . . . . .	237
8.3.1	Two-dimensional cross-section . . . . .	237
8.3.2	Three-dimensional simulations . . . . .	244
8.4	Conclusions . . . . .	245
8.A	Literature . . . . .	248
8.B	Nomenclature . . . . .	249
8.C	Summary . . . . .	252
8.D	Author contribution . . . . .	252
8.E	Copyright permission . . . . .	252
9	Summary and Outlook . . . . .	253
9.1	Summary . . . . .	253
9.2	Outlook . . . . .	255
2.A	Literature . . . . .	259
9.B	Nomenclature . . . . .	260
A	List of Publications . . . . .	A-1
B	Curriculum Vitae . . . . .	B-1
C	Declaration . . . . .	C-1

# List of Figures

1.1	Variety of extrusion profiles . . . . .	1
1.2	Sketch of a profile extrusion line . . . . .	2
1.3	Example of an extrusion die . . . . .	2
1.4	Flow channel and simulated ratios between axial velocity and the objective velocity . . . . .	3
2.1	Shear deformation of a square region $OABC$ about the angle $\Theta$ to the parallelogram $OAB'C'$ within the time interval $\Delta t = t_2 - t_1$ . . . . .	7
2.2	Spring with modulus $G$ and damper with viscosity $\eta$ connected in series (Maxwell model) . . . . .	8
2.3	Stress $\sigma_{xy}$ as a function of time $t$ for three different relaxation times $\lambda_{1,i}$ . . . . .	9
2.4	Generalized Maxwell model represented by $n$ Maxwell models connected in parallel . . . . .	10
2.5	Spring with modulus $G$ and damper with viscosity $\eta$ connected in parallel (Kelvin model) . . . . .	11
2.6	Strain $\Theta$ as a function of time $t$ for three different retardation times $\lambda_{2,i}$ . . . . .	12
2.7	Shear viscosity $\eta(\dot{\gamma}_{xy})$ -functions as a function of shear-rate $\dot{\gamma}$ . . . . .	13
2.8	Schematic view of uniaxial, biaxial and planar extensional flow . . . . .	15
2.9	Trouton ratio $Tr$ as a function of elongational rate $\dot{\epsilon}$ in uniaxial extension . . . . .	16
2.10	Shear viscosity $\eta(\dot{\gamma}, T)$ as a function of shear-rate $\dot{\gamma}$ for different values of temperature $T$ . . . . .	17
2.11	Shear viscosity (a) and extensional viscosity (b) as predicted by the Oldroyd-B model . . . . .	20
2.12	Shear viscosity (a) and extensional viscosity (b) as predicted by the SPTT model . . . . .	21
2.13	Space and time discretization in the finite volume method. . . . .	23
3.1	Schematic representation of the stress in a 1-D problem . . . . .	38
3.2	Scanning positions (planar contraction); lengths are normalized with half the downstream channel height $H_2$ . . . . .	42
3.3	Detailed isometric view of mesh M1 in the contraction area (planar contraction) . . . . .	43
3.4	Detailed view of the center plane for the three meshes (planar contraction) . . . . .	43
3.5	Comparison of the velocity component $U_y$ obtained by using the standard linear interpolation and our improved method at line b-1 for mesh M1 (planar contraction) . . . . .	44
3.6	Comparison between measured and predicted velocity in the upstream section (planar contraction) . . . . .	45
3.7	Comparison between measured and predicted velocity in the upstream section (planar contraction) . . . . .	46
3.8	Comparison between measured and predicted velocity in the downstream section (planar contraction) . . . . .	46

*List of Figures*

3.9	Comparison between measured and predicted shear stress in the upstream section (planar contraction) . . . . .	46
3.10	Comparison between measured and predicted shear stress in the upstream section (planar contraction) . . . . .	47
3.11	Comparison between measured and predicted shear stress in the downstream section (planar contraction) . . . . .	47
3.12	Comparison between measured and predicted shear stress in the downstream section (planar contraction) . . . . .	47
3.13	Comparison between measured and predicted first normal stress difference in the upstream section (planar contraction) . . . . .	48
3.14	Comparison between measured and predicted first normal stress difference in the upstream section (planar contraction) . . . . .	48
3.15	Comparison between measured and predicted first normal stress difference in the downstream section (planar contraction) . . . . .	48
3.16	Comparison between measured and predicted first normal stress difference in the downstream section (planar contraction) . . . . .	49
3.17	Detailed isometric view of mesh M1 in the contraction area (square-square contraction) . . . . .	50
3.18	Detailed view of the center plane for the three meshes (square-square contraction)	50
3.19	Dimensionless vortex length $\chi$ as a function of the maximum Courant number $Co_{max}$ for a Deborah number of $De = 5.9$ (square-square contraction) . . . .	51
3.20	Dimensionless vortex length as a function of the Deborah number (square-square contraction) . . . . .	52
3.21	Dimensionless axial velocity profile at the centerline of the square-square contraction . . . . .	53
3.22	Dimensionless axial velocity profile at the centerline of the square-square contraction . . . . .	54
4.1	Sketch of the geometry for the startup of a viscoelastic Poiseuille flow . . . .	75
4.2	Centerline velocity as a function of time during the start-up of a Poiseuille flow of an Oldroyd-B fluid ( $\beta = 0.01$ ) for different elasticity numbers . . . . .	77
4.3	$ Q_{num} - Q_{exact} $ as a function of the time-step size $\Delta t$ at $T = t/\lambda = 0.1$ using a mesh with $\Delta y = 0.005$ and an elasticity number of $E = 1$ . . . . .	78
4.4	$ Q_{num} - Q_{exact} $ as a function of the cell size $\Delta y$ at $T = t/\lambda = 50$ with an elasticity number of $E = 1$ . . . . .	79
4.5	Centerline velocity and error as a function of time during the start-up of a Poiseuille flow of an Oldroyd-B fluid ( $\beta = 0.01$ ) for different implementations ( $\Delta t/\lambda = 0.000625$ and $\Delta y = 0.005$ ) . . . . .	80
4.6	Sketch of the geometry with primary and secondary vortices . . . . .	81

*List of Figures*

4.7	Vertical $\Psi_{xx}$ profile and horizontal $\Psi_{xy}$ profile for a 2D cavity simulation at $We = 1$ and $T = 8$ simulated on a mesh with 128x128 hexahedral cells with two different boundary conditions for $\tau_P$ . . . . .	82
4.8	View of the meshes . . . . .	83
4.9	$\max(\tau_{P,xx})$ over time $T$ as a function of different time-steps for $We = 1.0$ using mesh M3 with the CUBISTA scheme . . . . .	84
4.10	Decay of the initial residuals of the linear equations for $\Psi_{xx}$ and $p$ using the upwind and the CUBISTA scheme at $We = 1.0$ with mesh M3 . . . . .	85
4.11	$\max(\tau_{P,xx})$ over time $T$ for mesh M3 and $\Delta T = 0.005$ as a function of different Weissenberg numbers and convection schemes . . . . .	86
4.12	Convergence of the $x$ -coordinate of the primary vortex with different meshes, convection schemes and Weissenberg numbers . . . . .	90
4.13	Convergence of the $y$ -coordinate of the primary vortex with different meshes, convection schemes and Weissenberg numbers . . . . .	90
4.14	Shift of the location of the primary vortex predicted with mesh M3 and CUBISTA scheme ( $We = 0.0 \rightarrow 2.0$ in steps of 0.2) . . . . .	91
4.15	Streamlines in the $xy$ -, $xz$ - and $yz$ -planes for different Weissenberg numbers using mesh M3 and CUBISTA . . . . .	92
4.16	Comparison of streamlines in the secondary eddies in the $xy$ -plane for different Weissenberg numbers using mesh M3 and CUBISTA . . . . .	93
4.17	Change of upstream secondary eddy in the $xy$ -plane from outflow to inflow using mesh M3 and upwind differencing . . . . .	94
4.18	$\Psi$ field in the $xy$ -plane using mesh M3 and CUBISTA . . . . .	96
4.19	$\tau_P$ field in the $xy$ -plane using mesh M3 and CUBISTA . . . . .	97
4.20	Velocity magnitude in the $xy$ -plane using mesh M3 and CUBISTA . . . . .	99
4.21	$\xi$ field in the $xy$ -plane using mesh M3 and CUBISTA . . . . .	101
4.22	Vertical and horizontal velocity profiles at $We = 1.0$ for different meshes and differencing schemes . . . . .	103
4.23	Vertical and horizontal velocity profiles as a function of the Weissenberg number using mesh M3 and CUBISTA . . . . .	104
4.24	Snapshots of streamlines in the $xy$ -plane for $We = 160.0$ using mesh M3 and CUBISTA . . . . .	105
5.1	Local coordinate system $\zeta$ for determining the stress value at the wall $\tau_{P,fe}$ . . . . .	123
5.2	Geometry of the planar Poiseuille flow . . . . .	124
5.3	Meshes used for the validation of the extrapolation boundary condition . . . . .	124
5.4	Results for the planar Poiseuille flow on three different meshes . . . . .	126
5.5	Relative $L_1$ -error of the shear stress and velocity as a function of the dimensionless cell size for the planar Poiseuille flow . . . . .	127
5.6	Geometry of the axisymmetric 4:1 contraction flow . . . . .	127

*List of Figures*

5.7	Detailed view of the contraction area from $z = -R_1$ to $z = +R_1$ for the various meshes . . . . .	128
5.8	Isolines of $\det(\mathbf{c})$ at $De = 6$ using mesh M1 . . . . .	130
5.9	Axial velocity $\tilde{\mathbf{U}}_z$ and normal stress $\tilde{\tau}_{P,zz}$ as a function of the axial position at the centerline $r/R_2 = 0$ for the isothermal case for different Deborah numbers and meshes . . . . .	131
5.10	Dimensionless vortex length $\chi$ as a function of the Deborah number $De$ for various meshes . . . . .	132
5.11	Streamlines for $De = 0, 1, 5, 10$ for the isothermal case using mesh M4 . . .	133
5.12	Normalized velocities and stresses as a function of the distance $\xi$ for isothermal viscoelastic flow at $De = 0$ using various meshes . . . . .	134
5.13	Normalized velocities and stresses as a function of the distance $\xi$ for isothermal viscoelastic flow at $De = 1$ using various meshes . . . . .	135
5.14	Normalized velocities and stresses as a function of the distance $\xi$ for isothermal viscoelastic flow at $De = 5$ using various meshes . . . . .	136
5.15	Temperature $T$ , axial normal stress $\tilde{\tau}_{P,zz}$ and velocity $\tilde{\mathbf{U}}_z$ as a function of the axial position on the line $r = 0.97R_2$ for different values of $\alpha$ at $De = 5$ and $\Delta T = 0\text{K}$ using various meshes . . . . .	138
5.16	Dimensionless energy source term $\tilde{Q}$ and temperature $T$ as a function of the axial position on the line $r = 0.87R_2$ for different values of $\alpha$ at $De = 5$ and $\Delta T = 0\text{K}$ using various meshes . . . . .	140
5.17	Dimensionless vortex length $\chi$ as a function of the temperature jump $\Delta T$ at $De = 1$ and $\alpha = 0$ for various meshes . . . . .	141
5.18	Dimensionless vortex length $\chi$ as a function of the temperature jump $\Delta T$ and $\alpha$ at $De = 5$ for various meshes . . . . .	142
5.19	Temperature isolines for different temperature jumps $\Delta T$ at $De = 5$ and $\alpha = 0$ using mesh M4 . . . . .	143
5.20	Streamlines for different temperature jumps $\Delta T$ at $De = 5$ and $\alpha = 0$ using mesh M4 . . . . .	144
5.21	Axial velocity $\tilde{\mathbf{U}}_z$ , temperature $T$ and dimensionless energy source term $\tilde{Q}$ as a function of the radial distance at the outlet for different temperature jumps and values of $\alpha$ at $De = 5$ using mesh M4 . . . . .	145
6.1	Domain and boundary conditions for a single phase Poiseuille flow . . . . .	177
6.2	Single-phase flow between two parallel plates . . . . .	178
6.3	Domain and boundary conditions for a shear flow parallel to a flat interface at different viscosities . . . . .	179
6.4	Volume fraction and velocity profiles across a planar interface with a shear-flow parallel to the interface at $\eta_r = 10$ . . . . .	180
6.5	Domain and boundary conditions for a pressure difference due to a cylindrical interface with surface tension . . . . .	182

List of Figures

6.6	Volume fraction and pressure profiles across a cylindrical interface with surface tension . . . . .	183
6.7	Domain and boundary conditions for a stratified two-phase Poiseuille flow between two parallel plates . . . . .	184
6.8	Volume fraction, velocity and stress profiles of the Poiseuille two-phase flow simulation at a constant $\delta/\Delta x = 1$ . . . . .	190
7.1	Comparison of the hyperbolic tangent profile (Eq. 7.17) and the converged solution of Eq. 7.16 . . . . .	206
7.2	Domain of the validation case . . . . .	208
7.3	Isolines of $\alpha_\varphi = 0.5$ at $t = 2\pi$ for different grids compared to the initial state. . . . .	209
7.4	Isolines of $\alpha_\varphi = 0.05, 0.5$ and $0.95$ at $t = 2\pi$ for $\Delta x = 0.01$ compared to the initial state . . . . .	210
7.5	Determination of the order of the error decrease for the area conservation . . . . .	211
7.6	Domain of the droplet deformation simulations . . . . .	212
7.7	$D^*$ against $t/\tau_{em}$ for different time steps at $Ca = 0.43$ for M3 . . . . .	213
7.8	$D^*$ against $t/\tau_{em}$ for the different meshes and $Ca$ at $\Delta t = 0.00125$ s . . . . .	215
7.9	Isolines of $\alpha_\varphi = 0.05, 0.5$ and $0.95$ for $t/\tau_{em} = 0$ and $t/\tau_{em} = 30$ for mesh M3 . . . . .	216
7.10	$D^*$ against $t/\tau_{em}$ for different values of $\Delta\tau$ for mesh M3 and $Ca = 0.43$ . . . . .	217
7.11	$D^*$ against $t/\tau_{em}$ compared to the simulations of Yue et al. [10] and Habla et al. for different values of $\beta_m$ for mesh M3 and $Ca = 0.43$ . . . . .	217
7.12	Illustration of the adaptive mesh refinement on mesh M6-3D for $Ca = 0.43$ . . . . .	218
7.13	Deformation parameter $D^*$ against the dimensionless time $t/\tau_{em}$ compared to the measurements of Sibillo et al. and the simulations of Yue et al. and Habla et al. . . . .	220
7.14	$D'/D'_{ss}$ against $t/\tau_{em}$ compared to the measurements of Sibillo et al. for the highest subcritical Capillary number $Ca_{inf}$ explored . . . . .	221
7.15	Z-normal plane colored by the local flow-type parameter $\xi$ at $t/\tau_{em} = 30$ using mesh M6-3D . . . . .	222
7.16	Z-normal plane colored by the pressure at $t/\tau_{em} = 30$ using mesh M6-3D . . . . .	222
7.17	Z-normal plane colored by the respective stress components at $t/\tau_{em} = 30$ using mesh M6-3D . . . . .	223
8.1	Screw- and barrel-rotation . . . . .	236
8.2	Geometry of the extruder (a), sample lines (b), mesh M1 (c), length are in <i>mm</i> . . . . .	238
8.3	$T_{min}$ (solid lines), $T_{max}$ (dotted lines) and $T_{av}$ (dashed lines) as a function of the dimensionless time for the three different meshes using screw-rotation . . . . .	238
8.4	$T_{min}$ (solid lines), $T_{max}$ (dotted lines) and $T_{av}$ (dashed lines) as a function of the dimensionless time for screw- and barrel-rotation using mesh M3 . . . . .	240
8.5	Local velocity ((a) and (b)) and temperature profiles ((c) and (d)) at the sampling lines $A - B$ ((a) and (c)) and $C - D$ ((b) and (d)) at $\omega_{max}t = 150$ using mesh M1 . . . . .	241

*List of Figures*

8.6	$T_{min}$ (solid lines), $T_{max}$ (dotted lines) and $T_{av}$ (dashed lines) as a function of the dimensionless time for barrel-rotation . . . . .	242
8.7	Temperature field for the two-dimensional cross-section at $\omega_{max}t = 150$ using screw-rotation . . . . .	243
8.8	Area-averaged temperature in the cross-sectional plane after one full turn of the screw as a function of the dimensionless time for different discharge rates	244
8.9	Local velocity profiles at the sampling lines $A - B$ (a) $F_r = 0.1$ , (c) $F_r = 0.4$ , (e) $F_r = 0.9$ and $C - D$ (b) $F_r = 0.1$ , (d) $F_r = 0.4$ , (f) $F_r = 0.9$ in the cross-sectional plane after one full turn of the screw at $\omega_{max}t = 150$ . . . . .	246
8.10	Local temperature profiles at the sampling lines A-B and C-D in the cross-sectional plane after one full turn of the screw at $\omega_{max}t = 150$ . . . . .	247
9.1	Immersed Boundary Method (IBM) for twin-screw extruder simulation . . . . .	256
9.2	Simulation of the flow of a viscoelastic fluid in a partially filled twin-screw extruder . . . . .	257



# List of Tables

3.1	Properties of the meshes used for the planar contraction . . . . .	43
3.2	Physical properties of the fluid used in the square-square contraction . . . . .	49
3.3	Properties of the meshes used for the square-square contraction . . . . .	50
4.1	Properties of the meshes . . . . .	81
4.2	Location of the primary vortex for different Weissenberg numbers, meshes and convection schemes . . . . .	87
4.3	Comparison of the predicted location of the primary vortex center with the log-conformation reformulation ('log') and the standard formulation ('std') with mesh M3 and CUBISTA . . . . .	88
4.4	Comparison of the predicted location of the primary vortex center with the upwind, CUBISTA and QUICK scheme with mesh M3 and CUBISTA at $We = 1.0$ . . . . .	89
5.1	Details of the meshes used for the axisymmetric 4:1 contraction . . . . .	128
6.1	Fluid properties . . . . .	184
6.2	Meshes used for mesh convergence analysis . . . . .	185
6.3	Error calculation for Poiseuille two-phase flow simulation . . . . .	187
6.4	Rate of convergence for Poiseuille two-phase flow simulation . . . . .	188
7.1	Area within the 0.5 isoline before and after the rotation and the relative deviation referred to the initial state's area and the area of a perfect circle. . . . .	211
7.2	Meshes used for the transient droplet deformation simulations . . . . .	213
7.3	Steady-state values of $D^*$ for meshes M4 and M6-3D, the simulations of Yue et al. and Habla et al. as well as the measurements of Sibillo et al. . . . .	219
8.1	Minimum, maximum and area-averaged temperature for the two-dimensional cross-section simulations at $\omega_{max}t = 150$ . . . . .	239



# 1 Introduction

## 1.1 Background

With the worldwide turnover of chemicals valuing € 2744 billion in 2011 (European Union: € 539 billion) the chemical industry constitutes one of the largest economical sectors in the world and virtually supplies all other sectors. [1] Moreover, the chemical industry is ever growing as for instance exemplified by the chemical turnover increase of over 28 % in the European Union on a ten year perspective. Polymers contribute to the overall chemical output with a striking amount of 24.3 % in the European Union in 2011. [1] Polymers are used in numerous applications as for example packaging, paints, insulation, adhesives or as molded parts due to their inexpensiveness, good processability and their outstanding physical properties like formability, durability and chemical, electrical and thermal resistance.

Because of the limited global resources and the severe environmental challenges the world faces today sustainability has become a focal point in the chemical industry over the last decades. But not only because of these environmental issues but also in order to remain competitive in a global market a further development of classical processes and products is essential nowadays. Consequently, research and development (R & D) is more important for chemical companies than ever before. The energy intensity as measured by the energy input per unit of chemicals production already halved on a twenty year perspective as one of the results of these efforts. [1]

In the course of further development, the classical design process, which heavily relied upon intuition, experience and empiricism, shifted drastically towards new design alternatives being based on detailed physical and chemical modeling. This shift was mainly facilitated by the decreasing cost of computers and the developments in computational science, which meanwhile allow to perform complex calculations at low computational costs. Detailed modeling can not only provide a better insight into production processes and predict product properties but in some cases may even completely render expensive experimental setups unnecessary and be a stand-alone tool for innovative new design of processes.

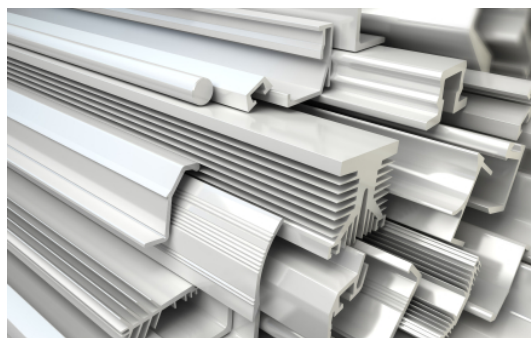


**Figure 1.1:** Variety of extrusion profiles.

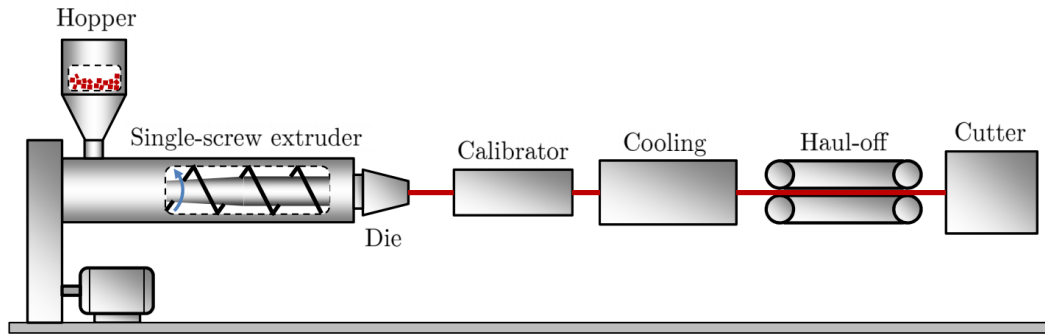


**Figure 1.2:** Sketch of a profile extrusion line.

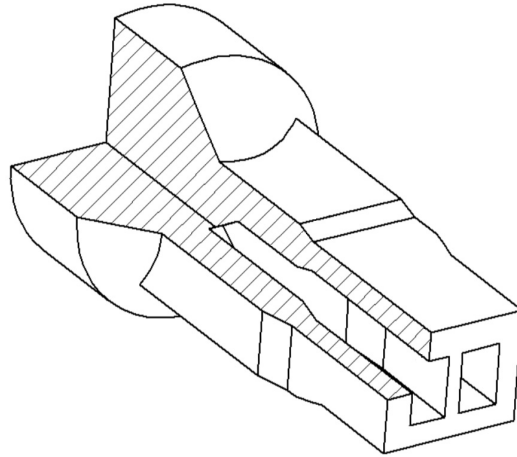
Computational Fluid Dynamics (CFD) is a promising and already well-established discipline in the field of numerical modeling. By use of CFD the behavior of fluids in the production process can be predicted and thereby assist to propose better apparatus designs and improve product properties. As an example CFD is nowadays widely used in designing profile extrusion lines. Films, pellets, cables, tubes and differently shaped profiles (cf. Fig. 1.1) are examples of the variety of extrusion products.

Fig. 1.2 shows a typical plastics profile extrusion line, which commonly consists of a single-screw extruder, which is fed with plastic pellets through a hopper, the extrusion die, a calibrator and cooling stage, a haul-off and a saw. The extruder melts and homogenizes the polymer and builds up the required pressure to feed the extrusion die. The extrusion die gives the polymer the desired form of the profile. The calibrator has two objectives, which are to prescribe final outer dimensions of the profile and to solidify the outer layers of the polymer to ensure sufficient rigidity for the remaining cooling step. [2] Subsequently, the profile is hauled-off and cut to a specified length. A typical extrusion die is shown in Fig. 1.3: the main objective of extrusion die design is to find an optimal die geometry such that a continuous polymer stream is shaped into an extrudate profile with the prescribed product dimensions. [3] This main objective is mostly achieved by finding a balanced die, which delivers the polymer at a uniform velocity over the cross-section to the exit. [4] The opposite - flow imbalance - leads to distortion of the profile.

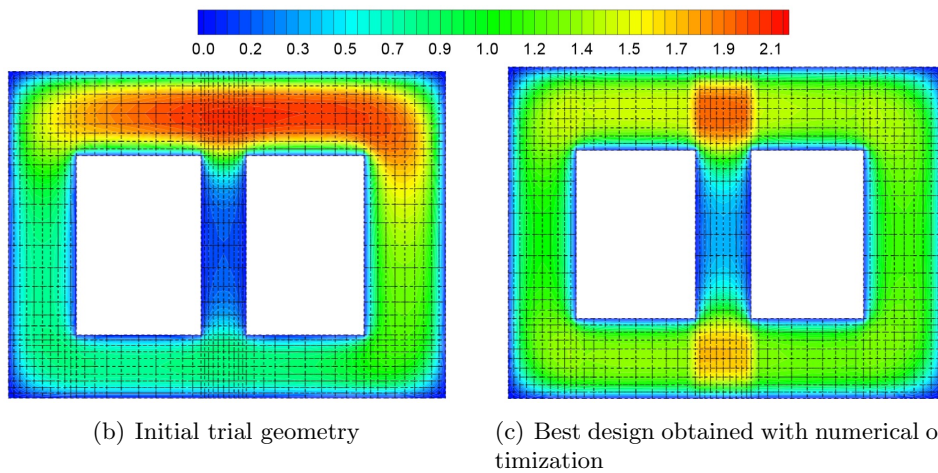


**Figure 1.3:** Example of an extrusion die.

## 1 Introduction



(a) Flow channel of a profile extrusion die



(b) Initial trial geometry

(c) Best design obtained with numerical optimization

**Figure 1.4:** Flow channel (a) and simulated ratios between axial velocity and the objective velocity at the die exit (b, c). [5]

Unfortunately, finding a balanced die is a difficult task even for rather simple profiles. Besides that, there are many - sometimes even conflicting - secondary objectives that need to be fulfilled such as a low pressure drop over the die, a maximum possible production rate of the extrudate as well as a high quality of the product in terms of a minimum level of internal stresses and the avoidance of rheological defects and thermal degradation. [6] The traditional die design approach requires the designer to vary the die geometry on a trial-and-error basis. This process is repeatedly started over again before finding the desired die shape. As such, this approach relies extensively on the experience of the designer and is a very time consuming and cost expensive task. Recently, the possibilities of using CFD in this design stage were discovered, see for example Wang [7]. By use of CFD the flow at the die exit can be predicted numerically from the rheological properties and the operating conditions and thereby help to drastically reduce the number of die prototypes and significantly speed up this design process and reduce the costs. By now, even completely automated optimization routines were developed by parametrizing the geometry and aggregating the various objectives in a single objective function. [8, 9] In Fig. 1.4 (a) the flow channel of a profile extrusion die used

in the optimization study of Nóbrega et al. [5] is depicted. A comparison of the numerically predicted velocity at the die exit cross-section for the initial trial design and the optimized design is shown in Fig. 1.4 (b) and (c). With use of the automatic optimization routine a die design was found, which is much more balanced in terms of having a more uniform axial velocity at the die exit compared to the initial design.

In spite of these achievements, there is still a gap between the engineer's need and the current state-of-the-art and challenges in numerical modeling - and here in particular in CFD simulation of polymer processing - still remain at hand: typically, polymeric flows include numerous phenomena, which require the use of models to describe these as for instance non-isothermicity, viscoelasticity and multiphase flows. In most of the currently performed numerical studies one or often even more phenomena are neglected and/or drastically simplified. However, the predicted results will only be as good as the ability of the model itself to describe the real-world [10] and in some cases the predicted behavior may - as a result of these simplifications - severely deviate from the real behavior. Furthermore, due to the nature of molten polymers the flow behavior is very complex, which commonly requires the simulations to be performed three-dimensionally and transiently. However, this is very expensive in terms of computation time and thus high-order methods to obtain accurate solutions even on coarse grids and time-steps as well as fast solution strategies are highly needed.

## 1.2 Objectives

The objective of this thesis is to develop new numerical models and improve existing ones for use in the field of polymer processing. Thereby, focus is set on the development and implementation of models for viscoelastic multiphase flows, non-isothermal models as well as improving the underlying numerical algorithms in terms of stability, accuracy and efficiency. This thesis is organized such that each chapter can be read independently of each other.

In *Chapter 2* the fundamental and comprehensive theory for the following chapters is presented. Focus is set on viscoelastic behavior in general, conservation laws to describe the behavior of fluid flows and the numerical solution of which by use of the finite volume method.

A semi-implicit method for handling the viscoelastic constitutive equation to promote stability and avoid checkerboarding effects is developed in *Chapter 3*. Simulation results for the viscoelastic flow in a three-dimensional planar and a three-dimensional square-square contraction are presented to show the benefits of using this technique. Comparison of the numerical predictions is pursued with experimental measurements and other simulation results depicted from the literature.

## 1 Introduction

In *Chapter 4* The log-conformation reformulation (LCR) is implemented in the collocated finite volume method OpenFOAM<sup>®</sup> in order to remedy the high Weissenberg number problem, which is a general numerical instability in the simulation of viscoelastic flows. The implementation is outlined and focus is set on efficiency and accuracy. Validation is done by comparison with an analytical solution for the startup Poiseuille flow of a viscoelastic fluid. Simulation results for time-dependent and three-dimensional lid-driven flows under demanding conditions are subsequently presented.

A general module to handle non-isothermal effects in viscoelastic flows is developed in *Chapter 5*. Furthermore, an accurate extrapolation boundary condition for the viscoelastic constitutive equation on solid walls is developed, which can be used for any type of mesh and viscoelastic constitutive equation. A steady viscoelastic Poiseuille flow shows the improved accuracy of the boundary condition. Simulation of non-isothermal flows in an axisymmetric contraction are presented and the results compared to a similar numerical study.

A new two-phase model for viscoelastic fluids governed by the Oldroyd-B equation is derived in *Chapter 6*. The derivation is based on conditional volume averaging of the single-phase equations and subsequent closure modeling. Reformulation of the model, which is motivated from a numerical point of view, is done and the numerical implementation is outlined. Thorough validation of the model is pursued with basic flow scenarios including a single-phase Poiseuille flow as well as a two-phase shear flow and a pressure-driven flow of stratified fluids. Surface tension closure is tested with a quiescent cylinder.

In *Chapter 7* the conditionally volume averaged viscoelastic two-phase model is improved in order to be able to handle moving and deforming interfaces. As it was shown that the model requires a sufficient spatial resolution of the interfacial transition region an intermediate step is adopted in order to ensure a constant interface thickness. The intermediate step is tested with a rotating cylinder. Two-dimensional and three-dimensional simulations of a Newtonian droplet deforming in a viscoelastic matrix under steady simple shear is presented and comparison is made with experimental data.

In *Chapter 8* the question of frame invariance of viscous dissipation is addressed, which is a controversial subject in literature. Single-screw extruders are often simplified in analytical approaches by keeping the screw fixed and rotating the barrel. The question, whether the results obtained are equal to the real case, in which the barrel is stationary and barrel is rotated, is addressed by transient two-dimensional and three-dimensional simulations of the temperature rise in a single-screw extruder.

The final *Chapter 9* gives a summary of this thesis and provides suggestions for further research, which are either directly tied to the manuscripts presented in this work or serve as proposals for new fields of research.

## 1.A Literature

- [1] Cefic, Facts and figures 2012: The european chemicals industry in a worldwide perspective (2012).
- [2] J. M. Nóbrega, O. S. Carneiro, J. A. Covas, F. T. Pinho, P. J. Oliveira, Design of Calibrators for Extruded Profiles. Part 1: Modeling the Thermal Interchanges, *Polym. Eng. Sci.* 44 (12) (2004) 2216–2228.
- [3] H. H. Winter, H. G. Fritz, Design of dies for the extrusion of sheets and annular parisons: the distribution problem, *Polym. Eng. Sci.* 26 (1986) 543–553.
- [4] A. Zolfaghari, A. H. Behraves, E. Shakouri, E. Soury, An innovative method of die design and evaluation of flow balance for thermoplastics extrusion profiles, *Polym. Eng. Sci.* 49 (2009) 1793–1799.
- [5] J. M. Nóbrega, O. S. Carneiro, F. T. Pinho, P. J. Oliveira, Flow Balancing in Extrusion Dies for Thermoplastic Profiles, *Int. Polym. Proc.* 18 (12) (2003) 307–312.
- [6] O. S. Carneiro, J. M. Nóbrega, F. T. Pinho, P. J. Oliveira, Computer aided rheological design of extrusion dies for profiles, *J. Mater. Process. Technol.* 114 (2001) 75–86.
- [7] Y. Wang, The flow distribution of molten polymers in slit dies and coathanger dies through three-dimensional finite element analysis, *Polym. Eng. Sci.* 31 (1991) 204–212.
- [8] S. R. Vaddiraju, M. Kostic, L. Reifschneider, A. Pla-Dalmau, V. Rykalin, A. Bross, Extrusion simulation and experimental validation to optimize precision die design, *SPE ANTEC Tech. Papers* 1 (2004) 76–80.
- [9] N. Lebaal, F. Schmidt, S. Puissant, D. Schlaefli, Design of optimal extrusion die for a range of different materials, *Polym. Eng. Sci.* 49 (2009) 432–440.
- [10] J. H. Ferziger, M. Peric, *Computational methods for fluid dynamics*, Springer, 2002.



# 2 Theory

## 2.1 Viscoelasticity

Polymers consist of long-chain macromolecules, which are composed of repeated subunits. Due to their complex chemical structure the rheological behavior of molten polymers is non-Newtonian since it is considerably different from ideally Newtonian fluids. In particular, polymers are classified as viscoelastic materials. Viscoelasticity means that polymers show an intermediate behavior in between that of ideal fluids, which behave purely viscous, and ideal solids, which behave purely elastic. If polymers are deformed at small deformation amplitudes and deformation rates the macromolecules have given enough time to relax through Brownian motion and the linear viscoelastic range prevails. However, if deformation amplitudes and rates increase, the time to relax becomes smaller and the macromolecules start to orient with the flow. As a result, their behavior becomes dependent on time, deformation and deformation rate and non-linearity of material properties prevails. [1]

### 2.1.1 Linear viscoelasticity

#### Relaxation time

In accordance to Owens and Phillips [2] the small deformation of a rectangle  $OABC$  to the parallelogram  $OAB'C'$  within the time-interval  $\Delta t = t_2 - t_1$  is considered in the following, see Fig. 2.1. The angle  $\Theta$ , which is independent of the coordinates  $x$ ,  $y$  and  $z$ , is called strain. For small strain  $\Theta$  one can define a relative deformation gradient  $\gamma_{xy}(t_2, t_1)$

$$\gamma_{xy}(t_2, t_1) = \frac{x(t_2) - x(t_1)}{y(t_1)} = \tan \Theta(t_2) \stackrel{\Theta \rightarrow 0}{\approx} \Theta(t_2) \quad (2.1)$$

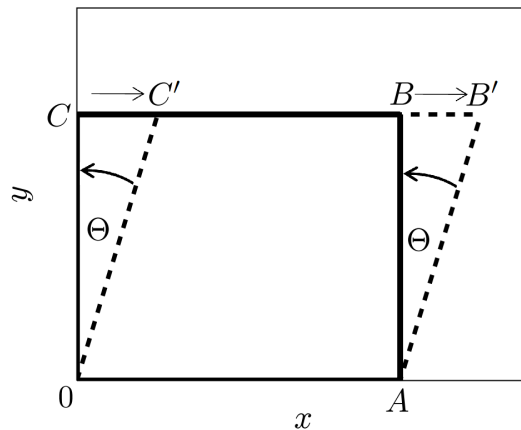


**Figure 2.1:** Shear deformation of a square region  $OABC$  about the angle  $\Theta$  to the parallelogram  $OAB'C'$  within the time interval  $\Delta t = t_2 - t_1$ . [2]

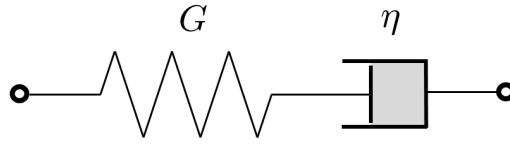


**Figure 2.2:** Spring with modulus  $G$  and damper with viscosity  $\eta$  connected in series (Maxwell model).

For a Hookean spring the relation between shear stress  $\sigma_{xy}$  and strain  $\Theta$  is linear

$$\sigma_{xy}(t) = G\Theta(t) \quad (2.2)$$

$G$  is the rigidity modulus of the material. If the material is a Newtonian fluid the relation between shear stress  $\sigma_{xy}$  and rate of deformation  $\dot{\gamma}_{xy}$  is linear

$$\sigma_{xy}(t) = \eta \dot{\gamma}_{xy} \left( \overset{\Theta \rightarrow 0}{\approx} \eta \frac{\partial \Theta}{\partial t} \right) \quad (2.3)$$

In the following a step function in time is considered for strain  $\Theta(t)$ , which can mathematically be written as a heaviside-function

$$\Theta(t) = \Theta_0 H(t) = \begin{cases} 0 & \text{if } t < 0 \\ \Theta_0/2 & \text{if } t = 0 \\ \Theta_0 & \text{if } t > 0 \end{cases} \quad (2.4)$$

The resulting stress in a Hookean linear elastic material is

$$\sigma_{xy}(t) = G\Theta_0 H(t) \quad (2.5)$$

The shear stress is constant in time with a value of  $G\Theta_0$  after imposition of the strain  $\Theta_0$ . For a Newtonian fluid the resulting shear stress is

$$\sigma_{xy}(t) = \eta\Theta_0\delta(t) \quad (2.6)$$

where  $\delta(t)$  is the Dirac delta function. The abrupt strain results in an infinite stress value at time  $t = 0$  and is  $0 \forall t \neq 0$ .

The simplest possibility to describe viscoelastic material behavior is by combination of an elastic spring and a viscous damper, which are connected in series, see Fig. 2.2. This is the so-called Maxwell model. Stress is equal in the damper and spring,  $\sigma_{xy}(t) = \sigma_{xy,V}(t) = \sigma_{xy,E}(t)$ , and strain (or rate of deformation) sums up,  $\Theta(t) = \Theta_V(t) + \Theta_E(t)$  (or  $\dot{\gamma}_{xy}(t) = \dot{\gamma}_{xy,V}(t) + \dot{\gamma}_{xy,E}(t)$ ). Thus, one can write

$$\dot{\gamma}_{xy}(t) = \frac{\partial \gamma_{xy,V}}{\partial t} + \frac{\partial \gamma_{xy,E}}{\partial t} = \frac{1}{\eta} \sigma_{xy}(t) + \frac{1}{G} \frac{\partial \sigma_{xy}}{\partial t} \quad (2.7)$$

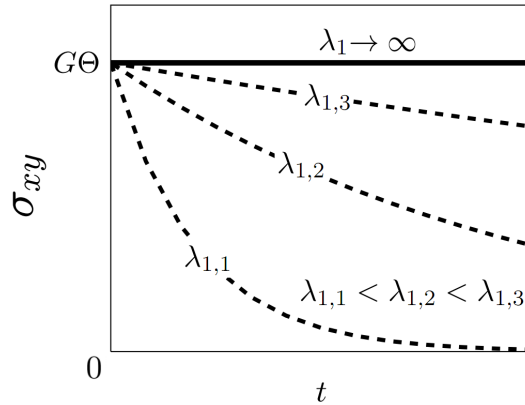


**Figure 2.3:** Stress  $\sigma_{xy}$  as a function of time  $t$  for three different relaxation times  $\lambda_{1,i}$ .

Integration of Eq. 2.7 leads to the following expression [2]

$$\sigma_{xy}(t) = \int_{s=-\infty}^t \frac{\eta}{\lambda_1} \exp\left(-\frac{t-s}{\lambda_1}\right) \gamma_{xy}(s) ds \quad (2.8)$$

The constant  $\lambda_1 = \eta/G$  is called *relaxation time*. Considering the step-strain function described by Eq. 2.4 the Maxwell model has the following particular solution [2]

$$\sigma_{xy}(t) = G\Theta_0 \exp\left(-\frac{t}{\lambda_1}\right) \quad (2.9)$$

From Eq. 2.9 one finds that the initial stress  $G\Theta_0$  caused by the sudden strain  $\Theta_0$  relaxes exponentially to  $G\Theta_0 e^{-1}$  within the time interval  $\lambda_1 = \eta/G$ . The Maxwell model thus predicts exponential decay of stress as exerted by a constant strain. This can be thought of an exponentially fading memory of the material. If the viscosity of the damper is decreased or the elasticity of the spring is increased, the time required for relaxation of the stress increases and vice versa. This is shown in Fig. 2.3, in which Eq. 2.9 is plotted for three different relaxation times and the limiting case of  $\lambda_1 \rightarrow \infty$ , which corresponds to a purely elastic material. Relaxation times can vary from  $10^{-12}$  s for water to 28 h for glass. Low density polyethylene has a typical relaxation time in the range of 10 s. [2]

The ratio between relaxation time and observation time  $T$  of the process under consideration is called the *Deborah number*  $De$  and characterizes the rheological behavior of the material

$$De = \frac{\lambda_1}{T} \quad (2.10)$$

Viscous materials with  $\lambda_1 \rightarrow 0$  result in  $De \rightarrow 0$  and elastic materials with  $\lambda_1 \rightarrow \infty$  in  $De \rightarrow \infty$ . Low values of  $De$  correspond to viscous material behavior and large values in elastic material behavior. In contrast, if the observation time increases the material will behave more viscous than in a shorter period of time. This way one can explain for example that glass is commonly understood as a solid material, but given a long enough period of time

glass can indeed flow. Another dimensionless number used in this regard is the *Weissenberg number*  $Wi$  (sometimes denoted  $We$ ), which is the ratio of the relaxation time of the material and a characteristic time of the flow, e.g. the inverse of the rate of deformation  $\dot{\gamma}_{xy}^{-1}$

$$Wi = \lambda_1 \dot{\gamma}_{xy} \quad (2.11)$$

If the flow under consideration is fast and rapid deformations occur ( $\dot{\gamma}_{xy}^{-1} \rightarrow 0$ ), the material will not be given enough time to relax and adapt to the flow and thus behavior of the material becomes more elastic. However, such a clear discrimination between the *Deborah number* and the *Weissenberg number* is not always made in literature and they are often used synonymously.

### Relaxation spectra

Polymers are generally composed of macromolecules of different chain length. As a result, such materials exhibit a relaxation time spectrum rather than a single relaxation time. A more sophisticated model to describe such a material is the generalized Maxwell model, which consists of  $n$  Maxwell elements connected in parallel, see Fig. 2.4. Each macromolecule chain length is represented by a Maxwell entity and associated with a characteristic relaxation time  $\lambda_{1,i}$ . In this model, strain (or rate of deformation) is equal in all Maxwell entities and the total stress is the sum of the stress of all Maxwell entities  $\sigma_{xy,i}(t)$

$$\sigma_{xy}(t) = \sum_{i=1}^n \sigma_{xy,i}(t) \quad (2.12)$$

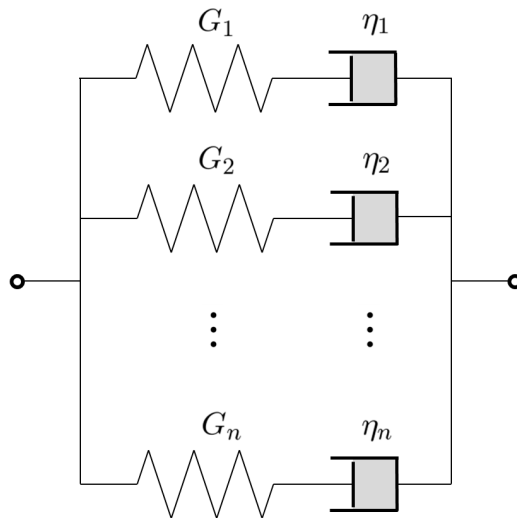


**Figure 2.4:** Generalized Maxwell model represented by  $n$  Maxwell models connected in parallel.

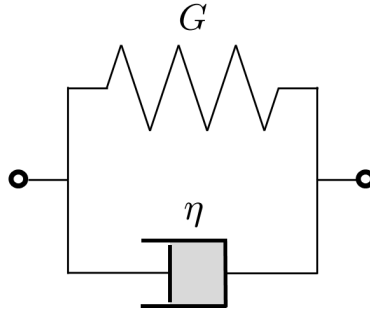


**Figure 2.5:** Spring with modulus  $G$  and damper with viscosity  $\eta$  connected in parallel (Kelvin model).

### Retardation time

The Maxwell model cannot describe the behavior of creep and of creep recovery, a behavior commonly exhibited by viscoelastic solids. [1] We will therefore consider the sudden imposition of a shear stress in accordance to Owens and Phillips [2] in the following

$$\sigma_{xy}(t) = \begin{cases} 0 & \text{if } t < 0 \\ \sigma_{xy,0} & \text{if } t \geq 0 \end{cases} \quad (2.13)$$

A Hookean spring will strain instantaneously at time  $t = 0$  to the level  $\frac{\sigma_{xy,0}}{G}$

$$\Theta(t) = \begin{cases} 0 & \text{if } t < 0 \\ \frac{\sigma_{xy,0}}{G} & \text{if } t \geq 0 \end{cases} \quad (2.14)$$

A Newtonian fluid on the other hand will start to flow with the rate of deformation being  $\frac{\sigma_{xy,0}}{\eta}$

$$\gamma_{xy}(t) = \begin{cases} 0 & \text{if } t < 0 \\ \frac{\sigma_{xy,0}}{\eta}t & \text{if } t \geq 0 \end{cases} \quad (2.15)$$

In order to describe creep behavior, the material is modeled with a viscous damper and an elastic spring connected in parallel, see Fig. 2.5. This is the so-called Kelvin model. Strain (or rate of deformation) is equal in the spring and damper  $\Theta(t) = \Theta_V(t) = \Theta_E(t)$  (or  $\dot{\gamma}_{xy}(t) = \dot{\gamma}_{xy,V}(t) = \dot{\gamma}_{xy,E}(t)$ ) and stress sums up  $\sigma_{xy}(t) = \sigma_{xy,V}(t) + \sigma_{xy,E}(t)$ . Thus, one can write

$$\sigma_{xy}(t) = G\Theta + \eta\frac{\partial\Theta}{\partial t} \quad (2.16)$$

The solution of Eq. 2.16 with the stress function given in Eq. 2.13 is [2]

$$\Theta(t) = \frac{\sigma_{xy,0}}{G} \left[ 1 - \exp\left(-\frac{t}{\lambda_2}\right) \right] \quad (2.17)$$

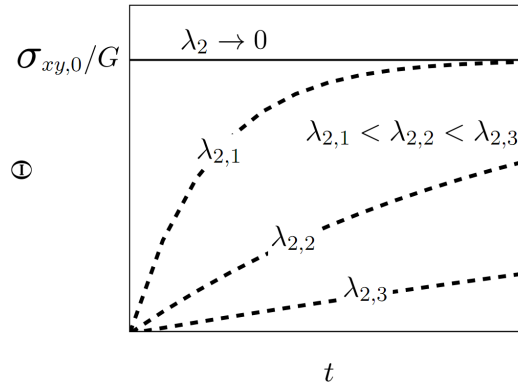


**Figure 2.6:** Strain  $\Theta$  as a function of time  $t$  for three different retardation times  $\lambda_{2,i}$ .

$\lambda_2 = \eta/G$  is called *retardation time*. In contrast to an elastic material, which strains to the level  $\frac{\sigma_{xy,0}}{G}$  immediately after imposition of the stress, the strain of a viscoelastic material will reach the value  $\frac{\sigma_{xy,0}}{G}(1 - e^{-1})$  within the time interval  $\lambda_2$ . In Fig. 2.6 strain as a function of time is plotted for three different retardation times  $\lambda_{2,i}$  and an ideal elastic spring ( $\lambda_2 \rightarrow 0$ ). If the elasticity of the spring increases or the viscosity of the damper decreases, the material creeps faster and vice versa. Considering an experiment in which the stress is suddenly removed, the Kelvin model predicts complete strain recovery. Polymer melts in general do not show such a behavior, but creep recovery is only partial. In order to allow for such a behavior at least another damper must be connected in series. [1, 2]

The ratio between relaxation and retardation time is the so-called *retardation factor*  $\beta$  and determines the amount of creep to stress relaxation of a material

$$\beta = \frac{\lambda_1}{\lambda_2} \quad (2.18)$$

### 2.1.2 Non-linear viscoelasticity

Industrial processes for manufacturing polymers involve rapid and large deformations of the material and the non-linear viscoelastic range prevails. Properties such as viscosity become functions of time, deformation and rate of deformation. In the following the non-linear behavior of polymers under two ideal flow conditions often studied, which are a steady simple shear flow and a steady shear-free extensional flow, will be discussed.

#### Shear flow

Shear flows are easy to generate and thus most widely used in experimental characterization of polymers. A simple shear flow is defined by the following velocity field

$$\mathbf{U}_s(y) = \begin{pmatrix} \dot{\gamma}_{xy}y \\ 0 \\ 0 \end{pmatrix} \quad (2.19)$$

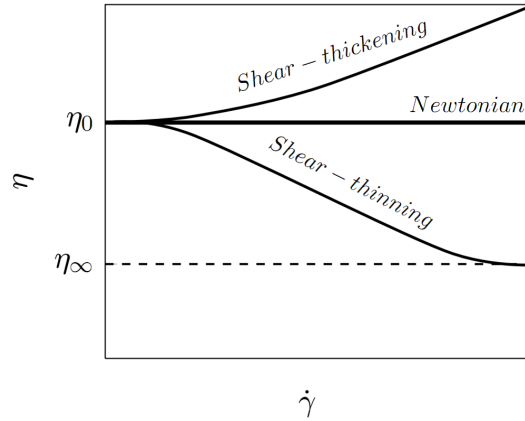


**Figure 2.7:** Shear viscosity  $\eta(\dot{\gamma})$ -functions as a function of shear-rate  $\dot{\gamma}$ .

For Newtonian fluids a linear relation between shear-rate and stress holds

$$\sigma_{xy} = \eta \frac{\partial \mathbf{U}_{s,x}}{\partial y} = \eta \dot{\gamma}_{xy} \quad (2.20)$$

Non-Newtonian fluids do not show a linear relationship. Instead, there is a non-linear relationship expressed by an apparent viscosity  $\eta(\dot{\gamma})$ , which is a function of the shear-rate  $\dot{\gamma} \equiv ||\dot{\gamma}_{xy}||$

$$\sigma_{xy} = \eta(\dot{\gamma}) \dot{\gamma}_{xy} \quad (2.21)$$

Viscosity is commonly also time-dependent for a viscoelastic fluid and viscosity as a function of shear-rate  $\dot{\gamma}$  as shown in Fig. 2.7 is usually reported under steady-state conditions

$$\eta(\dot{\gamma}) = \lim_{t \rightarrow \infty} \frac{\sigma_{xy}(t)}{\dot{\gamma}_{xy}} \quad (2.22)$$

Polymers show shear-thinning (or pseudo-plastic) behavior, while other non-Newtonian materials can also exhibit shear-thickening, see Fig. 2.7. The zero shear-rate viscosity  $\eta_0$  is defined as

$$\eta_0 = \lim_{\dot{\gamma} \rightarrow 0} \eta(\dot{\gamma}) \quad (2.23)$$

Besides a shear stress polymers exert normal stresses in steady simple shear and the Cauchy stress tensor takes the form

$$\boldsymbol{\sigma} = \begin{pmatrix} \sigma_{xx} & \sigma_{xy} & 0 \\ \sigma_{yx} & \sigma_{yy} & 0 \\ 0 & 0 & \sigma_{zz} \end{pmatrix} \quad (2.24)$$

It is noted here that the Cauchy stress tensor is always symmetric, i.e.  $\sigma_{xy} = \sigma_{yx}$ . Viscoelastic fluids can generally be considered as incompressible and thus normal stresses are isotropic and

## 2 Theory

do not cause any deformation. Only differences between normal stresses cause deformations and are of relevance. [1] Thus, another two viscometric functions besides the apparent viscosity  $\eta(\dot{\gamma})$  are identified, which are the first and a second normal stress difference,  $N_1$  and  $N_2$ , respectively

$$\sigma_{xx} - \sigma_{yy} = \Psi_1(\dot{\gamma}) \dot{\gamma}_{xy}^2 = N_1(\dot{\gamma}) \quad (2.25)$$

$$\sigma_{yy} - \sigma_{zz} = \Psi_2(\dot{\gamma}) \dot{\gamma}_{xy}^2 = N_2(\dot{\gamma}) \quad (2.26)$$

$\Psi_1$  and  $\Psi_2$  are called first and second normal stress coefficients, respectively.  $N_1$  is positive, while  $N_2$  is negative and much smaller for polymers. Presence of normal stress differences is the reason for quite spectacular flows such as die swelling and rod climbing. [2]

### Extensional flow

Knowledge of the behavior of polymers in extensional flows is important since many industrial processes, such as spinning, extrusion take-off or vacuum forming involve stretching of the fluid [3]. Three different types of extensional flows can be distinguished, which are uniaxial extensional flow

$$\mathbf{U}_u(x, y, z) = \begin{pmatrix} \dot{\epsilon}x \\ -\frac{\dot{\epsilon}}{2}y \\ -\frac{\dot{\epsilon}}{2}z \end{pmatrix} \quad (2.27)$$

biaxial extensional flow

$$\mathbf{U}_b(x, y, z) = \begin{pmatrix} \frac{\dot{\epsilon}}{2}x \\ \frac{\dot{\epsilon}}{2}y \\ -\dot{\epsilon}z \end{pmatrix} \quad (2.28)$$

and planar extensional flow [4]

$$\mathbf{U}_p(x, z) = \begin{pmatrix} \dot{\epsilon}x \\ 0 \\ -\dot{\epsilon}z \end{pmatrix} \quad (2.29)$$

A schematic view of the three extensional flows is shown in Fig. 2.8. The fluid undergoes no shearing and thus the Cauchy stress tensor takes the following general form

$$\boldsymbol{\sigma} = \begin{pmatrix} \sigma_{xx} & 0 & 0 \\ 0 & \sigma_{yy} & 0 \\ 0 & 0 & \sigma_{zz} \end{pmatrix} \quad (2.30)$$



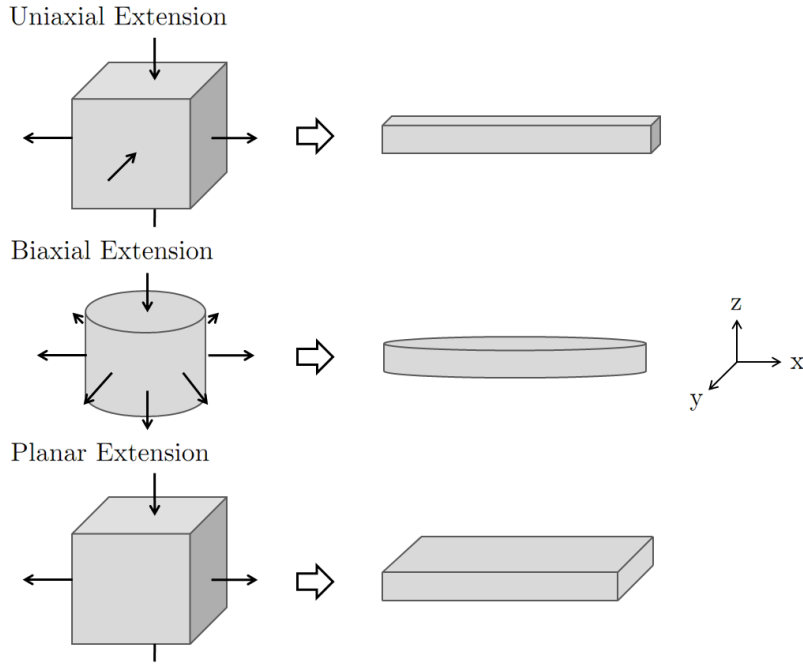


**Figure 2.8:** Schematic view of uniaxial, biaxial and planar extensional flow. [1]

In extension only one material property is measurable, which is the elongational viscosity. For uniaxial and planar extension, the elongational viscosity is defined as

$$\eta_E(\dot{\epsilon}) = \frac{\sigma_{xx} - \sigma_{yy}}{\dot{\epsilon}} \quad (2.31)$$

while for biaxial extension the elongational viscosity is [4]

$$\eta_{E,b}(\dot{\epsilon}) = \frac{\sigma_{xx} - \sigma_{zz}}{\dot{\epsilon}} \quad (2.32)$$

Again, elongational viscosities are functions of time  $t$  and viscosities are commonly reported under steady-state conditions

$$\eta_E(\dot{\epsilon}) = \lim_{t \rightarrow \infty} \frac{\sigma_{xx}(t) - \sigma_{yy}(t)}{\dot{\epsilon}} \quad (2.33)$$

The ratio between elongational viscosity and zero shear-rate viscosity is called Trouton ratio  $Tr(\dot{\epsilon}) = \frac{\eta_E(\dot{\epsilon})}{\eta_0}$ . For a Newtonian fluid in uniaxial extension the Trouton ratio is  $Tr = 3$ . Polymers have the same ratio only for close to zero elongational rates

$$\lim_{\dot{\epsilon} \rightarrow 0} \eta_{E,u}(\dot{\epsilon}) = 3\eta_0 \quad (2.34)$$

For small elongational rates polymers commonly exhibit extension-thickening and after undergoing a maximum in the Trouton ratio show extension-thinning for large extensional rates,

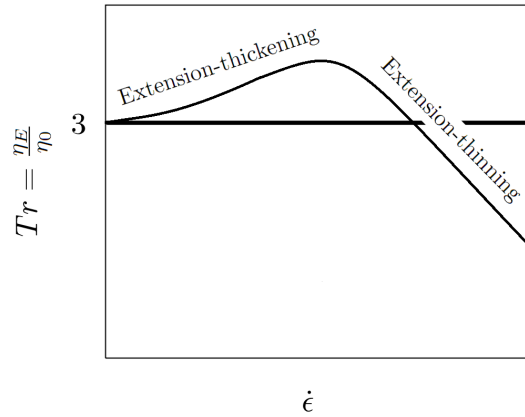


**Figure 2.9:** Trouton ratio  $Tr$  as a function of elongational rate  $\dot{\epsilon}$  in uniaxial extension.

see Fig. 2.9. The limit of the Trouton ratio for small elongational rates under planar extension is

$$\lim_{\dot{\epsilon} \rightarrow 0} \eta_{E,p}(\dot{\epsilon}) = 4\eta_0 \quad (2.35)$$

while for biaxial one finds [4]

$$\lim_{\dot{\epsilon} \rightarrow 0} \eta_{E,b}(\dot{\epsilon}) = 6\eta_0 \quad (2.36)$$

Extensional effects can play a major role for the fluid behavior. An example of a visually striking phenomenon is the tubeless syphon effect. [2]

### 2.1.3 Temperature dependencies

Material properties such as viscosity or relaxation time are dependent on temperature. In industrial polymer processing temperatures can vary over a wide range and consequently temperature dependencies have to be taken into account. If the viscoelastic material property can be shifted by a single factor to one master curve, the material is considered thermorheologically simple and time-temperature-superposition (TTS) can be used. In doing so, quantities of stress are shifted vertically with the factor  $b_T$  and quantities of time, such as relaxation time, horizontally with  $a_T$  [1]

$$\lambda_1(\dot{\gamma}, T) = a_T \lambda_{1,R}(\dot{\gamma}) \quad (2.37)$$

$T$  is temperature and  $\lambda_{1,R}$  is called reduced relaxation time. Viscosity, which is defined by stress divided by shear rate and thus includes both stress and time, is shifted with  $a_T/b_T$

$$\eta(\dot{\gamma}, T) = \frac{a_T}{b_T} \eta_R(\dot{\gamma}) \quad (2.38)$$

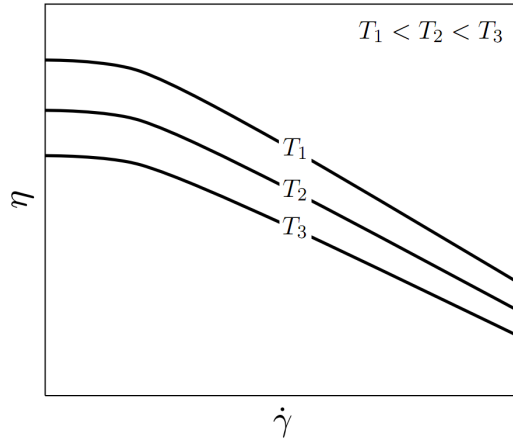


**Figure 2.10:** Shear viscosity  $\eta(\dot{\gamma}, T)$  as a function of shear-rate  $\dot{\gamma}$  for different values of temperature  $T$ .

Similar,  $\eta_R$  is called reduced viscosity. Due to the increased Brownian motion of the macromolecules, viscosity decreases with increasing temperature. This behavior is shown in Fig. 2.10.

The vertical shift factor is defined as [1]

$$b_T = \frac{T_{ref} \rho_{ref}}{T \rho} \quad (2.39)$$

where  $\rho$  is density and the index  $_{ref}$  refers to reference values for temperature and density. Usually  $b_T \approx 1$ , which is why the vertical shift can be neglected in most cases. [1] The horizontal shift is calculated with appropriate models, such as the Williams-Landel-Ferry (WLF) model [5]

$$\log(a_T) = -\frac{C_1(T - T_{ref})}{C_2 + (T - T_{ref})} \quad (2.40)$$

The WLF model can be used for  $T \leq T_g + 100K$ , where  $T_g$  is glass transition temperature. For higher temperatures, the Arrhenius law is more appropriate [1]

$$\log(a_T) = -\frac{E_A}{R} \left( \frac{1}{T} - \frac{1}{T_{ref}} \right) \quad (2.41)$$

Another model often used for modeling temperature dependencies of polymers is the Vogel equation [6]

$$\log(a_T) = C_1 + \frac{C_2}{T - T_{ref}} \quad (2.42)$$

### 2.1.4 Constitutive equations

In order to be able to predict the stresses in a fluid, closure relations for the Cauchy stress tensor  $\boldsymbol{\sigma}$  are needed, which relate the stresses to kinematics and material properties. Therefore, the Cauchy stress tensor is first decomposed as

$$\boldsymbol{\sigma} = -p\mathbf{I} + \boldsymbol{\tau} \quad (2.43)$$

where  $\mathbf{I}$  is the identity matrix and  $p$  is called pressure, which is defined as the negative average of the diagonal stress components  $p = -\frac{1}{3}\text{tr}(\boldsymbol{\sigma})$ .  $\text{tr}$  denotes the trace of a matrix and  $\boldsymbol{\tau}$  is the deviatoric stress or extra-stress tensor. [2]

#### Newtonian

According to Eq. 2.3 the Cauchy stress in a Newtonian fluid is proportional to the rate of deformation (or rate of strain). For a general type of flow the deviatoric stress can be calculated by [7]

$$\boldsymbol{\tau} = 2\eta\mathbf{D} - \frac{2}{3}\eta(\nabla \cdot \mathbf{U})\mathbf{U} = \eta \left[ \nabla\mathbf{U} + (\nabla\mathbf{U})^T - \frac{2}{3}(\nabla \cdot \mathbf{U})\mathbf{U} \right] \quad (2.44)$$

where  $2\mathbf{D}$  is the rate of deformation tensor. It is noted here that for an incompressible fluid  $\nabla \cdot \mathbf{U} = 0$  holds, which is why the last term of Eq. 2.44 is zero.

#### Generalized Newtonian Liquid

Generalized Newtonian Liquids are fluids in which the constant relationship between stress and rate of deformation is replaced by a more general non-linear relationship according to Eq. 2.21. This leads to

$$\boldsymbol{\tau} = 2\eta(\dot{\gamma})\mathbf{D} \quad (2.45)$$

The non-constant viscosity is a function of the shear-rate  $\dot{\gamma}$ , which is defined as the second invariant of the rate of deformation tensor [2]

$$\dot{\gamma} = 2\sqrt{\mathbf{D} : \mathbf{D}} \quad (2.46)$$

Model relations for  $\eta(\dot{\gamma})$  are for example Power-Law, Cross or Carreau. These models can be used for fitting data obtained from shear viscosity measurements (cf. Fig. 2.7). However, since generalized Newtonian Liquids do not exhibit normal stresses in steady simple shear elastic material behavior cannot be predicted their use is limited to relatively simple flows, in which elastic effects are negligible. [2]

### Viscoelastic

In order to be able to model arbitrary types of polymer flows and predict elastic effects, more sophisticated constitutive equations are needed. Viscoelastic constitutive equations can be categorized into differential and integral constitutive equations. In this work differential models will be considered only. The deviatoric stress tensor is commonly first decomposed into two additive terms, a Newtonian solvent contribution with viscosity  $\eta_S$  and a viscoelastic contribution  $\boldsymbol{\tau}_P$ , which is governed by an appropriate constitutive equation

$$\boldsymbol{\tau} = \boldsymbol{\tau}_S + \boldsymbol{\tau}_P = 2\eta_S\mathbf{D} + \boldsymbol{\tau}_P \quad (2.47)$$

Two viscoelastic constitutive equations, both from the family of Oldroyd-type equations, will be presented in the following since they are used in the subsequent chapters.

- Oldroyd-B

The perhaps simplest viscoelastic constitutive equation is the Oldroyd-B equation proposed by Oldroyd in 1950 [8]

$$\boldsymbol{\tau}_P + \lambda_1 \overset{\nabla}{\boldsymbol{\tau}}_P = \eta_P \left[ \nabla\mathbf{U} + (\nabla\mathbf{U})^T \right] \quad (2.48)$$

$\eta_P$  is the polymeric viscosity and  $\overset{\nabla}{\boldsymbol{\tau}}_P$  denotes the upper-convected time derivative, which is defined as

$$\overset{\nabla}{\boldsymbol{\tau}}_P = \frac{\partial \boldsymbol{\tau}_P}{\partial t} + \nabla \cdot (\mathbf{U}\boldsymbol{\tau}_P) - (\nabla\mathbf{U})^T \cdot \boldsymbol{\tau}_P - \boldsymbol{\tau}_P \cdot \nabla\mathbf{U} \quad (2.49)$$

The Oldroyd-B equation can be derived from molecular theory, in which dumbbells are suspended in a Newtonian solvent. The dumbbells consist of two beads connected by a spring obeying the Hookean Law. The Oldroyd-B model predicts a constant shear viscosity and an extensional viscosity, which blows up at a finite extensional rate, see Fig. 2.11. The model is only suitable for modeling dilute polymeric solutions. [2]

The retardation time of the model is

$$\lambda_2 = \frac{\eta_S}{\eta_P + \eta_S} \lambda_1 = \frac{\eta_S}{\eta_0} \lambda_1 \quad (2.50)$$

and consequently the retardation factor is

$$\beta = \frac{\eta_S}{\eta_0} \quad (2.51)$$

The Oldroyd-B model in conjunction with no solvent contribution ( $\eta_S = 0$  or  $\lambda_2 = 0$ ) reduces to the so-called upper-convected-Maxwell model.

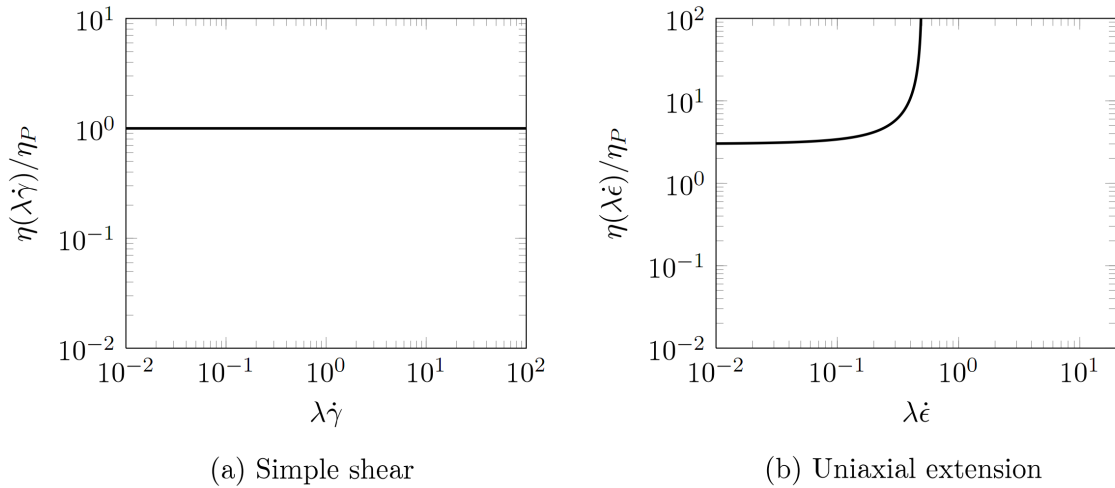


**Figure 2.11:** Shear viscosity (a) and extensional viscosity (b) as predicted by the Oldroyd-B model.

- Simplified Phan-Thien-Tanner (SPTT)

A more accurate viscoelastic constitutive equation is the simplified Phan-Thien-Tanner (SPTT) model, which was derived by network theory and can be used to model the rheological behavior of concentrated solutions and polymer melts. [9] Two versions of the SPTT model are available, an exponential and a linearized form. In this work, the linearized version will be used

$$\left(1 + \frac{\epsilon \lambda_1}{\eta_P} \text{tr}(\boldsymbol{\tau}_P)\right) \boldsymbol{\tau}_P + \lambda_1 \overset{\nabla}{\boldsymbol{\tau}}_P = \eta_P \left[\nabla \mathbf{U} + (\nabla \mathbf{U})^T\right] \quad (2.52)$$

$\epsilon$  is the extensibility parameter with which the extensional viscosity can be limited. It is noted that for  $\epsilon = 0$  the Oldroyd-B model is recovered. The shear and elongational viscosities predicted by the SPTT model predict are shown in Fig. 2.12 for three different values of  $\epsilon$ . The model predicts shear-thinning behavior and limits the elongational viscosity, which has a maximum for intermediate values of  $\lambda \dot{\epsilon}$  for small values of  $\epsilon$ .

- Multi-mode models

As already discussed polymers consist of macromolecules with not only a single chain length but a length distribution. Consequently, there is a relaxation spectrum rather than a single relaxation time. A relaxation spectrum is modeled according to Eq. 2.12

$$\boldsymbol{\tau}_P = \sum_{i=1}^N \boldsymbol{\tau}_{P,i} \quad (2.53)$$

The stress of each mode  $\boldsymbol{\tau}_{P,i}$  is calculated by a viscoelastic constitutive equation with the respective relaxation time  $\lambda_{1,i}$  and model parameters, such as for example polymeric viscosity  $\eta_{P,i}$  and extensibility parameter  $\epsilon_i$ .

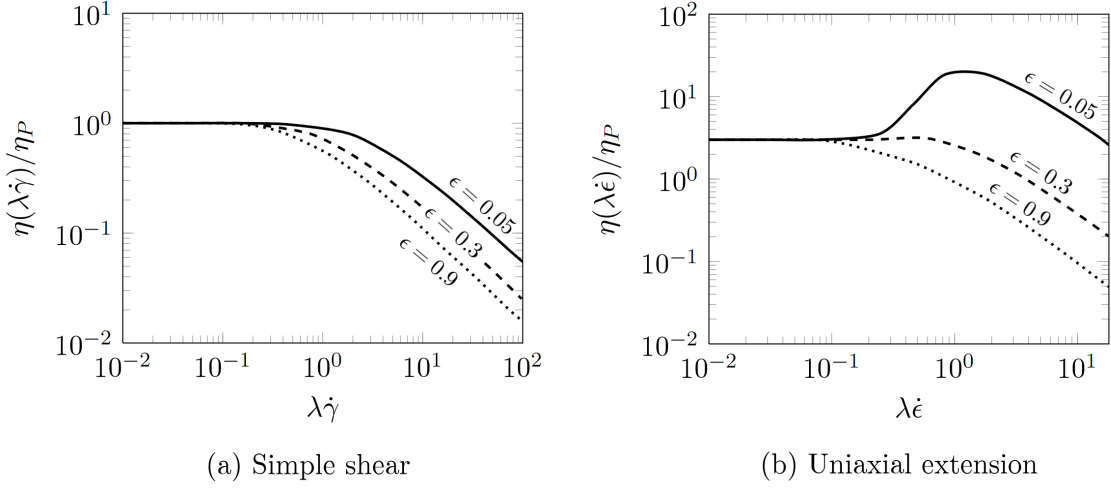


**Figure 2.12:** Shear viscosity (a) and extensional viscosity (b) as predicted by the SPTT model. [10]

## 2.2 Conservation laws

Conservation laws are derived from conservation of extensive properties such as mass, linear and angular momentum, species or energy. Conservation of mass states that for a closed system mass  $m$  must remain constant over time  $t$  ( $\frac{dm}{dt} = 0$ ), while for momentum conservation the rate of change of momentum must equal to the external forces  $F$  acting on the closed system ( $\frac{d(m\mathbf{U})}{dt} = F$ ). Energy conservation holds if the rate of change of internal energy equals the sources and sinks  $W$  of the same ( $\frac{d(mu)}{dt} = W$ ). [11]

The respective extensive property  $\Phi$  can be calculated by integration of an intensive property  $\varphi$  over the closed system - the control mass  $CM$  - according to [7]

$$\Phi = \int_{V_{CM}} \rho\varphi dV \quad (2.54)$$

where  $V_{CM}$  is the volume of the control mass. With use of the Reynolds-Transport-Theorem Eq. 2.54 can be formulated in terms of control volumes  $CV$  [7]

$$\frac{d}{dt} \int_{V_{CM}} \rho\varphi dV = \frac{d}{dt} \int_{V_{CV}} \rho\varphi dV + \oint_{S_{CV}} \rho\varphi(\mathbf{U} - \mathbf{U}_b) \cdot \mathbf{n}_S dS \quad (2.55)$$

where  $S$  is the surface area,  $\mathbf{U}_b$  is the velocity of the control volume surface at point  $S$  and the vector  $\mathbf{n}_S$  is the unit normal vector pointing outward of the control volume at point  $S$ . It is most convenient to consider steady control volumes, thus  $\mathbf{U}_b = 0$ . Volumetric

and surface-based sources and sinks,  $Q_V$  and  $\mathbf{Q}_S$ , respectively, can be distinguished and one obtains a general conservation equation [11]

$$\frac{d}{dt} \int_{V_{CV}} \rho \varphi dV + \oint_{S_{CV}} \rho \varphi \mathbf{U} \cdot \mathbf{n}_S dS = \int_{V_{CV}} Q_V(\varphi) dV + \oint_{S_{CV}} \mathbf{Q}_S(\varphi) \cdot \mathbf{n}_S dS \quad (2.56)$$

An equivalent differential form can be formulated

$$\frac{\partial \rho \varphi}{\partial t} + \nabla \cdot (\rho \mathbf{U} \varphi) = Q_V(\varphi) + \nabla \cdot \mathbf{Q}_S(\varphi) \quad (2.57)$$

Conservation of mass, for which  $\varphi = 1$ , leads to

$$\frac{\partial \rho}{\partial t} + \nabla \cdot (\rho \mathbf{U}) = 0 \quad (2.58)$$

The rate of change of linear momentum, for which  $\varphi = \mathbf{U}$ , must equal the surface-force exerted by the Cauchy stress tensor  $\boldsymbol{\sigma}$  and the force exerted by gravity, which is a volumetric source

$$\frac{\partial \rho \mathbf{U}}{\partial t} + \nabla \cdot (\rho \mathbf{U} \mathbf{U}) = \nabla \cdot \boldsymbol{\sigma} + \rho \mathbf{g} \quad (2.59)$$

Conservation of energy, for which  $\varphi = u$ , states that the rate of change of internal energy must equal the energy transported by conduction, which is denoted by the term  $\nabla \cdot \mathbf{q}$ . All other possible sources/sinks are summarized in the term  $\rho Q_u$

$$\frac{\partial \rho u}{\partial t} + \nabla \cdot (\rho \mathbf{U} u) = -\nabla \cdot \mathbf{q} + \rho Q_u \quad (2.60)$$

Polymers can commonly be considered as incompressible ( $\rho = \text{const.}$ ) and thus the conservation of mass simplifies to

$$\nabla \cdot \mathbf{U} = 0 \quad (2.61)$$

Incompressibility and use of the decomposition of the Cauchy stress tensor and the deviatoric stress tensor according to Eqs. 2.43 and 2.47, respectively, leads to

$$\frac{\partial \mathbf{U}}{\partial t} + \nabla \cdot (\mathbf{U} \mathbf{U}) - \nabla \cdot \nu_S \nabla \mathbf{U} = -\nabla p^* + \frac{1}{\rho} \nabla \cdot \boldsymbol{\tau}_P \quad (2.62)$$

where  $\nu_S = \frac{\eta_S}{\rho}$  is the kinematic viscosity. By use of a modified pressure  $p^* = \frac{1}{\rho} (p - \rho \mathbf{g} \cdot \mathbf{x})$  the gravity term cancels out.  $\mathbf{x}$  denotes the position vector. [7]



Assuming constant pressure and incompressibility the internal energy can be written as  $\partial u = c_P \partial T$  and thus the conservation of energy can be reformulated to an equation for temperature  $T$  [7]

$$\frac{\partial T}{\partial t} + \nabla \cdot (\mathbf{U}T) - \nabla \cdot \frac{k}{\rho c_P} \nabla T = \frac{1}{c_P} Q_u \quad (2.63)$$

In Eq. 2.63 heat conduction was expressed by Fourier's Law  $\mathbf{q} = -k \nabla T$ , where  $k$  is the thermal conductivity.

## 2.3 Finite volume method

The conservation laws, Eqs. 2.61-2.63, in conjunction with an appropriate viscoelastic constitutive equation, Eqs. 2.48, 2.52 or 2.53, constitute a set of partial differential equations, which cannot be solved analytically for almost any problem. Thus, numerical procedures are required for solution by discretizing the solution domain in time and space. Appropriate discretization techniques are for example finite difference method (FDM), finite element method (FEM) or finite volume method (FVM). The latter of which is used in this thesis and shortly outlined in the following.

### 2.3.1 Discretization of the solution domain

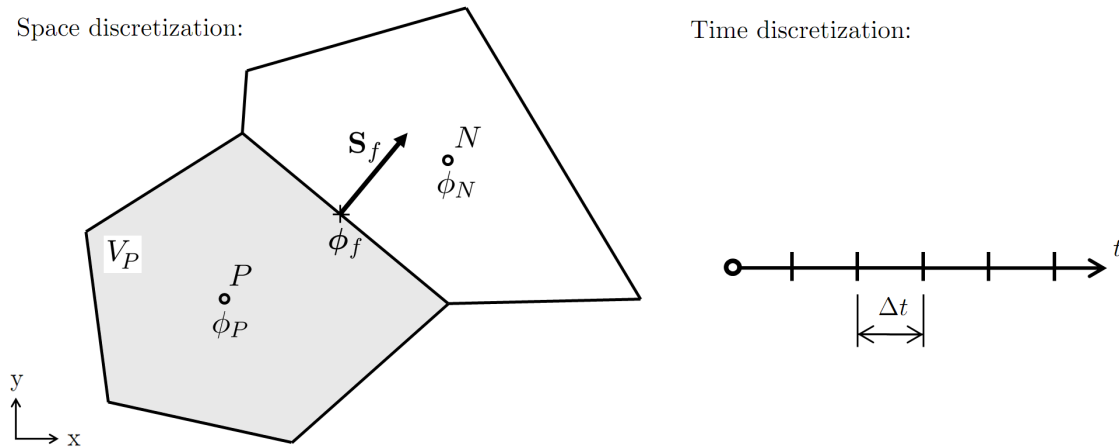


**Figure 2.13:** Space and time discretization in the finite volume method.

The solution domain is first discretized in space and time, see Fig. 2.13. Time discretization is achieved by dividing the continuous time into a finite number of discrete time-steps  $\Delta t$ . Space discretization is achieved by dividing the solution domain into a finite number of non-overlapping volumes (or cells). Finite volume methods can be distinguished between staggered and collocated methods. In the staggered method, variables are defined and stored in either the cell center or the cell face, while in the collocated finite volume method all variables  $\phi$  are stored in the cell center and values on cell faces  $\phi_f$  are obtained from interpolation of the

values of adjacent cells. The collocated finite volume method will be used in this work. Cell centers  $\mathbf{x}_P$  and cell face centers  $\mathbf{x}_f$  are defined in the center of mass [12]

$$\int_{V_P} (\mathbf{x} - \mathbf{x}_P) dV = 0, \quad \int_{S_f} (\mathbf{x} - \mathbf{x}_f) dS = 0 \quad (2.64)$$

### 2.3.2 Equation discretization

All partial differential equations Eqs. 2.61-2.63 and Eqs. 2.48 and 2.52 have a similar form and can be reduced to a standard transport equation for the variable  $\phi$  [11]

$$\underbrace{\frac{\partial \phi}{\partial t}}_{\text{temporal term}} + \underbrace{\nabla \cdot (\mathbf{U}\phi)}_{\text{convection term}} - \underbrace{\nabla \cdot (\Gamma_\phi \nabla \phi)}_{\text{diffusion term}} = \underbrace{S_\phi(\phi)}_{\text{source term}} \quad (2.65)$$

$\Gamma_\phi$  is the diffusion coefficient. Only four different terms arise in the standard transport equation, which are the temporal term, the convection term, the diffusion term and a source term. For solution of Eq. 2.65 the standard transport equation is first integrated over the volume of cell  $P$ ,  $V_P$ ,

$$\int_{V_P} \frac{\partial \phi}{\partial t} dV + \int_{V_P} \nabla \cdot (\mathbf{U}\phi) dV - \int_{V_P} \nabla \cdot (\Gamma_\phi \nabla \phi) dV = \int_{V_P} S_\phi(\phi) dV \quad (2.66)$$

Eq. 2.66 will be used to discuss the discretization practices of the four terms in the following.

- Temporal term

Discretization of the temporal term can be achieved with the *Euler* method according to

$$\int_{V_P} \frac{\partial \phi}{\partial t} dV = \frac{\phi^{n+1} - \phi^n}{\Delta t} V_P \quad (2.67)$$

where the exponents  $n$  and  $n + 1$  of the variable  $\phi^n$  and  $\phi^{n+1}$  denote  $\phi^n = \phi(t)$  and  $\phi^{n+1} = \phi(t + \Delta t)$ , respectively. The Euler method is first-order accurate and bounded if the remaining terms (the convection, diffusion and source term) are calculated at time-level  $n + 1$ . In this case the method is called *implicit* Euler

$$\frac{\phi^{n+1} - \phi^n}{\Delta t} V_P = R(\phi^{n+1}) \quad (2.68)$$

On the other, if the remaining terms are calculated with the value of the variable at time-level  $n$  the method is called *explicit* Euler

$$\frac{\phi^{n+1} - \phi^n}{\Delta t} V_P = R(\phi^n) \quad (2.69)$$

Another scheme related to the discretization technique of Eq. 2.67 is the *Crank-Nicholson* scheme, which is a second-order accurate and bounded scheme

$$\frac{\phi^{n+1} - \phi^n}{\Delta t} V_P = 0.5R(\phi^n) + 0.5R(\phi^{n+1}) \quad (2.70)$$

Independently of the time-level the remaining terms are calculated with, second-order accuracy can also be achieved with a three time-level *Gear* (or *backward*) scheme

$$\int_{V_P} \frac{\partial \phi}{\partial t} dV = \frac{1.5\phi^{n+1} - 2\phi^n + 0.5\phi^{n-1}}{\Delta t} V_P \quad (2.71)$$

Similar to before the exponent  $n - 1$  in  $\phi^{n-1}$  denotes  $\phi^{n-1} = \phi(t - \Delta t)$ . The drawback of the scheme is that it is unbounded due to its extrapolative nature. [11]

- Convection term

For calculation of the convection term the volume integral is first converted into a surface integral by use of the Gauss theorem. The value of which is then calculated by a summation over cell faces

$$\int_{V_P} \nabla \cdot (\mathbf{U}\phi) dV = \sum_f (\mathbf{U}\phi)_f \cdot \mathbf{S}_f = \sum_f F_f \phi_f \quad (2.72)$$

where  $\mathbf{S}_f$  is the normal vector to face  $f$  with its length proportional to the cell face area, see Fig. 2.13.  $F_f$  denotes the flux over the cell face,  $F_f = \mathbf{U}_f \cdot \mathbf{S}_f$ . Various convection based schemes based on the sign (or direction) of the flux  $F_f$  are available to obtain the face value  $\phi_f$ . A first-order and bounded scheme is the *upwind* scheme:

$$\phi_f = \begin{cases} \phi_P & \text{if } F \geq 0 \\ \phi_N & \text{if } F < 0 \end{cases} \quad (2.73)$$

However, the truncation error resembles a diffusive flux. The effect of which is called numerical diffusion and leads to very low accuracy of this scheme. [12] A more accurate scheme of second-order is *linear interpolation* (or *central differencing*)

$$\phi_f = f_x \phi_P + (1 - f_x) \phi_N \quad (2.74)$$

where the weight is calculated with the distances (cf. Fig. 2.13)

$$f_x = \frac{fN}{PN} \quad (2.75)$$

However, solutions obtained with linear interpolation can be prone to unphysical oscillations since the scheme is unbounded. In an approach to overcome this issue and obtain a compromise between accuracy and boundedness *blended* schemes are used, which are a combination of upwind differencing and central differencing

$$\phi_f = (1 - \gamma) (\phi_f)_{UD} + \gamma (\phi_f)_{CD} \quad (2.76)$$

where  $\gamma$  is the blending factor, which is calculated on a face-by-face basis with use of various boundedness criteria. [11]

- Diffusion term

Similar to the convection term, the volume integral of the diffusion term is first transformed into a surface integral and then calculated by summation over cell faces

$$\int_{V_P} \nabla \cdot (\Gamma_\phi \nabla \phi) dV = \sum_f (\Gamma_\phi \nabla \phi)_f \cdot \mathbf{S}_f = \sum_f (\Gamma_\phi)_f (\nabla \phi)_f \cdot \mathbf{S}_f \quad (2.77)$$

For orthogonal meshes, for which  $\overline{PN} \parallel \mathbf{S}_f$  holds, the face gradient term  $(\nabla \phi)_f \cdot \mathbf{S}_f$  can be calculated directly by

$$(\nabla \phi)_f \cdot \mathbf{S}_f = |\mathbf{S}_f| \frac{\phi_N - \phi_P}{|\overline{PN}|} \quad (2.78)$$

This *linear* scheme is second-order accurate and conservative, but unbounded. In case of non-orthogonal meshes a non-orthogonal correction is necessary. [11]

- Source terms

Source terms are all other terms, which cannot be expressed as temporal, convection or conduction terms. Source terms can be arbitrary functions of the variable  $\phi$ . The source terms are first linearized ( $S_\phi = Su + Sp \phi$ ) and then integrated over the volume with a second-order accurate scheme [11]

$$\int_{V_P} S_\phi(\phi) dV = Su V_P + Sp V_P \phi_P \quad (2.79)$$

- Spatial terms

Spatial derivatives, which can be gradient or divergence terms, are again first transformed to surface integrals with use of the Gauss theorem and then calculated by summation over cell

faces, where cell face values  $\phi_f$  are obtained with appropriate interpolation methods such as *linear interpolation* [11]

$$\int_{V_P} \nabla \phi dV = \sum_f \phi_f \mathbf{S}_f \quad (2.80)$$

$$\int_{V_P} \nabla \cdot \phi dV = \sum_f \phi_f \cdot \mathbf{S}_f \quad (2.81)$$

### 2.3.3 Boundary and initial conditions

In section 2.3.1 the discretization of the solution domain was outlined. Initial conditions are necessary in order to be able to calculate the time derivative in the first time-step since values at time  $\phi^n$  are required. Furthermore, boundary values are required in order to be able to calculate spatial derivatives in cells next to the solution domain boundary. Values of  $\phi_f$  and  $(\nabla \phi)_f$  cannot simply be obtained from interpolation, but need to be specified at cell faces coinciding with the solution domain. Two general types of boundary conditions can be distinguished, *Dirichlet* and *Neumann* boundary conditions. One can either specify the value on the boundary face  $\phi_b$  (Dirichlet boundary condition) or the gradient  $(\nabla \phi)_b$  (Neumann boundary condition). All other boundary conditions can be expressed as either one or a combination of both. [12]

### 2.3.4 Solution of sets of linear equations

Discretization of Eq. 2.65 leads to a set of linear equations, one for each cell, with which the new values  $\phi_j^{n+1}$  corresponding to time  $t + \Delta t$  can be calculated for each cell  $j$ . The new value in a cell  $P$ ,  $\phi_P^{n+1}$ , is both dependent on the value  $\phi_P^n$  of the previous time step (and  $\phi_P^{n-1}$  if a three time-level temporal scheme is used) and on the neighboring cell values  $\phi_{P,N}^{n+1}$ , because the terms  $\phi_f$  and  $(\nabla \phi)_f$  require interpolation with the values from neighboring cells. The linear equation for cell  $P$  thus reads [12]

$$a_P \phi_P^{n+1} + \sum_N a_{P,N} \phi_{P,N}^{n+1} = b_P \quad (2.82)$$

Terms calculated with  $\phi_P^n$  (and  $\phi_P^{n-1}$ ) are absorbed in  $b_P$ . Contributions to the diagonal coefficient  $a_P$  can stem from the temporal term, for which the Euler and Crank-Nicholson scheme create a coefficient  $\frac{V_P}{\Delta t}$ , while a Gear scheme creates a coefficient of  $1.5 \frac{V_P}{\Delta t}$ ; from the source-term creating a coefficient of  $S_P V_P$ ; and from the convection and diffusion term if they are treated implicitly (i.e. calculated with values  $\phi_P^{n+1}$ ). Contributions to the off-diagonal coefficients  $a_{P,N}$  can stem from the convection and diffusion term if they are treated implicitly (i.e. calculated with values  $\phi_{P,N}^{n+1}$ ).  $b_P$  comprises contributions from the temporal term, for which Euler and Crank-Nicholson contribute with  $\frac{\phi_P^n}{\Delta t} V_P$ , while the Gear scheme contributes with  $\frac{2\phi_P^n - 0.5\phi_P^{n-1}}{\Delta t} V_P$ ; from the convection and diffusion term if either they are treated explicitly

(i.e. calculated with values  $\phi_P^n$  and  $\phi_{P,N}^n$ ) or if a Crank-Nicholson scheme is used; and from the source-term with the contribution  $Su V_P$ . The set of linear equations can be written in matrix form as [12]

$$[A] [\phi^{n+1}] = [b] \quad (2.83)$$

where  $[A]$  is a  $N \times N$ -dimensional matrix and  $[\phi^{n+1}]$  and  $[b]$  are  $N$ -dimensional vectors.  $N$  is the number of control volumes. The matrix  $[A]$  is a sparse matrix since only adjacent cells can create non-zero off-diagonal coefficients. The set of linear equations is usually not solved directly with exact methods, but iteratively with appropriate linear solvers that preserve the sparseness. Conjugate gradient (CG) methods, such as preconditioned bi-conjugate gradient (PBiCG), preconditioned conjugate gradient (PCG) or bi-conjugate gradient stabilized (BiCGstab) solvers, are widely used. [7]

## 2.A Literature

- [1] J. Aho, Rheological characterization of polymer melts in shear and extension: measurement reliability and data for practical processing, Ph.D. thesis, Tampere University of Technology (2011).
- [2] R. G. Owens, T. N. Phillips, Computational rheology, Imperial Publish Press, 2002.
- [3] J. F. Stevenson, Elongational flow of polymer melts, *AIChE J.* 18 (1972) 540–547.
- [4] J. M. Dealy, Extensional flow of non-Newtonian fluids - a review, *Polym. Eng. Sci.* 11 (1971) 433–445.
- [5] M. L. Williams, R. F. Landel, J. D. Ferry, The temperature dependence of relaxation mechanisms in amorphous polymers and other glass-forming liquids, *J. Am. Chem. Soc.* 77 (1955) 3701–3706.
- [6] G. C. Berry, T. G. Fox, The viscosity of polymers and their concentrated solutions, *Adv. Polymer Sci.* 5 (1968) 261–357.
- [7] J. H. Ferziger, M. Peric, Computational methods for fluid dynamics, Springer, 2002.
- [8] J. G. Oldroyd, On the formulation of rheological equations of state, *Proc. Roy. Soc. Lond.* 200 (1950) 523–541.
- [9] N. Phan-Thien, R. I. Tanner, A new constitutive model derived from network theory, *J. Non-Newtonian Fluid Mech.* 2 (1977) 353–365.
- [10] A. C. B. Bogaerds, Stability analysis of viscoelastic flows, Ph.D. thesis, Technische Universiteit Eindhoven (2002).
- [11] H. Jasak, Error analysis and estimation for the finite volume method with applications to fluid flows, Ph.D. thesis, Imperial College University of London (1996).
- [12] H. Rusche, Computational fluid dynamics of dispersed two-phase flows at high phase fractions, Ph.D. thesis, Imperial College University of London (2002).

## 2.B Nomenclature

Normal symbols represent scalar quantities and boldface symbols represent vector and tensor quantities in general.

### Roman Symbols

Symbol	Description	Unit
$a_P$	Diagonal coefficient of computational cell $P$	
$a_{P,N}$	Off-diagonal coefficient of computational cell $P$	
$a_T$	Horizontal shift factor	$[-]$
$A$	Matrix	
$b$	Vector of source terms	
$b_P$	Source term of computational cell $P$	
$b_T$	Vertical shift factor	$[-]$
$C_1$	Constant of Williams-Landel-Ferry model or constant of Vogel model	$[-]$ $[-]$
$C_2$	Constant of Williams-Landel-Ferry model or constant of Vogel model	$[K]$ $[K]$
$c_P$	Heat capacity	$[\frac{m^2}{s^2K}]$
$\mathbf{D}$	Rate of deformation tensor	$[s^{-1}]$
$E_A$	Activation energy	$[\frac{kgm^2}{s^2mol}]$
$f_x$	Weight factor	$[-]$
$F$	Force or volumetric flux	$[\frac{kgm}{s^2}]$ $[\frac{m^3}{s}]$
$F_f$	Flux through face $f$	$[\frac{m^3}{s}]$
$\mathbf{g}$	Gravitational acceleration vector	$[\frac{m}{s^2}]$
$G$	Rigidity modulus	$[\frac{kg}{ms^2}]$
$H$	Heaviside-function	$[-]$
$i$	Index	$[-]$
$\mathbf{I}$	Identity matrix	$[-]$
$k$	Thermal conductivity	$[\frac{kgm}{s^3K}]$
$m$	Mass	$[kg]$
$\mathbf{n}_S$	Unit normal vector to surface at point $S$	$[-]$
$N$	Number of stress modes	$[-]$



## 2 Theory

<b>Symbol</b>	<b>Description</b>	<b>Unit</b>
$N_1$	First normal stress difference	$[\frac{kg}{ms^2}]$
$N_2$	Second normal stress difference	$[\frac{kg}{ms^2}]$
$p$	Pressure	$[\frac{kg}{ms^2}]$
$p^*$	Modified pressure	$[\frac{kg}{ms^2}]$
$\mathbf{q}$	Heat flux	$[\frac{kgm^2}{s^3}]$
$Q_u$	Internal energy source or sink	$[\frac{kgm^2}{s^3}]$
$\mathbf{Q}_S$	Surface-based source or sink	
$Q_V$	Volumetric source or sink	
$R$	Ideal gas constant	$[\frac{kgm^2}{s^2molK}]$
	or right hand side of discretized equation	
$S$	Surface area	$[m^2]$
$S_{CV}$	Surface area of control volume	$[m^2]$
$\mathbf{S}_f$	Surface area normal vector at cell face $f$	$[m^2]$
$S_\phi$	Source term	
$Sp$	Source term linear dependent of variable	
$Su$	Source term independent of variable	
$t$	Time	$[s]$
$T$	Observation time	$[s]$
	or temperature	$[K]$
$T_g$	Glass transition temperature	$[K]$
$T_{ref}$	Reference temperature	$[K]$
$u$	Specific internal energy	$[\frac{m^2}{s^2}]$
$\mathbf{U}$	Velocity	$[\frac{m}{s}]$
$\mathbf{U}_f$	Velocity at cell-face $f$	$[\frac{m}{s}]$
$\mathbf{U}_s$	Shear velocity field	$[\frac{m}{s}]$
$V$	Volume	$[m^3]$
$V_{CM}$	Volume of control mass	$[m^3]$
$V_{CV}$	Volume of control volume	$[m^3]$
$V_P$	Volume of computational cell $P$	$[m^3]$
$W$	Energy source or sink	$[\frac{kgm^2}{s^3}]$
$x$	Position	$[m]$
$\mathbf{x}$	Position vector	$[m]$

Symbol	Description	Unit
$\mathbf{x}_f$	Face center of a cell	[m]
$\mathbf{x}_P$	Cell center of computational cell P	[m]
$y$	Position	[m]
$z$	Position	[m]

### Greek Symbols

Symbol	Description	Unit
$\gamma$	Blending factor	[-]
$\dot{\gamma}$	Shear-rate	[s <sup>-1</sup> ]
$\gamma_{xy}$	Relative deformation gradient	[-]
$\dot{\gamma}_{xy}$	Rate of deformation	[s <sup>-1</sup> ]
$\dot{\gamma}_{xy,E}$	Rate of deformation of spring	[s <sup>-1</sup> ]
$\dot{\gamma}_{xy,V}$	Rate of deformation of damper	[s <sup>-1</sup> ]
$\Gamma_\phi$	Diffusion coefficient	
$\delta$	Dirac delta function	[-]
$\Delta t$	Time interval	[s]
$\nabla$	Nabla (gradient) operator	[m <sup>-1</sup> ]
$\nabla \cdot$	Divergence operator	[m <sup>-1</sup> ]
$\epsilon$	Extensibility parameter of SPTT model	[-]
$\dot{\epsilon}$	Extension-rate	[s <sup>-1</sup> ]
$\eta$	Dynamic viscosity	[ $\frac{kg}{ms}$ ]
$\eta_0$	Zero shear-rate viscosity	[ $\frac{kg}{ms}$ ]
$\eta_E$	Elongational viscosity	[ $\frac{kg}{ms}$ ]
$\eta_{E,b}$	Biaxial elongational viscosity	[ $\frac{kg}{ms}$ ]
$\eta_{E,p}$	Planar elongational viscosity	[ $\frac{kg}{ms}$ ]
$\eta_{E,u}$	Uniaxial elongational viscosity	[ $\frac{kg}{ms}$ ]
$\eta_P$	Polymeric viscosity	[ $\frac{kg}{ms}$ ]
$\eta_S$	Solvent viscosity	[ $\frac{kg}{ms}$ ]
$\Theta$	Angle or strain	[°]
$\Theta_0$	Strain level	[°]
$\Theta_E$	Angle or strain of spring	[°]

## 2 Theory

Symbol	Description	Unit
$\Theta_V$	Angle or strain of damper	[ $^\circ$ ]
$\lambda_1$	Relaxation time	[s]
$\lambda_{1,i}$	Relaxation time of $i$ -th Maxwell mode	[s]
$\lambda_{1,R}$	Reduced relaxation time	[s]
$\lambda_2$	Retardation time	[s]
$\nu$	Kinematic viscosity	[ $\frac{m^2}{s}$ ]
$\nu_S$	Kinematic solvent viscosity	[ $\frac{m^2}{s}$ ]
$\rho$	Density	[ $\frac{kg}{m^3}$ ]
$\rho_{ref}$	Reference density	[ $\frac{kg}{m^3}$ ]
$\Sigma$	Cauchy stress tensor	[ $\frac{kg}{ms^2}$ ]
$\sigma_{xx}$	Normal stress in x-direction	[ $\frac{kg}{ms^2}$ ]
$\sigma_{xy}$	Shear stress	[ $\frac{kg}{ms^2}$ ]
$\sigma_{xy,0}$	Shear stress level	[ $\frac{kg}{ms^2}$ ]
$\sigma_{xy,E}$	Elastic shear stress in spring	[ $\frac{kg}{ms^2}$ ]
$\sigma_{xy,i}$	Shear stress of $i$ -th Maxwell mode	[ $\frac{kg}{ms^2}$ ]
$\sigma_{xy,V}$	Viscous shear stress in damper	[ $\frac{kg}{ms^2}$ ]
$\sigma_{yy}$	Normal stress in y-direction	[ $\frac{kg}{ms^2}$ ]
$\sigma_{zz}$	Normal stress in z-direction	[ $\frac{kg}{ms^2}$ ]
$\tau$	Deviatoric or extra-stress tensor	[ $\frac{kg}{ms^2}$ ]
$\tau_P$	Polymeric stress tensor	[ $\frac{kg}{ms^2}$ ]
$\tau_{P,i}$	Polymeric stress tensor of the $i$ -th mode	[ $\frac{kg}{ms^2}$ ]
$\tau_S$	Solvent stress tensor	[ $\frac{kg}{ms^2}$ ]
$\phi$	General variable	
$\phi_b$	Variable value on Dirichlet boundary	
$\phi_f$	General variable at cell face $f$	
$\phi_N$	General variable at computational cell $N$	
$\phi_P$	General variable at computational cell $P$	
$\varphi$	General intensive property	
$\Phi$	General extensive property	
$\Psi_1$	First normal stress coefficient	[ $\frac{kg}{ms}$ ]
$\Psi_2$	Second normal stress coefficient	[ $\frac{kg}{ms}$ ]

## Subscripts, Superscripts and Oversymbols

Symbol	Description
$\mathbf{Q}^{n-1}$	Time level $n - 1$
$\mathbf{Q}^n$	Time level $n$
$\mathbf{Q}^{n+1}$	Time level $n + 1$
$\mathbf{Q}^T$	Transpose of matrix $\mathbf{Q}$
$\overset{\nabla}{\mathbf{Q}}$	Upper-convected time derivative

## Nondimensional Groups

Symbol	Description	Definition
$De$	Deborah number	$\frac{\lambda_1}{T}$
$Tr$	Trouton ratio	$\frac{\eta E}{\eta_0}$
$Wi$	Weissenberg number	$\lambda_1 \dot{\gamma}_{xy}$
$\beta$	Retardation factor	$\frac{\lambda_1}{\lambda_2}$ or $\frac{\eta S}{\eta_0}$

## Abbreviations

Abbreviation	Description
BiCGstab	Bi-conjugate gradient stabilized
CG	Conjugate gradient
CM	Control mass
CV	Control volume
FDM	Finite difference method
FEM	Finite element method
FVM	Finite volume method
PBiCG	Preconditioned bi-conjugate gradient
PCG	Preconditioned conjugate gradient
SPTT	Simplified Phan-Thien-Tanner
TTS	Time temperature superposition
WLF	Williams-Landel-Ferry

# 3 Semi-implicit stress formulation for viscoelastic models: Application to three-dimensional contraction flows

## 3.1 Introduction

Over the last decades the use of finite-volume methods has become very popular in the simulation of viscoelastic flows, mainly due to the beneficial memory and time savings when comparing to finite-element methods. [1, 2]

Finite-volume methods can be divided into methods using staggered grids and non-staggered (collocated) grids. In the latter all variables are located at the centroid of the control volumes. Examples of the staggered finite-volume method are the work of Hu and Joseph, who simulated the flow around a circular cylinder using the upper Convected Maxwell model [3], and Sasmal [4], who applied a staggered finite-volume approach to the simulation of the flow in an abrupt axisymmetric contraction. Although inherently ensuring a strong coupling between all variables and thereby avoiding decoupling effects the main drawback of staggered grid methods is the difficult extension to complex non-orthogonal grids.

Despite the possible appearance of decoupling phenomena resulting in unphysical checkerboard fields of pressure [5] and velocity [6], the easy extension of the collocated finite-volume method to non-orthogonal grids seems to outweigh this drawback. In addition, efficient interpolation techniques have been developed to avoid these decoupling effects. [7, 8] Noteworthy developments of the collocated finite-volume method for viscoelastic flow are by the group of Oliveira [6, 9, 10] and more recently the development of a solver for the free-to-use software OpenFOAM<sup>®</sup> [11], which has already been applied to the simulation of three-dimensional contraction flows [12] and extended to the simulation of nonisothermal [13] and multiphase flows [14].

Discretizing the pressure gradient in the collocated method with the use of second-order linear interpolation leads to a relationship between alternate nodal pressures rather than adjacent ones, which may result in checkerboard fields for pressure. This is the case in Newtonian and viscoelastic flow. The most widely used remedy to that problem is the use of the interpolation scheme of Rhie and Chow [7], which has subsequently been numerous times revised and improved, for example by Majumdar [15], Choi [16] and Yu et al. [17]. In the simulation of viscoelastic flow with collocated finite-volume methods velocity checkerboard fields can also arise, which are due to a similar effect when discretizing the divergence of stress. The problem has first been addressed by Oliveira et al. [6] by finding an adequate cell-face interpolation for stress. The interpolation is done in the spirit of Rhie and Chow [7]. Although already ensuring a

strong coupling, an inconsistency in the sense that steady-state solutions depend upon the time-step ( $\Delta t$ ) was eliminated in a later publication. [8]

In the work of Favero et al. [11] second-order linear interpolation is used to obtain cell-face stress values in the approximation of the stress divergence, which - depending on the geometry and flow conditions - may lead so severe velocity checkerboarding. To remedy this issue, a new interpolation technique is developed in this work, which is also based on the interpolation of Rhie and Chow [7], similar to the work of Oliveira et al. [6] and Matos et al. [8]. Yet, besides ensuring a strong coupling between velocity and stress, this new approach allows for the deformation part of the constitutive equation to be treated implicitly in the momentum equation, which makes the numerical method somewhat more stable by increasing the elliptic operator in the momentum equation.

Contraction flows are of major importance in polymer processing and have been studied extensively for over three decades now. [18] The contraction gives rise to locally complex profiles being difficult to predict numerically, which is why this geometry evolved as a benchmark problem to test numerical algorithms. [19] Our new approach is tested with a three-dimensional 3.97:1 planar contraction as it is used in the experiments of Quinzani et al. [20] and a three-dimensional 4:1 square-square contraction, which was experimentally examined by Sousa et al. [21]. A simplified Phan-Thien-Tanner (SPTT) model is used to describe the viscoelastic fluid in both cases.

This work is organized as follows: In Section 3.2 the governing equations, our new interpolation method for stress and the numerical algorithm are described. In Section 3.3 the new interpolation technique is tested with a planar and a square-square contraction. The results are compared to experimental values and numerical data from the literature. Section 3.4 closes with a summary.

## 3.2 Governing equations and numerical method

### 3.2.1 Governing equations

In this work we consider the flow of an incompressible and isothermal viscoelastic fluid. The governing equations are the mass and momentum balance

$$\nabla \cdot \mathbf{U} = 0 \tag{3.1}$$

$$\rho \left( \frac{\partial \mathbf{U}}{\partial t} + \nabla \cdot (\mathbf{U}\mathbf{U}) \right) = -\nabla p + \nabla \cdot \boldsymbol{\tau} \tag{3.2}$$

where  $\mathbf{U}$  is the velocity,  $\rho$  is the density,  $t$  is time,  $p$  is pressure and  $\boldsymbol{\tau}$  is the total stress, which can be written as the sum of a solvent and polymer contribution for a general Maxwell-type fluid

$$\boldsymbol{\tau} = \boldsymbol{\tau}_S + \boldsymbol{\tau}_P \quad (3.3)$$

The Newtonian law holds for the solvent contribution

$$\boldsymbol{\tau}_S = \eta_S \left[ \nabla \mathbf{U} + (\nabla \mathbf{U})^T \right] \quad (3.4)$$

where  $\eta_S$  is the solvent viscosity. For the polymeric contribution  $\boldsymbol{\tau}_P$ , the linear SPTT equation may hold in this work [22]

$$\left( 1 + \frac{\epsilon \lambda}{\eta_P} \text{tr}(\boldsymbol{\tau}_P) \right) \boldsymbol{\tau}_P + \lambda \overset{\nabla}{\boldsymbol{\tau}}_P = \eta_P \left[ \nabla \mathbf{U} + (\nabla \mathbf{U})^T \right] \quad (3.5)$$

where  $\epsilon$  is the extensibility parameter,  $\lambda$  is the relaxation time and  $\eta_P$  is the polymer viscosity.  $\overset{\nabla}{\boldsymbol{\tau}}_P$  denotes the upper-convected time derivative defined as

$$\overset{\nabla}{\boldsymbol{\tau}}_P = \frac{\partial \boldsymbol{\tau}_P}{\partial t} + \nabla \cdot (\mathbf{U} \boldsymbol{\tau}_P) - (\nabla \mathbf{U})^T \cdot \boldsymbol{\tau}_P - \boldsymbol{\tau}_P \cdot \nabla \mathbf{U} \quad (3.6)$$

The retardation ratio  $\beta$  is defined as the ratio between solvent viscosity  $\eta_S$  and total viscosity  $\eta_0 = \eta_S + \eta_P$

$$\beta = \frac{\eta_S}{\eta_0} = \frac{\eta_S}{\eta_S + \eta_P} \quad (3.7)$$

Introducing the stress-splitting of Eq. 3.3 together with the Newtonian law Eq. 3.4 into the momentum equation a modified Stokes problem is obtained

$$\rho \left( \frac{\partial \mathbf{U}}{\partial t} + \nabla \cdot (\mathbf{U} \mathbf{U}) \right) - \nabla \cdot \eta_S \nabla \mathbf{U} = -\nabla p + \nabla \cdot \boldsymbol{\tau}_P \quad (3.8)$$

### 3.2.2 Numerical method

#### Both-Side-Diffusion

In case of  $\beta \rightarrow 0$  the elliptic diffusion term in Eq. 3.8 becomes small, however, in order to ensure numerical stability the elliptic term is required to be the dominant term over the entire range of retardation ratios. The both-side-diffusion (BSD) [23] technique therefore introduces an additional elliptic term proportional to  $\eta_P$  into the momentum equation

$$\rho \left( \frac{\partial \mathbf{U}}{\partial t} + \nabla \cdot (\mathbf{U} \mathbf{U}) \right) - \nabla \cdot \eta_0 \nabla \mathbf{U} = -\nabla p + \nabla \cdot \boldsymbol{\tau}_P - \nabla \cdot \eta_P \nabla \mathbf{U} \quad (3.9)$$

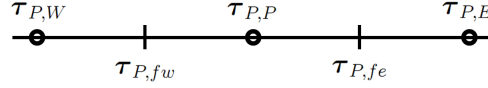


**Figure 3.1:** Schematic representation of the stress in a 1-D problem.

### Velocity-stress decoupling

The above described model was recently implemented in the software package OpenFOAM<sup>®</sup> by Favero et al. [11]. OpenFOAM<sup>®</sup> uses a non-staggered finite-volume method (FVM) and is capable of handling not only complex mesh types such as tetrahedral and polyhedral meshes, but also dynamic mesh techniques such as adaptive remeshing as well as prescribed and solution-dependent mesh motions. Convective terms were discretized by the first-order up-wind scheme due to its inherent stability benefits and the avoidance of oscillations. Diffusion terms and the pressure gradient were evaluated by second-order linear interpolation onto cell faces with an explicit non-orthogonal correction. Continuity was ensured by the SIMPLE pressure-correction technique. Despite its flexibility and the implementation of the most commonly used constitutive equations, the major drawback of this numerical algorithm is that it is prone to produce velocity checkerboard fields, which is caused by a velocity-stress decoupling. The reason for that can be explained as follows:

The divergence of the polymeric stress in the momentum equation is numerically evaluated by a second-order Gaussian formula

$$\int_{V_P} \nabla \cdot \boldsymbol{\tau}_P dV = \sum_f \mathbf{S}_f \cdot \boldsymbol{\tau}_{P,f} \quad (3.10)$$

where the cell face values  $\boldsymbol{\tau}_{P,f}$  are obtained from second-order linear interpolation. However, this leads to decoupling between velocity and stress, which can be easily shown for a 1-D problem (cf. Fig. 3.1)

$$\begin{aligned} \sum_f \mathbf{S}_f \cdot \boldsymbol{\tau}_{P,f} &= \mathbf{S}_{fe} \cdot \boldsymbol{\tau}_{P,fe} + \mathbf{S}_{fw} \cdot \boldsymbol{\tau}_{P,fw} \\ &= \mathbf{S}_{fw} \cdot \frac{1}{2} (\boldsymbol{\tau}_{P,E} + \boldsymbol{\tau}_{P,P}) + \mathbf{S}_{fe} \cdot \frac{1}{2} (\boldsymbol{\tau}_{P,P} + \boldsymbol{\tau}_{P,W}) \\ &\stackrel{|\mathbf{S}_{fi}|=1}{=} \frac{1}{2} (\boldsymbol{\tau}_{P,E} - \boldsymbol{\tau}_{P,W}) \end{aligned} \quad (3.11)$$

The stress-divergence in point  $P$ , which is used to calculate the velocity in  $P$  with use of the momentum balance, does not depend anymore on the stress value in  $P$ , but only on the stress values of the adjacent cells  $E$  and  $W$ . A proposed solution by the group of Oliveira [6, 24, 8] is an explicit correction to the linearly interpolated stress values similar to the standard Rhie-Chow interpolation [7]: stresses are linearly interpolated onto the cell-faces, but terms of the constitutive equation being proportional to the velocity gradient are evaluated directly on the cell-face. This technique guarantees a strong coupling between velocity and stress. Although initially having an inconsistency in the sense that converged solutions were dependent upon



the time-step, this deficiency was eliminated in a later work by finding an interpolation, in which the time-derivative term was fully linearly interpolated onto cell faces. [8]

### Semi-implicit handling of the constitutive equation

During this work we developed a different approach, which even allows for a more implicit handling of the constitutive equation. The technique can be applied to a variety of constitutive equations such as the Oldroyd-B, Giesekus and FENE-type models. In this work the technique is exemplified for the SPTT model. The derivation starts by reordering the terms of the constitutive equation and division by the relaxation time

$$\begin{aligned} & \left( \frac{1}{\lambda} + \frac{\epsilon}{\eta_P} \text{tr}(\boldsymbol{\tau}_P) \right) \boldsymbol{\tau}_P + \frac{\partial \boldsymbol{\tau}_P}{\partial t} + \nabla \cdot (\mathbf{U} \boldsymbol{\tau}_P) \\ &= \frac{\eta_P}{\lambda} \left[ \nabla \mathbf{U} + (\nabla \mathbf{U})^T \right] + (\nabla \mathbf{U})^T \cdot \boldsymbol{\tau}_P + \boldsymbol{\tau}_P \cdot \nabla \mathbf{U} \end{aligned} \quad (3.12)$$

Next, we cast the equation into a semi-discretized form by discretizing terms on the l.h.s. and leaving terms on the r.h.s. as they are, which is similar to deriving the well-known pressure-correction methods

$$\mathbb{A}_P^{\boldsymbol{\tau}} \boldsymbol{\tau}_P = \mathbb{H}_P^{\boldsymbol{\tau}}(\boldsymbol{\tau}_P) + \frac{\eta_P}{\lambda} \left[ \nabla \mathbf{U} + (\nabla \mathbf{U})^T \right] + (\nabla \mathbf{U})^T \cdot \boldsymbol{\tau}_P + \boldsymbol{\tau}_P \cdot \nabla \mathbf{U} \quad (3.13)$$

$\mathbb{A}_P^{\boldsymbol{\tau}}$  denotes the diagonal coefficient formed by the contributions from the three terms on the l.h.s. of Eq. 3.12. In the time-stepping procedure, which we use in this work, the time derivatives are approximated with a second-order accurate three-point scheme. For a thorough discussion we refer the reader to the work of Xue et al. [25]. In this case the diagonal coefficient is

$$\mathbb{A}_P^{\boldsymbol{\tau}} = \left( 1/\lambda + \frac{\epsilon}{\eta_P} \text{tr}(\boldsymbol{\tau}_{P,P}^n) \right) V_P + \frac{3}{2} \frac{V_P}{\Delta t} + a_P^C \quad (3.14)$$

The term  $a_P^C$  comprises the contributions from the convection term to the diagonal. For simplicity, we will use a first-order upwind scheme in this work, although higher-order schemes such as the Gamma [26] and the CUBISTA [27] scheme have been successfully tested. The term  $\mathbb{H}_P^{\boldsymbol{\tau}}(\boldsymbol{\tau}_P)$  comprises the explicit part of the inertia term and the off-diagonal convection contributions

$$\mathbb{H}_P^{\boldsymbol{\tau}}(\boldsymbol{\tau}_P) = \frac{2\boldsymbol{\tau}_{P,P}^n - \frac{1}{2}\boldsymbol{\tau}_{P,P}^{n-1}}{\Delta t} V_P - \sum_N a_N \boldsymbol{\tau}_{P,N} \quad (3.15)$$

The polymeric stress can be obtained by division of Eq. 3.13 with the diagonal coefficient

$$\boldsymbol{\tau}_P = \underbrace{\frac{\mathbb{H}_P^{\boldsymbol{\tau}}(\boldsymbol{\tau}_P)}{\mathbb{A}_P^{\boldsymbol{\tau}}}}_{\tilde{\boldsymbol{\tau}}_P} + \frac{1}{\mathbb{A}_P^{\boldsymbol{\tau}}} \left\{ \frac{\eta_P}{\lambda} \left[ \nabla \mathbf{U} + (\nabla \mathbf{U})^T \right] + (\nabla \mathbf{U})^T \cdot \boldsymbol{\tau}_P + \boldsymbol{\tau}_P \cdot \nabla \mathbf{U} \right\} \quad (3.16)$$

$\widetilde{\boldsymbol{\tau}}_P$  summarizes the contribution of the three terms on the l.h.s. of Eq. 3.12 to the polymeric stress  $\boldsymbol{\tau}_P$ . Next, we take the divergence of Eq. 3.16, because this is the relevant coupling term between stress and velocity appearing in the momentum equation

$$\begin{aligned} \nabla \cdot \boldsymbol{\tau}_P = \\ \nabla \cdot \widetilde{\boldsymbol{\tau}}_P + \nabla \cdot \left\{ \frac{1}{\mathbb{A}_P^{\boldsymbol{\tau}}} \left\{ \frac{\eta_P}{\lambda} [\nabla \mathbf{U} + (\nabla \mathbf{U})^T] + (\nabla \mathbf{U})^T \cdot \boldsymbol{\tau}_P + \boldsymbol{\tau}_P \cdot \nabla \mathbf{U} \right\} \right\} \end{aligned} \quad (3.17)$$

The divergence of the deformation part can be recast into a diffusion term and a correction term stemming from the non-constant pre-factor

$$\begin{aligned} \nabla \cdot \boldsymbol{\tau}_P = \nabla \cdot \widetilde{\boldsymbol{\tau}}_P + \nabla \cdot \frac{\eta_P}{\mathbb{A}_P^{\boldsymbol{\tau}} \lambda} \nabla \mathbf{U} + \nabla \mathbf{U} \cdot \nabla \frac{\eta_P}{\mathbb{A}_P^{\boldsymbol{\tau}} \lambda} \\ + \nabla \cdot \left\{ \frac{1}{\mathbb{A}_P^{\boldsymbol{\tau}}} \left\{ (\nabla \mathbf{U})^T \cdot \boldsymbol{\tau}_P + \boldsymbol{\tau}_P \cdot \nabla \mathbf{U} \right\} \right\} \end{aligned} \quad (3.18)$$

Introducing Eq. 3.18 into the momentum equation Eq. 3.9, we obtain

$$\begin{aligned} \rho \left( \frac{\partial \mathbf{U}}{\partial t} + \nabla \cdot (\mathbf{U} \mathbf{U}) \right) - \nabla \cdot \left( \eta_0 + \frac{\eta_P}{\mathbb{A}_P^{\boldsymbol{\tau}} \lambda} \right) \nabla \mathbf{U} \\ = \\ -\nabla p + \nabla \cdot \widetilde{\boldsymbol{\tau}}_P + \nabla \cdot \left\{ \frac{1}{\mathbb{A}_P^{\boldsymbol{\tau}}} \left\{ (\nabla \mathbf{U})^T \cdot \boldsymbol{\tau}_P + \boldsymbol{\tau}_P \cdot \nabla \mathbf{U} \right\} \right\} \\ + \nabla \mathbf{U} \cdot \nabla \frac{\eta_P}{\mathbb{A}_P^{\boldsymbol{\tau}} \lambda} - \nabla \cdot \eta_P \nabla \mathbf{U} \end{aligned} \quad (3.19)$$

It can be seen from Eq. 3.19 that our method allows for the deformation contribution in the constitutive equation to be treated implicitly in the momentum equation and thus allows for a semi-implicit handling of the constitutive equation. This promotes the stability of our numerical algorithm. The divergence of  $\widetilde{\boldsymbol{\tau}}_P$  is numerically treated as a standard divergence term (see Eq. 3.10) with the cell-face values being obtained from linear interpolation. The diffusion-correction term (the fourth term on the r.h.s. of Eq. 3.19) is treated as a standard source term with second-order Gaussian integration.

### Pressure-correction equation

To obtain the pressure equation, Eq. 3.19 is recast into a semi-discretized form

$$\mathbb{A}_P^{\mathbf{U}} \mathbf{U} = \mathbb{H}_P^{\mathbf{U}}(\mathbf{U}) - \nabla p + \frac{1}{\rho} \nabla \cdot \left\{ \frac{1}{\mathbb{A}_P^{\boldsymbol{\tau}}} \left\{ (\nabla \mathbf{U})^T \cdot \boldsymbol{\tau}_P + \boldsymbol{\tau}_P \cdot \nabla \mathbf{U} \right\} \right\} \quad (3.20)$$

where the new velocity field can be obtained by division by the diagonal coefficient

$$\mathbf{U} = \underbrace{\frac{\mathbb{H}_P^{\mathbf{U}}(\mathbf{U})}{\mathbb{A}_P^{\mathbf{U}}}}_{\widetilde{\mathbf{U}}} + \frac{1}{\mathbb{A}_P^{\mathbf{U}}} \left\{ -\nabla p + \frac{1}{\rho} \nabla \cdot \left\{ \frac{1}{\mathbb{A}_P^{\boldsymbol{\tau}}} \left\{ (\nabla \mathbf{U})^T \cdot \boldsymbol{\tau}_P + \boldsymbol{\tau}_P \cdot \nabla \mathbf{U} \right\} \right\} \right\} \quad (3.21)$$

The momentum balance must also hold on cell-faces

$$\mathbf{U}_f = \tilde{\mathbf{U}}_f + \frac{1}{\mathbb{A}_P^{\mathbf{U}}|_f} \left\{ -\nabla p + \frac{1}{\rho} \nabla \cdot \left\{ \frac{1}{\mathbb{A}_P^{\boldsymbol{\tau}}} \{ (\nabla \mathbf{U})^T \cdot \boldsymbol{\tau}_P + \boldsymbol{\tau}_P \cdot \nabla \mathbf{U} \} \right\} \right\} |_f \quad (3.22)$$

where interpolated terms are obtained from linear interpolation. A Poisson-equation for pressure is obtained by taking the divergence and assuming that the new velocity field must be divergence-free (i.e.  $\nabla \cdot \mathbf{U}_f = 0$ )

$$\begin{aligned} \nabla \cdot \frac{1}{\mathbb{A}_P^{\mathbf{U}}|_f} \nabla p = \\ \nabla \cdot \tilde{\mathbf{U}}_f + \nabla \cdot \frac{1}{\rho \mathbb{A}_P^{\mathbf{U}}|_f} \nabla \cdot \left\{ \frac{1}{\mathbb{A}_P^{\boldsymbol{\tau}}} \{ (\nabla \mathbf{U})^T \cdot \boldsymbol{\tau}_P + \boldsymbol{\tau}_P \cdot \nabla \mathbf{U} \} \right\} |_f \end{aligned} \quad (3.23)$$

The last term on the r.h.s. is numerically evaluated on cell-faces. We note here that this kind of approximation is similar to the approximation used in Eq. 3.22 and is done in all of the pressure-correction techniques. We therefore obtain the final form of the pressure equation

$$\begin{aligned} \nabla \cdot \frac{1}{\mathbb{A}_P^{\mathbf{U}}|_f} \nabla p = \\ \nabla \cdot \tilde{\mathbf{U}}_f + \nabla \cdot \frac{1}{\rho \mathbb{A}_P^{\mathbf{U}}|_f} \nabla \cdot \left\{ \frac{1}{\mathbb{A}_P^{\boldsymbol{\tau}}|_f} \{ (\nabla_f^\perp \mathbf{U})^T \cdot \boldsymbol{\tau}_{P,f} + \boldsymbol{\tau}_{P,f} \cdot \nabla_f^\perp \mathbf{U} \} \right\} \end{aligned} \quad (3.24)$$

The face normal gradient is approximated with a second-order accurate scheme as (cf. Fig. 3.1)

$$\nabla_{fe}^\perp \mathbf{U} = \frac{\mathbf{U}_E - \mathbf{U}_P}{|\mathbf{d}|} \quad (3.25)$$

where  $\mathbf{d}$  is the distance vector between the centroids of the two adjoining cells.

Despite the fact of increasing the elliptic operator in the momentum equation, the major advantage of our method is the strict avoidance of velocity-stress decoupling. The last step of evaluating the stretching and rotation term of the constitutive equation on cell-faces directly (Eq. 3.24) is therefore of major importance.

### 3.2.3 Numerical algorithm

In this work we use a variant of the PISO algorithm. A thorough discussion on the various pressure-correction techniques for transient viscoelastic flow can be found in Xue et al. [25]. We found that the initial step of solving the momentum equation did not improve the iterative convergence of the pressure equation or even impair it in creeping flow conditions. Furthermore, this is not a necessary step to obtain the final velocity field and is thus omitted in this work. Pressure-velocity correction is instead addressed by solving the pressure equation only and then updating the fluxes and velocities with the new pressure guess  $p^*$  according to Eq. 3.22 and 3.21, respectively. The pressure equation Eq. 3.24 is solved twice with the intermediate step of updating  $\tilde{\mathbf{U}}_f$ . A conjugate-gradient solver with AMG preconditioning at a tolerance of  $10^{-10}$  is used as the linear solver for the pressure equation. The constitutive

equation is solved after the PISO-loop with a BiCGstab solver in conjunction with a Cholesky preconditioner at a tolerance of  $10^{-8}$ . The very small tolerances of the linear solvers are justified by the fact that we are interested in assessing the time-step dependency of the converged solutions, similar to the work of Matos et al. [8]. Simulations were stopped, if the residuals of all variables fall below a value of  $10^{-8}$ .

### 3.3 Results

In this section we present the simulation results for a three-dimensional planar contraction and a square-square contraction.

#### 3.3.1 Planar contraction

Quinzani et al. [20] examined the flow of a well-characterized polymer solution (5.0 wt-% polyisobutylene dissolved in tetradecane) through a planar contraction in order to have a basis of comparison to assess the predictive quality of various constitutive equations in describing the fluid behavior in such type of flows. The contraction ratio is  $H_1/H_2 = 3.97$  and the slit width  $2W$  in the experiments is large compared to the upstream channel height  $2H_1$  ( $W/H_1 = 40$ ), which is why the geometry is commonly approximated two-dimensionally in numerical studies, see for example Azaizez et al. [28] and Favero et al. [11].  $H_1$  is half the upstream channel height and  $H_2$  half the downstream channel height. Velocity and stress profiles were attentively measured with laser-doppler velocimetry (LDV) and flow-induced birefringence (FIB). The profiles were obtained at the center plane of the contraction (i.e. half the slit width  $W/2$ ). The scanning locations are summarized in Fig. 3.2.

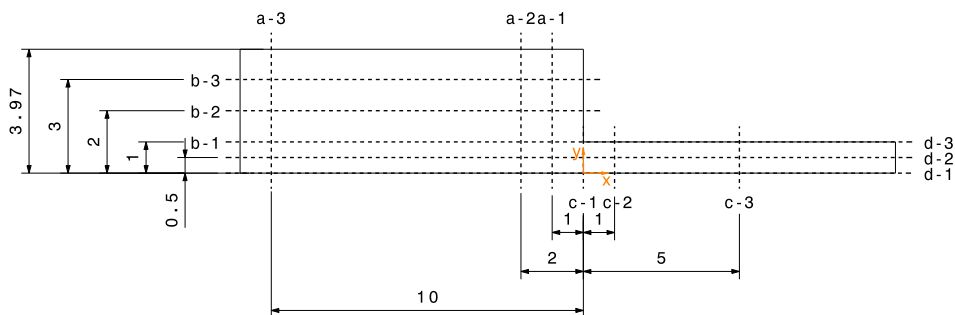


**Figure 3.2:** Scanning positions (planar contraction); lengths are normalized with half the downstream channel height  $H_2$ .

We intend to fully capture the three-dimensionality of the flow by doing three-dimensional simulations. Nonetheless, flow symmetry is assumed by making use of the two symmetry planes in transversal direction. The upstream channel length is  $L_1/H_2 = 40$  and the

**Table 3.1:** Properties of the meshes used for the planar contraction.

	M1	M2	M3
$N_{cells}$	302,400	592,440	1,020,600
$\Delta x_{min}/2H_2$	0.0130	0.0111	0.0079
$\Delta y_{min}/2H_2$	0.0139	0.0115	0.0091
$\Delta z_{min}/2H_2$	0.0147	0.0127	0.0103

downstream channel length is  $L_2/H_2 = 160$  in the simulations. We impose a uniform velocity at the inlet and zero gradient for the stresses. Three meshes were used to prove mesh independency of our results. The meshes are graded towards the solid walls, since these are the regions where the largest gradients are to be expected. The total cell number and normalized lengths of the smallest cell are listed in Table 3.1 for the three meshes. A detailed isometric view of mesh M1 is shown in Fig. 3.3. Detailed views of the three meshes in the center plane, in which the experimental profiles were measured and the simulation data is compared to, are shown in Fig. 3.4.

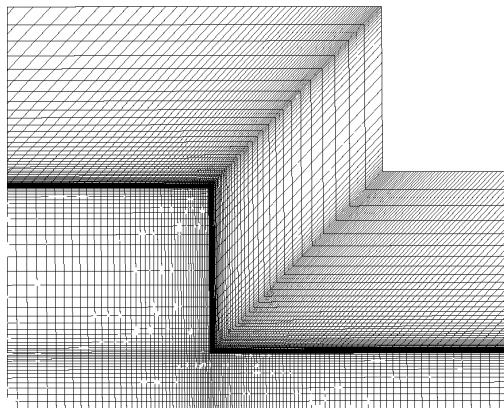


**Figure 3.3:** Detailed isometric view of mesh M1 in the contraction area (planar contraction).

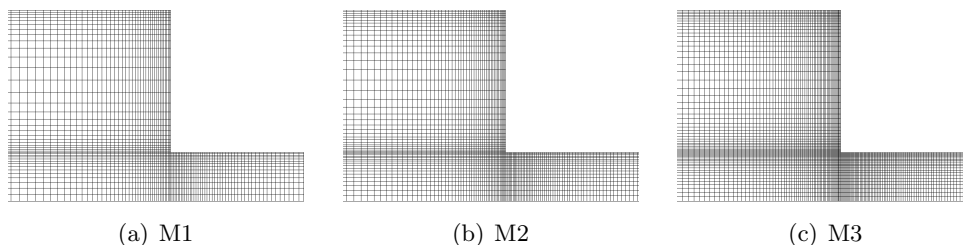


**Figure 3.4:** Detailed view of the center plane for the three meshes (planar contraction).

A similar three-dimensional simulation of the experiments of Quinzani et al. [20] was recently done by Mu et al. [29] using a finite-element code. However, in their study a rather coarse

mesh was used without showing mesh convergence of the obtained results. The values of the parameter of the SPTT used herein can be found in Mu et al. [29]. The values are  $\epsilon = 0.25$  and  $\lambda = 0.03$  s.

In Fig. 3.5 we show an upstream velocity profile obtained by using the standard linear interpolation with the solver developed by Favero et al. [11] and the same profile obtained when using our improved method. One can clearly see the zig-zag-pattern close to the wall when using a linear interpolation, while with our improved method a smooth profile is obtained. This is the result of the strong coupling between velocity and stress. When using the linear interpolation solver, a slight checkerboard pattern of the velocity magnitude was visible almost in the whole domain, not only close to the wall, whereas the flow field was completely smooth with our new method. No difference in the average simulation time per time-step or total number of iterations needed for convergence is found between our new interpolation technique and the standard linear interpolation. This is similar to Matos et al. [8], who found that the total number of iterations is similar between linear interpolation and their Rhie-Chow-type interpolation - except for the case of very small time-steps, for which the linear interpolation diverged.

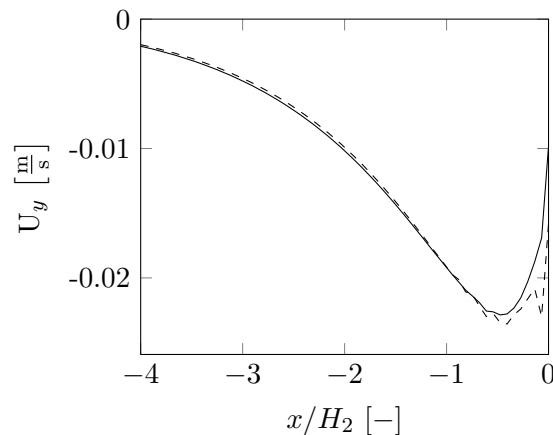


**Figure 3.5:** Comparison of the velocity component  $U_y$  obtained by using the standard linear interpolation and our improved method at line b-1 for mesh M1 (planar contraction).  
 (---): standard linear interpolation, (—): improved method.

We now turn to the comparison with the experimental profiles of Quinzani et al. [20] and the simulations of Mu et al. [29]. The results are shown in Figs. 3.6 - 3.16. Our results are clearly converged for all profiles and flow variables under consideration. In Fig. 3.6 the vertical velocity profiles are shown. When approaching the contraction area, the fluid gets accelerated in the center while decelerating in the wall-near regions. Our predicted profiles are in quantitative agreement with the measurements of Quinzani et al. [20], while the velocity in the center of profile a-1 predicted by Mu et al. [29] perceivably deviates from the measurements and Mu et al. only obtain qualitative agreement. The horizontal velocity profiles are in good agreement with the experiments (cf. Fig. 3.7). There is a noticeable deviation from the results of Mu et al. [29] at line b-1 close to the reentrant corner. In the downstream channel, the

axial velocity profile is slightly overpredicted in the center of the channel, however, not to such an extent as in the simulations of Mu et al. [29], see Fig. 3.8. Comparing line c-3 to the analytical solution of Cruz et al. [30] for fully developed channel flow of a SPTT fluid we find a qualitative agreement. The reason for the lack of quantitative agreement is due to our simulations being performed for a rectangular channel rather than a two-dimensional channel. The pressure gradient in the analytical solution was chosen such that the average velocities in the analytical solution and the simulation are equal. The agreement with the analytical solution lets us conclude that deviations from the measurements must stem from a mismatching of the assumed rheology with the real fluid. The upstream shear stress profiles (cf. Fig. 3.9 and 3.10) are in very good agreement with the experimental profiles, except for the maximum value of profile a-1, which is slightly overpredicted by our simulation. We find that our simulations are generally in better agreement with the experimental data than the results of Mu et al. [29] for all upstream shear stress profiles. The downstream shear stress profile shown in Fig. 3.11 is in qualitative agreement with the experimental data with some distinct deviations, particularly in the wall-near region and for the profiles close to the contraction area. The axial shear stress profiles are again in almost quantitative agreement with the experimental values (cf. Fig. 3.12), whereas the results of Mu et al. [29] are only in qualitative agreement with the experimental data. The maximum value of the shear stress found at the reentrant corner decreases towards the center (line d-2), where it has a local maximum and further downstream increases to a constant value. In the centerline (line d-3), no local overshoot can be found for the shear stress. The vertical profile of the first normal stress difference  $N$  is also in very good agreement with the experimental data, see Fig. 3.13. Our predicted maximum value in the center for the two lines a-1 and a-2 close to the contraction is in much better agreement with the experimental value than the predictions of Mu et al. [29]. However, for the horizontal profiles in the upstream channel (Fig. 3.14), the vertical downstream profiles (Fig. 3.15) and the axial profiles (Fig. 3.16) we observe distinct deviations for all profiles from the measurements.

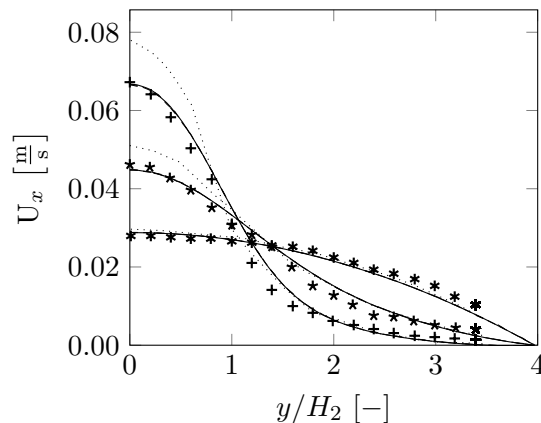


**Figure 3.6:** Comparison between measured and predicted velocity in the upstream section (planar contraction).  
 (+): measured at a-1, (\*): measured at a-2, (\*): measured at a-3, (.....): simulation of Mu et al. [29], (- -): M1, (- · -): M2, (—): M3.

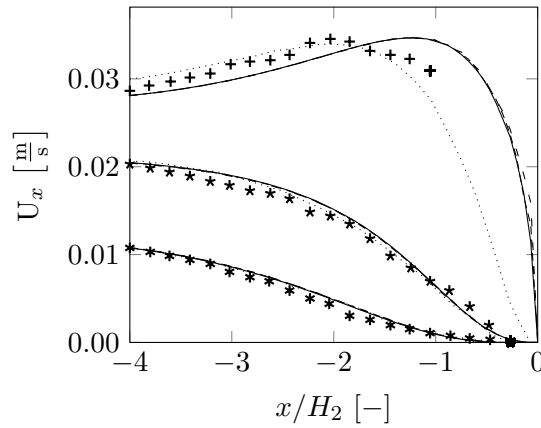


**Figure 3.7:** Comparison between measured and predicted velocity in the upstream section (planar contraction).  
 (+): measured at b-1, (\*): measured at b-2, (\*): measured at b-3, (.....): simulation of Mu et al. [29], (- -): M1, (-·-·): M2, (—): M3.

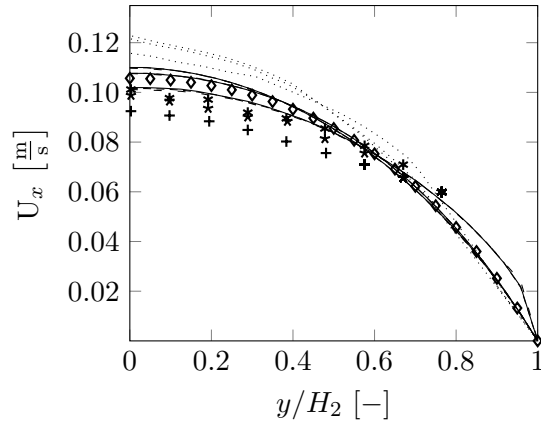


**Figure 3.8:** Comparison between measured and predicted velocity in the downstream section (planar contraction).  
 (+): measured at c-1, (\*): measured at c-2, (\*): measured at c-3, (◇): analytical solution of Cruz et al., (.....): simulation of Mu et al. [29], (- -): M1, (-·-·): M2, (—): M3.

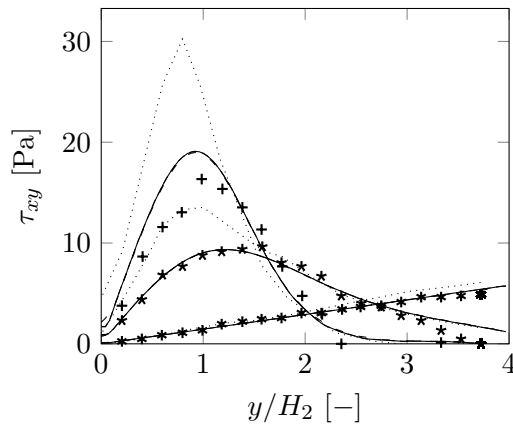


**Figure 3.9:** Comparison between measured and predicted shear stress in the upstream section (planar contraction).  
 (+): measured at a-1, (\*): measured at a-2, (\*): measured at a-3, (.....): simulation of Mu et al. [29], (- -): M1, (-·-·): M2, (—): M3.



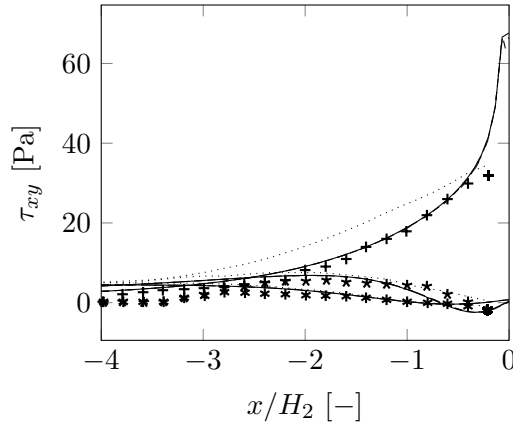


**Figure 3.10:** Comparison between measured and predicted shear stress in the upstream section (planar contraction).

(+): measured at b-1, (\*) : measured at b-2, (\*) : measured at b-3, (.....): simulation of Mu et al. [29], (- - -): M1, (-·-·-): M2, (—): M3.

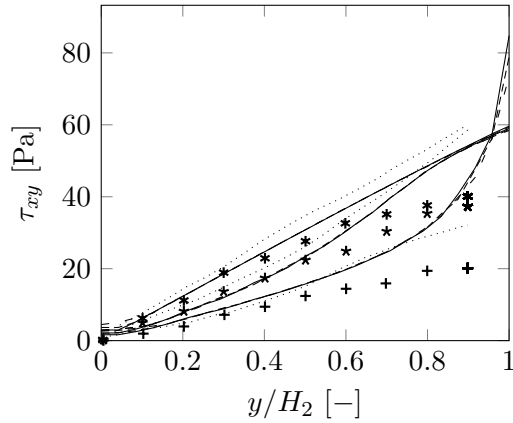


**Figure 3.11:** Comparison between measured and predicted shear stress in the downstream section (planar contraction).

(+): measured at c-1, (\*) : measured at c-2, (\*) : measured at c-3, (.....): simulation of Mu et al. [29], (- - -): M1, (-·-·-): M2, (—): M3.

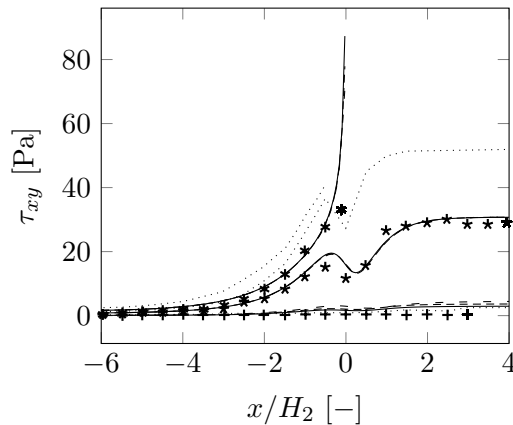


**Figure 3.12:** Comparison between measured and predicted shear stress in the downstream section (planar contraction).

(+): measured at d-1, (\*) : measured at d-2, (\*) : measured at d-3, (.....): simulation of Mu et al. [29], (- - -): M1, (-·-·-): M2, (—): M3.

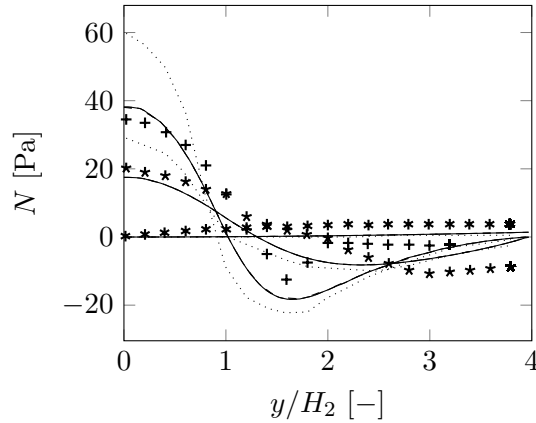


**Figure 3.13:** Comparison between measured and predicted first normal stress difference in the upstream section (planar contraction).  
 (+): measured at a-1, (\*): measured at a-2, (\*): measured at a-3, (.....): simulation of Mu et al. [29], (- -): M1, (-·-·): M2, (—): M3.

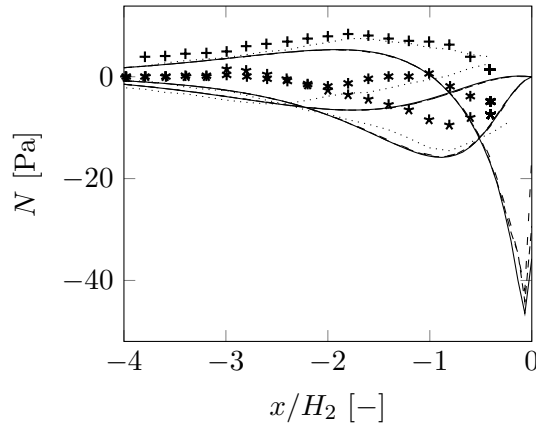


**Figure 3.14:** Comparison between measured and predicted first normal stress difference in the upstream section (planar contraction).  
 (+): measured at b-1, (\*): measured at b-2, (\*): measured at b-3, (.....): simulation of Mu et al. [29], (- -): M1, (-·-·): M2, (—): M3.

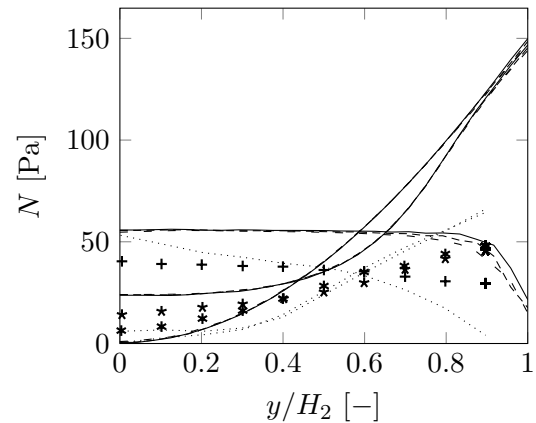


**Figure 3.15:** Comparison between measured and predicted first normal stress difference in the downstream section (planar contraction).  
 (+): measured at c-1, (\*): measured at c-2, (\*): measured at c-3, (.....): simulation of Mu et al. [29], (- -): M1, (-·-·): M2, (—): M3.

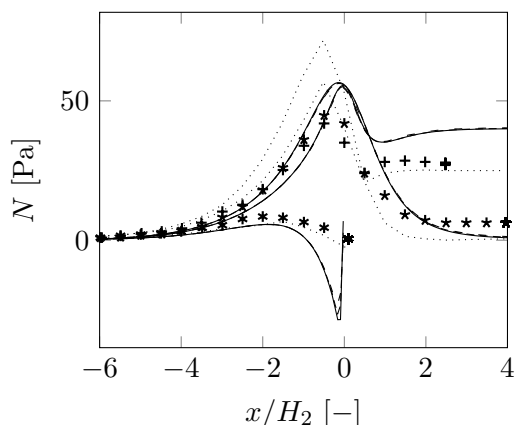


**Figure 3.16:** Comparison between measured and predicted first normal stress difference in the downstream section (planar contraction).  
 (+): measured at d-1, (\*) : measured at d-2, (\*) : measured at d-3, (.....): simulation of Mu et al. [29], (- - -): M1, (----): M2, (—): M3.

### 3.3.2 Square-square contraction

Alves et al. [31] and later Sousa et al. [21] visualized the flow of a viscoelastic fluid through a square-square contraction with particle image velocimetry (PIV) and streak line photography. The fluid used in their experiments is a solution composed of water and glycerol, which is doped with PAA. The SPTT fit is listed in Table 3.2. In the work of Sousa et al. they considered four different contraction ratios, however, we will only focus on the results for the contraction ratio of  $2H_1/2H_2 = 4$  in that work. Vortex lengths and axial velocity profiles at the centerline were measured as a function of the Deborah number at creeping flow conditions. Moreover, they proposed a flow pattern map with different flow regimes ranging from Newtonian-like flow, vortex enhancement, diverging streamlines to unsteady flow.

**Table 3.2:** Physical properties of the fluid used in the square-square contraction. [21]

$\rho$ $\left[ \frac{\text{kg}}{\text{m}^3} \right]$	$\eta_S$ $\left[ \frac{\text{kg}}{\text{m}\cdot\text{s}} \right]$	$\eta_P$ $\left[ \frac{\text{kg}}{\text{m}\cdot\text{s}} \right]$	$\lambda$ [s]	$\varepsilon$ [-]
1156	0.03	1.62	32	0.06

The upstream and downstream channel lengths in the simulation are chosen to be  $L_1/H_2 = 40$  and  $L_2/H_2 = 160$ , respectively. Flow symmetry is again assumed by making use of the symmetry planes in transversal direction, although we are aware of the fact that with this simplification we restrict ourselves to the steady flow regions, which ranged up to a Deborah number of approximately  $De \approx 300$  for the 4:1 contraction ratio in the experiments. A uniform velocity was assumed at the inlet and a zero gradient for the stresses. The mesh properties are listed in Table 3.3. A detailed isometric view of mesh M1 at the contraction is shown in Fig. 3.17 and the center planes of the three meshes are shown in Fig. 3.18.

**Table 3.3:** Properties of the meshes used for the square-square contraction.

	M1	M2	M3
$N_{cells}$	31,590	114,660	388,962
$\Delta x_{min}/2H_2$	0.0216	0.0148	0.0100
$\Delta y_{min}/2H_2 (= \Delta z_{min}/2H_2)$	0.0220	0.0144	0.0096

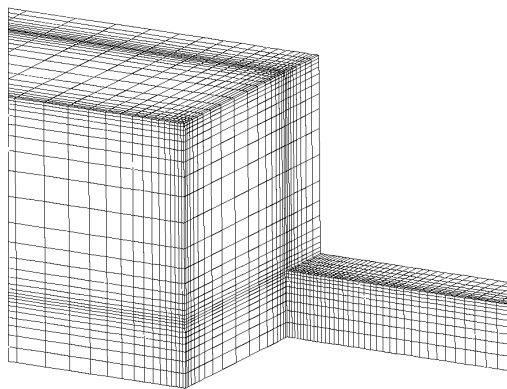


**Figure 3.17:** Detailed isometric view of mesh M1 in the contraction area (square-square contraction).

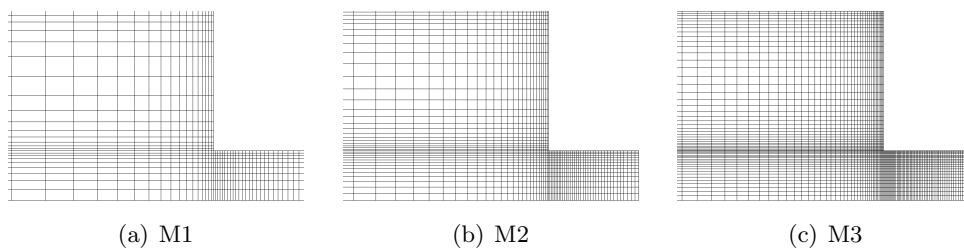


**Figure 3.18:** Detailed view of the center plane for the three meshes (square-square contraction).

Simulations were performed for thirteen different Deborah numbers  $De = \lambda U_2/H_2$  in the experimentally determined range of steady flows, with a maximum value of  $De = 310.59$ .  $U_2$  denotes the average velocity in the downstream channel. To prove the robustness of our algorithm, we note that stable and convergent simulations were continued up to a Deborah number of  $De = 700$  without loss of positive definiteness of the conformation tensor. This was ensured by verifying  $\det(\mathbf{c}) \geq 0$ . However, we note that in this case we are already in the region of unsteady flows, which we do not address correctly with making use of symmetry planes. Simulations were stopped at  $De = 700$  due to clearly leaving the steady region, however, we note that no upper limit in the Deborah number was found for this case. Velocity

checkerboard fields were not present in any of the simulations even at those very large Deborah numbers. Since we are interested in the steady solutions in this work, we also examined the use of under-relaxing the momentum equation and the pressure in our time-stepping algorithm. The under-relaxation parameter were 0.8 for both. This significantly helped to speed up the simulations to reach the stopping criteria, since larger time-steps were realizable. Simulations times for  $De = 108$  and a time step corresponding to a maximum Courant number of  $Co_{max} \leq 0.5$  are approximately 195 s simulation time per second of real-time for mesh M1, 25 min for mesh M2 and 2.5 h for mesh M3. The general trend of decreasing maximum Deborah number with mesh refinement could not be verified, since simulations were stable for all three meshes and Deborah numbers considered, however, we expect our algorithm to behave in a similar way.

Fig. 3.19 shows the dimensionless vortex length  $\chi = L_R/2H_1$  as a function of the maximum Courant number  $Co_{max} = (\frac{\Delta t U}{\Delta x})_{max}$ , which was used to determine the time-step  $\Delta t$  of our time-stepping algorithm.  $L_R$  is the vortex length at the upstream wall. The figure illustrates the consistency of our method in the sense that the final steady-state recirculating flow length is independent of the time-step  $\Delta t$ . Thus, the final formulation for the interpolation of the stress onto cell-faces is proved to be invariant of the time-step  $\Delta t$ , similar to the formulation found in Matos et al. [8]. For larger Deborah numbers, however, we note that the maximum Courant number that can be used diminishes in view of obtaining stable and convergent solutions.

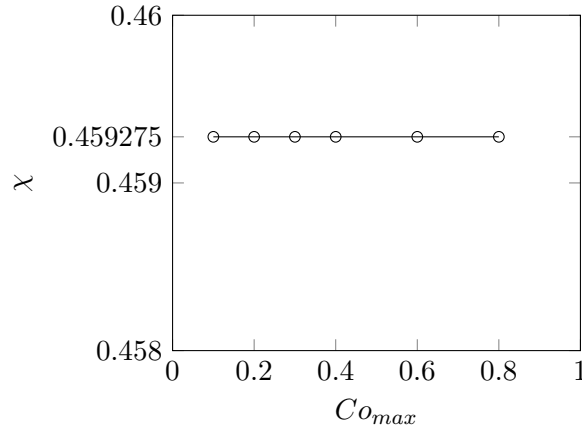


**Figure 3.19:** Dimensionless vortex length  $\chi$  as a function of the maximum Courant number  $Co_{max}$  for a Deborah number of  $De = 5.9$  (square-square contraction).

Fig. 3.20 illustrates the dependence of the dimensionless vortex length  $\chi$  on the Deborah number. The predicted vortex lengths are in very good agreement with both the measured and simulated values of Sousa et al. [21] in the Newtonian-like flow regime ( $De \lesssim 1.5$ ) and the vortex enhancement region ( $1.5 \lesssim De \lesssim 15$ ). In the Newtonian-like flow regime the elastic forces are negligible small and the fluid behaves similar to an ideal Newtonian fluid. In the vortex enhancement region the vortex length is significantly increasing due to the strong elastic effects. In the regime of diverging streamlines ( $15 \lesssim De \lesssim 300$ ) the simulated

recirculating flow lengths perceptibly depart from the measurements. In the experiments the effect of diverging streamlines occurred simultaneously with the vortex enhancement effect. Diverging streamlines were not obtained numerically and, moreover, a saturation effect was found numerically in the sense that the rate at which the recirculating flow increases with decreasing Deborah number. This is in contrast to the experiments, in which an almost linear increase can be found. The predicted vortex lengths are sufficiently independent of the mesh as can be seen in Fig. 3.19 and a better agreement with mesh refinement can be excluded. We believe that the deviation is due to the deficiency of the SPTT model to describe this flow behavior.

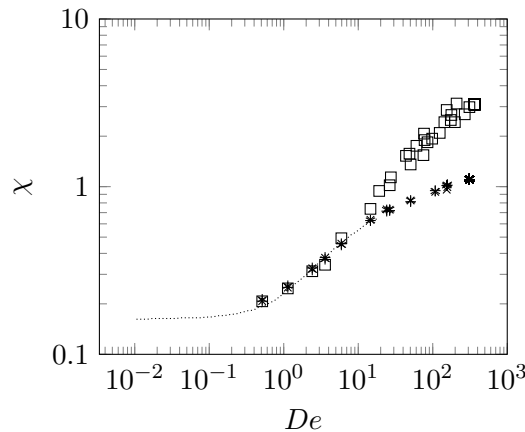


**Figure 3.20:** Dimensionless vortex length as a function of the Deborah number (square-square contraction).  
 (□): measurements of Sousa et al. [21], (.....): simulation of Sousa et al. [21],  
 (×): M1, (+): M2, (\*): M3.

In Fig. 3.21 we present the axial velocity profiles at the centerline for three different Deborah numbers in the diverging streamlines regime. When approaching the contraction area in the upstream channel, there is a point at which the fluid accelerates. At the contraction a distinct overshoot in the axial velocity is present after which the fluid decelerates again until reaching developed flow conditions. With increasing elastic effects (or Deborah number) the point, where the fluid accelerates, significantly shifts upstream, the peak becoming more distinct and the downstream length, at which developed flow conditions are found, is shifted downstream. For the smallest Deborah number, both the point at which the fluid accelerates and the upstream slope is predicted quite good, however, there is no pronounced peak at the contraction but a smooth overshoot, which stretches out far into the downstream channel. However, it is noted that for lower Deborah numbers a sharp peak is predicted at the contraction (cf. Fig. 3.22). At larger Deborah numbers, the point of fluid acceleration is perceptibly underpredicted. This is in agreement with the results shown in Fig. 3.20. The point, where developed flow conditions are reached is shifted far downstream in the simulations when comparing to the experimental data.

3 Semi-implicit stress formulation for viscoelastic models: Application to three-dimensional contraction flows

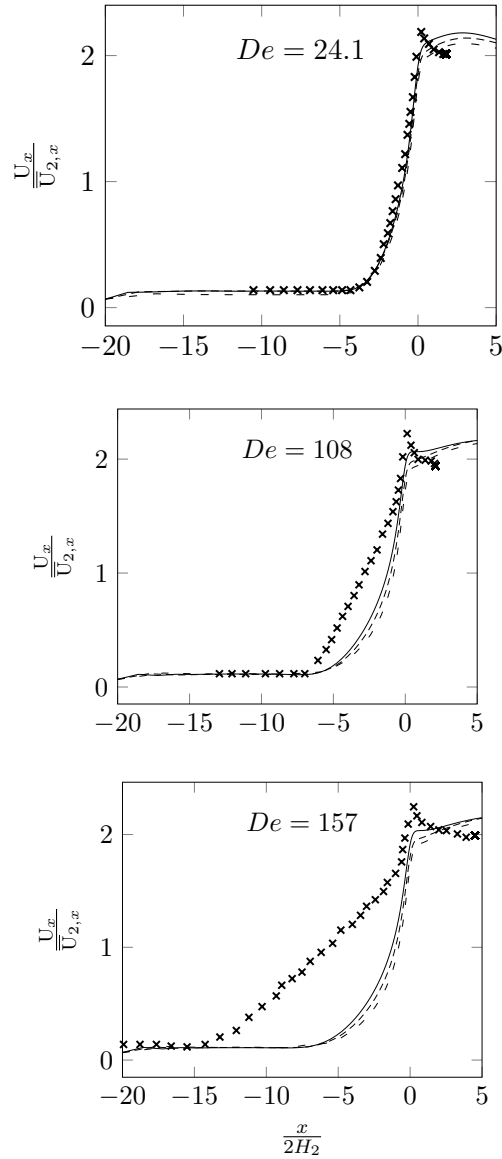


**Figure 3.21:** Dimensionless axial velocity profile at the centerline of the square-square contraction.

( $\times$ ): measurements of Sousa et al. [21], (- -): M1, (-·-·): M2, (—): M3.

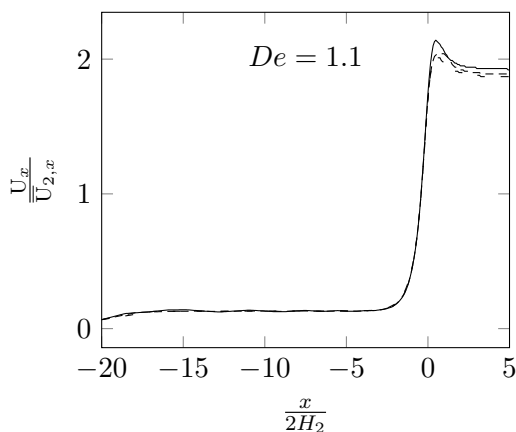


**Figure 3.22:** Dimensionless axial velocity profile at the centerline of the square-square contraction.  
 (- -): M1, (-·-·): M2, (—): M3.

## 3.4 Conclusions

In this work we developed a new approximation for the divergence of stress in the collocated finite-volume method. This technique not only completely avoids the presence of unphysical checkerboard patterns of velocity, but also allows for a semi-implicit handling of the constitutive equation, which promotes the numerical stability of our algorithm. The method is proved to be consistent in the sense that converged solutions are independent of the time-step  $\Delta t$ . Applying the method to the simulation of three-dimensional planar and square-square contraction flows of a SPTT-fluid, we were able to obtain stable and accurate solutions over a wide range of Deborah numbers. Mesh convergence of the results was shown in all cases. A comparison of the numerical predictions with the experimental data for the planar contraction showed generally good agreement for velocity, shear-stress and first-normal stress difference with the agreement being better in the upstream channel than in the downstream channel. The simulations of the flow through a square-square contraction are in good agreement with the experimental data in the Newtonian-like and vortex enhancement flow regime. However, in the diverging streamline regime distinct deviations between simulation and experiment were found, which we assume to be caused by a deficiency of the SPTT model to describe the flow behavior in this flow regime.



## 3.A Literature

- [1] S.-C. Xue, N. Phan-Thien, R. I. Tanner, Numerical study of secondary flows of viscoelastic fluid in straight pipes by an implicit finite volume method, *J. Non-Newtonian Fluid Mech.* 59 (1995) 191–213.
- [2] M. A. Alves, F. T. Pinho, P. J. Oliveira, Effect of a high resolution differencing scheme on finite-volume predictions of viscoelastic flows, *J. Non-Newtonian Fluid Mech.* 93 (2000) 287–314.
- [3] H. H. Hu, D. D. Joseph, Numerical simulation of viscoelastic flow past a cylinder, *J. Non-Newtonian Fluid Mech.* 37 (1990) 347–377.
- [4] G. P. Sasmal, A finite volume approach for calculation of viscoelastic flow through an abrupt axisymmetric contraction, *J. Non-Newtonian Fluid Mech.* 56 (1995) 15–47.
- [5] J. H. Ferziger, M. Peric, *Computational methods for fluid dynamics*, Springer, 2002.
- [6] P. J. Oliveira, F. T. Pinho, G. A. Pinto, Numerical simulation of non-linear elastic flows with a general collocated finite-volume method, *J. Non-Newtonian Fluid Mech.* 79 (1998) 1–43.
- [7] C. M. Rhie, W. L. Chow, Numerical study of the turbulent flow past an airfoil with trailing edge separation, *AIAA J.* 21 (1983) 1525–1532.
- [8] H. M. Matos, M. A. Alves, P. J. Oliveira, New formulation for stress calculation: Application to viscoelastic flow in a T-junction, *Numer. Heat Transfer, Part B* 56 (2009) 351–371.
- [9] M. A. Alves, P. J. Oliveira, F. T. Pinho, Benchmark solutions for the flow of Oldroyd-B and PTT fluids in planar contractions, *J. Non-Newtonian Fluid Mech.* 110 (2003) 45–75.
- [10] A. Afonso, P. J. Oliveira, F. T. Pinho, M. A. Alves, The log-conformation tensor approach in the finite-volume method framework, *J. Non-Newtonian Fluid Mech.* 157 (2009) 55–65.
- [11] J. L. Favero, A. R. Secchi, N. S. M. Cardozo, H. Jasak, Viscoelastic flow analysis using the software OpenFOAM and differential constitutive equations, *J. Non-Newtonian Fluid Mech.* 165 (2010) 1625–1636.
- [12] L. Holmes, J. Favero, T. Osswald, Numerical simulation of three-dimensional viscoelastic planar contraction flow using the software OpenFOAM, *Comput. Chem. Eng.* 37 (2012) 64–73.

- [13] F. Habla, A. Woitalka, S. Neuner, O. Hinrichsen, Development of a methodology for numerical simulation of non-isothermal viscoelastic fluid flows with application to axisymmetric 4:1 contraction flows, accepted in *Chemical Engineering Journal*, <http://dx.doi.org/10.1016/j.cej.2012.07.060> (2012).
- [14] F. Habla, H. Marschall, O. Hinrichsen, L. Dietsche, H. Jasak, J. L. Favero, Numerical simulation of viscoelastic two-phase flows using OpenFOAM, *Chem. Eng. Sci.* 66 (2011) 5487–5496.
- [15] S. Majumdar, Role of underrelaxation in momentum interpolation for calculation of flow with nonstaggered grids, *Numer. Heat Transfer* 13 (1988) 125–132.
- [16] S. K. Choi, Note on the use of momentum interpolation method for unsteady flows, *Numer. Heat Transfer A* 36 (1999) 545–550.
- [17] B. Yu, W.-Q. Tao, J.-J. Wei, Y. Kawaguchi, T. Tagawa, H. Ozoe, Discussion on momentum interpolation method for collocated grids of incompressible flow, *Numer. Heat Transfer B* 42 (2002) 141–166.
- [18] D. V. Boger, Viscoelastic flows through contractions, *Ann. Rev. Fluid Mech.* 19 (1987) 157–182.
- [19] P. J. Oliveira, F. T. Pinho, Plane contraction flows of upper convected Maxwell and Phan-Thien-Tanner fluids as predicted by a finite-volume method, *J. Non-Newtonian Fluid Mech.* 88 (1999) 63–88.
- [20] L. M. Quinzani, R. C. Armstrong, R. A. Brown, Birefringence and laser-doppler velocimetry (LDV) studies of viscoelastic flow through a planar contraction, *J. Non-Newtonian Fluid Mech.* 52 (1994) 1–36.
- [21] P. Sousa, P. Coelho, M. Oliveira, M. Alves, Effect of the contraction ratio upon viscoelastic fluid flow in three-dimensional square-square contractions, *Chem. Eng. Sci.* 66 (2011) 998–1009.
- [22] N. Phan-Thien, R. I. Tanner, A new constitutive equation derived from network theory, *J. Non-Newtonian Fluid Mech.* 2 (1977) 353–365.
- [23] R. Guénette, M. Fortin, A new mixed finite element method for computing viscoelastic flows, *J. Non-Newtonian Fluid Mech.* 60 (1995) 27–52.
- [24] P. J. Oliveira, F. T. Pinho, Numerical procedure for the computation of fluid flow with arbitrary stress-strain relationships, *Numer. Heat Transfer, Part B* 35 (1999) 295–315.

- [25] S.-C. Xue, R. I. Tanner, N. Phan-Thien, Numerical modelling of transient viscoelastic flows, *J. Non-Newtonian Fluid Mech.* 123 (2004) 33–58.
- [26] J. Jasak, H. G. Weller, A. D. Gosman, High resolution NVD differencing scheme for arbitrarily unstructured meshes, *Int. J. Numer. Meth. Fluids* 31 (1999) 431–449.
- [27] M. A. Alves, P. J. Oliveira, F. T. Pinho, A convergent and universally bounded interpolation scheme for the treatment of advection, *Int. J. Numer. Meth. Fluids* 41 (2003) 47–75.
- [28] J. Azaizez, R. Guénette, A. Ait-Kadi, Numerical simulation of viscoelastic flows through a planar contraction, *J. Non-Newtonian Fluid Mech.* 62 (1996) 253–277.
- [29] Y. Mu, G. Zhao, X. Wu, J. Zhai, Modeling and simulation of three-dimensional planar contraction flow of viscoelastic fluids with PTT, Giesekus and FENE-P constitutive models, *Appl. Math. Comput.* 218 (2012) 8429–8443.
- [30] D. O. A. Cruz, F. T. Pinho, P. J. Oliveira, Analytical solutions for fully developed laminar flow of some viscoelastic liquids with a Newtonian solvent contribution, *J. Non-Newtonian Fluid Mech.* 132 (2005) 28–35.
- [31] M. A. Alves, F. T. Pinho, P. J. Oliveira, Visualizations of Boger fluid flows in a 4:1 square-square contraction, *AIChE J.* 51 (2005) 2908–2922.

## 3.B Nomenclature

Normal symbols represent scalar quantities and boldface symbols represent vector and tensor quantities in general.

### Roman Symbols

Symbol	Description	Unit
$a_N$	Off-diagonal coefficient stemming from convection term	
$a_P^C$	Diagonal coefficient stemming from convection term of cell $P$	
$\mathbb{A}_P^U$	Diagonal coefficient of semi-discretized momentum equation of cell $P$	
$\mathbb{A}_P^\tau$	Diagonal coefficient of semi-discretized constitutive equation of cell $P$	
$\mathbf{c}$	Conformation tensor	$[-]$
$\mathbf{d}$	Distance between two adjoining cell centers	$[m]$
$H_1$	Upstream channel height	$[m]$
$H_2$	Downstream channel height	$[m]$
$\mathbb{H}_P^U$	Off-diagonal coefficients and source-vector of semi-discretized momentum equation of cell $P$	
$\mathbb{H}_P^\tau$	Off-diagonal coefficients and source-vector of semi-discretized constitutive of cell $P$	
$L_1$	Upstream channel length	$[m]$
$L_2$	Downstream channel length	$[m]$
$L_R$	Vortex length	$[m]$
$N$	Number of adjacent cells	$[-]$
	or first normal stress difference	$[\frac{kg}{ms^2}]$
$p$	Pressure	$[\frac{kg}{ms^2}]$
$\mathbf{S}_f$	Surface area normal vector at cell face $f$	$[m^2]$
$\mathbf{S}_{fe}$	Surface area normal vector at cell face $fe$	$[m^2]$
$\mathbf{S}_{fw}$	Surface area normal vector at cell face $fw$	$[m^2]$
$\mathbf{U}$	Velocity	$[\frac{m}{s}]$
$\mathbf{U}_E$	Velocity at cell $E$	$[\frac{m}{s}]$
$\mathbf{U}_f$	Velocity at cell-face $f$	$[\frac{m}{s}]$
$\mathbf{U}_P$	Velocity at cell $P$	$[\frac{m}{s}]$
$U_2$	Average downstream channel velocity	$[\frac{m}{s}]$

3 Semi-implicit stress formulation for viscoelastic models: Application to three-dimensional contraction flows

Symbol	Description	Unit
$U_x$	Axial velocity component	$[\frac{m}{s}]$
$U_y$	Vertical velocity component	$[\frac{m}{s}]$
$\tilde{\mathbf{U}}$	Semi-discretized velocity contribution	$[\frac{m}{s}]$
$t$	Time	$[s]$
$V_P$	Volume of computational cell $P$	$[m^3]$
$W$	Slit width	$[m]$
$x$	Position	$[m]$
$y$	Position	$[m]$

Greek Symbols

Symbol	Description	Unit
$\Delta t$	Time step size	$[s]$
$\Delta x$	Characteristic length of computational cell	$[m]$
$\nabla$	Nabla (gradient) operator	$[m^{-1}]$
$\nabla \cdot$	Divergence operator	$[m^{-1}]$
$\nabla_f^\perp$	Face normal gradient at cell face $f$	$[m^{-1}]$
$\nabla_{fe}^\perp$	Face normal gradient at cell face $fe$	$[m^{-1}]$
$\epsilon$	Extensibility parameter of SPTT model	$[-]$
$\eta_0$	Zero shear-rate viscosity	$[\frac{kg}{ms}]$
$\eta_P$	Polymeric viscosity	$[\frac{kg}{ms}]$
$\eta_S$	Solvent viscosity	$[\frac{kg}{ms}]$
$\lambda$	Relaxation time	$[s]$
$\rho$	Density	$[\frac{kg}{m^3}]$
$\boldsymbol{\tau}$	Deviatoric or extra-stress tensor	$[\frac{kg}{ms^2}]$
$\boldsymbol{\tau}_P$	Polymeric stress tensor	$[\frac{kg}{ms^2}]$
$\boldsymbol{\tau}_{P,E}$	Polymeric stress tensor in computational cell $E$	$[\frac{kg}{ms^2}]$
$\boldsymbol{\tau}_{P,f}$	Polymeric stress tensor at cell face $f$	$[\frac{kg}{ms^2}]$
$\boldsymbol{\tau}_{P,fe}$	Polymeric stress tensor at cell face $fe$	$[\frac{kg}{ms^2}]$
$\boldsymbol{\tau}_{P,fw}$	Polymeric stress tensor at cell face $fw$	$[\frac{kg}{ms^2}]$
$\boldsymbol{\tau}_{P,N}$	Polymeric stress tensor in computational cell $N$	$[\frac{kg}{ms^2}]$
$\boldsymbol{\tau}_{P,P}$	Polymeric stress tensor in computational cell $P$	$[\frac{kg}{ms^2}]$
$\boldsymbol{\tau}_{P,W}$	Polymeric stress tensor in computational cell $W$	$[\frac{kg}{ms^2}]$

3 Semi-implicit stress formulation for viscoelastic models: Application to three-dimensional contraction flows

Symbol	Description	Unit
$\widetilde{\boldsymbol{\tau}}_P$	Semi-discretized stress contribution	$[\frac{kg}{ms^2}]$
$\boldsymbol{\tau}_S$	Solvent stress tensor	$[\frac{kg}{ms^2}]$
$\tau_{xx}$	Axial normal stress	$[\frac{kg}{ms^2}]$
$\tau_{xy}$	Shear stress	$[\frac{kg}{ms^2}]$

### Subscripts, Superscripts and Oversymbols

Symbol	Description
$det(\mathbf{Q})$	Determinant of matrix $\mathbf{Q}$
$\mathbf{Q}_E$	Property $\mathbf{Q}$ in computational cell $E$
$\mathbf{Q}_f$	Property $\mathbf{Q}$ at cell face $f$
$\mathbf{Q}_{fe}$	Property $\mathbf{Q}$ at cell face $fe$
$\mathbf{Q}_{fw}$	Property $\mathbf{Q}$ at cell face $fw$
$\mathbf{Q}_{max}$	Maximum of $\mathbf{Q}$ in computation domain
$\mathbf{Q}^{n-1}$	Time level $n - 1$
$\mathbf{Q}^n$	Time level $n$
$\mathbf{Q}^{n+1}$	Time level $n + 1$
$\mathbf{Q}_P$	Property $\mathbf{Q}$ in computational cell $P$
$\mathbf{Q}^T$	Transpose of matrix $\mathbf{Q}$
$\mathbf{Q}_W$	Property $\mathbf{Q}$ in computational cell $W$
$\mathbf{Q}^*$	Estimate of variable $\mathbf{Q}$
$\nabla$	Upper-convected time derivative
$\widetilde{\mathbf{Q}}$	Semi-discretized contribution
$\mathbf{Q} _f$	$\mathbf{Q}$ linearly interpolated to cell face $f$

### Nondimensional Groups

Symbol	Description	Definition
$\beta$	Retardation factor	$\frac{\eta_S}{\eta_0}$
$Co$	Courant number	$\frac{\Delta t U}{\Delta x}$
$De$	Deborah number	$\frac{\lambda U_2}{H_2}$
$\chi$	Dimensionless vortex length	$\frac{L_R}{2H_1}$

## **Abbreviations**

<b>Abbreviation</b>	<b>Description</b>
AMG	Algebraic multigrid
BiCGstab	Bi-conjugate gradient stabilized
BSD	Both-side-diffusion
CUBISTA	Convergent and universally bounded interpolation scheme for treatment of advection
FENE	Finite extensible non-linear elastic
FIB	Flow-induced birefringence
FVM	Finite volume method
LDV	Laser-doppler velocimetry
l.h.s.	Left hand side
r.h.s.	Right hand side
PAA	Poly acrylic acid
PISO	Pressure implicit with splitting of operator
PIV	Particle image velocimetry
SIMPLE	Semi-implicit method for pressure linked equations
SPTT	Simplified Phan-Thien-Tanner

## 3.C Summary

In this chapter a new formulation for the divergence of the viscoelastic stress for the collocated (cell-centered) finite-volume method is proposed. The reformulation allows for a semi-implicit handling of the constitutive equation, which promotes the numerical stability. Simulations of a three-dimensional planar and a square-square contraction show the robustness of this technique. The new formulation is completely devoid of unphysical checkerboard patterns of the velocity, which are present when using standard approximations for the divergence in conjunction with non-staggered grid methods. The consistency is ensured by giving results, which are independent of the time-step  $\Delta t$  for steady-state problems. The results for the planar contraction are generally in good agreement with experimental data for velocity, shear stress and first-normal stress difference. Stable simulations for the square-square contraction could be performed over a wide range of Deborah numbers. The vortex length is in agreement with the experimental results in the Newtonian-like and vortex-enhancement flow regime, however, the results deviate from the experiments in the diverging streamline regime.

## 3.D Author contribution

The author of this thesis contributed to this publication by discovering the possible occurrence of decoupling effects when using the solver developed by Favero et al. [11], by having the idea of the semi-implicit reformulation, by implementing this reformulation in the software package *OpenFOAM*<sup>®</sup>, by proposing the concept of the validation base to show the benefits when using this reformulation, by doing the simulation runs for Figs. 3.5 and 3.19 and by writing the whole manuscript.

## 3.E Copyright permission

This chapter is originated from the following publication:

F. Habla, A. Obermeier, O. Hinrichsen, Semi-implicit stress formulation for viscoelastic models: Application to three-dimensional contraction flows, *Journal of Non-Newtonian Fluid Mechanics* 199 (2013) 70-79.

Reprinted with permission from Elsevier Ltd.



# 4 Numerical simulation of the viscoelastic flow in a three-dimensional lid-driven cavity using the log-conformation reformulation in OpenFOAM®

## 4.1 Introduction

Simulation of complex viscoelastic flows at high Weissenberg numbers is an outstanding challenge. Fortunately, the last years provided significant progress in developing stable and accurate numerical algorithms. [1, 2, 3] Benchmark problems used in academia to test numerical algorithms include contraction flows [4, 3], flows around spheres [5, 6] and cavity flows [2, 7, 8] besides others.

Most of the work on cavity flows done so far was solely theoretically motivated, which is mainly because remarkably complex flow patterns develop in this very simple geometry. [9] Nevertheless, predicting and understanding the flow inside cavities is also of particular industrial relevance for short-dwell and flexible blade coaters. [10] Numerical simulation of the flow of a Newtonian fluid inside a cavity is straightforward and literature on that is exhausting, e.g. Sheu and Tsai [11], who studied the steady flow topology in a three-dimensional lid-driven cavity with a finite-element method at a Reynolds number of  $Re = 400$ . In contrast, predicting the flow of a viscoelastic fluid in a cavity is demanding and literature about that is few so far. A reason for the little interest may partly be due to the comparatively very low Weissenberg number that can be achieved. For example, Demir [12] studied the transient flow of a viscoelastic fluid governed by the upper convected Criminale-Ericson-Filbey (CEF) equation and the maximum Weissenberg number obtained was only  $We_{max} = 0.01$  for all Reynolds numbers considered. Similar to others, Demir [12] imposed a uniform velocity at the moving lid, which leads to discontinuities at the two upper corners. This limits the maximum attainable Weissenberg number typically to below 0.2. [13] More recent works impose regularized boundary conditions in order to have a vanishing velocity and velocity gradient at the two upper corners, see for example Fattal and Kupferman [7]. However, a thin boundary layer close to the lid and a singular point for the conformation tensor at the downstream upper corner remain, which still leave this problem to be difficult and pose an upper limit for the Weissenberg number. [8]

Fattal and Kupferman [2, 7] proposed the so-called log-conformation reformulation (LCR), in which a logarithmized evolution equation for the conformation tensor is solved instead of solving the constitutive equation itself. This removes the exponential variation of the stress (and also the conformation tensor) at stagnation points. The new variable (the

logarithm of the conformation tensor) can better be approximated by polynomial-based interpolation schemes than the exponentially behaving conformation tensor (or stress) itself. A beneficial side-effect of this technique is that the positive-definiteness of the conformation tensor is always preserved. Fattal and Kupferman tested this technique for a two-dimensional viscoelastic cavity flow of a FENE-CR [2] and Oldroyd-B [7] fluid and they presented stable simulations up to a Weissenberg number of 5. Oscillations in the kinetic energy show the loss of convergence and the onset of a transient flow pattern for Weissenberg numbers above 3. Pan and Hao [14] applied the log-conformation technique in operator-splitting form to their finite-element code and simulated the two-dimensional Stokes flow of a viscoelastic fluid in a cavity up to a Weissenberg number of 3. They solve the logarithmized evolution equation for the conformation tensor on a coarser grid than the velocity, similar as it was done in the work of Fattal and Kupferman [2, 7]. This reduces the number of high frequency modes, which, in turn, further stabilizes the solution of the logarithmized equation. A first-order upwind difference scheme was used for discretizing the advection term of the constitutive equation in that work. Upwind differencing, however, is known to be least accurate as it introduces a large amount of numerical diffusion, although this helps to stabilize the solution and significantly increases the maximum achievable Weissenberg number. Oliveira [9] used a finite-volume method to simulate the steady flow and the transient recoil of a FENE-CR fluid with a regularized boundary condition and a comparatively large retardation ratio of 0.79. The maximum Weissenberg number was 10 for creeping flow conditions ( $Re = 0$ ). The advection term of the constitutive equation was discretized with the convergent and highly accurate CUBISTA scheme, which is formally of order three. [15] Yapici et al. [16] used a finite-volume method code, in which they also use the upwind scheme for treating the convective term in the constitutive equation. They performed simulations for the flow of an Oldroyd-B fluid in a cavity at different Reynolds numbers and presented results up to a Weissenberg number of 1 for creeping flow conditions.

In this work, the log-conformation reformulation is implemented in the collocated finite-volume based open-source software *OpenFOAM*®. Results are presented for the flow of an Oldroyd-B fluid in a startup Poiseuille flow and a three-dimensional cavity at creeping flow conditions. The remaining of this work is organized as follows: in Section 4.2 the governing equations are presented and the theory of the log-conformation approach is explained. In the following Section 4.3 the numerical implementation in *OpenFOAM*® is described. In Section 4.4 the results for the startup of Poiseuille flow and the three-dimensional lid-driven cavity are presented and discussed. Finally, in Section 4.5 this work ends with a summary.

## 4.2 Mathematical background

### 4.2.1 Governing equations

We consider the flow of an incompressible and isothermal viscoelastic fluid, which is governed by the Oldroyd-B constitutive equation. [17] The balance equations are the mass and momentum balance

$$\nabla \cdot \mathbf{U} = 0 \quad (4.1)$$

$$\rho \left( \frac{\partial \mathbf{U}}{\partial t} + \nabla \cdot (\mathbf{U}\mathbf{U}) \right) = -\nabla p + \nabla \cdot \boldsymbol{\tau} \quad (4.2)$$

where  $\mathbf{U}$  is the velocity,  $\rho$  is the density,  $t$  is time,  $p$  is pressure and  $\boldsymbol{\tau}$  is the extra stress tensor, which can be written as the sum of a solvent and polymer contribution

$$\boldsymbol{\tau} = \boldsymbol{\tau}_S + \boldsymbol{\tau}_P \quad (4.3)$$

For the solvent contribution the Newtonian law holds

$$\boldsymbol{\tau}_S = \eta_S \left[ \nabla \mathbf{U} + (\nabla \mathbf{U})^T \right] \quad (4.4)$$

where  $\eta_S$  is the solvent viscosity. For the polymeric contribution  $\boldsymbol{\tau}_P$ , the Oldroyd-B equation may hold in this work, although it should be noted here that numerous other constitutive equations, such as the Giesekus, SPTT or FENE-type models as well as multi-mode models are forthcoming within this framework. The Oldroyd-B equation is defined as follows

$$\boldsymbol{\tau}_P + \lambda \overset{\nabla}{\boldsymbol{\tau}}_P = \eta_P \left[ \nabla \mathbf{U} + (\nabla \mathbf{U})^T \right] \quad (4.5)$$

where  $\lambda$  is the relaxation time and  $\eta_P$  is the polymer viscosity.  $\overset{\nabla}{\boldsymbol{\tau}}_P$  denotes the upper-convected time derivative

$$\overset{\nabla}{\boldsymbol{\tau}}_P \equiv \frac{\partial \boldsymbol{\tau}_P}{\partial t} + \nabla \cdot (\mathbf{U}\boldsymbol{\tau}_P) - (\nabla \mathbf{U})^T \cdot \boldsymbol{\tau}_P - \boldsymbol{\tau}_P \cdot \nabla \mathbf{U} \quad (4.6)$$

The retardation ratio  $\beta$  is defined as the ratio between solvent viscosity  $\eta_S$  and total viscosity  $\eta_0 = \eta_S + \eta_P$

$$\beta = \frac{\eta_S}{\eta_0} = \frac{\eta_S}{\eta_S + \eta_P} \quad (4.7)$$

The Oldroyd-B equation may be rewritten in terms of the conformation tensor  $\mathbf{c}$

$$\boldsymbol{\tau}_P = \frac{\eta_P}{\lambda} (\mathbf{c} - \mathbf{I}) \quad (4.8)$$

where  $\mathbf{I}$  is the identity matrix. Using Eq. 4.8 the constitutive equation Eq. 4.5 becomes

$$\frac{\partial \mathbf{c}}{\partial t} + \nabla \cdot (\mathbf{Uc}) - (\nabla \mathbf{U})^T \cdot \mathbf{c} - \mathbf{c} \cdot \nabla \mathbf{U} = \frac{1}{\lambda} (\mathbf{I} - \mathbf{c}) \quad (4.9)$$

Instead of Eq. 4.5, Eq. 4.9 can be solved and subsequently the polymeric stress obtained with use of Eq. 4.8.

## 4.2.2 Log-conformation approach

The conformation tensor  $\mathbf{c}$  is required to be strictly positive definite for the evolution equation Eq. 4.9 to be well-posed. In flows of high elasticity, this property may be violated, which often results in the numerical computation to fail. The main issue was shown for a 1-D problem [7]: in areas of high deformation rates the stretching and relaxation terms exhibit exponential growth. The only term to balance this growth is the convection term. However, since the convection term is based on polynomial interpolations, the convection term fails to balance the exponential amplification, which then results in the numerical simulation to blow up. To cope with this instability, Fattal and Kupferman [2] suggested a logarithmic transformation of Eq. 4.9, which became known as the 'log-conformation approach' and will shortly be outlined in the following.

Since the conformation tensor  $\mathbf{c}$  is a symmetric positive-definite (SPD) matrix, it can be diagonalized according to

$$\mathbf{c} = \mathbf{R} \cdot \mathbf{\Lambda} \cdot \mathbf{R}^T \quad (4.10)$$

$\mathbf{\Lambda}$  is a diagonal matrix consisting of the three eigenvalues of  $\mathbf{c}$  on the diagonal and  $\mathbf{R}$  is an orthogonal matrix, which is formed by the three eigenvectors of  $\mathbf{c}$ . Any diagonal matrix can be logarithmized by taking the logarithm element-wise on the diagonal. The logarithm of the conformation tensor  $\mathbf{c}$  is thus defined as

$$\mathbf{\Psi} = \log(\mathbf{c}) = \mathbf{R} \cdot \log(\mathbf{\Lambda}) \cdot \mathbf{R}^T \quad (4.11)$$

Accordingly,  $\mathbf{\Psi}$  is now our new variable. The main feature of the log-conformation reformulation is the following decomposition of the velocity gradient  $\nabla \mathbf{U}$

$$\nabla \mathbf{U} = \mathbf{\Omega} + \mathbf{B} + \mathbf{N} \cdot \mathbf{c}^{-1} \quad (4.12)$$

where  $\mathbf{\Omega}$  and  $\mathbf{N}$  are both anti-symmetric matrices.  $\mathbf{B}$  is a symmetric and traceless matrix, which commutes with  $\mathbf{c}$ .  $\mathbf{\Omega}$  accounts for rotations,  $\mathbf{B}$  accounts for pure extensions and the last term of Eq. 4.12 acts as a 'dummy part'. [4] Introducing this decomposition into Eq. 4.9, one easily obtains

$$\frac{\partial \mathbf{c}}{\partial t} + \nabla \cdot (\mathbf{Uc}) - (\mathbf{\Omega} \cdot \mathbf{c} - \mathbf{c} \cdot \mathbf{\Omega}) - 2\mathbf{B} \cdot \mathbf{c} = \frac{1}{\lambda} (\mathbf{I} - \mathbf{c}) \quad (4.13)$$

In order to obtain the matrices  $\mathbf{\Omega}$  and  $\mathbf{B}$  the velocity gradient is first rotated into the principal axes of the conformation tensor  $\mathbf{c}$  [18]

$$\mathbf{R}^T \cdot \nabla \mathbf{U} \cdot \mathbf{R} = \mathbf{R}^T \cdot \mathbf{\Omega} \cdot \mathbf{R} + \mathbf{R}^T \cdot \mathbf{B} \cdot \mathbf{R} + \mathbf{R}^T \cdot \mathbf{N} \cdot \mathbf{c}^{-1} \cdot \mathbf{R} \quad (4.14)$$

For a three-dimensional flow problem we subsequently define

$$\widetilde{\mathbf{M}} = \begin{pmatrix} \tilde{m}_{xx} & \tilde{m}_{xy} & \tilde{m}_{xz} \\ \tilde{m}_{yx} & \tilde{m}_{yy} & \tilde{m}_{yz} \\ \tilde{m}_{zx} & \tilde{m}_{zy} & \tilde{m}_{zz} \end{pmatrix} = \mathbf{R}^T \cdot \nabla \mathbf{U} \cdot \mathbf{R} \quad (4.15)$$

The matrices  $\mathbf{\Omega}$  and  $\mathbf{B}$  can now be obtained by

$$\mathbf{\Omega} = \mathbf{R} \cdot \begin{pmatrix} 0 & \omega_{xy} & \omega_{xz} \\ \omega_{yx} & 0 & \tilde{m}_{yz} \\ \omega_{zx} & \omega_{zy} & 0 \end{pmatrix} \cdot \mathbf{R}^T, \quad \mathbf{B} = \mathbf{R} \cdot \begin{pmatrix} \tilde{m}_{xx} & 0 & 0 \\ 0 & \tilde{m}_{yy} & 0 \\ 0 & 0 & \tilde{m}_{zz} \end{pmatrix} \cdot \mathbf{R}^T \quad (4.16)$$

where  $\omega_{ij} = (\Lambda_{jj}\tilde{m}_{ij} + \Lambda_{ii}\tilde{m}_{ji}) / (\Lambda_{ii} - \Lambda_{jj})$ . In case of  $\Lambda_{ii} = \Lambda_{jj}$  this would result in an undefined division by zero. Fortunately, this is only the case for the first time-step when  $\mathbf{c} = \mathbf{I}$ . In that case, we set  $\mathbf{\Omega} = \mathbf{0}$  and  $\mathbf{B} = 1/2 [\nabla \mathbf{U} + (\nabla \mathbf{U})^T]$ . Finally, we can rewrite Eq. 4.13 in terms of our new variable  $\mathbf{\Psi}$ :

$$\frac{\partial \mathbf{\Psi}}{\partial t} + \nabla \cdot (\mathbf{U} \mathbf{\Psi}) - (\mathbf{\Omega} \cdot \mathbf{\Psi} - \mathbf{\Psi} \cdot \mathbf{\Omega}) - 2\mathbf{B} = \mathbf{R} \cdot \left[ \frac{1}{\lambda} (\mathbf{\Lambda}^{-1} - \mathbf{I}) \right] \cdot \mathbf{R}^T \quad (4.17)$$

After solving this equation the inverse transformation can be applied. The newly obtained  $\mathbf{\Psi}$  is decomposed according to

$$\mathbf{\Psi} = \mathbf{R} \cdot \mathbf{\Lambda}_{\mathbf{\Psi}} \cdot \mathbf{R}^T \quad (4.18)$$

and the conformation tensor can be calculated by

$$\mathbf{c} = \exp(\mathbf{\Psi}) = \mathbf{R} \cdot \exp(\mathbf{\Lambda}_{\mathbf{\Psi}}) \cdot \mathbf{R}^T \quad (4.19)$$

It is emphasized here that the relation between the eigenvalues of the conformation tensor  $\mathbf{\Lambda}$  and the eigenvalues of the working variable  $\mathbf{\Lambda}_{\mathbf{\Psi}}$  is

$$\mathbf{\Lambda} = \exp(\mathbf{\Lambda}_{\mathbf{\Psi}}) \quad (4.20)$$

while the eigenvectors  $\mathbf{R}$  are the same for both  $\mathbf{c}$  and  $\mathbf{\Psi}$ . This is relevant in view of implementing an efficient numerical algorithm, which is described in the following chapter.

One of the main advantages of the log-conformation is the strict positive-definiteness of the conformation tensor. This will be ensured even on the discrete level. Thereby, the high

Weissenberg number instability is removed. [7] The positive-definiteness can be verified by checking  $\det(\mathbf{c}) \geq 0$ .

## 4.3 Numerical method

In this section we seek to describe the numerical method developed in this work. The above described model is implemented in the software package OpenFOAM® and the developed solver can be thought of a further-development of the initial work by Favero et al. [19] and our continuative paper [20].

### 4.3.1 Discretization schemes

The advection term in the constitutive equation will be discretized either by the upwind scheme or by the CUBISTA scheme. The upwind scheme is first-order accurate and known to introduce an excessive amount of numerical diffusion, although it is highly stable. [21] For most complex problems it is inadequate and should generally be avoided. The CUBISTA convection differencing scheme developed by Afonso et al. [15] is a high-accuracy scheme specially developed for the convection term of viscoelastic constitutive equations. The scheme is based on the third-order QUICK scheme and is formally of order three on uniform meshes and smooth flows. It can be described in Sweby's diagram [22] by

$$\varphi(r) = \max \{0, \min (1.5, 1.5r, 0.75 + 0.25r)\} \quad (4.21)$$

where  $\varphi$  is the flux limiter and  $r$  is the ratio of successive gradients of the interpolated variable  $\phi$ . [15] Jasak et al. [23] introduced a modification in order to avoid the need for determining the value  $\phi_U$  in the far upwind cell, which is impractical for unstructured meshes. With this modification  $r$  is calculated from

$$r = 2 \frac{\mathbf{d} \cdot (\nabla \phi)_C}{\phi_D - \phi_C} - 1 \quad (4.22)$$

where  $\mathbf{d}$  is the distance vector between node  $C$  and the downwind node  $D$ . The face value  $\phi_f$  is then blended with  $\varphi(r)$  between the face value obtained by upwind differencing  $\phi_{f,UD}$  and the face value obtained by central differencing  $\phi_{f,CD}$

$$\phi_f = (1 - \varphi)\phi_{f,UD} + \varphi\phi_{f,CD} \quad (4.23)$$

In this way the convection term is discretized fully implicitly as it only contributes to the matrix but not to the source vector. This implementation is in contrast to the deferred correction approach used in Afonso et al. [15], in which the part corresponding to the upwind scheme is discretized implicitly, while the remaining higher-order part is discretized explicitly, thereby ensuring diagonal dominance. The CUBISTA scheme in the deferred correction

approach was recently applied to the convection term in the log-conformation formulation within the collocated finite-volume framework by Afonso et al. [24].

The convection term in the momentum balance is negligible in all simulations of this work. Nevertheless, the term is retained and discretized with the same scheme as the one used in the constitutive equation.

The time derivatives appearing in the momentum and logarithmized constitutive equation are discretized with a generalized three-point scheme, also known as 'Gear' scheme. This scheme is second-order accurate in time, however, it increases the storage requirements due to the need of storing the variables at steps  $n$  and  $n - 1$ . This scheme was thoroughly evaluated by Xue et al. [25] for a transient Poiseuille flow of a viscoelastic fluid. The generalized three-point scheme was found to have the smallest relative error and allowed the largest time-step in their simulations. At the first time-step, however, only the initial conditions are known and the variables  $n - 1$  do not exist yet. Due to that, the implicit Euler scheme is used for the first time-step. The diffusion term in the momentum balance is discretized by second-order accurate linear interpolation in conjunction with Gaussian integration. In case of non-orthogonal meshes a correction approach is used as being explained in Jasak [26] in order to retain second-order accuracy. A second-order Gaussian formula for source terms (all terms but the inertia and convection term in Eq. 4.17) is applied. The velocity gradient, which must first be computed before doing the decomposition shown in Eq. 4.12, is also calculated using a second-order accurate Gauss formula based on linear interpolations.

### 4.3.2 Momentum equation discretization

Introducing the stress-splitting of Eq. 4.3 together with the Newtonian law Eq. 4.4 into the momentum equation and discretizing the time derivative results in

$$\begin{aligned} & \rho \left( \frac{3 \mathbf{U}^{n+1}}{2 \Delta t} + \nabla \cdot (\mathbf{U}^{n+1} \mathbf{U}^{n+1}) \right) - \nabla \cdot \eta_S \nabla \mathbf{U}^{n+1} \\ = & \\ & -\nabla p^{n+1} + \nabla \cdot \boldsymbol{\tau}_P^{n+1} + \rho \left( \frac{2 \mathbf{U}^n - \frac{1}{2} \mathbf{U}^{n-1}}{\Delta t} \right) \end{aligned} \quad (4.24)$$

In case of creeping flow conditions ( $Re \rightarrow 0$ ) and negligible solvent contributions ( $\eta_S \rightarrow 0$ ) Eq. 4.24 becomes singular. To ensure Eq. 4.24 to be solvable and allow for an update of the velocity field an additional elliptic term proportional to  $\eta_P$  can be introduced

$$\begin{aligned} & \rho \left( \frac{3 \mathbf{U}^{n+1}}{2 \Delta t} + \nabla \cdot (\mathbf{U}^{n+1} \mathbf{U}^{n+1}) \right) - \nabla \cdot \eta_0 \nabla \mathbf{U}^{n+1} \\ = & \\ & -\nabla p^{n+1} + \nabla \cdot \boldsymbol{\tau}_P^{n+1} - \nabla \cdot \eta_P \nabla \mathbf{U}^{n+1} + \rho \left( \frac{2 \mathbf{U}^n - \frac{1}{2} \mathbf{U}^{n-1}}{\Delta t} \right) \end{aligned} \quad (4.25)$$

This is known as the both-side-diffusion (BSD) technique [25] and is often used to stabilize simulations even in non-creeping flow conditions and non-zero solvent viscosities. The BSD, however, is not a proper choice for transient problems as it introduces a large portion of transient diffusion and may cause fictitious responses. [25] The problem exists if the diffusion terms on the l.h.s. and r.h.s. do not cancel out exactly. In that case, the resulting error is diffusion-like in time. This may either be because velocities of different time-steps are used for the two terms ( $\mathbf{U}^{n+1}$  for the term on the l.h.s. and  $\mathbf{U}^n$  for the term on the r.h.s) or if - although using  $\mathbf{U}^{n+1}$  for both terms as shown in Eq. 4.25 - no convergence is achieved within a time-step. However, if convergence is achieved the two terms cancel out exactly and the negative side-effects of BSD can be avoided. A further discussion follows in Section 4.3.5.

For solving the momentum balance we need to impose boundary conditions for  $\boldsymbol{\tau}_P$ . Although no PDE is solved for  $\boldsymbol{\tau}_P$  (it is calculated from Eq. 4.8) we need to impose boundary conditions in order to be able to calculate the divergence of  $\boldsymbol{\tau}_P$  with use of the Gauss theorem. On solid walls we will therefore either assign a second-order extrapolation boundary condition as described in Habla et al. [27] or a zero gradient boundary condition. The second-order extrapolation method is generally used since it is more accurate (but less stable). If stability is an issue we reduce the order of the extrapolation to first-order, which is done by neglecting terms proportional to the first spatial derivative of  $\boldsymbol{\tau}_P$ . Eventually, this first-order extrapolation is equal to the zero gradient boundary condition.

### 4.3.3 Flux formulation and pressure equation

Terms on the l.h.s. of Eq. 4.24 or 4.25 are evaluated implicitly and terms on the r.h.s. explicitly. A pressure-correction equation is obtained by casting these equations into a semi-discretized form, in which all terms but the pressure gradient are discretized. The time-indicator  $n + 1$  is dropped in the following for readability. We can write

$$\mathbb{A}_P^{\mathbf{U}} \mathbf{U} = \mathbb{H}_P^{\mathbf{U}}(\mathbf{U}) - \nabla p \quad (4.26)$$

The term  $\mathbb{H}_P^{\mathbf{U}}(\mathbf{U})$  comprises the off-diagonal coefficients and the (explicit) source terms. By division with the diagonal coefficient  $\mathbb{A}_P^{\mathbf{U}}$  the velocity can be written as

$$\mathbf{U} = \frac{\mathbb{H}_P^{\mathbf{U}}(\mathbf{U})}{\mathbb{A}_P^{\mathbf{U}}} - \frac{1}{\mathbb{A}_P^{\mathbf{U}}} \nabla p \quad (4.27)$$

After linear interpolation, the flux through cell-faces can be obtained by taking the dot product with the cell-face area vector  $\mathbf{S}_f$

$$F = \bar{\mathbf{U}} \cdot \mathbf{S}_f \approx \frac{\overline{\mathbb{H}_P^{\mathbf{U}}(\mathbf{U})}}{\overline{\mathbb{A}_P^{\mathbf{U}}}} \cdot \mathbf{S}_f - |\mathbf{S}_f| \frac{1}{\overline{\mathbb{A}_P^{\mathbf{U}}}} \nabla_f^\perp p \quad (4.28)$$



The linear interpolation onto the cell-faces is denoted by the overbar. Finally, taking the divergence and making use of the mass balance, Eq. 4.1, which must also hold on cell-faces, we arrive at an equation for pressure

$$\nabla \cdot \left( |\mathbf{S}_f| \frac{1}{\mathbb{A}_P^{\mathbf{U}}} \nabla_f^\perp p \right) = \nabla \cdot \left( \frac{\mathbb{H}_P^{\mathbf{U}}(\mathbf{U})}{\mathbb{A}_P^{\mathbf{U}}} \cdot \mathbf{S}_f \right) \quad (4.29)$$

#### 4.3.4 Constitutive equation discretization

Eq. 4.17 is discretized as follows

$$\begin{aligned} & \frac{3}{2} \frac{\Psi^{n+1}}{\Delta t} + \nabla \cdot (\mathbf{U}^{n+1} \Psi^{n+1}) \\ & = \\ & (\boldsymbol{\Omega}^{n+1} \cdot \Psi^{n+1} - \Psi^{n+1} \cdot \boldsymbol{\Omega}^{n+1}) + 2\mathbf{B}^{n+1} \\ & + \mathbf{R}^{n+1} \cdot \left[ \frac{1}{\lambda} (\boldsymbol{\Lambda}^{n+1-1} - \mathbf{I}) \right] \cdot \mathbf{R}^{n+1T} + \frac{2\Psi^n - \frac{1}{2}\Psi^{n-1}}{\Delta t} \end{aligned} \quad (4.30)$$

where the discretization of the convective term with the CUBISTA scheme is omitted due to readability. Terms on the l.h.s. are discretized implicitly, while terms on the r.h.s. are discretized explicitly. When doing outer-iterations per time-step, the terms belonging to time-step  $n + 1$  on the r.h.s. are calculated with the most recent guess for the respective variable. Due to the hyperbolic nature of Eq. 4.30 we only need to assign boundary conditions at the inlet, but not at solid walls and outlets.

#### 4.3.5 Solution algorithm

In view of developing a code suitable for the simulation of time-dependent viscoelastic flows, we adopted a PISO algorithm. Given known  $\mathbf{U}^n$ ,  $p^n$ ,  $\boldsymbol{\tau}^n$ ,  $\boldsymbol{\Lambda}^n$  and  $\mathbf{R}^n$  (as well as  $\mathbf{U}^{n-1}$  and  $\boldsymbol{\tau}^{n-1}$  to calculate the Gear time-derivative) the algorithm can be summarized as follows

- 1.) (optionally) Solve the momentum equation to obtain a new velocity guess  $\mathbf{U}^*$  (Eq. 4.24 or Eq. 4.25).
- 2.) Calculate  $\mathbb{A}_P^{\mathbf{U}}$  and  $\mathbb{H}_P^{\mathbf{U}}(\mathbf{U}^*)$  (Eq. 4.26).
- 3.) Solve the pressure equation (Eq. 4.29) to obtain a new pressure guess  $p^*$ .
- 4.) Correct the velocity with  $p^*$  to obtain  $\mathbf{U}^{**}$  (Eq. 4.27).
- 5.) Update  $\mathbb{H}_P^{\mathbf{U}}(\mathbf{U}^{**})$  using the new velocity guess  $\mathbf{U}^{**}$ .
- 6.) Solve the pressure equation to arrive at  $p^{n+1}$ .

- 7.) Correct the velocity with  $p^{n+1}$  to obtain  $\mathbf{U}^{n+1}$  (Eq. 4.27).
- 8.) Update the polymeric stress. Therefore:
  - 8.1.) Decompose the velocity gradient  $\nabla\mathbf{U}^{n+1}$  (refer to Eqs. 4.15 and 4.16).
  - 8.2.) Solve the logarithmized constitutive equation in order to obtain  $\Psi^{n+1}$  (Eq. 4.17).
  - 8.3.) Calculate the eigenvalues  $\Lambda^{n+1}$  and eigenvectors  $\mathbf{R}^{n+1}$  with use of Eqs. 4.18 and 4.20 and store them until the next time-step.
  - 8.4.) Do the inverse transformation to obtain  $\boldsymbol{\tau}^{n+1}$  (Eqs. 4.19 and 4.8).
- 9.) (optionally) Repeat from step 1. until final convergence is achieved (therefore, set  $p^n = p^{n+1}$ ,  $\mathbf{U}^n = \mathbf{U}^{n+1}$  and  $\Psi^n = \Psi^{n+1}$  as the new initial guesses).

In contrast to the common PISO technique, we omit the initial step of obtaining a velocity guess by solving the momentum equation in case of creeping flow conditions ( $Re \rightarrow 0$ ). The reason is that this step was found to impair the iterative convergence of the subsequent solution of the pressure equation under that conditions. We note that this is not a necessary step for obtaining final convergence of pressure and velocity.

The difference between the two diffusion terms on the l.h.s. and r.h.s. of Eq. 4.25 is that the term on the l.h.s. is evaluated implicitly, while the term on the r.h.s. is calculated explicitly with the latest velocity guess. In particular, this means: in the first solution of the pressure equation (step 3), the explicit BSD term is calculated with the velocity guess  $\mathbf{U}^*$ , while the term on the l.h.s. of Eq. 4.25 is treated implicitly. If one would stop after the first pressure iteration, this would result in a large portion of transient diffusion. Instead, after the first pressure solution the term  $\mathbb{H}_P^{\mathbf{U}}(\mathbf{U})$ , which comprises the explicit terms and in particular the BSD term on the r.h.s., is updated (step 5) by use of the newer velocity guess  $\mathbf{U}^{**}$ . Due to that, the negative side-effect of a transient diffusion caused by the BSD is severely diminished after having solved the pressure equation for the second time. Nevertheless, in order to obtain full convergence within a time-step and to completely avoid the side-effects of BSD additional outer iterations can be performed (step 9). Only if full convergence is achieved both diffusion terms on the l.h.s. and r.h.s. cancel out and only then the solutions with and without BSD are identical. Unfortunately, the number of outer iterations to obtain full convergence is considerably larger when using BSD, which is undesirable due to the associated increase of simulation time. Due to that, our numerical algorithm only uses BSD if flows without a solvent contribution ( $\eta_S \rightarrow 0$  or  $\beta \rightarrow 0$ ) and creeping flow conditions ( $Re \rightarrow 0$ ) are considered, in which a solution without BSD is impossible due to the pressure equation becoming singular.

In view of obtaining an efficient numerical algorithm it is emphasized here that the eigenvalues and eigenvectors are calculated only once per time-step (once per outer-iteration in case of using step 9) due to its computational costs, rather than doing the calculation twice as for example being explained in Tomé et al. [4]. After having solved Eq. 4.30, the eigenvalues  $\mathbf{\Lambda}_\Psi$  are calculated with the characteristic equation  $\det(\Psi - \lambda_\Psi \mathbf{I})$ , for which the coefficients  $a$ ,  $b$  and  $c$  of the equation  $\lambda_\Psi^3 + a\lambda_\Psi^2 + b\lambda_\Psi + c = 0$  are defined by

$$\begin{aligned} a &= -\Psi_{xx} - \Psi_{yy} - \Psi_{zz} \\ b &= \Psi_{xx}\Psi_{yy} + \Psi_{xx}\Psi_{zz} + \Psi_{yy}\Psi_{zz} - \Psi_{xy}\Psi_{yx} - \Psi_{xz}\Psi_{zx} - \Psi_{yz}\Psi_{zy} \\ c &= -\Psi_{xx}\Psi_{yy}\Psi_{zz} - \Psi_{xy}\Psi_{yz}\Psi_{zx} - \Psi_{xz}\Psi_{yx}\Psi_{zy} + \Psi_{xz}\Psi_{yy}\Psi_{zx} + \Psi_{xy}\Psi_{yx}\Psi_{zz} + \Psi_{xx}\Psi_{yz}\Psi_{zy} \end{aligned}$$

The cubic equation is solved with Cardano's method to obtain the three eigenvalues  $\lambda_{\Psi,1}$ ,  $\lambda_{\Psi,2}$  and  $\lambda_{\Psi,3}$ . Subsequently the corresponding eigenvectors are determined by calculating the 3 sub-determinants  $sd_{i,jk}$  of the matrix  $A_i = \Psi - \lambda_{\Psi,i} \mathbf{I}$  ( $sd_{i,jk} = A_{i,jj}A_{i,kk} - A_{i,jk}A_{i,kj}$  with  $j, k = x, y, z$ ;  $j \neq k$  and  $i = 1, 2, 3$ ). The eigenvectors are calculated based on the largest sub-determinant, e.g. if  $sd_{i,yz} > sd_{i,xy}$  and  $sd_{i,yz} > sd_{i,xz}$ , then the eigenvector  $EV(\lambda_{\Psi,i})$  is

$$EV(\lambda_{\Psi,i}) = \begin{pmatrix} 1 \\ (A_{i,yz}A_{i,xy} - A_{i,zz}A_{i,yx}) / |sd_{i,yz}| \\ (A_{i,zy}A_{i,yx} - A_{i,yy}A_{i,zx}) / |sd_{i,yz}| \end{pmatrix} \quad (4.31)$$

Subsequently the eigenvectors are scaled to length 1 by division with the magnitude. This procedure is done on a per-cell basis. Finally, after taking the exponential of the eigenvalues and thereby obtaining  $\mathbf{\Lambda}$ , the eigenvalue and eigenvector matrices  $\mathbf{\Lambda}$  and  $\mathbf{R}$ , respectively, are stored for the next time-step (or outer-iteration in case of using step 9), in which they are needed to decompose the velocity gradient (Eq. 4.12).

Initial conditions are a quiescent ( $\mathbf{U} = \mathbf{0}$ ) and relaxed fluid ( $\Psi = \mathbf{0}$ ). In the first time-step, we set  $\mathbf{\Lambda} = \mathbf{I}$  and  $\mathbf{R} = \mathbf{I}$ .

A biconjugate gradient stabilized (BiCGstab) solver is used to solve the logarithmized constitutive equation (Eq. 4.17) and the momentum balance (Eq. 4.24 or Eq. 4.25) in conjunction with a Cholesky preconditioner at a tolerance of  $10^{-7}$ . The pressure equation is solved with a conjugate gradient (CG) solver with an Algebraic Multigrid (AMG) preconditioner. The iteration of the first solution of the pressure equation is stopped, if either the residual falls below a tolerance of  $10^{-7}$  or if the ratio of current to initial residual falls below 0.05. The second pressure solution is stopped only if the residual is below a value of  $10^{-8}$ .

## 4.4 Results and Discussion

### 4.4.1 Startup Poiseuille flow

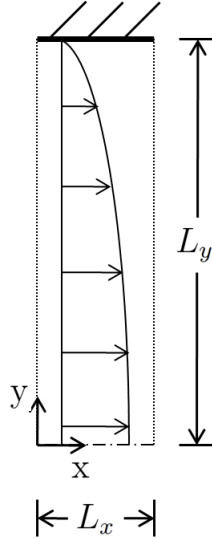


**Figure 4.1:** Sketch of the geometry for the startup of a viscoelastic Poiseuille flow.

First we will validate our numerical algorithm and show the order of convergence with respect to the time-step size and the grid size. Therefore, we consider the startup of a Poiseuille flow of a viscoelastic fluid, for which there is an analytical solution. [28] The sketch of this problem is shown in Fig. 4.1. We impose periodic boundary conditions on the left and right boundary and discretize the domain with only one cell in x-direction. The length  $L_x$  can then be chosen arbitrarily (we use  $L_x = 0.1$ ) according to D’Avino and Hulsen [29]. We set  $L_y = 0.5$  and use a normalized cell size of  $\Delta y = L_y/N_y = 0.005$  resulting in  $N_y = 200$  cells in y-direction. On the top wall we use a no-slip condition for velocity, a zero gradient condition for pressure and the second-order extrapolation boundary condition for  $\tau_P$  as described in Habla et al. [27]. At the bottom we make use of a symmetry boundary condition for all variables.

The flow is created by instantaneously imposing a pressure gradient  $\frac{dp}{dx}$  as an additional body source in the momentum balance at time  $T = t/\lambda = 0$ . The elasticity number, which is the only dimensionless number for this problem, is defined as  $E = \frac{\lambda\eta_0}{\rho L_y^2}$ . The retardation ratio is set to  $\beta = 0.01$ .  $\bar{U}_x$  denotes the average velocity over the cross section  $\bar{U}_x = -L_y^2 \frac{dp}{dx} / (3\eta_0)$  for  $T \rightarrow \infty$  and is used to make velocities dimensionless.  $U_0$  denotes the dimensionless centerline velocity and  $Q$  is the flow rate over the cross section.

The momentum balance (step 1, cf. section 4.3.5) is solved. In order to check the rate of convergence with respect to the time-step size, the convergence within a time-step must strictly be ensured. Thus, we assume that full convergence within a time-step is reached if the initial residuals of all three sets of linear equations (i.e. momentum balance, the first

pressure equation and the  $\Psi$  evolution equation) fell below a value of  $10^{-5}$ . If not, additional outer iterations are performed (step 9).

In Fig. 4.2 we present the predicted centerline velocity as a function of time for three distinct elasticity numbers in comparison with the analytical solution. One can clearly see that our numerical algorithm is capable of accurately predicting the analytical solution in the transient region and also the final steady-state value. To ensure stability the time-step size for the case with  $E = 100$  had to be decreased to  $\Delta t = 0.000625$ . We note that simulations at even higher elasticity numbers are possible, however, the dimensionless time-step size would have to be further decreased. In Fig. 4.3 we present the absolute value of the relative error of the flow rate  $|Q_{\text{num}} - Q_{\text{exact}}|$  as a function of the dimensionless time-step size  $\Delta t$  for the case of  $E = 1$ . One can clearly see that our numerical algorithm is second-order convergent with respect to the time-step size, which was to be expected due to the use of second-order Gear discretization of the time-derivatives. In Fig. 4.4 we report the same relative error as a function of the normalized cell size  $\Delta y$ . One can verify the second-order convergence with respect to the grid size of our numerical algorithm. However, we note that in this problem the convection terms are zero, which is why the choice of the discretization scheme does not have an effect on the convergence rate and even the upwind scheme would result in second-order behavior. For other problems, in which the convection terms are dominant, second-order accuracy will only be preserved when using the algorithm in conjunction with an adequate high-order convection scheme, such as the CUBISTA. In Fig. 4.5 we plot the centerline velocity and the error in the Euclidean norm over the whole vertical velocity profile [30]

$$e_{U_x}(T) = \sqrt{\frac{1}{N_y} \sum_i (U_{x,num}(Y_i, T) - U_{x,exact}(Y_i, T))^2}$$

against time in the vicinity of the first peak at  $E = 1$ . Simulations are done with and without BSD as well as with and without outer-iterations (step 9) to underline the statements of section 3.3. If considering the global velocity plot ( $0 \leq T \leq 15$ ) differences between the four simulations are barely visible. In the vicinity of the first peak one can confirm that both the velocity and the errors are identical for the simulations with and without use of BSD if full convergence within a time-step is achieved. The simulated centerline velocity exactly predicts the analytical solution with the choice of  $\Delta t = 0.000625$  and  $\Delta y = 0.005$ . However, if no outer-iterations are performed (if step 9 is omitted) the predicted centerline velocity with and without BSD deviates perceptibly from the analytical solution. Noticeably, the simulation with BSD gives a different response than the simulation without BSD. Furthermore, the error of the simulation with BSD is larger throughout the whole time-interval plotted in Fig. 4.5 than the error of the simulation without BSD, which confirms the lesser accuracy of BSD in time-dependent flows if no outer-iterations are performed.

4 Numerical simulation of the viscoelastic flow in a three-dimensional lid-driven cavity using the log-conformation reformulation in OpenFOAM®

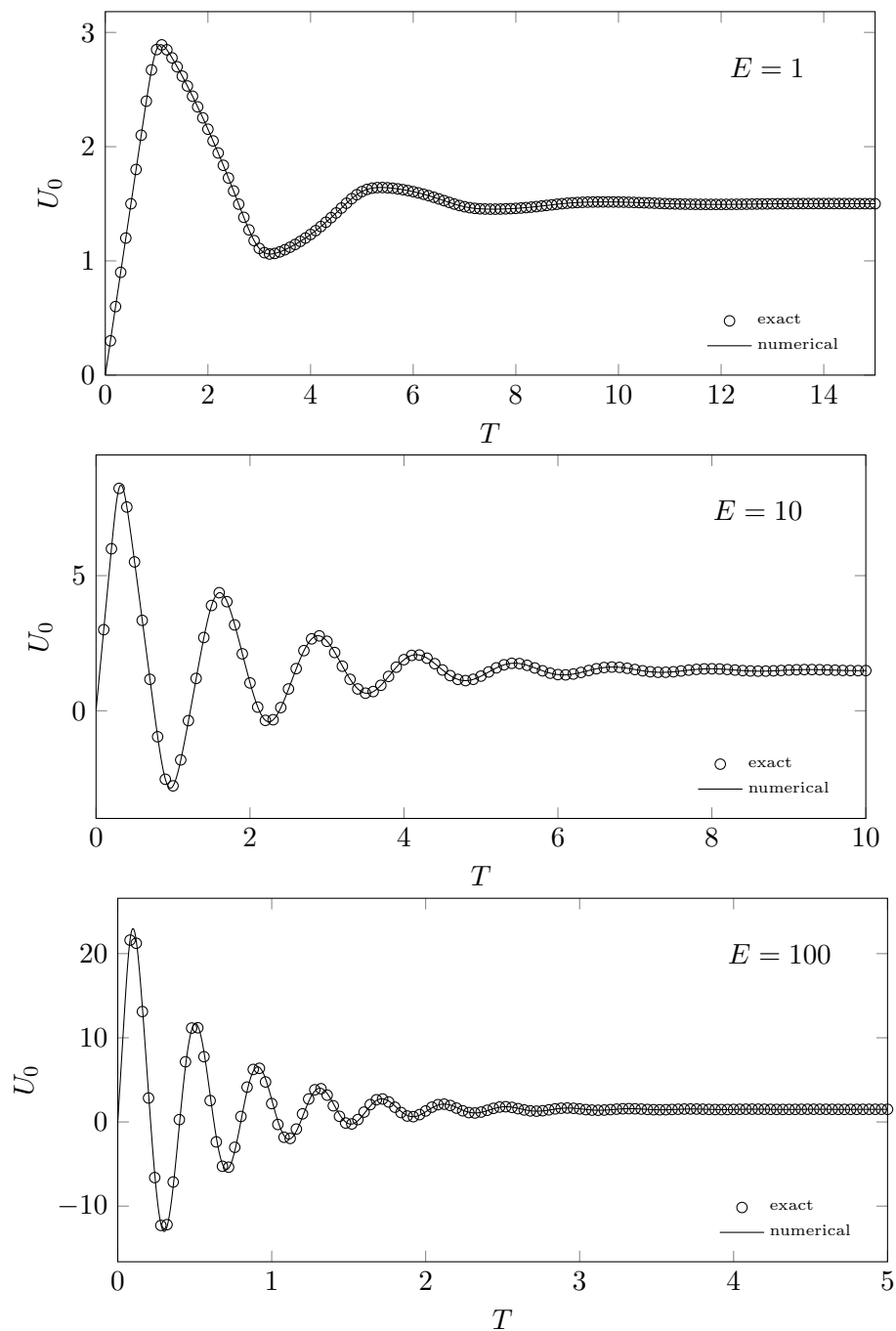


**Figure 4.2:** Centerline velocity as a function of time during the start-up of a Poiseuille flow of an Oldroyd-B fluid ( $\beta = 0.01$ ) for different elasticity numbers:  $E = 1$  ( $\Delta t/\lambda = 0.0025$ ),  $E = 10$  ( $\Delta t/\lambda = 0.0025$ ) and  $E = 100$  ( $\Delta t/\lambda = 0.000625$ ).

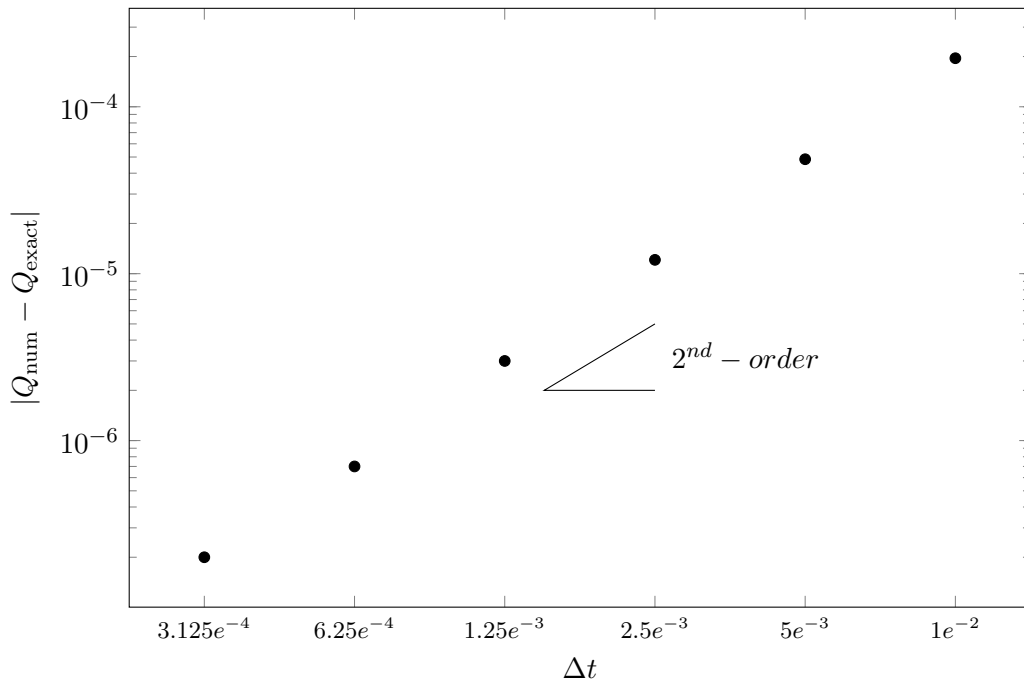


**Figure 4.3:**  $|Q_{\text{num}} - Q_{\text{exact}}|$  as a function of the time-step size  $\Delta t$  at  $T = t/\lambda = 0.1$  using a mesh with  $\Delta y = 0.005$  and an elasticity number of  $E = 1$ .

#### 4.4.2 Cavity flow

In this section we apply our numerical algorithm to simulate the flow inside a three-dimensional cavity, where the flow is created by the top wall moving in axial direction. Fig. 4.6 shows a sketch of the cubic geometry and the  $xy$ -plane at  $z = L/2$ , in which most results are presented in the following.

##### Case setup

The simulations are performed under creeping flow conditions, which are defined by a Reynolds number  $Re = \frac{LU_{x,max}\rho}{\eta_0} = 0$ . This is done by setting the time-derivative term and the convection term of the momentum balance to zero.  $L$  denotes the edge length of the cube and we define  $U_{x,max}$  as the velocity of the top wall in the center (i.e. for  $x = z = L/2$ ) since we will use a normalized velocity profile in the following. The retardation ratio is set to  $\beta = 0.5$ , while the relaxation time  $\lambda$  is varied such as to obtain the respective Weissenberg number  $We = \frac{\lambda U_{x,max}}{L} = 0.0$ .

No-slip boundary conditions are used for the velocity at all walls except the top wall, which is moving in  $x$ -direction with the following normalized velocity profile (cf. Fattal and Kupferman [7])

$$U_{x,lid}(x, z, t) = 128 \left[ 1 + \tanh 8 \left( t - \frac{1}{2} \right) \right] x^2 (1-x)^2 z^2 (1-z)^2 \quad (4.32)$$

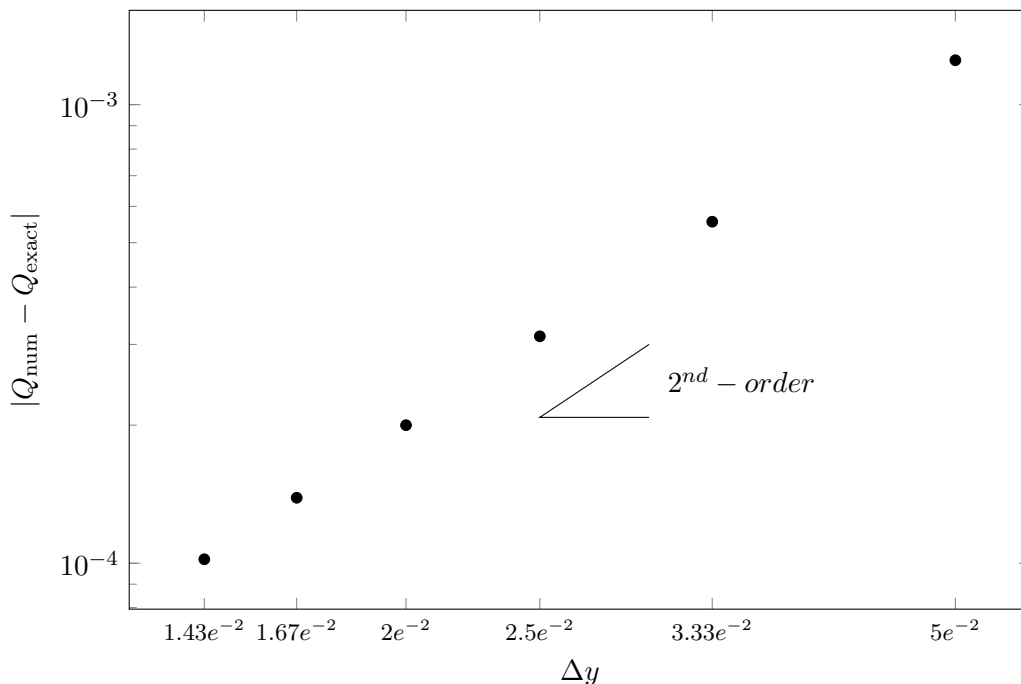


**Figure 4.4:**  $|Q_{\text{num}} - Q_{\text{exact}}|$  as a function of the cell size  $\Delta y$  at  $T = t/\lambda = 50$  with an elasticity number of  $E = 1$ .

The velocity is smoothly increased with time and reaches its maximum of  $U_{x,\text{max}} = 1$  at the center of the lid (i.e.  $x = z = 0.5$ ) for times  $t \gtrsim 1$ . Moreover, the velocity at the boundaries is zero, i.e.  $U_{x,\text{lid}} = 0$  for  $x, z = 0$  or  $x, z = 1$ . Presented results for velocities are made dimensionless by division with  $U_{x,\text{max}}$ , stresses by division with  $\frac{\eta_0 U_{x,\text{max}}}{L}$  and the dimensionless time is defined by  $T = \frac{t U_{x,\text{max}}}{L}$ .

For pressure and  $\tau_P$  we assign zero gradient boundary conditions at all boundaries. We refrain from using the second-order extrapolation boundary condition for  $\tau_P$  due to the presence of stability problems at high Weissenberg numbers associated with it. We examined the effect of using the zero gradient boundary condition on the simulation results by computing a 2D lid-driven cavity flow with the two different boundary conditions and comparing the simulation results with Fattal and Kupferman [7] at a Weissenberg number of  $We = 1.0$ . In Fig. 4.7 we plot the profiles for  $\Psi_{xx}$  and  $\Psi_{xy}$  at time  $T = 8$  computed with a mesh of 128x128 hexahedral cells without grading. We find that our simulation results are in very good agreement with the results of Fattal and Kupferman [7]. Furthermore, we hardly find any difference between our simulations performed with the zero gradient boundary condition and the second-order extrapolation method confirming that the zero gradient method is in fact a valid choice for this flow problem as it produces proper results, which moreover appear to be of similar accuracy as the results obtained with the second-order extrapolation method. Eventually, we believe that the better stability of the zero gradient method more than outweighs the (slightly) less accuracy associated with it for the lid-driven cavity problem.



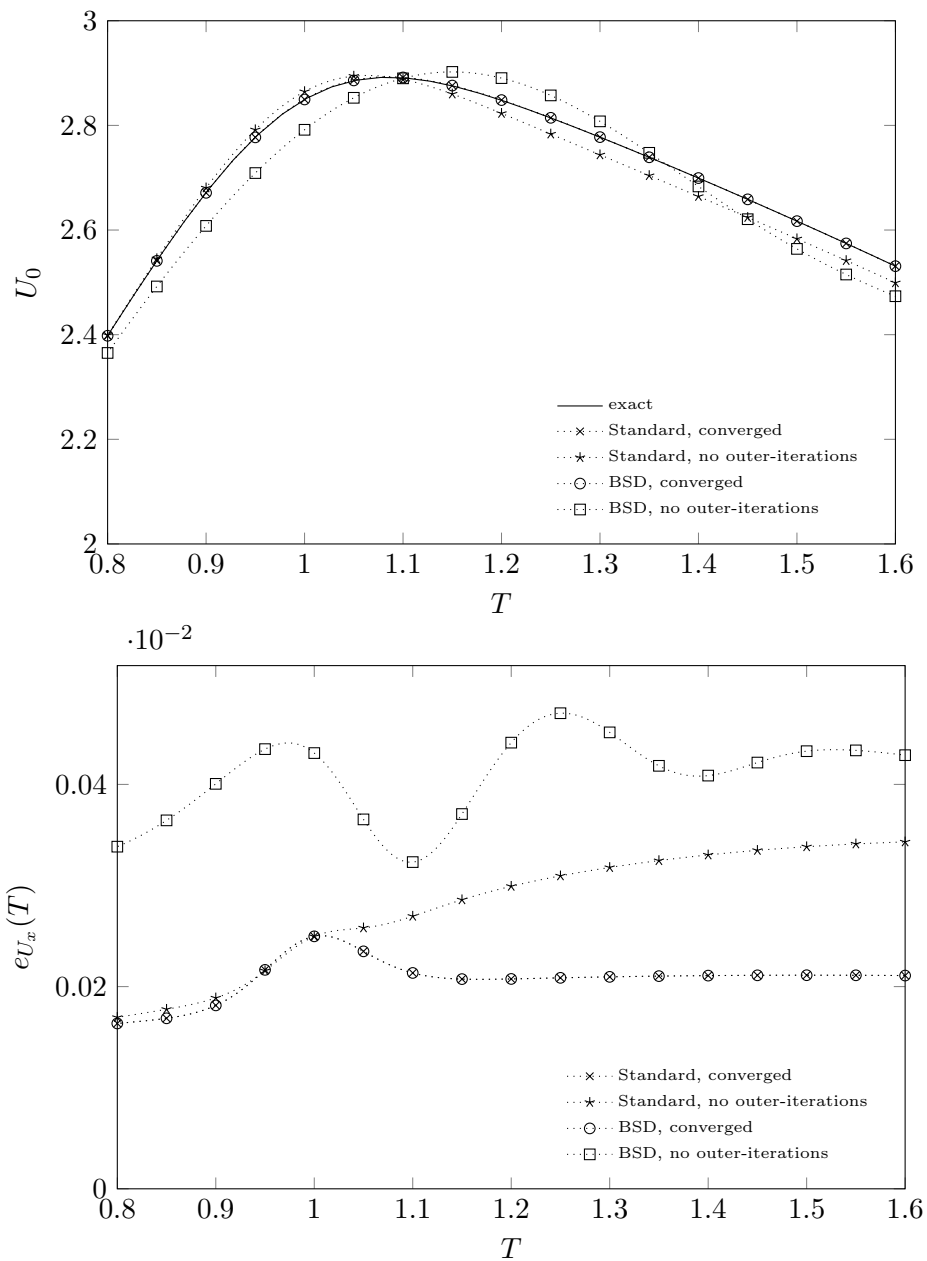


**Figure 4.5:** Centerline velocity and error as a function of time during the start-up of a Poiseuille flow of an Oldroyd-B fluid ( $\beta = 0.01$ ) for different implementations ( $\Delta t/\lambda = 0.000625$  and  $\Delta y = 0.005$ ).

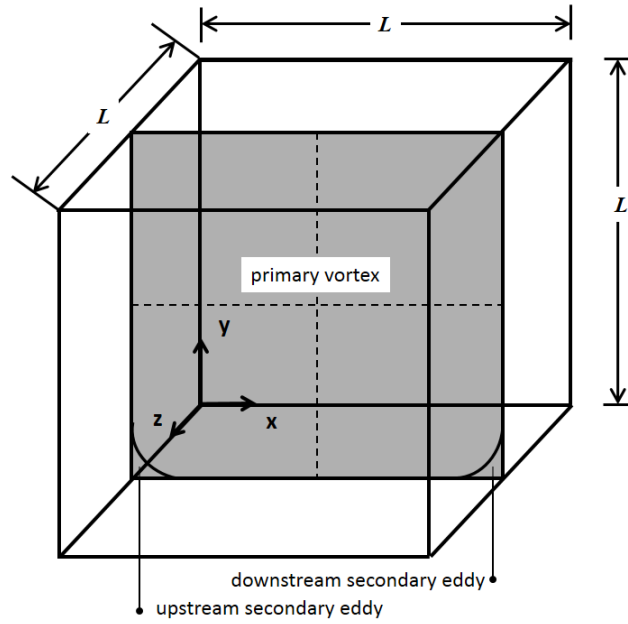


**Figure 4.6:** Sketch of the geometry with primary and secondary vortices.

The first step of solving the momentum balance (step 1, cf. section 4.3.5) is omitted in this case due to the creeping flow conditions. A fixed number of three outer-iterations (step 9, cf. Section 4.3.5) is used.

In order to check mesh convergence of the results four hexahedral meshes with different resolutions were created (M1 - M4). Another tetrahedral mesh (M5) with a cell count comparable to mesh M2 was created to show the ability of our numerical algorithm to handle unstructured meshes. All five meshes have non-uniform cell sizes with the size of the cells being smaller in wall-near regions, where the largest gradients are present. The properties of the five meshes are listed in Table 4.1, while Fig. 4.8 provides a view of the five meshes.

**Table 4.1:** Properties of the meshes.

Meshes	Number of cells per edge	Total cell count	$\Delta x_{min}/L$
M1	20	8,000	0.0198
M2	40	64,000	0.0103
M3	60	216,000	0.0069
M4	80	512,000	0.0056
M5	-	72,159	-

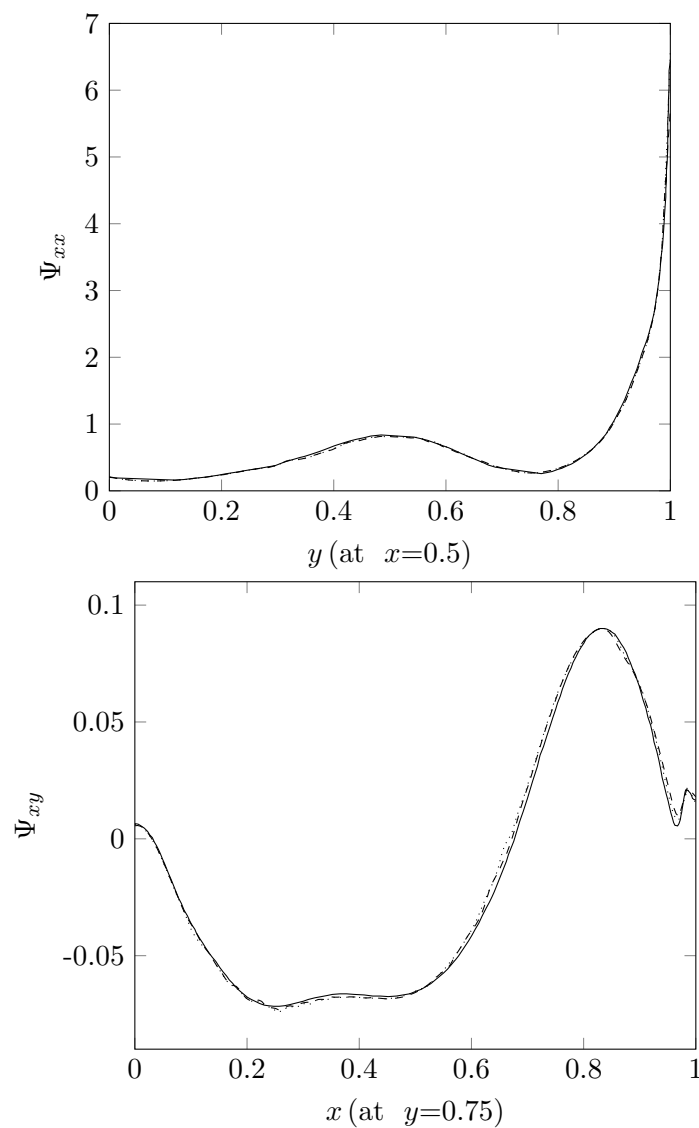
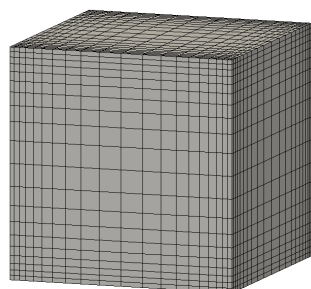
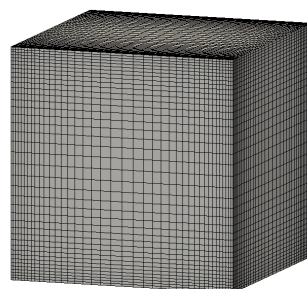


**Figure 4.7:** Vertical  $\Psi_{xx}$  profile and horizontal  $\Psi_{xy}$  profile for a 2D cavity simulation at  $We = 1$  and  $T = 8$  simulated on a mesh with  $128 \times 128$  hexahedral cells with two different boundary conditions for  $\tau_P$ . (.....): Zero gradient boundary condition, (---): Second-order extrapolation boundary condition [27], (—): Results of Fattal and Kupferman [7].

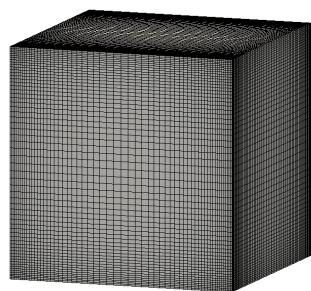
4 Numerical simulation of the viscoelastic flow in a three-dimensional lid-driven cavity using the log-conformation reformulation in OpenFOAM®



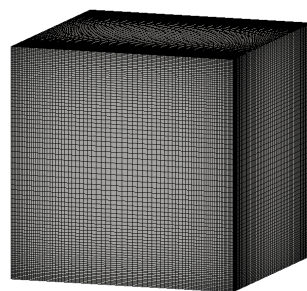
M1



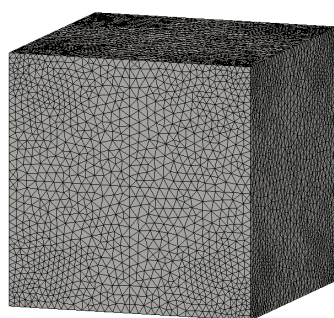
M2



M3



M4



M5

**Figure 4.8:** View of the meshes.

Fig. 4.9 shows the maximum value of  $\tau_{P,xx}$  in the domain as a function of different time-steps. The temporal evolution of  $\max(\tau_{P,xx})$  is very sensitive to the time-step and thus allows to check for temporal convergence of the results. All time-steps qualitatively predict the same trend. However, already in the beginning ( $T \leq 40.2$ ) the result with the largest time-step ( $\Delta T = 0.01$ ) slightly deviates from the results with finer time-steps, while the simulation time when using the very small time-steps is already quite large. This is why we decided to use  $\Delta T = 0.005$  for all simulations in the remaining work.

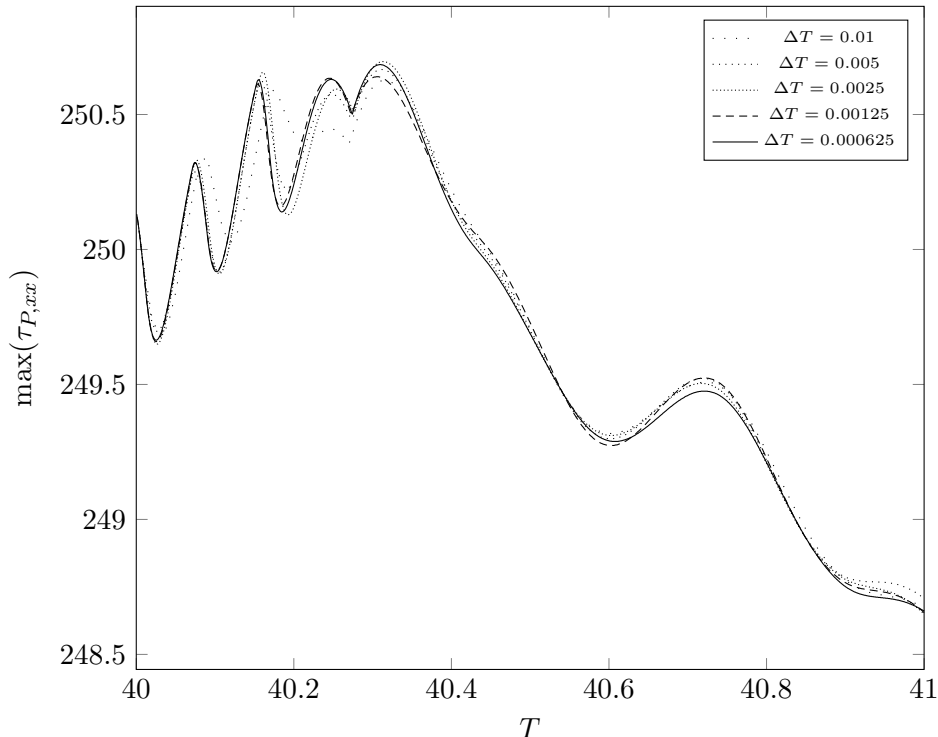


**Figure 4.9:**  $\max(\tau_{P,xx})$  over time  $T$  as a function of different time-steps for  $We = 1.0$  using mesh M3 with the CUBISTA scheme.

The time duration of each simulation was initially set to  $T = 40$ , which was sufficient to obtain converged results for small Weissenberg numbers and particularly when using the upwind differencing scheme. However, for the simulations at higher Weissenberg numbers ( $We \gtrsim 1.0$ ) in conjunction with the CUBISTA scheme  $T = 40$  was insufficient to result in convergence and we thus extended the time duration on a case by case basis. This is illustrated in Figs. 4.10 and 4.11. Fig. 4.10 shows the decay of the initial residuals of the linear equations for  $\Psi_{xx}$  and  $p$  for upwind, CUBISTA and the QUICK scheme at  $We = 1.0$ . When using upwind differencing, the residuals decay below  $10^{-5}$  within  $T < 10$  and are converging for all three meshes M1-M3 within the time duration. On the other hand, simulations with the CUBISTA and the QUICK scheme are not converging with the residuals oscillating around a constant value for  $T > 10$  for all three meshes. The CUBISTA scheme shows slightly better iterative convergence than the QUICK scheme, although both schemes behave quite similar. We assume that this is because the CUBISTA obeys the Convection Boundedness Criterion (CBC), but the QUICK does not. We conclude that the piecewise variation of the

CUBISTA scheme is not the reason for the residuals not decaying below some critical value, but remaining constant from about  $T = 10$ . Fig. 4.11 shows that the maximum normal stress value in x-direction in the domain remains constant for the upwind scheme from  $T > 10$ , while for the CUBISTA scheme this variable oscillates around a mean value. Finally, we believe that the non-convergence and non-steadiness of  $\max(\tau_{P,xx})$  with the CUBISTA scheme is due to this scheme predicting an oscillatory vortex flow and thus the overall flow remains in a transient state. We find that a time duration of  $T = 40$  is not sufficient for  $We = 1.4$ . The time had to be increased to  $T = 80$  in order to have  $\max(\tau_{P,xx})$  oscillating around a constant value, which is the case from  $T > 60$  onwards, see Fig. 4.11. Besides, we note that the absolute value of  $\max(\tau_{P,xx})$  deviates perceptibly between upwind and CUBISTA at  $We = 1.0$  owing to the low accuracy of the upwind scheme.

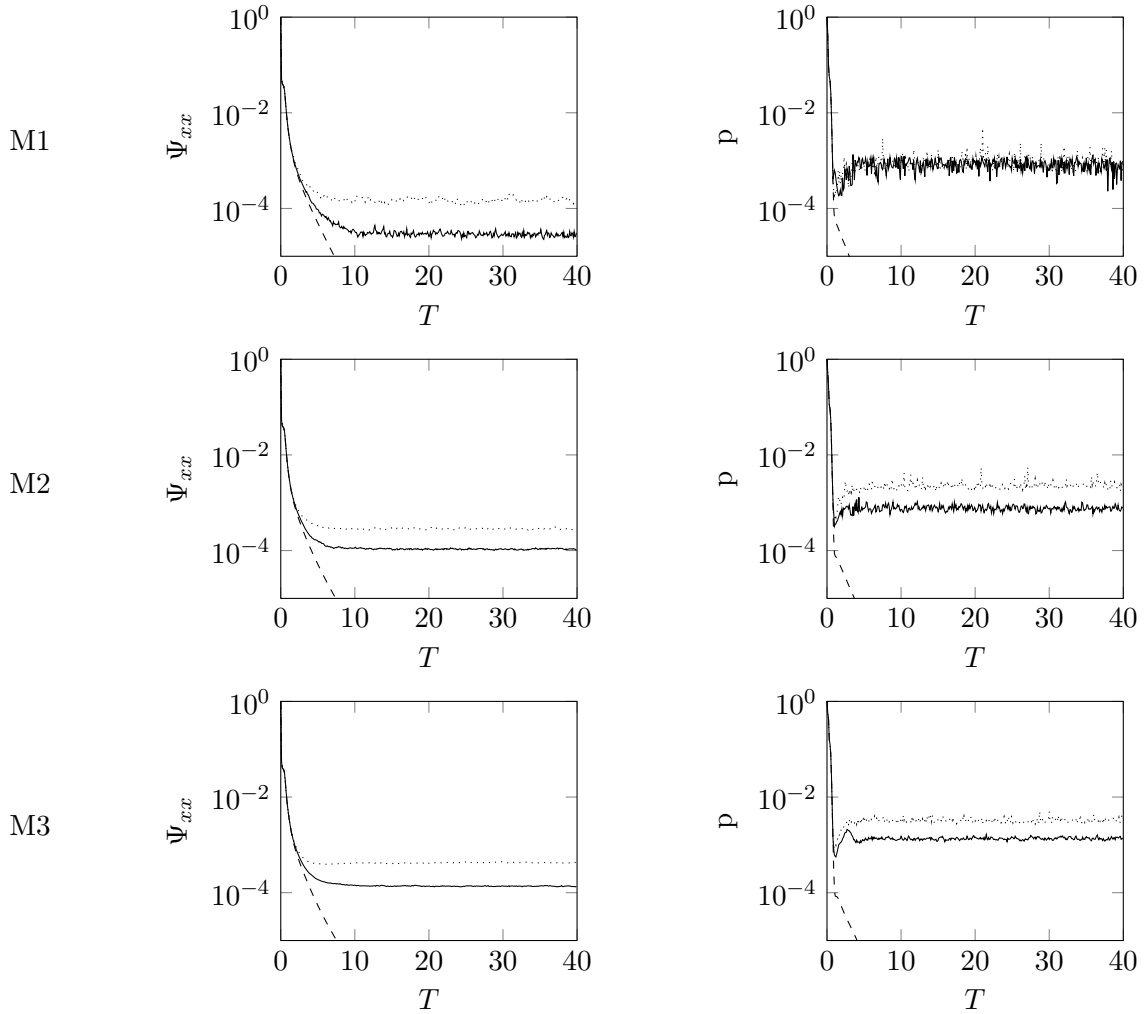


**Figure 4.10:** Decay of the initial residuals of the linear equations for  $\Psi_{xx}$  and  $p$  using the upwind and the CUBISTA scheme at  $We = 1.0$  with mesh M3. (—): CUBISTA, (.....): QUICK, (---): Upwind.

### Primary vortex center

Table 4.2 presents the  $x$ - and  $y$ -coordinates of the primary vortex center in the  $xy$ -plane at  $z = 0.5$  and gives an overview of all cases simulated in this work. The vortex center

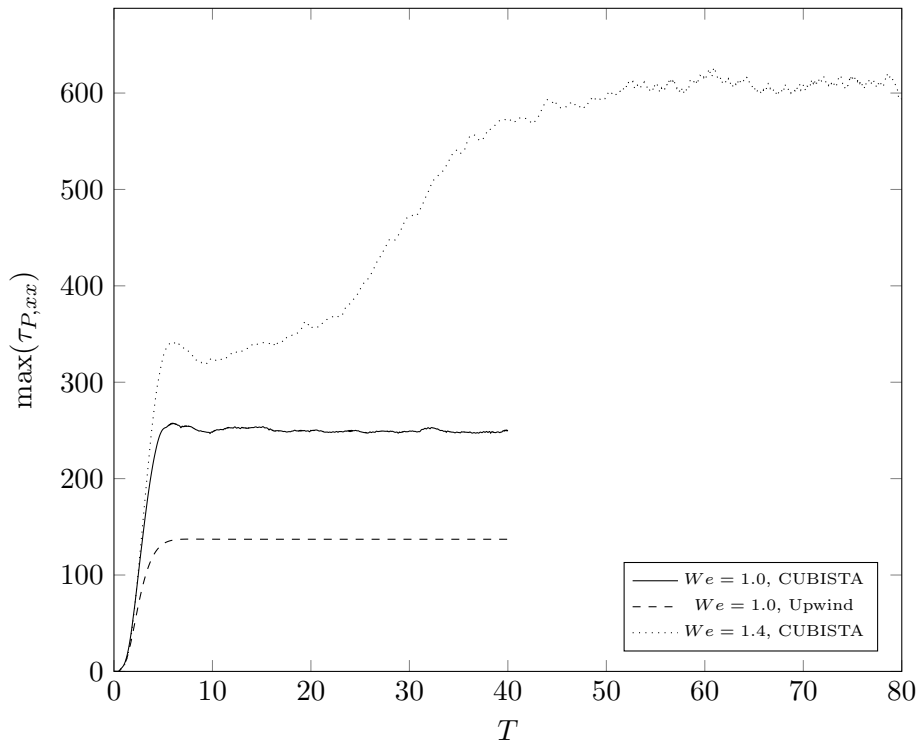


**Figure 4.11:**  $\max(\tau_{P,xx})$  over time  $T$  for mesh M3 and  $\Delta T = 0.005$  as a function of different Weissenberg numbers and convection schemes.

of a simulation was determined with an accuracy of three-decimal places. Simulations with meshes M1-M3 were carried out with the two convection schemes until  $We = 2.0$ . Simulations at larger Weissenberg numbers were not considered due to the loss of spatial convergence. For mesh M3 and CUBISTA, however, the Weissenberg number was further increased beyond  $We = 2.0$  in order to check for numerical stability. This is discussed in Section 4.4.2. Additionally, simulations for the Weissenberg numbers of  $We = 0.0$ , 1.0 and 2.0 were performed with mesh M4 and the CUBISTA scheme to check the spatial convergence of the results in more detail. Another simulation was performed for mesh M5 at  $We = 1.0$  to show that the use of a tetrahedral mesh in conjunction with the CUBISTA scheme can give similar results to a comparable hexahedral mesh (mesh M2). Values in brackets indicate cases, which did not converge in the sense that the residuals of at least one out of all linear equations did not decrease below  $10^{-5}$ . Converged simulation were obtained only with the upwind differencing scheme for the whole range of Weissenberg numbers and all meshes. For the CUBISTA scheme, converged results could not be obtained for any Weissenberg number and mesh under consideration. We note that in the Newtonian limit  $We = 0.0$  there is no convection contribution in the constitutive equation and thus upwind and CUBISTA are identical. Values with the superscript <sup>1</sup> denote that the primary vortex center oscillated with respect to the x- and y- coordinates at the third decimal place. Boxes with the *n.a.* abbreviation denote that simulations were not performed.

A comparison of the log-conformation reformulation ('log') with the standard ('std') methodology (i.e. solving Eq. 4.5 directly) is shown in Table 4.3. We were able to perform stable

**Table 4.2:** Location of the primary vortex for different Weissenberg numbers, meshes and convection schemes.

We	M1						M2						M3						M4						M5							
	CUBISTA			UPWIND			CUBISTA			UPWIND			CUBISTA			UPWIND			CUBISTA			UPWIND			CUBISTA			CUBISTA				
	x	y		x	y		x	y		x	y		x	y		x	y		x	y		x	y		x	y		x	y			
0.0	0.500	0.759		0.500	0.759		0.500	0.762		0.500	0.762		0.500	0.762		0.500	0.763		0.500	0.763		0.500	0.763		0.500	0.763		0.500	0.763		0.500	0.763
0.2	(0.494)	(0.762)		0.494	0.762		(0.494)	(0.766)		0.494	0.762		(0.495)	(0.767)		0.494	0.767		0.494	0.767		0.494	0.768		0.494	0.768		0.494	0.768		0.494	0.768
0.4	(0.483)	(0.768)		0.486	0.768		(0.482)	(0.773)		0.484	0.774		(0.482)	(0.773)		0.483	0.774		0.483	0.774		0.483	0.774		0.483	0.774		0.483	0.774		0.483	0.774
0.6	(0.472)	(0.773)		0.479	0.772		(0.467)	(0.779)		0.474	0.779		(0.468)	(0.780)		0.471	0.779		0.471	0.779		0.471	0.779		0.471	0.779		0.471	0.779		0.471	0.779
0.8	(0.463)	(0.777)		0.473	0.777		(0.455)	(0.784)		0.465	0.784		(0.453)	(0.785)		0.462	0.785		0.462	0.785		0.462	0.785		0.462	0.785		0.462	0.785		0.462	0.785
1.0	(0.453)	(0.783)		0.467	0.781		(0.442)	(0.788)		0.458	0.788		(0.441)	(0.790)		0.454	0.789		0.454	0.789		0.454	0.789		0.454	0.789		0.454	0.789		0.454	0.789
1.2	(0.443)	(0.788)		0.463	0.784		(0.430)	(0.793)		0.451	0.791		(0.429)	(0.794)		0.446	0.793		0.446	0.793		0.446	0.793		0.446	0.793		0.446	0.793		0.446	0.793
1.4	(0.436)	(0.793)		0.460	0.786		(0.422)	(0.797)		0.446	0.795		(0.419)	(0.798)		0.440	0.796		0.440	0.796		0.440	0.796		0.440	0.796		0.440	0.796		0.440	0.796
1.6	(0.429)	(0.799)		0.457	0.789		(0.412)	(0.800)		0.441	0.798		(0.407)	(0.800)		0.434	0.799		0.434	0.799		0.434	0.799		0.434	0.799		0.434	0.799		0.434	0.799
1.8	(0.420)	(0.802)		0.455	0.792		(0.402) <sup>1</sup>	(0.803) <sup>1</sup>		0.437	0.801		(0.398)	(0.802)		0.429	0.801		0.429	0.801		0.429	0.801		0.429	0.801		0.429	0.801		0.429	0.801
2.0	(0.417)	(0.806)		0.454	0.793		(0.396) <sup>1</sup>	(0.804) <sup>1</sup>		0.433	0.802		(0.389) <sup>1</sup>	(0.804) <sup>1</sup>		0.425	0.803		0.425	0.803		0.425	0.803		0.425	0.803		0.425	0.803		0.425	0.803



simulations until  $We = 0.6$  with the standard method. From  $We = 0.8$  the solution diverged with the standard method, while with the log-conformation method we were able to perform simulations far beyond this Weissenberg number as explained in the remainder. This underlines the large improvement in stability. We find that the results for the primary vortex center are similar with only minor differences, from which we can conclude that both methods produce results of similar accuracy. However, we are aware of the fact that this result holds only for very small Weissenberg numbers and this finding might not be the same for other flow problems, in which one is able to obtain results at higher Weissenberg numbers with the standard method. In terms of CPU time, we find that the log-conformation method is slower by only 6.3% for the case with the largest Weissenberg number at which a comparison was possible ( $We = 0.6$ , mesh M3). The computation time is 57.4 h for the standard method and 61.0 h for the log-conformation method on one core of an Intel Xeon 2.4 Ghz. The small increase in computational time when using the log-conformation is both due to the efficient implementation of the eigenvalue/eigenvector routine, but also because the solution of the pressure equation (steps 3 and 6, cf. section 4.3.5) is taking very long and is the bottleneck in the algorithm. Parallelization was pursued in this work for up to 8 cores and the scaling is almost linear.

**Table 4.3:** Comparison of the predicted location of the primary vortex center with the log-conformation reformulation ('log') and the standard formulation ('std') with mesh M3 and CUBISTA.

We	std		log	
	x	y	x	y
0.2	0.495	0.767	0.495	0.767
0.4	0.481	0.774	0.482	0.773
0.6	0.466	0.780	0.468	0.780
0.8		<sup>1</sup>	0.453	0.785

<sup>1</sup>diverged

In Table 4.4 we additionally compare the predicted primary vortex center at  $We = 1.0$  with simulation results obtained with the QUICK scheme and find that QUICK and CUBISTA give very similar results for the position of the vortex center and behave similar in terms of mesh convergence, however, with the QUICK scheme appearing to be slightly more accurate than the CUBISTA scheme.

Fig. 4.12 shows the  $x$ -shift of the location of the primary vortex center in negative  $x$ -direction with increasing Weissenberg number as a function of the mesh and convection scheme. The six plots show convergence in the  $x$ -shift at low Weissenberg number until  $We \approx 0.4$ , from which the plots starts to split showing distinction in the different schemes and meshes used. Comparing both convection schemes, the CUBISTA scheme shows better

**Table 4.4:** Comparison of the predicted location of the primary vortex center with the upwind, CUBISTA and QUICK scheme with mesh M3 and CUBISTA at  $We = 1.0$ .

	M1		M2		M3	
	x	y	x	y	x	y
Upwind	0.467	0.781	0.458	0.788	0.454	0.789
QUICK	0.447	0.782	0.441	0.789	0.441	0.790
CUBISTA	0.453	0.783	0.442	0.788	0.441	0.790

mesh convergence within the range of Weissenberg number simulated. As the Weissenberg number increases to  $We = 2.0$ , the graphs begin to flatten. Meshes M2 and M3 in conjunction with CUBISTA are close showing good spatial convergence of these results.

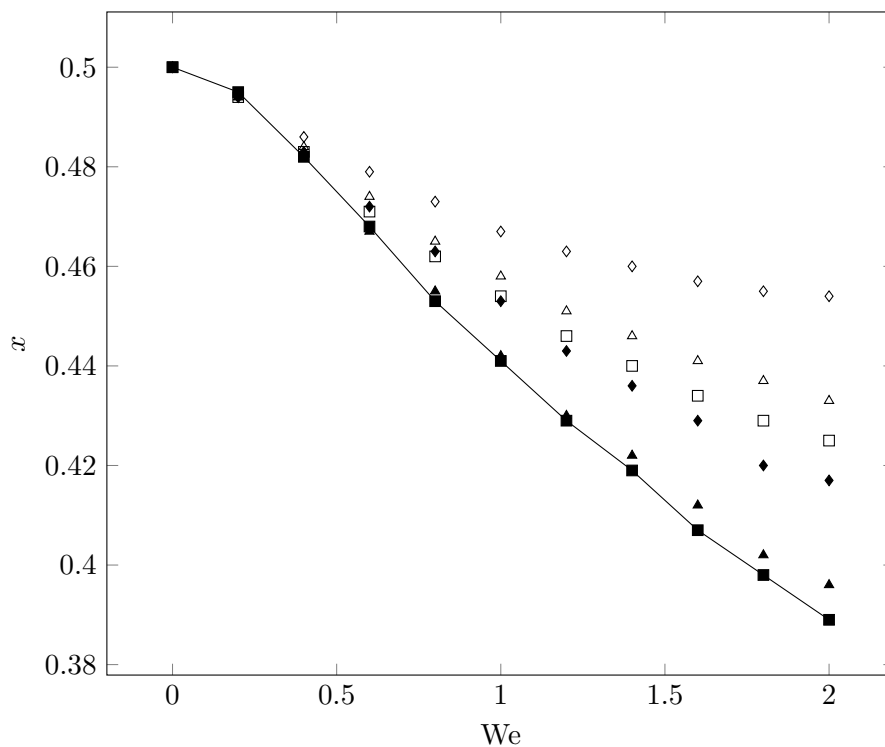
Fig. 4.13 depicts the  $y$ -shift of the location of the primary vortex center in positive  $y$ -direction with increasing Weissenberg number. Independent of the convection schemes used the results of meshes M2 and M3 show good convergence with one another. However, with the coarser mesh M1 the spatial convergence is quite poor for all Weissenberg numbers. A flattening of the plots is again observed with increasing Weissenberg numbers, similar as in Fig. 4.12.

Fig. 4.14 shows the shift of the location of the primary vortex center in the  $xy$ -plane with increasing Weissenberg number predicted with the most accurate simulations (M3 and CUBISTA). The primary vortex center shifts upstream towards the upper left corner as the Weissenberg number gets larger. An explanation for this behavior follows in the remainder.

### Streamlines

In this section the streamlines in the  $xy$ -,  $xz$ - and  $yz$ -planes intersecting the primary vortex center are analyzed. The plots in Fig. 4.15 show the streamlines for different Weissenberg numbers using mesh M3 and CUBISTA. First we present the streamlines for the Newtonian limit, e.g.  $We = 0.0$ , as a reference. The streamlines are symmetrical in the  $xz$ - and  $yz$ -plane about the  $xy$ -plane. Furthermore, the streamlines in the  $xy$ -plane are also symmetrical about the  $yz$ -plane, however, with the flow being in opposite direction for  $x > 0.5$  and  $x < 0.5$ , contrary to the  $yz$ - and  $xz$ -plane where the flow is aligned in the same direction. The streamlines in the  $xy$ -plane form closed circles. The streamlines in the  $yz$ -plane are the limiting case such that for  $x < 0.5$  the direction is upwards, while for  $x > 0.5$  the flow direction is downwards.

With increasing Weissenberg number, the flow patterns of the streamlines in  $xy$ -,  $xz$ - and  $yz$ -planes change remarkably, indicating that elastic effects are becoming dominant. Closed circles are no longer observed in the  $xy$ -plane. Instead, a distinct asymmetrical behavior formed. The shift of the primary vortex center in the negative  $x$ -direction and positive



**Figure 4.12:** Convergence of the  $x$ -coordinate of the primary vortex with different meshes, convection schemes and Weissenberg numbers.  
 (◆): M1 CUBISTA, (◇): M1 UPWIND, (▲): M2 CUBISTA, (△): M2 UPWIND,  
 (—■): M3 CUBISTA, (□): M3 UPWIND.

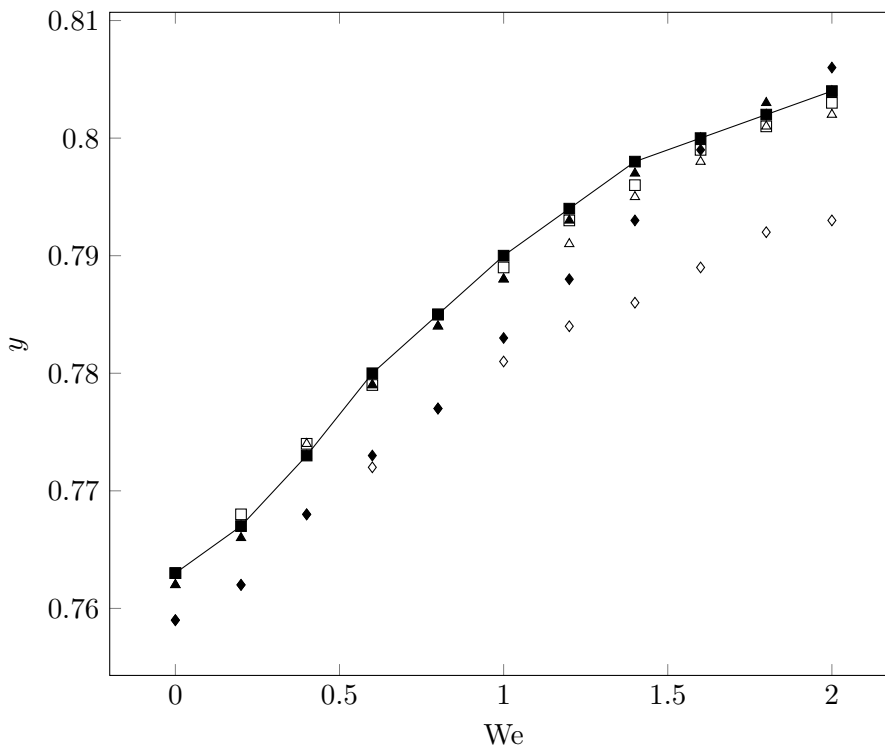


**Figure 4.13:** Convergence of the  $y$ -coordinate of the primary vortex with different meshes, convection schemes and Weissenberg numbers.  
 (◆): M1 CUBISTA, (◇): M1 UPWIND, (▲): M2 CUBISTA, (△): M2 UPWIND,  
 (—■): M3 CUBISTA, (□): M3 UPWIND.

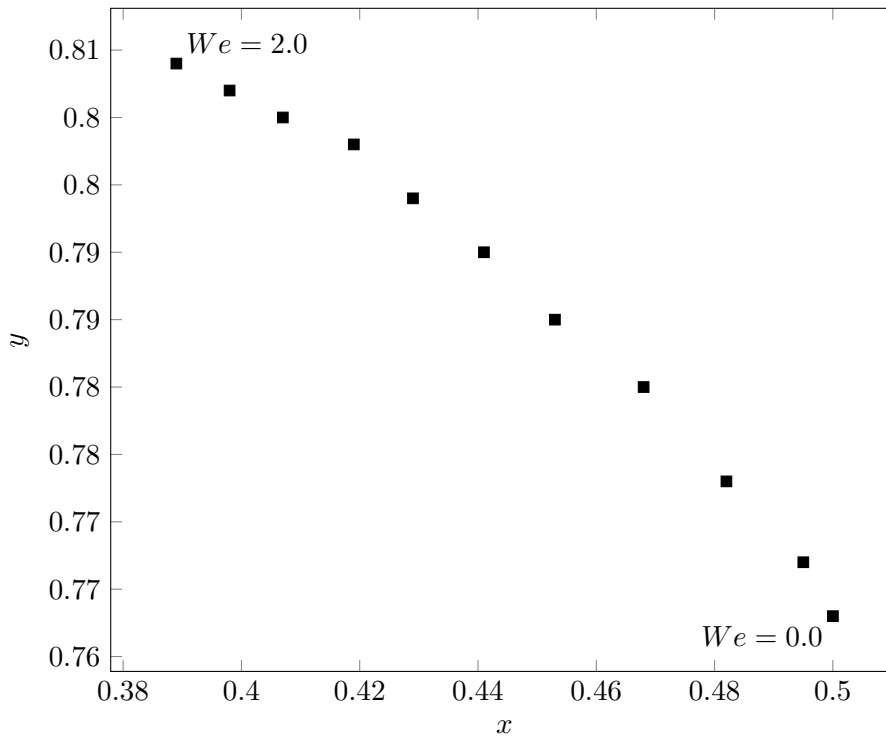


**Figure 4.14:** Shift of the location of the primary vortex predicted with mesh M3 and CUBISTA scheme ( $We = 0.0 \rightarrow 2.0$  in steps of 0.2).  
(—■): M3 CUBISTA

$y$ -direction can also be noticed from Fig. 4.15. The shift of the location of the primary vortex can be explained by the first normal stress difference ( $N_1 = \tau_{P,xx} - \tau_{P,yy}$ ) trying to contract the fluid in flow direction close to the lid, which causes the recirculation center of the fluid to move away from the downstream wall and pushes it further upstream. [31, 13]

Symmetrical behavior in the  $xz$ - and  $yz$ -planes still exists for  $We = 1.0$ , however, the symmetrical behavior in the  $xz$ - and  $yz$ -planes is lost at  $We = 2.0$ , indicating the onset of oscillations of those streamlines. At  $We = 1.0$ , two stagnation points are observed in the  $xz$ -plane along the centerline at  $z = 0.5$ . One is formed for  $x < 0.5$  and the other for  $x > 0.5$ . A similar observation is made at  $We = 2.0$ . In the  $yz$ -plane, no stagnation point is observed at  $We = 1.0$ , but one is observed for  $We = 2.0$ .

Enlarged views of the streamlines in the secondary eddies are presented in Figs. 4.16 and 4.17. In the case of the Newtonian limit, fluid is entering the downstream secondary eddy from  $z$ -direction and the eddy serves as an inflow to the primary vortex, while the upstream secondary eddy serves as the corresponding outflow in  $z$ -direction and thus fluid is leaving the primary vortex via the upstream secondary eddy. Contrary, at  $We = 1.0$  and  $2.0$  both the downstream and upstream secondary eddy serve as inflows and fluid enters the primary vortex from both. Fig. 4.17 shows the transition of the upstream secondary eddy from outflow to inflow, which occurs between  $We = 0.6$  and  $0.8$ .

4 Numerical simulation of the viscoelastic flow in a three-dimensional lid-driven cavity using the log-conformation reformulation in OpenFOAM®

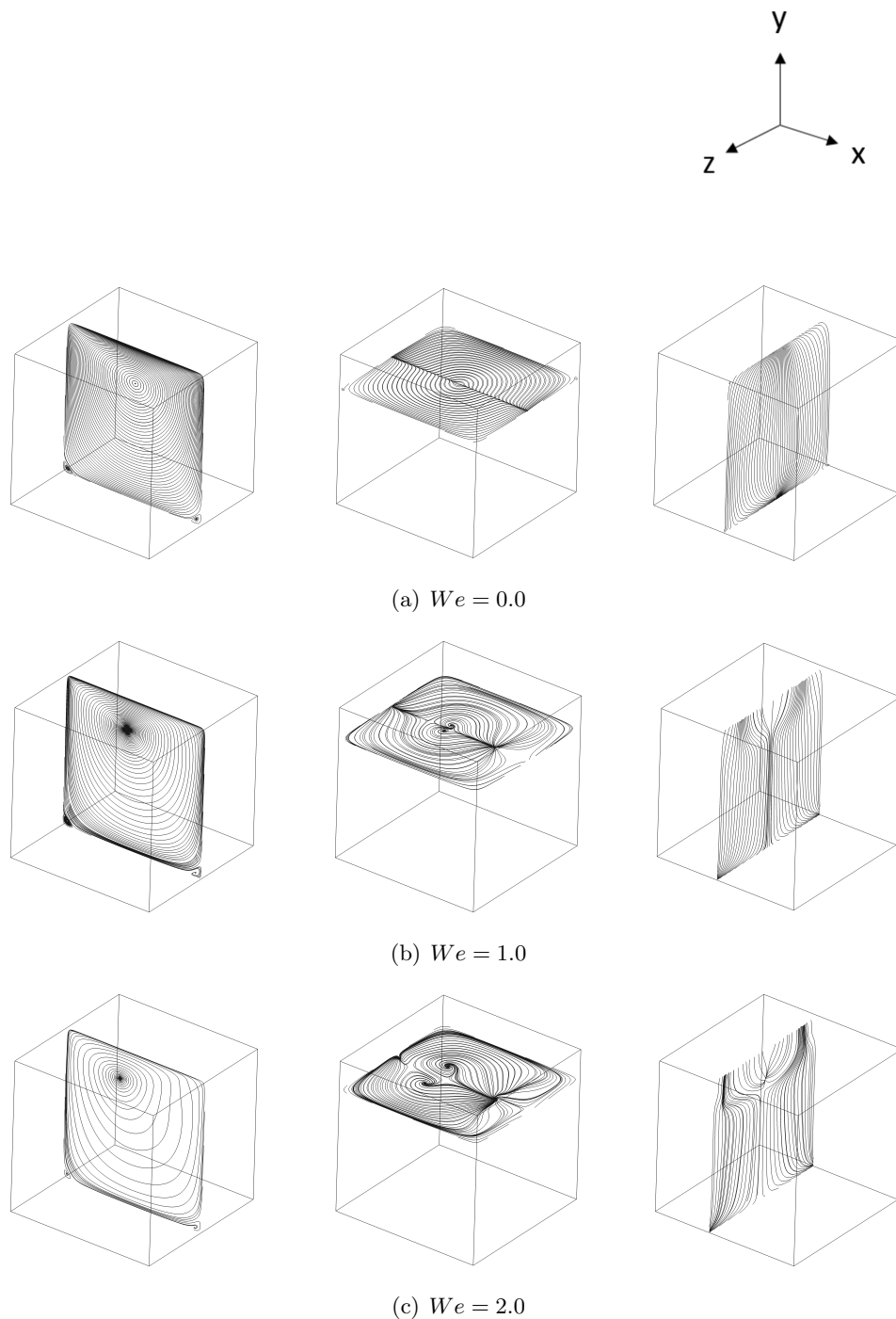


**Figure 4.15:** Streamlines in the  $xy$ -,  $xz$ - and  $yz$ -planes for different Weissenberg numbers using mesh M3 and CUBISTA.

4 Numerical simulation of the viscoelastic flow in a three-dimensional lid-driven cavity using the log-conformation reformulation in OpenFOAM®

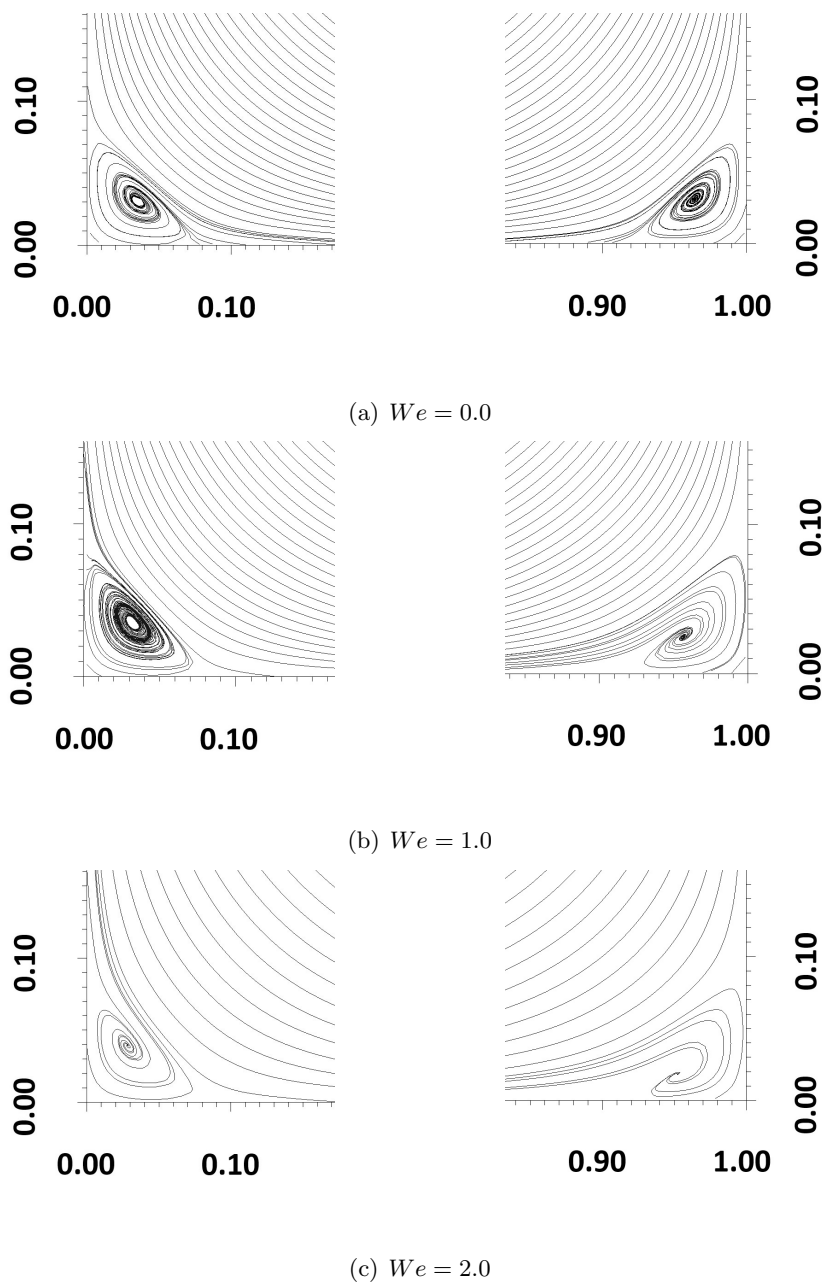
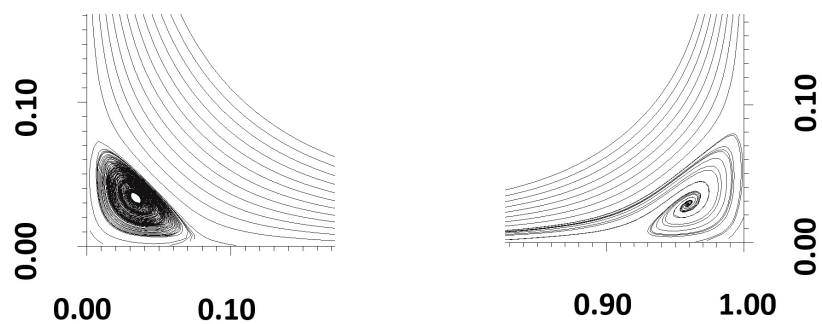
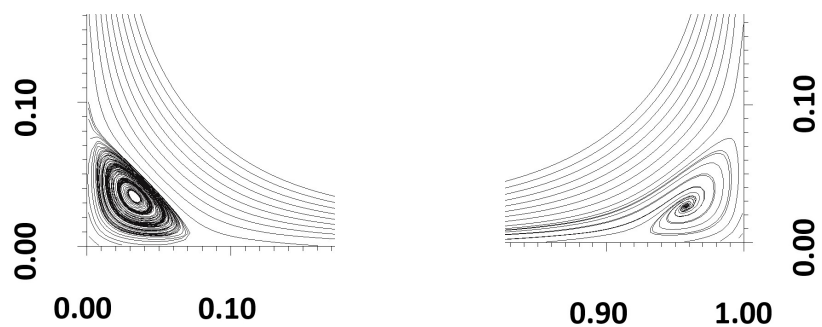


**Figure 4.16:** Comparison of streamlines in the secondary eddies in the  $xy$ -plane for different Weissenberg numbers using mesh M3 and CUBISTA.



(a)  $We = 0.6$



(b)  $We = 0.8$

**Figure 4.17:** Change of upstream secondary eddy in the  $xy$ -plane from outflow to inflow using mesh M3 and upwind differencing.

## Fields

The profiles of the log-conformation tensor  $\Psi$  in the  $xy$ -plane are shown in Fig 4.18, while the corresponding stress  $\tau_P$  fields are shown in Fig 4.19. A very thin boundary layer is observed at the top of the moving lid for  $\Psi_{xx}$ . Also, a distinct maxima is observed at the upper right corner for both  $\Psi_{xy}$  and  $\Psi_{yy}$  with the maxima at  $\Psi_{xy}$  further away from the corner in negative  $x$ -direction. These results are in agreement with those found in Hao and Pan [8] and Grillet et al. [13]. The fields of the log-conformation tensor  $\Psi$  are generally smooth considering that the values observed at the respective Weissenberg number for the three components develop gradually from maxima to minima. However, when considering the  $\tau_P$  fields as shown in Fig 4.19, sharp and distinct fields are observed with very large gradients for the all three components. Similar to the  $\Psi$  field, the normal stress in  $x$ -direction forms a thin boundary layer at the lid and there is a pronounced maximum at the right upper corner for the shear stress  $\Psi_{xy}$  and normal stress  $\Psi_{yy}$ . Generally, one observes resemblance of the  $\Psi$  and  $\tau_P$  fields, with  $\tau_P$  fields having sharper gradients. The reason for the sharp gradients in  $\tau_P$  and smoothness in  $\Psi$  is that  $\tau_P$  is linked exponentially to  $\Psi$  as described by Eq. 4.11. In both profiles, sharp boundary layers at the top next to the lid and singularities at the corner of the lid cavity are a result of elasticity. With increasing Weissenberg number, one observes from the scale that the maximum value increases, with more distinct (or higher) stress regions within the lid-cavity for the higher Weissenberg number.



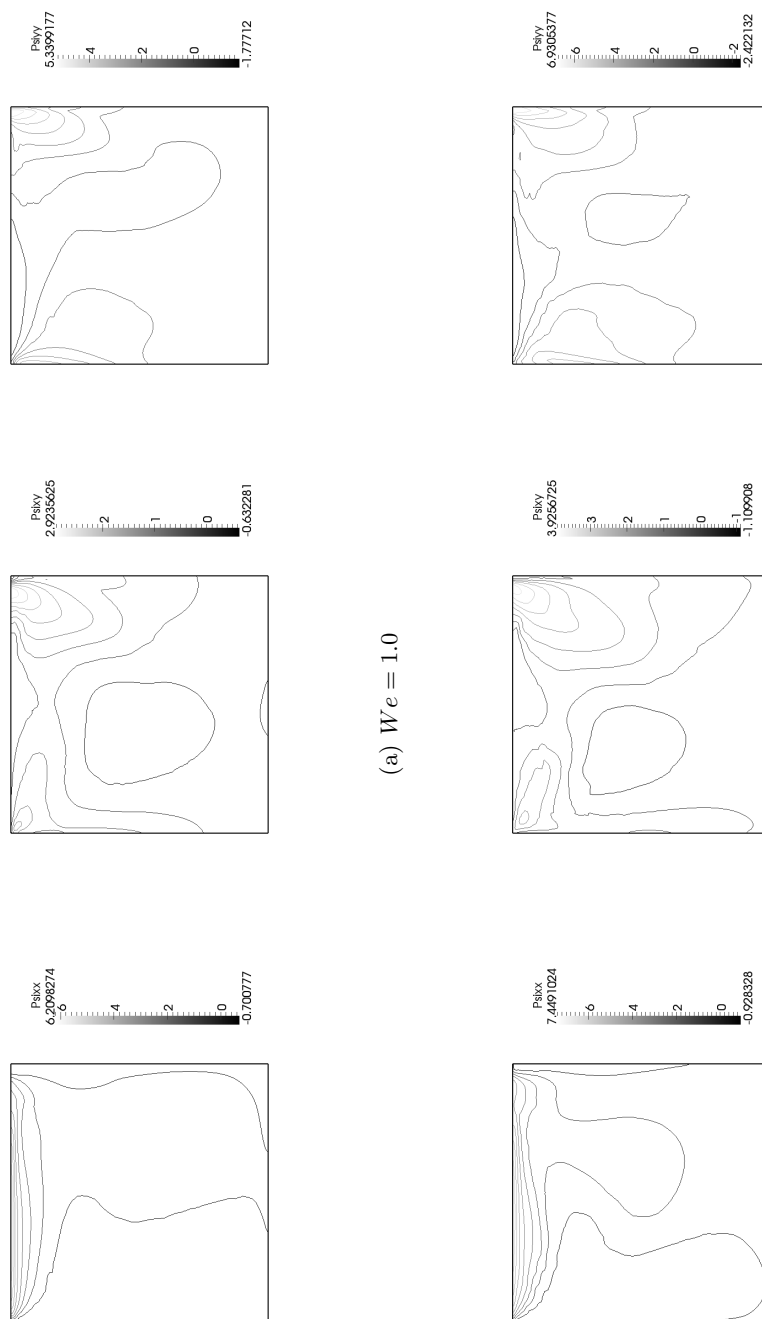


**Figure 4.18:**  $\Psi$  field in the xy-plane using mesh M3 and CUBISTA.

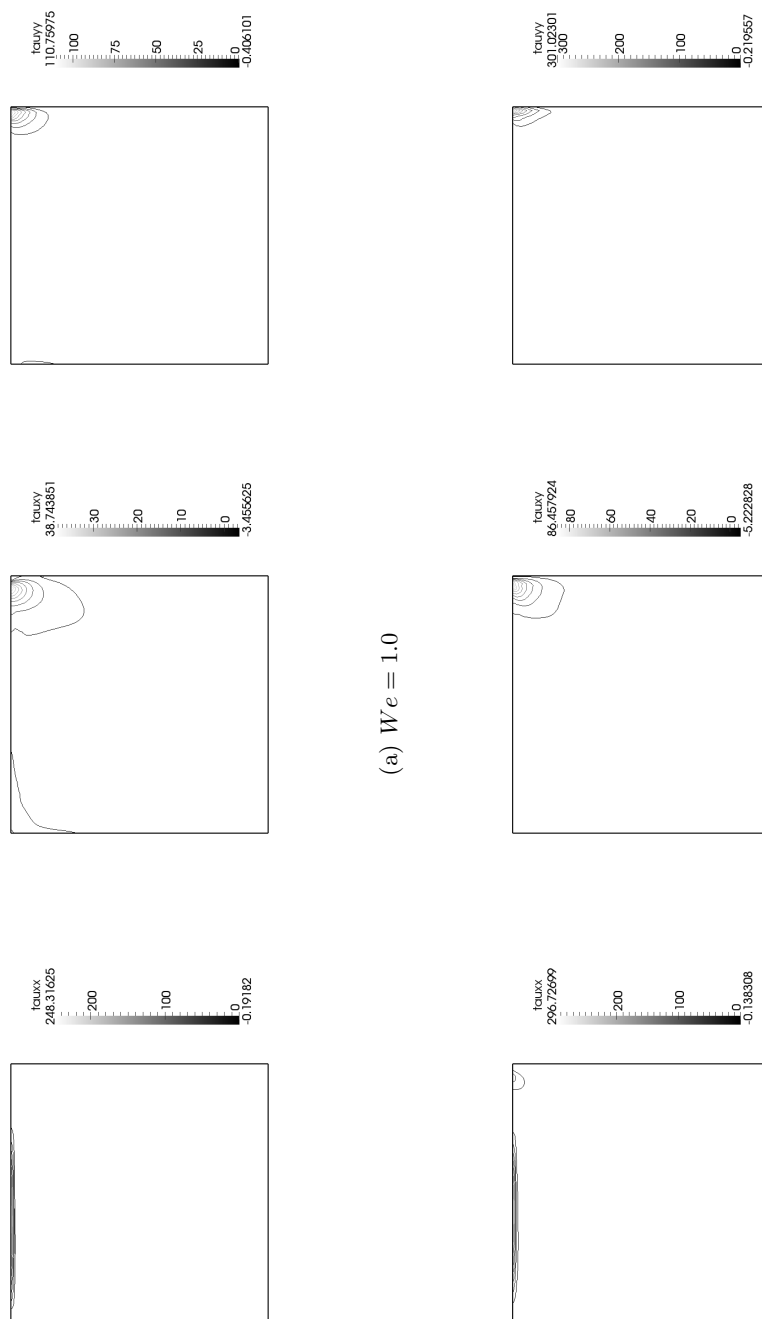
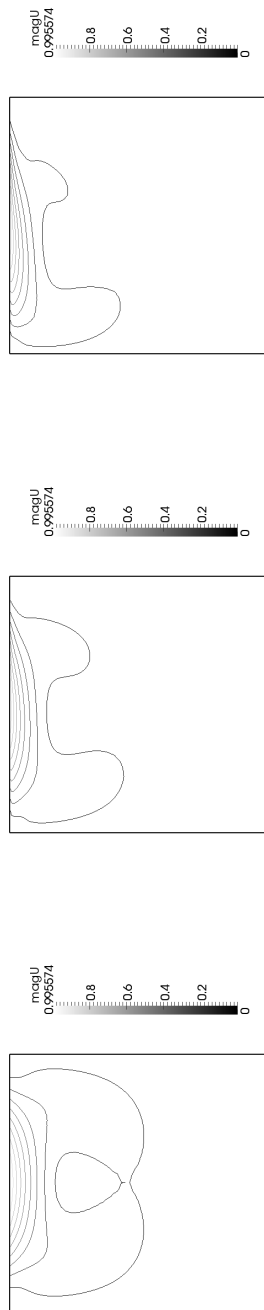


Figure 4.19:  $\tau_P$  field in the xy-plane using mesh M3 and CUBISTA.

*4 Numerical simulation of the viscoelastic flow in a three-dimensional lid-driven cavity using the log-conformation reformulation in OpenFOAM®*

The magnitude of the velocity is shown in Fig 4.20. With increasing Weissenberg number, the boundary layer next to the lid becomes thinner and shifts in upstream direction. As elasticity becomes important, a larger region in the  $xy$ -plane will experience low velocity magnitude.



(a)  $We = 0.0$  (b)  $We = 1.0$  (c)  $We = 2.0$

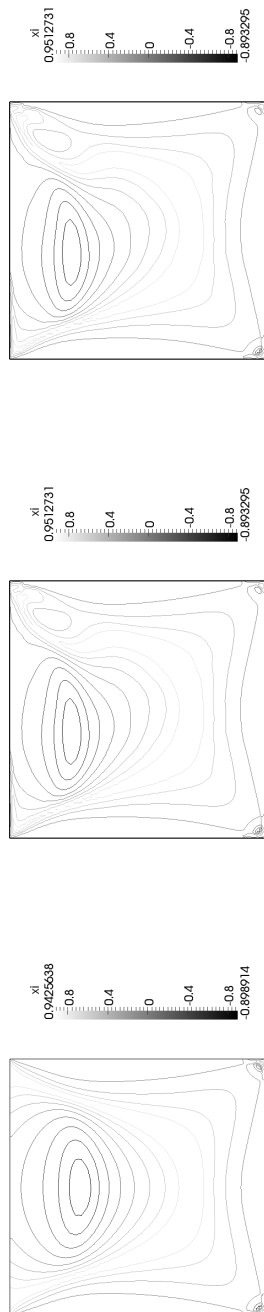
**Figure 4.20:** Velocity magnitude in the xy-plane using mesh M3 and CUBISTA.

To identify the regions where the fluid is sheared, elongated or moved as a rigid body we will use the normalized flow-type classifier  $\xi$  proposed by Mompean et al. [32]

$$\xi = \frac{1 - X}{1 + X}$$

where  $X$  is the Astarita's parameter. [33] The scalar  $\xi$  is  $\xi = 0$  for simple shear flow,  $\xi = 1$  for extensional flow and  $\xi = -1$  if the fluid is in a rigid body motion.

The results for the flow-type classifier are shown in Fig. 4.21. Isocontours for the Newtonian limit ( $We = 0.0$ ) are presented as a reference, wherein a symmetrical field is found similar to the velocity field. A shear flow is present close to the vertical walls and the bottom wall. Away from those walls towards the primary vortex center, a change from shear to extensional flow is found. The flow then goes through another transition, transforming from extensional flow into rigid body motion at the primary vortex center. The primary vortex center is pure rigid body motion. Extensional flows are also observed at the secondary eddies. When increasing the Weissenberg number a similar field is observed as in the case of a Newtonian fluid. The only visible change is that the amount of extensional flow at the downstream corner just next to the lid becomes larger with increasing elasticity. Furthermore, the area of rigid body motion shifts to the upper left, which is in agreement with the shift of the primary vortex center, see Fig. 4.14.



(a)  $We = 0.0$  (b)  $We = 1.0$  (c)  $We = 2.0$

**Figure 4.21:**  $\xi$  field in the xy-plane using mesh M3 and CUBISTA.

### Velocity profiles

Two velocity profiles are investigated; the vertical profile of the velocity in  $x$ -direction  $U_x$  at  $x = 0.5$  and the horizontal profile of the velocity in the  $y$ -direction  $U_y$  at  $y = 0.5$  in the  $xy$ -plane at  $z = 0.5$ .

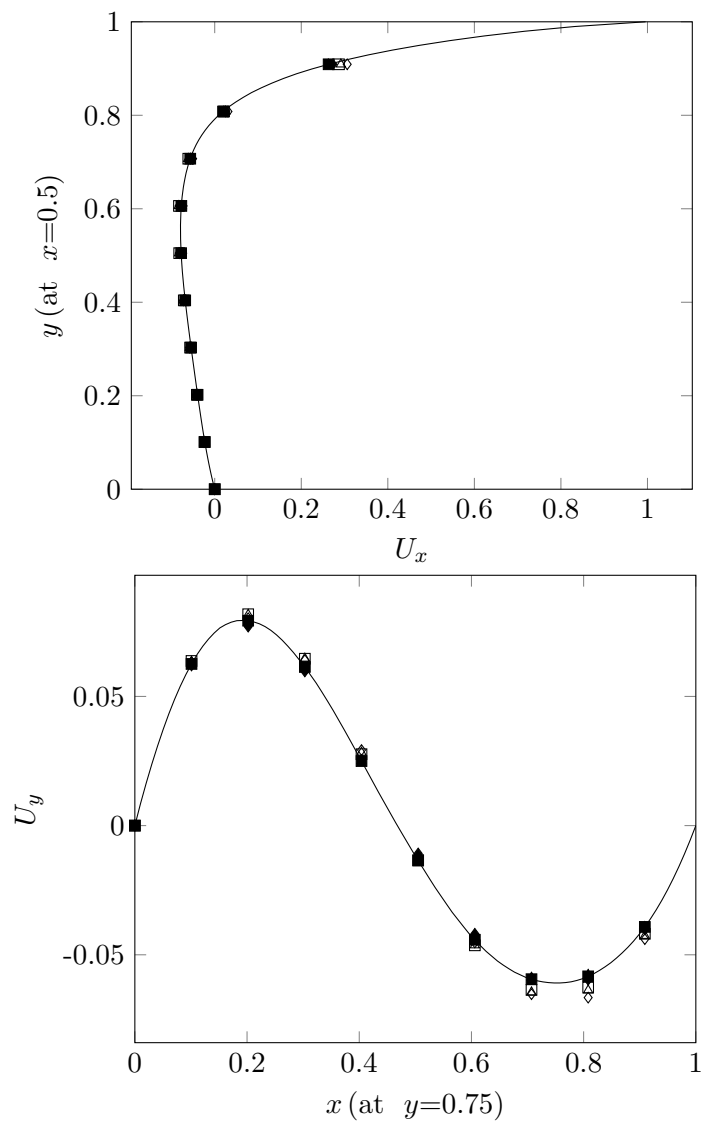
The velocity profiles at  $We = 1.0$  with respect to the different meshes and the two convection scheme are presented in Fig. 4.22. The mesh and the convection scheme have little influence on the vertical  $U_x$  profiles and sufficiently good convergence of the plots is observed. Major differences in  $U_x$  are present at the top of the lid-cavity. On the other hand, horizontal  $U_y$  profiles do not show such a good convergence for  $0.1 < x < 0.4$  and  $0.5 < x < 0.9$ , where the minima and maxima are.

Fig. 4.23 shows the change in the velocity profiles with increasing Weissenberg number. Generally, as the effect of elasticity becomes large, so is the resistance to flow resulting in smaller velocity values. This can be observed from both  $U_x$  and  $U_y$  profiles, showing the largest maxima and minima at  $We = 0.0$ . From the vertical  $U_x$  profiles one observes that the boundary layer is becoming thinner with increasing Weissenberg number. This implies that the velocity gradient close to the lid is increasing with increasing Weissenberg number. The maximum of the horizontal  $U_y$  profiles are shifting in negative  $x$ -direction with increasing Weissenberg number. This implies that more elastic fluids tend to move closer to the left vertical wall of the lid cavity, with the maximum value of  $U_y$  decreasing. Furthermore, the minimum on the right side is observed to perceptibly flatten with increasing Weissenberg number.

### Simulations at higher Weissenberg number

In this section, the findings when even further increasing the Weissenberg number with M3 CUBISTA are discussed. It was observed that the results obtained were strongly unsteady due to the presence of oscillations with respect to the primary vortex center and in some cases even two primary vortex centers formed at higher Weissenberg numbers. As a result, we find it purposeless to display these results. Instead, we only report on the stability of the numerical algorithm.

The highest Weissenberg number simulated in this work was  $We = 160.0$ , however, we like to point out that it is possible to even further increase the Weissenberg number and no critical Weissenberg number was found in terms of stability. However, the increase was stopped due to the unawareness of those results in terms of accuracy. Snapshots of the primary vortex center at  $We = 160.0$  with M3 CUBISTA are presented in Fig. 4.24. One can see that drastic changes of the primary vortex occur. This underlines the complexity of a viscoelastic flow in a considerably simple geometry at high Weissenberg numbers.



**Figure 4.22:** Vertical and horizontal velocity profiles at  $We = 1.0$  for different meshes and differencing schemes.  
 ( $\blacklozenge$ ): M1 Cubista, ( $\circ$ ): M1 Upwind, ( $\blacktriangle$ ): M2 Cubista, ( $\triangle$ ): M2 Upwind, ( $\blacksquare$ ): M3 Cubista, ( $\square$ ): M3 Upwind.



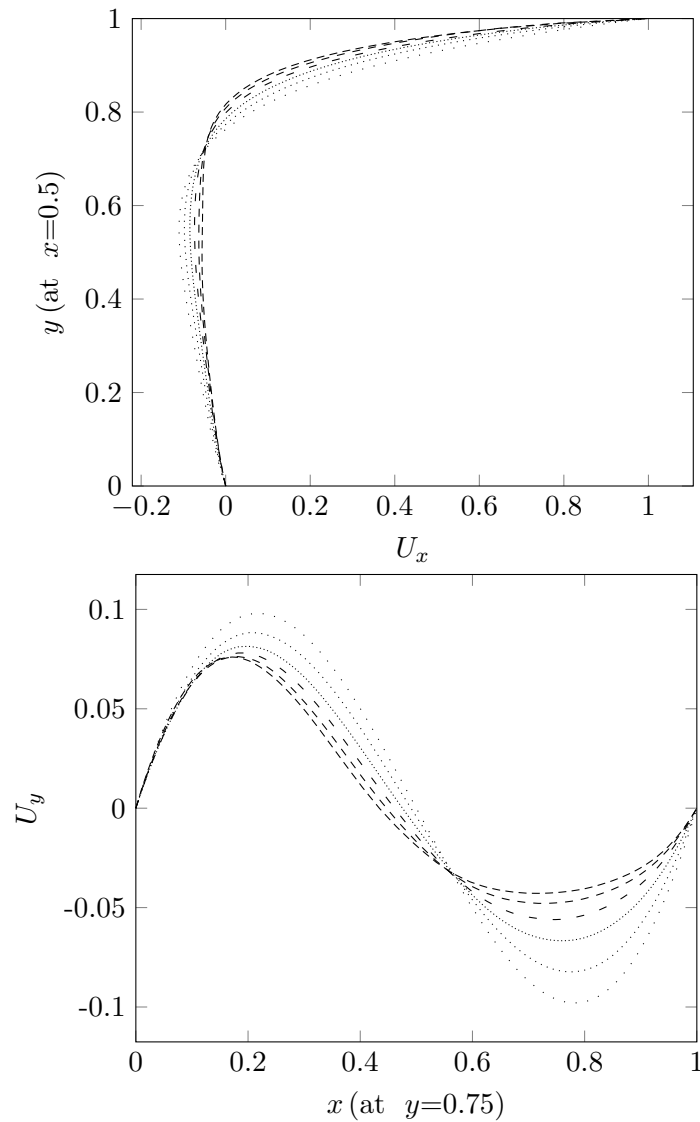


**Figure 4.23:** Vertical and horizontal velocity profiles as a function of the Weissenberg number using mesh M3 and CUBISTA.  
 (····):  $We = 0.0$ , (-----):  $We = 0.4$ , (- · - ·):  $We = 0.8$ , (- - -):  $We = 1.2$ ,  
 (- - -):  $We = 1.6$ , (- · - · -):  $We = 2.0$

4 Numerical simulation of the viscoelastic flow in a three-dimensional lid-driven cavity using the log-conformation reformulation in OpenFOAM®

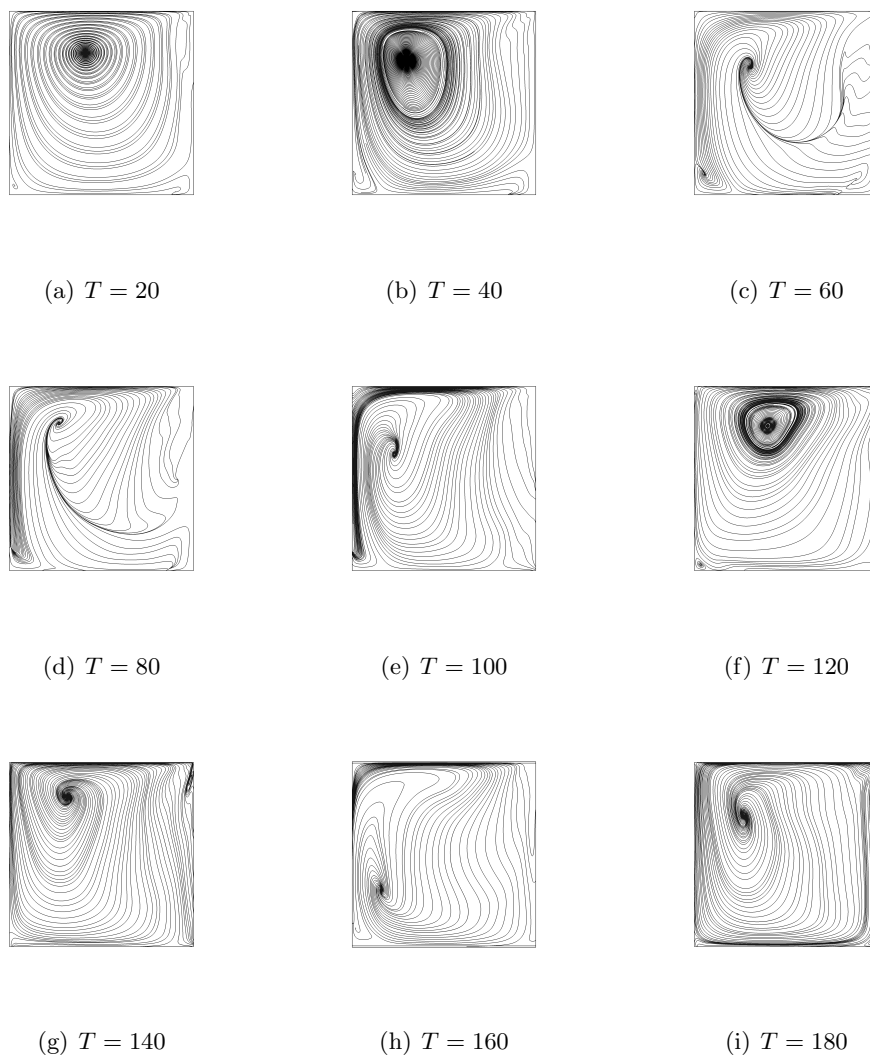


**Figure 4.24:** Snapshots of streamlines in the  $xy$ -plane for  $We = 160.0$  using mesh M3 and CUBISTA.

## 4.5 Summary

In this work, the log-conformation reformulation as proposed by Fattal and Kupferman [2] is adopted and implemented in the finite-volume CFD-software *OpenFOAM*®. This reformulation allows to extenuate the well-known high Weissenberg number problem, which is omnipresent when pursuing numerical simulations of flows at high elasticities. The implementation is done such as to finally obtain a second-order accurate algorithm in time and space when using an adequate convection scheme such as the CUBISTA. This behavior was shown by simulation of a transient Poiseuille flow. The implementation is capable of performing fully three-dimensional and transient simulations on arbitrary meshes, which was demonstrated by simulating the transient lid-driven flow in a cubic cavity.

No upper limit in the Weissenberg number could be found in terms of stability and we present results for a Weissenberg numbers of  $We = 160.0$ . However, questions of accuracy at such large Weissenberg numbers remain and generally finer meshes and time-steps would be necessary, which, however, is out of question due to the overhead in computation time.

A simulation on the tetrahedral mesh with CUBISTA was successful, showing the capability of our numerical algorithm to handle unstructured meshes, although it should also be noted that the tetrahedral mesh produces less accurate results than a comparable hexahedral mesh.

The spatial convergence of the results for the location of the primary vortex center and the velocity profiles is sufficient. Furthermore, the convergence of the results with respect to the time-step was shown. Even though the high accurate CUBISTA scheme and a second-order time scheme is used in this work, one should note that accuracy is still an issue at high Weissenberg numbers and the large computational times strictly preclude the use of even finer meshes and smaller time-steps.

As the Weissenberg number gets larger, the influence of the elasticity on the flow rheology becomes more distinct. This is demonstrated by the change in the streamlines, the change of the velocity profiles and fields for stress, velocity and the flow classifier.

## 4.A Literature

- [1] F. P. T. Baaijens, Mixed finite element methods for viscoelastic flow analysis: a review, *J. Non-Newton. Fluid Mech.* 79 (1998) 361–385.
- [2] R. Fattal, R. Kupferman, Constitutive laws for the matrix-logarithm of the conformation tensor, *J. Non-Newton. Fluid Mech.* 123 (2004) 281–285.
- [3] D. Trebotich, P. Colella, G. H. Miller, A stable and convergent scheme for viscoelastic flow in contraction channels, *J. Comp. Phys.* 205 (2005) 315–342.
- [4] M. F. Tomé, A. Castelo, A. M. Afonso, F. T. Pinho, M. A. Alves, Application of the log-conformation technique to 3D free surface flows, in: *Congreso de Métodos Numéricos en Ingeniería*, 2009.
- [5] V. Warichet, V. Legat, Adaptive high-order prediction of the drag correction factor for the upper-convected Maxwell fluid, *J. Non-Newton. Fluid Mech.* 73 (1997) 95–114.
- [6] M. A. Hulsen, E. A. J. F. Peters, B. H. A. A. van den Brule, A new approach to the deformation fields method for solving complex flows using integral constitutive equations, *J. Non-Newton. Fluid Mech.* 98 (2001) 201–221.
- [7] R. Fattal, R. Kupferman, Time-dependent simulation of viscoelastic flows at high Weissenberg number using the log-conformation representation, *J. Non-Newton. Fluid Mech.* 126 (2005) 23–37.
- [8] J. Hao, T.-W. Pan, Simulation for high Weissenberg number viscoelastic flow by a finite volume method, *Appl. Math. Lett.* 20 (2007) 988–993.
- [9] P. J. Oliveira, Viscoelastic lid-driven cavity flows, in: *CMNE/CILAME 2007, Porto, Portugal (AMPTAC)* (2007) 1–16.
- [10] C. K. Aidun, N. G. Triantafillopoulos, J. D. Benson, Global stability of a lid-driven cavity with throughflow: flow visualization studies, *Phys. Fluids A* 3 (1991) 2081–2091.
- [11] T. W. H. Sheu, S. F. Tsai, Flow topology in a steady three-dimensional lid-driven cavity, *Comput. Fluids* 31 (2002) 911–934.
- [12] H. Demir, Numerical modelling of viscoelastic cavity driven flow using finite difference simulations, *Appl. Math. Comput.* 166 (2005) 64–83.

- [13] A. M. Grillet, B. Yang, B. Khomani, E. S. G. Shaqfeh, Modeling of viscoelastic lid driven cavity flow using finite element simulations, *J. Non-Newton. Fluid Mech.* 88 (1999) 99–131.
- [14] T. W. Pan, J. Hao, Numerical simulation of a lid-driven cavity viscoelastic flow at high Weissenberg numbers, *C. R. Acad. Sci. Paris Ser. I* 344 (2007) 283–286.
- [15] M. A. Alves, P. J. Oliveira, F. T. Pinho, A convergent and universally bounded interpolation scheme for the treatment of advection, *Int. J. Numer. Meth. Fl.* 41 (2003) 47–75.
- [16] K. Yapici, B. Karasozen, Y. Uludag, Finite volume simulation of viscoelastic laminar flow in a lid-driven cavity, *J. Non-Newton. Fluid Mech.* 164 (2009) 51–65.
- [17] J. G. Oldroyd, On the formulation of rheological equations of state, *Proc. Roy. Soc. London Ser. A* 200 (1950) 523–541.
- [18] H. Damanik, J. Hron, A. Ouazzi, S. Turek, A monolithic FEM approach for the log-conformation reformulation (LCR) of viscoelastic flow problems, *J. Non-Newton. Fluid Mech.* 165 (2010) 1105–1113.
- [19] J. L. Favero, A. R. Secchi, N. S. M. Cardozo, H. Jasak, Viscoelastic flow simulation: Development of a methodology of analysis using the software OpenFOAM and differential constitutive equations, *J. Non-Newton. Fluid Mech.* 28 (2009) 31–36.
- [20] F. Habla, A. Obermeier, O. Hinrichsen, Semi-implicit stress formulation for viscoelastic models: Application to three-dimensional contraction flows, *J. Non-Newton. Fluid Mech.* 199 (2013) 70–79.
- [21] B. P. Leonard, Why you should not use 'hybrid' 'power-law' or related exponential schemes for convective modelling - there are much better alternatives, *Int. J. Numer. Meth. Fl.* 20 (1995) 421–442.
- [22] P. K. Sweby, High resolution schemes using flux limiters for hyperbolic conservation laws, *SIAM J. Numer. Anal.* 21 (1984) 995–1011.
- [23] J. Jasak, H. G. Weller, A. D. Gosman, High resolution NVD differencing scheme for arbitrarily unstructured meshes, *Int. J. Numer. Meth. Fl.* 31 (1999) 431–449.
- [24] A. Afonso, P. J. Oliveira, F. T. Pinho, M. A. Alves, The log-conformation tensor approach in the finite-volume method framework, *J. Non-Newton. Fluid Mech.* 157 (2009) 55–65.

- [25] S.-C. Xue, R. I. Tanner, N. Phan-Thien, Numerical modelling of transient viscoelastic flows, *J. Non-Newton. Fluid Mech.* 123 (2004) 33–58.
- [26] H. Jasak, Error analysis and estimation for the finite volume method with applications to fluid flows, Ph.D. thesis, Imperial College University of London (1996).
- [27] F. Habla, A. Weitalka, S. Neuner, O. Hinrichsen, Development of a methodology for numerical simulation of non-isothermal viscoelastic fluids flows with application to axisymmetric 4:1 contraction flows, *Chem. Eng. Sci.* 207-208 (2012) 772–784.
- [28] N. D. Waters, M. J. King, Unsteady flow of an elastico-viscous liquid, *Rheol. Acta* 9 (1970) 345–355.
- [29] G. D’Avino, M. A. Hulsen, Decoupled second-order transient schemes for the flow of viscoelastic fluids without a solvent contribution, *J. Non-Newton. Fluid Mech.* 165 (2010) 1602–1612.
- [30] A. S. R. Duarte, A. I. P. Miranda, P. J. Oliveira, Numerical and analytical modeling of unsteady viscoelastic flows: the start-up and pulsating test case problems, *J. Non-Newton. Fluid Mech.* 154 (2008) 153–169.
- [31] P. Pakdel, S. H. Spiegelberg, G. H. McKinley, Cavity flows of elastic liquids: Two-dimensional flows, *Phys. Fluids* 9 (1997) 3123–3140.
- [32] G. Mompean, R. Thompson, P. S. Mendes, A general transformation procedure for differential viscoelastic models, *J. Non-Newton. Fluid Mech.* 111 (2003) 151–174.
- [33] G. Astarita, Objective and generally applicable criteria for flow classification, *J. Non-Newton. Fluid Mech.* 6 (1979) 69–76.

## 4.B Nomenclature

Normal symbols represent scalar quantities and boldface symbols represent vector and tensor quantities in general.

### Roman Symbols

Symbol	Description	Unit
$\mathbf{0}$	Vector or matrix with only zeros	
$a$	Coefficient of characteristic equation	$[-]$
$A_i$	Matrix belonging to the $i$ -th eigenvalue	$[-]$
$A_{i,jk}$	$jk$ -th element of the matrix belonging to the $i$ -th eigenvalue	$[-]$
$\mathbb{A}_P^U$	Diagonal coefficient of semi-discretized momentum equation of cell $P$	
$b$	Coefficient of characteristic equation	$[-]$
$\mathbf{B}$	Extensional matrix	$[s^{-1}]$
$c$	Coefficient of characteristic equation	$[-]$
$\mathbf{c}$	Conformation tensor	$[-]$
$\mathbf{d}$	Distance between two adjoining cell centers	$[m]$
$eU_x$	Error of the axial velocity	$[\frac{m}{s}]$
$\mathbb{H}_P^U$	Off-diagonal coefficients and source-vector of semi-discretized momentum equation of cell $P$	
$i$	Index	$[-]$
$\mathbf{I}$	Identity matrix	$[-]$
$j$	Index	$[-]$
$k$	Index	$[-]$
$L$	Cavity edge length	$[m]$
$L_x$	Axial length	$[m]$
$L_y$	Vertical length	$[m]$
$\tilde{m}_{ij}$	$ij$ -th element of rotated velocity gradient matrix	$[s^{-1}]$
$\widetilde{\mathbf{M}}$	Rotated velocity gradient matrix	$[s^{-1}]$
$\mathbf{N}$	Dummy matrix	$[s^{-1}]$
$N_y$	Number of cells in vertical direction	$[-]$
$p$	Pressure	$[\frac{kg}{ms^2}]$
$Q$	Flow rate over cross section	$[\frac{m^3}{s}]$

Symbol	Description	Unit
$r$	Ratio of successive gradients	$[-]$
$\mathbf{R}$	Eigenvector matrix	$[-]$
$\mathbf{S}_f$	Surface area normal vector at cell face $f$	$[m^2]$
$sd_{i,jk}$	$jk$ -th element of the sub-determinant belonging to the $i$ -th eigenvalue	$[-]$
$t$	Time	$[s]$
$\mathbf{U}$	Velocity	$[\frac{m}{s}]$
$U_x$	Velocity in x-direction	$[\frac{m}{s}]$
$U_{x,lid}$	Axial velocity of the moving lid	$[\frac{m}{s}]$
$U_{x,max}$	Maximum axial velocity	$[\frac{m}{s}]$
$U_y$	Velocity in y-direction	$[\frac{m}{s}]$
$x$	Position	$[m]$
$X$	Astarita's parameter	$[-]$
$y$	Position	$[m]$
$z$	Position	$[m]$

### Greek Symbols

Symbol	Description	Unit
$\Delta t$	Time step size	$[s]$
$\Delta T$	Dimensionless time step size	$[-]$
$\Delta y$	Vertical length of computational cell	$[m]$
$\nabla$	Nabla (gradient) operator	$[m^{-1}]$
$\nabla \cdot$	Divergence operator	$[m^{-1}]$
$\nabla_f^\perp$	Face normal gradient at cell face $f$	$[m^{-1}]$
$\eta_0$	Zero shear-rate viscosity	$[\frac{kg}{ms}]$
$\eta_P$	Polymeric viscosity	$[\frac{kg}{ms}]$
$\eta_S$	Solvent viscosity	$[\frac{kg}{ms}]$
$\lambda$	Relaxation time	$[s]$
$\lambda_\Psi$	Eigenvalue	$[-]$
$\lambda_{\Psi,i}$	$i$ -th eigenvalue	$[-]$
$\tilde{\Lambda}_{ii}$	$i$ -th eigenvalue	$[-]$



Symbol	Description	Unit
$\Lambda$	Eigenvalue matrix	[–]
$\Lambda_\Psi$	Logarithmized eigenvalue matrix	[–]
$\xi$	Flow-type classifier	[–]
$\rho$	Density	$[\frac{kg}{m^3}]$
$\tau$	Deviatoric or extra-stress tensor	$[\frac{kg}{ms^2}]$
$\tau_P$	Polymeric stress tensor	$[\frac{kg}{ms^2}]$
$\tau_{P,xx}$	Polymeric normal stress in x-direction	$[\frac{kg}{ms^2}]$
$\tau_S$	Solvent stress tensor	$[\frac{kg}{ms^2}]$
$\phi$	General variable	
$\phi_f$	General variable at cell face $f$	
$\phi_{f,CD}$	General variable at cell face $f$ obtained with central differencing	
$\phi_{f,UD}$	General variable at cell face $f$ obtained with upwind differencing	
$\phi_U$	General variable in upwind node $U$	
$\varphi$	Flux limiter	
$\Psi$	Logarithmic variable	[–]
$\Psi_{ij}$	$ij$ -th element of logarithmic variable	[–]
$\tilde{\omega}_{ij}$	$ij$ -th element of rotational matrix	$[s^{-1}]$
$\Omega$	Rotational matrix	$[s^{-1}]$

### Subscripts, Superscripts and Oversymbols

Symbol	Description
$\mathbf{Q}_C$	Property $\mathbf{Q}$ in computational cell $C$
$\mathbf{Q}_D$	Property $\mathbf{Q}$ in downwind node $D$
$\det(\mathbf{Q})$	Determinant of matrix $\mathbf{Q}$
$\mathbf{Q}_{exact}$	Exact value of $\mathbf{Q}$
$\mathbf{Q}^{n-1}$	Time level $n - 1$
$\mathbf{Q}^n$	Time level $n$
$\mathbf{Q}^{n+1}$	Time level $n + 1$
$\mathbf{Q}_{num}$	Numerically calculated value of $\mathbf{Q}$
$\mathbf{Q}^T$	Transpose of matrix $\mathbf{Q}$

<b>Symbol</b>	<b>Description</b>
$\mathbf{Q}_U$	Property $\mathbf{Q}$ in upwind node $U$
$\mathbf{Q}^*$	Estimate of variable $\mathbf{Q}$
$\mathbf{Q}^{**}$	Estimate of variable $\mathbf{Q}$
$\nabla \mathbf{Q}$	Upper-convected time derivative
$\tilde{\mathbf{Q}}$	Rotated matrix
$\overline{\mathbf{Q}}$	Linear interpolation of $\mathbf{Q}$ onto cell-face or average value
$ \mathbf{Q} $	Magnitude of $\mathbf{Q}$

### Nondimensional Groups

<b>Symbol</b>	<b>Description</b>	<b>Definition</b>
$\beta$	Retardation factor	$\frac{\eta_S}{\eta_0}$
$E$	Elasticity number	$\frac{\lambda \eta_0}{\rho L_y^2}$
$Re$	Reynolds number	$\frac{\rho L U}{\eta_0}$ or $\frac{\rho L U_{x,max}}{\eta_0}$
$T$	Dimensionless time	$\frac{t}{\lambda}$ or $\frac{t U_{x,max}}{L}$
$We$	Weissenberg number	$\frac{\lambda U_{x,max}}{L}$
$Y$	Dimensionless y-coordinate	$\frac{y}{L_y}$

### Abbreviations

<b>Abbreviation</b>	<b>Description</b>
AMG	Algebraic multigrid
BiCGstab	Bi-conjugate gradient stabilized
BSD	Both-side-diffusion
CBC	Convection Boundedness Criterion
CEF	Criminale-Ericson-Filbey
CG	Conjugate gradient
CUBISTA	Convergent and universally bounded interpolation scheme for treatment of advection
EV	Eigenvector
FENE	Finite extensible non-linear elastic
FENE-CR	Finite extensible non-linear elastic - Chilcott and Rallison
LCR	Log-conformation reformulation

<b>Abbreviation</b>	<b>Description</b>
l.h.s.	Left hand side
r.h.s.	Right hand side
PDE	Partial differential equation
PISO	Pressure implicit with splitting of operator
sd	Subdeterminant
SPD	Symmetric positive definite
SPTT	Simplified Phan-Thien-Tanner
QUICK	Quadratic upstream interpolation for convective kinematics

## 4.C Summary

In this work the log-conformation reformulation for viscoelastic constitutive equations as proposed by Fattal and Kupferman [2] is implemented in the open-source CFD-software *OpenFOAM*<sup>®</sup>, which is based on the collocated finite-volume method (FVM). The implementation includes an efficient eigenvalue and eigenvector routine and the algorithm finally is second-order accurate both in time and space, when using it in conjunction with an adequate convection scheme such as the CUBISTA scheme. [15] The newly developed solver is first validated with the analytical solution for a startup Poiseuille flow of a viscoelastic fluid and subsequently applied to the three-dimensional and transient simulation of a lid-driven cavity flow, in which the viscoelastic fluid is modeled by the Oldroyd-B constitutive equation. The results are presented for both the first-order upwind scheme and the CUBISTA scheme on four hexahedral meshes of different size in order to check for mesh convergence of the results and a tetrahedral mesh to show the applicability to unstructured meshes. The results obtained for various values of the Weissenberg number are presented and discussed with respect to the location of the primary vortex center, streamline patterns and velocity and stress profiles besides others. Sufficiently mesh converged results for Weissenberg numbers, which would have been impossible to obtain without use of the log-conformation reformulation, are obtained. An upper limit for the Weissenberg number in terms of stability could not be found.

## 4.D Author contribution

The author of this thesis contributed to this publication by implementing the log-conformation reformulation in the software package *OpenFOAM*<sup>®</sup>, by performing the startup of viscoelastic Poiseuille flow simulations, by setting up the cases for the cavity simulations and by writing the whole manuscript.

## 4.E Copyright permission

This chapter is originated from the following publication:

F. Habla, M. W. Tan, J. Haßberger, O. Hinrichsen, Numerical simulation of the viscoelastic flow in a three-dimensional lid-driven cavity using the log-conformation reformulation in *OpenFOAM*<sup>®</sup>, *Journal of Non-Newtonian Fluid Mechanics* 212 (2014) 47-62.

Reprinted with permission from Elsevier Ltd.

# 5 Development of a methodology for numerical simulation of non-isothermal viscoelastic fluid flows with application to axisymmetric 4:1 contraction flows

## 5.1 Introduction

Polymer chemistry and processing of polymers constitutes a large segment of the chemical process industry. The production process of the polymers is mostly non-isothermal in nature, as for example in plastification including heating and cooling sequences. Since flow properties are strongly dependent both upon rheology and temperature, it is of major interest to understand and predict such type of flows qualitatively and quantitatively.

In the last decades, CFD simulation evolved as an important tool to guide the engineers in the task of developing and improving such type of processes. However, there is still a gap between the engineers' needs and the current state-of-the-art, especially in complex problems, which is the case for non-isothermal viscoelastic fluids flows.

Although being quite a simple geometry, both planar and axisymmetric contraction flows are extensively studied in the literature. [1, 2, 3] This is mainly because the contraction results in locally complex flow profiles, which are difficult to predict numerically. In the vicinity of the re-entrant corner, large stress gradients are present, which may cause numerical algorithms to fail. As a result, this problem evolved as a benchmark problem in order to evaluate the stability of numerical algorithms. In the past decade, several studies focused on the simulation of non-isothermal contraction flows. [4, 5, 6] In doing so, one has to particularly focus on the thermorheological modeling, since viscoelastic fluids behave in between of ideally viscous fluids and ideally elastic solids. [7]

Although there is an ever increasing effort in research on non-isothermal flows of viscoelastic fluids, the efforts stay limited to academic problems and purposes. On the other hand, commercial packages are mostly limited to the analysis of non-Newtonian fluid flows, which are purely viscous without considering the effect of elasticity. A general and freely available solver for the simulation of non-isothermal viscoelastic flows, which is capable of handling complex and non-orthogonal meshes as well as both transient and steady-state problems, would therefore be of major importance.

Hence, this work deals with the development of a solver for computing non-isothermal flows of viscoelastic fluids as an extension to the isothermal viscoelastic fluid solver, which was recently

released within the open-source software *OpenFOAM*<sup>®</sup>. [8] The technique of handling non-isothermal flows therein strongly relies on the works of Peters [9, 10].

This work is organized as follows: In Section 5.2, the governing equations, the thermorheological modeling and the numerical algorithm are explained. A new generalized method for extrapolating stresses on solid walls in order to determine the stress divergence is proposed. In the subsequent Section 5.3, the extrapolation method is validated and its merits regarding accuracy and stability compared to the currently employed zero gradient method are shown. Next, the results for isothermal and non-isothermal 4:1 axisymmetric contractions are presented. In Section 5.4, the paper ends with a summary of the main conclusions.

## 5.2 Methodology

In this section, the governing equations are described and the thermorheological modeling is addressed. Subsequently, the numerical algorithm is shortly outlined.

### 5.2.1 Conservation and constitutive equation

The governing equations for incompressible, non-isothermal viscoelastic flows are the mass balance

$$\nabla \cdot \mathbf{U} = 0 \quad (5.1)$$

the momentum balance

$$\frac{\partial (\rho \mathbf{U})}{\partial t} + \nabla \cdot (\rho \mathbf{U} \mathbf{U}) = -\nabla p + \nabla \cdot \boldsymbol{\tau} \quad (5.2)$$

the energy balance

$$\frac{\partial (\rho u)}{\partial t} + \nabla \cdot (\rho \mathbf{U} u) = -\nabla \cdot \mathbf{q} + Q \quad (5.3)$$

together with a constitutive equation describing the polymer's stress behavior. In the above equations,  $\mathbf{U}$  denotes the velocity vector,  $\rho$  the density,  $t$  the time,  $p$  the pressure,  $\boldsymbol{\tau}$  the total stress tensor,  $u$  the specific internal energy,  $\mathbf{q}$  the heat flux and  $Q$  the internal energy source term taking into account both entropic and energetic effects. Note that the density may depend on the temperature within our approach, although this dependency is neglected in this work for simplicity.

In this work, the Oldroyd-B equation is used. [11] The total stress  $\boldsymbol{\tau}$  is thereby divided into a solvent (Newtonian) and a polymer (viscoelastic) contribution

$$\boldsymbol{\tau} = \boldsymbol{\tau}_S + \boldsymbol{\tau}_P \quad (5.4)$$

$\boldsymbol{\tau}_S$  is the solvent stress contribution defined by

$$\boldsymbol{\tau}_S = \eta_S(T) \left[ \nabla \mathbf{U} + (\nabla \mathbf{U})^T \right] \quad (5.5)$$

wherein  $\eta_S(T)$  is the temperature-dependent solvent viscosity.

For the viscoelastic contribution  $\boldsymbol{\tau}_P$  the upper-convected Maxwell equation holds

$$\boldsymbol{\tau}_P + \lambda(T) \overset{\nabla}{\boldsymbol{\tau}}_P = \eta_P(T) \left[ \nabla \mathbf{U} + (\nabla \mathbf{U})^T \right] \quad (5.6)$$

wherein  $\lambda(T)$  denotes the relaxation time and  $\eta_P(T)$  the polymer viscosity, both being a function of the temperature  $T$ .  $\overset{\nabla}{\boldsymbol{\tau}}_P$  denotes the upper-convected time derivative defined as

$$\overset{\nabla}{\boldsymbol{\tau}}_P = \frac{\partial \boldsymbol{\tau}_P}{\partial t} + \nabla \cdot (\mathbf{U} \boldsymbol{\tau}_P) - (\nabla \mathbf{U})^T \cdot \boldsymbol{\tau}_P - \boldsymbol{\tau}_P \cdot \nabla \mathbf{U} \quad (5.7)$$

Note, that multi-mode capability, in which the polymeric stress is the sum of  $m$  modes ( $\boldsymbol{\tau}_P = \sum_{k=1}^m \boldsymbol{\tau}_{P,k}$ ), as well as more thorough constitutive equations such as PTT and Pom-Pom models are forthcoming within this framework. [8]

The retardation ratio  $\beta$  is defined as

$$\beta = \frac{\eta_P}{\eta_0} = \frac{\eta_P}{\eta_S + \eta_P} \quad (5.8)$$

wherein  $\eta_0$  is the total viscosity. Note, that  $\beta$  is independent of the temperature  $T$  in this work as will be shown later.

## 5.2.2 Thermodynamical modeling

Using the heat capacity  $c_P$  at constant pressure one obtains an equation for temperature when introducing into the energy balance Eq. 5.3

$$\frac{\partial (\rho c_P T)}{\partial t} + \nabla \cdot (\rho c_P \mathbf{U} T) = -\nabla \cdot \mathbf{q} + Q \quad (5.9)$$

wherein  $c_P$  may be a function of temperature, although this is being neglected herein. The dependency of  $c_P$  on the macromolecule orientation is negligibly small as shown by Wapperom and Hulsen [12] and thus no modeling is needed here. The term  $Q$  due to internal heat production comprises two contributions, which are an irreversible part due to viscous dissipation and a reversible part due to entropy changes caused by the orientation of the macromolecule chains. [4] Considering this, the total source term for an Oldroyd-B fluid can then be written as [10]

$$Q = \boldsymbol{\tau}_S : \mathbf{D} + \alpha \boldsymbol{\tau}_P : \mathbf{D} + (1 - \alpha) \frac{\text{tr}(\boldsymbol{\tau}_P)}{2\lambda(T)} \quad (5.10)$$

where  $\mathbf{D}$  is the deformation rate tensor being  $\mathbf{D} = 1/2 [\nabla\mathbf{U} + (\nabla\mathbf{U})^T]$  and  $\alpha$  is an energy partitioning coefficient. The case of  $\alpha = 1$  is referred to as pure entropy elasticity, in which all mechanical energy is dissipated as heat corresponding to pure viscous material behavior. On the other hand, if  $\alpha = 0$ , all mechanical energy is stored as elastic energy corresponding to pure elastic material behavior. This mechanism is called pure energy elasticity. In this work, we follow the ideas of using an a-priori defined energy partitioning coefficient  $\alpha$ . [12, 6, 7] The commonly employed constitutive equations model the stresses only using the end-to-end vector of the macromolecules. Since energetic effects are caused by structural features being much smaller than the end-to-end vector, an additional structural variable would be needed for modeling these effects (i.e. without a-priori definition of  $\alpha$ ) as being discussed by Hütter et al. [13]. However, this is out of the scope of this study.

The temperature dependence of the relaxation time  $\lambda(T)$ , solvent and polymer viscosities  $\eta_S(T)$ ,  $\eta_P(T)$  are described as follows

$$\lambda(T) = a_T \lambda(T_0) \tag{5.11}$$

$$\eta_S(T) = a_T \eta_S(T_0) \tag{5.12}$$

$$\eta_P(T) = a_T \eta_P(T_0) \tag{5.13}$$

where  $T_0$  is a reference temperature and  $a_T$  is a shift factor obeying the Williams-Landel-Ferry (WLF) relation [14]

$$a_T = \exp\left(\frac{-C_1(T - T_0)}{C_2 + T - T_0}\right) \tag{5.14}$$

in which  $C_1$  and  $C_2$  are the WLF parameters. Since both viscosities  $\eta_S(T)$  and  $\eta_P(T)$  vary with the same shift factor  $a_T$ , the retardation ratio  $\beta$  as defined in Eq. 5.8 is constant over  $T$ .

The heat flux  $\mathbf{q}$  in Eq. 5.9 is calculated with Fourier's law

$$\mathbf{q} = -k\nabla T \tag{5.15}$$

where  $k$  is the thermal conductivity of the fluid, which is assumed to be no function of the temperature  $T$  and the polymer orientation in this work. However, modeling the temperature dependency of the thermal conductivity is straightforward. For an approach to model the dependency of  $k$  on the macromolecule orientation, the reader is referred to Wapperom et al. [4], in which the thermal conductivity is a linear function of the conformation tensor  $\mathbf{c} = \lambda/\eta_P\boldsymbol{\tau}_P + \mathbf{I}$ .



### 5.2.3 Discretization and numerical algorithm

The package *OpenFOAM*<sup>®</sup> is used for implementation. This package is based on the collocated finite volume method storing all variables in cell centers, i.e.  $\mathbf{U}$ ,  $p$ ,  $\boldsymbol{\tau}_P$  and  $T$ . A general two-point scheme is used for temporal discretization using two values in time to approximate the time-derivative, while the convective terms are discretized using the first-order upwind scheme. For a thorough discussion and validation of this scheme we refer the reader to Favero et al. [8]. Cell face values are obtained by second-order linear interpolation where needed, while volume integrals are obtained from second-order Gaussian integration.

In order to enhance numerical stability the DEVSS technique is used Gu enette and Fortin [15], which introduces an additional elliptic operator into the momentum equation Eq. 5.2, resulting in

$$\begin{aligned} \frac{\partial \rho \mathbf{U}}{\partial t} + \nabla \cdot (\rho \mathbf{U} \mathbf{U}) - \nabla \cdot (\eta_P(T) + \eta_S(T)) \nabla \mathbf{U} = \\ -\nabla p + \nabla \cdot \boldsymbol{\tau}_P - \nabla \cdot \eta_P(T) \nabla \mathbf{U} - \nabla \mathbf{U} \cdot \nabla \eta_S(T) \end{aligned} \quad (5.16)$$

The elliptic term on the l.h.s. is evaluated implicitly, while the elliptic term on the r.h.s. is evaluated explicitly. The last term on the r.h.s. is a correction term due to the non-constant, but locally varying solvent viscosity  $\eta_S(T)$ , which arises when using Eq. 5.5 in conjunction with Eq. 5.2.

The SIMPLE algorithm is adopted to handle the strongly coupled set of equations Eqs. 5.1, 5.6, 5.9 and 5.16. [16] The algorithm can be summarized as follows

- 1.) Solve the momentum balance Eq. 5.16 (optionally).
- 2.) Construct and solve a Poisson-type equation for pressure from the continuity equation Eq. 5.1.
- 3.) Correct the fluxes and velocities from the updated pressure field.
- 4.) Solve the constitutive equation Eq. 5.6.
- 5.) Solve the temperature equation Eq. 5.9 by using the expression Eq. 5.10.
- 6.) Update the physical properties, i.e. Eqs. 5.11, 5.12 and 5.13.
- 7.) Repeat from 1. for a given number of times ( $n = 1$ ) in this work).

Solving the momentum balance is an optional step and not necessary for convergence in the SIMPLE loop. We found that especially in flows with low values of the Reynolds number this step may even impair convergence in the subsequent pressure correction equation and

is therefore left out in this study. The Poisson-type equation for pressure is solved with a conjugate gradient method using an AMG preconditioner. A BiCGStab solver is used for stress and temperature in conjunction with a Cholesky preconditioner. The tolerances of the linear solvers are set to  $10^{-8}$  for pressure and  $10^{-6}$  for temperature and stress. Under-relaxation is applied with a value of 0.5 for pressure, temperature and stress and 0.8 for velocity, which was necessary for stable simulations at higher Deborah numbers. Simulations are stopped if the initial residual of the momentum equation for  $\mathbf{U}_x$  and  $\mathbf{U}_y$  falls below a value of  $10^{-6}$ , the constitutive equation for  $\tau_{P,xx}$ ,  $\tau_{P,xy}$  and  $\tau_{P,yy}$  below  $10^{-6}$ , the temperature equation below  $10^{-6}$  and the pressure correction equation below  $10^{-5}$ . In the axisymmetric simulations the same tolerance are used for  $\mathbf{U}_z$ ,  $\mathbf{U}_r$ ,  $\tau_{P,zz}$ ,  $\tau_{P,rz}$ ,  $\tau_{P,rr}$  and  $\tau_{P,\Theta\Theta}$ .

Zero initial conditions are specified for all variables except for temperature. At the inlet Neumann boundary conditions with a zero gradient are specified for pressure and stress, while for temperature and velocity a Dirichlet boundary condition is used. At the outlet a reference pressure is set using a Dirichlet boundary condition, while Neumann boundary conditions are used for stress, velocity and temperature. At solid walls, a Neumann boundary condition is used for pressure, while a no-slip Dirichlet boundary condition is employed for velocity and a Dirichlet boundary condition for temperature. Since the constitutive equation is of hyperbolic type, there is no need of assigning a wall boundary condition for stress. However, the divergence of the stress in the momentum balance Eq. 5.2 or 5.16 is numerically evaluated as follows

$$\int_{\partial V} \nabla \cdot \boldsymbol{\tau}_P dV \approx \sum_i \boldsymbol{\tau}_{P,fi} \cdot \mathbf{S}_{fi} \quad (5.17)$$

where  $V$  is the volume of the cell,  $\boldsymbol{\tau}_{P,fi}$  is the stress value at face  $i$  and  $\mathbf{S}_{fi}$  is the cell face area vector of face  $i$ . For cell faces in the interior, the value  $\boldsymbol{\tau}_{P,fi}$  is determined using linear interpolation of the cell centered values of the two adjoining cells. In case of a boundary cell face, this value needs to be specified. It should be noted here that this is only the case for the collocated finite volume method, since in the staggered arrangement, stresses are commonly solved for at cell-faces. [6] A zero gradient assumption is often used in literature, see for example Favero et al. [8] and Trebotich et al. [17], however, this can only be thought as a rough simplification as a zero gradient condition is not valid in almost any flow situation. This led to the development of analytically based boundary conditions, see for example Oliveira [18] and Tomé et al. [19]. In this case the constitutive equation is additionally solved on the boundary, i.e. on the cell face, by using the local velocity profile. This, however, is severely complicated when using arbitrary curved boundaries not aligned with the coordinate axes, nonorthogonal meshes and more complex constitutive equations. In view of industrial applications, for which complex geometries and nonorthogonal meshes are required, this approach is not justifiable. Our new approach therefore linearly extrapolates the stress value from interior cells in wall-normal direction onto the wall. This is illustrated in Fig. 5.1 for an arbitrarily shaped cell and a curved boundary. A local coordinate system  $\zeta$  normal to the centroid of the wall is

being used and the distances  $\zeta_i$  are determined by taking dot products. The unknown stress value  $\tau_{P,fe}$  at the boundary face is obtained by second-order linear regression according to

$$\tau_{P,fe} = \bar{\tau}_P - \bar{\zeta} \frac{\sum_i^n (\zeta_i - \bar{\zeta})(\tau_{P,fi} - \bar{\tau}_P)}{\sum_i^n (\zeta_i - \bar{\zeta})^2} \quad (5.18)$$

where  $\bar{\zeta}$  and  $\bar{\tau}_P$  are the arithmetic mean values of the  $n$  known  $\zeta_i$  and  $\tau_{P,fi} / \tau_{P,P}$  values. This approach is thus valid for arbitrary cell shapes, curved boundaries and any type of constitutive equation. A validation of this method and discussion regarding accuracy and stability will be pursued in the following chapter.

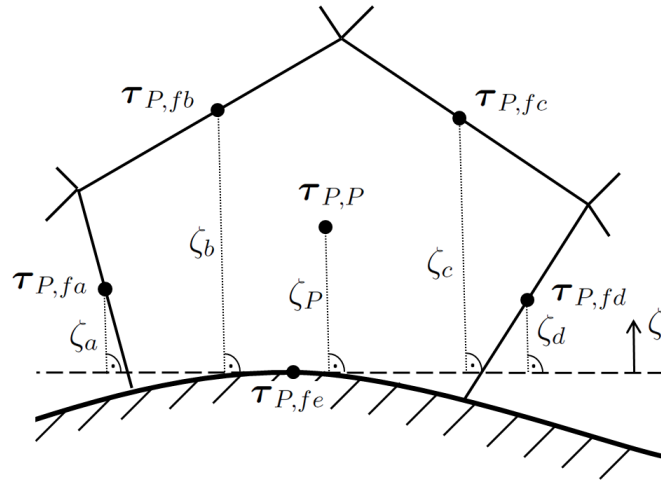


**Figure 5.1:** Local coordinate system  $\zeta$  for determining the stress value at the wall  $\tau_{P,fe}$ .

## 5.3 Results and discussion

### 5.3.1 Validation of the extrapolation method

In this section the afore introduced extrapolation method for stress is evaluated using a simple stationary planar Poiseuille flow. Isothermal conditions are assumed here for simplicity.

The geometry is shown in Fig. 5.2. A pressure difference is set between inlet (left) and outlet (right). Simulations will be performed on three different meshes shown in Fig. 5.3.

The fluid properties are taken from the work of Quinzani et al. [20]. The density of the fluid is  $\rho = 803.9 \text{ kg/m}^3$ , the polymer viscosity is  $\eta_P = 1.424 \text{ kg/ms}$  and the solvent viscosity is here taken as  $\eta_S = 0 \text{ kg/ms}$ , thus recovering the UCM model ( $\beta = 1$ ). The relaxation time is  $\lambda = 0.06 \text{ s}$ .

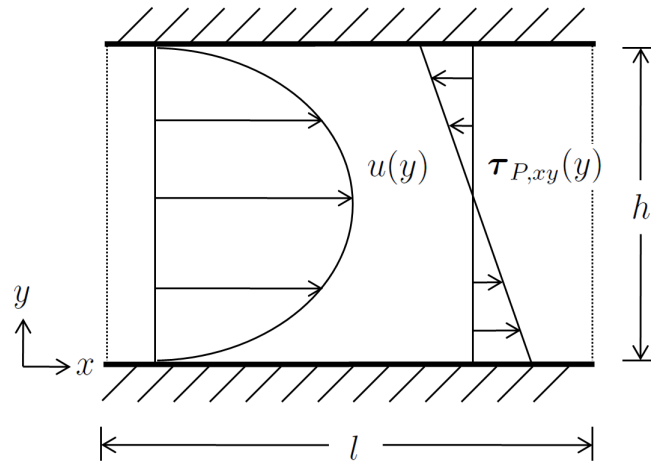


Figure 5.2: Geometry of the planar Poiseuille flow.

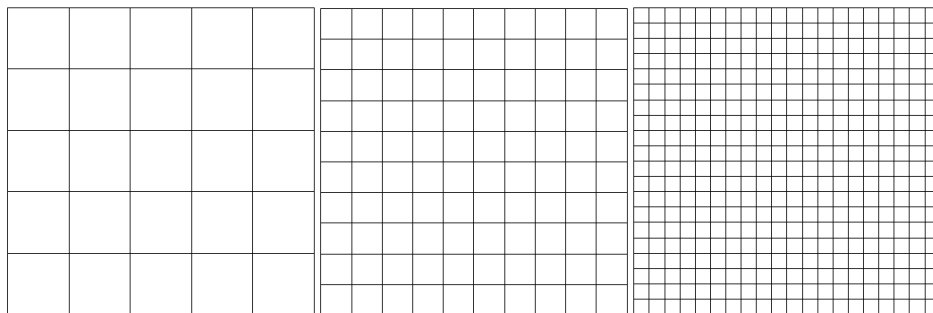


Figure 5.3: Meshes used for the validation of the extrapolation method.  
Left (M1): 25 cells (5 cells in each direction), middle (M2): 100 cells (10), right (M3): 400 (20).

The analytical velocity and shear stress profiles are as follows

$$\begin{aligned}\mathbf{U}_x(y) &= -\frac{h^2}{2\eta_p} \cdot \frac{\partial p}{\partial x} \left(1 - \frac{y}{h}\right) \cdot \frac{y}{h} \\ \tau_{P,xy}(y) &= -\frac{h}{2} \cdot \frac{\partial p}{\partial x} \left(1 - 2\frac{y}{h}\right)\end{aligned}$$

Using these expressions, the relative error in the  $L_1$ -norm for variable  $\phi$  is calculated

$$\epsilon_\phi = \sum_i^N \frac{|\phi_i^{exact} - \phi_i|}{|\phi_i^{exact}|}$$

where the  $N$  values are evaluated in the cell centers and at the solid walls.

Results are presented in terms of dimensionless variables according to  $\tilde{\mathbf{U}}_x = \mathbf{U}_x/\bar{\mathbf{U}}_x$  and  $\tilde{\tau}_{P,xy} = \tau_{P,xy}/\tau_{P,xy,max}$ , where  $\bar{\mathbf{U}}_x$  denotes the average velocity and  $\tau_{P,xy,max}$  the maximum shear stress. The Deborah number is  $De = \lambda\bar{\mathbf{U}}_x/h = 0.351$  and the Reynolds number is  $Re = \rho\bar{\mathbf{U}}_x h/\eta_p = 33$  for this case.

The predicted shear stress and velocity profiles together with the analytical solution are shown in Fig. 5.4. Simulations were performed both with the zero gradient method and the extrapolation method. For all of the three meshes, one finds that the zero gradient condition at the wall is reproduced for the shear stress as being forced. This results in a step profile of the shear stress throughout the height of the channel with all of the three meshes. It is noteworthy that for the middle and fine mesh (M2 and M3) two adjoining cells have the same shear stress value, which would be similar to halving the mesh resolution. An unphysical velocity profile is predicted for the coarse mesh (M1), while for meshes M2 and M3 the velocity profile is now physically correct, however, also being a step profile, which again is similar to halving the mesh resolution. Nevertheless, convergence to the analytical solution is achieved with mesh refinement. In contrast, when using the extrapolation method, the shear stress profile is predicted correctly on any of the three meshes and the values coincidence with the analytical solution. Even on the coarsest mesh M1 a physical velocity profile is predicted (however this is not visible due to the scaling of the axis), on which the zero gradient method predicted an unphysical solution. The predicted velocity values for mesh M2 and M3 almost coincide with the analytical solution. In Fig. 5.5 an error estimation was performed. One finds, that the shear stress profile is predicted at the linear solver tolerance, i.e.  $10^{-6}$  with the extrapolation method, while the error for the zero gradient method is approximately five orders of magnitude higher for all of the three meshes. The error for the velocity monotonically decreases for both methods, however, the error with the extrapolation method is at least one order of magnitude below the error when using the zero gradient method. This validation supports the major advantage of using the extrapolation method with respect to accuracy, in contrast to the commonly employed zero gradient method. [8, 17] This is in particular relevant since wall-near regions are the particularly troublesome regions when simulating viscoelastic

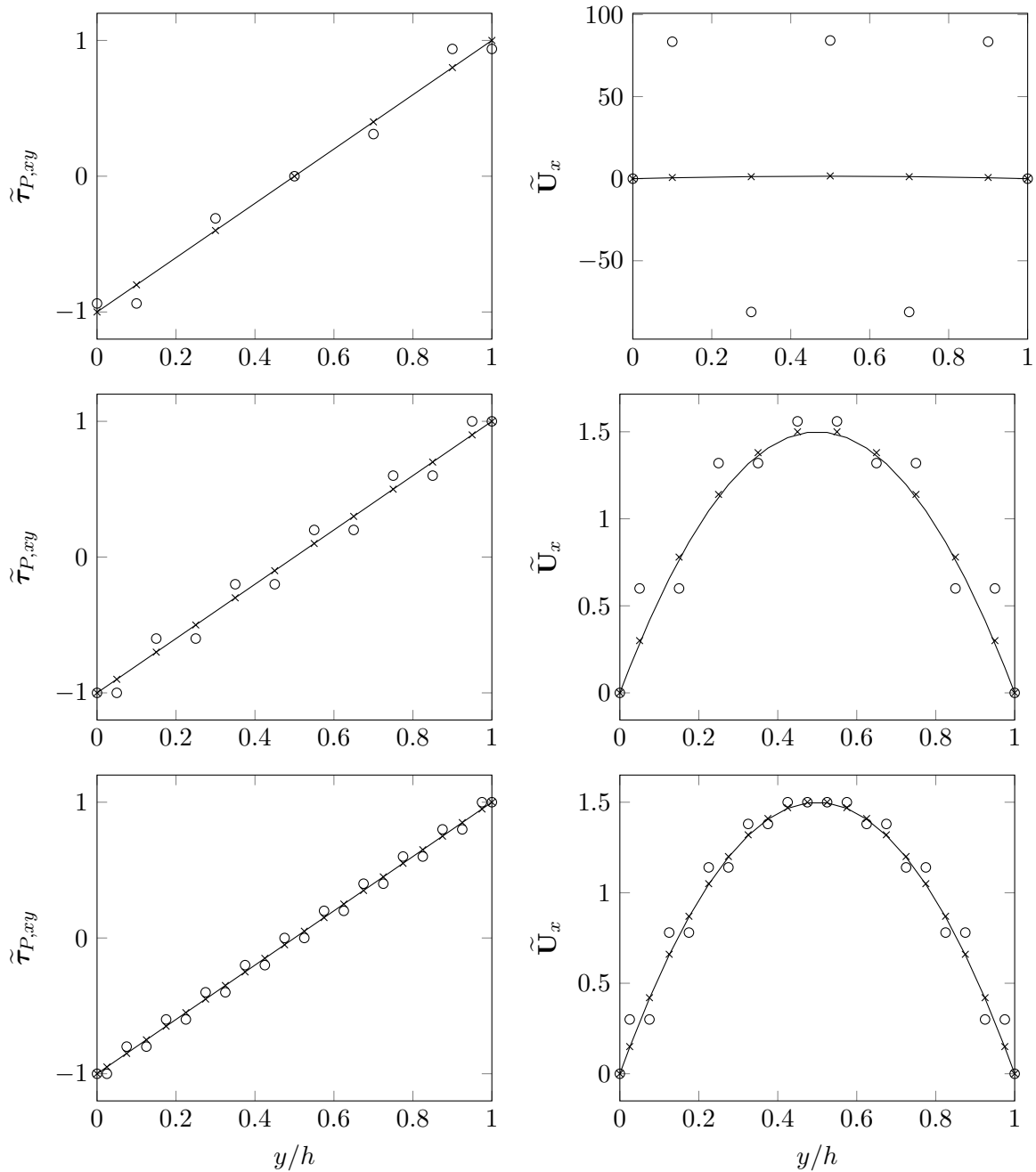


**Figure 5.4:** Predicted shear stress and velocity  $y$  profiles for the planar Poiseuille flow on three different meshes. M1, M2 and M3 from top to bottom. (—): analytical solution, (o): zero gradient method, (x): extrapolation method.

5 Development of a methodology for numerical simulation of non-isothermal viscoelastic fluid flows with application to axisymmetric 4:1 contraction flows

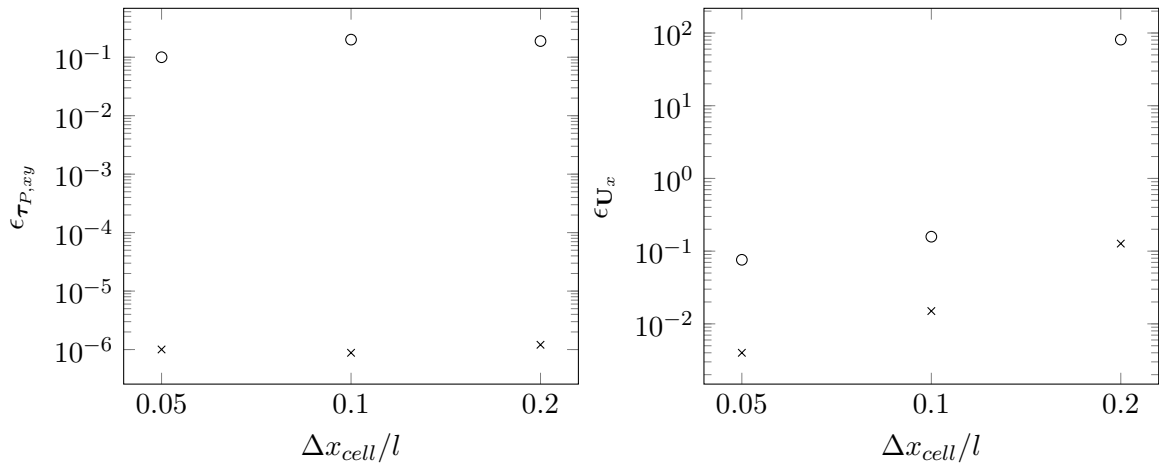


**Figure 5.5:** Relative  $L_1$ -error of the shear stress and velocity as a function of the dimensionless cell size for the planar Poiseuille flow. (○): zero gradient method, (×): extrapolation method.

fluid flows. [21] However, this validation case does not pose a problem regarding stability, as simulations can be performed for arbitrary values of the Deborah numbers. The effect of using the extrapolation method on the stability will be discussed in the next section for the axisymmetric 4:1 contraction.

### 5.3.2 Results for the axisymmetric 4:1 contraction flow

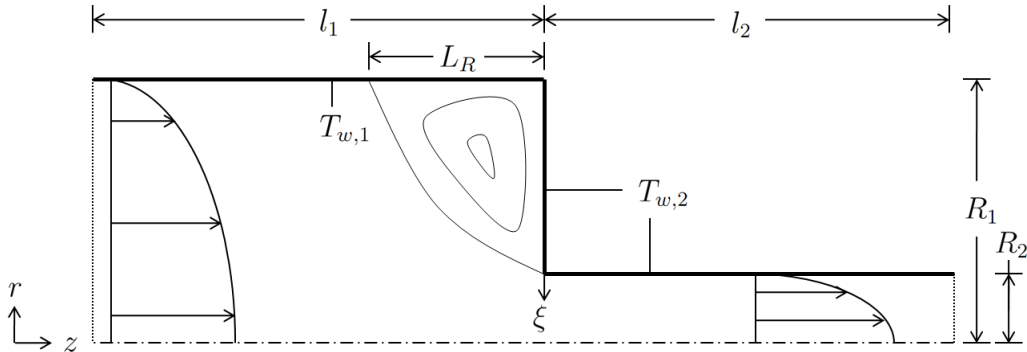


**Figure 5.6:** Geometry of the axisymmetric 4:1 contraction flow.

The geometry for the axisymmetric 4:1 contraction is shown in Fig. 5.6. The ratio of the radii is  $R_1/R_2 = 4$ . The upstream length is  $l_1 = 80 \cdot R_2$  and the downstream length is  $l_2 = 50 \cdot R_2$ . The downstream channel height is chosen to be  $R_2 = 0.0020604$  m. Simulations are performed on four different meshes. The specifications are listed in Table 5.1. A detailed view of the contraction area is shown in Fig. 5.7.

**Table 5.1:** Details of the meshes used for the axisymmetric 4:1 contraction.

	$N_{CV_s}$	$\Delta x_{min}/R_2$	$\Delta y_{min}/R_2$
M1	5100	0.024	0.035
M2	8133	0.019	0.028
M3	12796	0.015	0.022
M4	19692	0.012	0.018

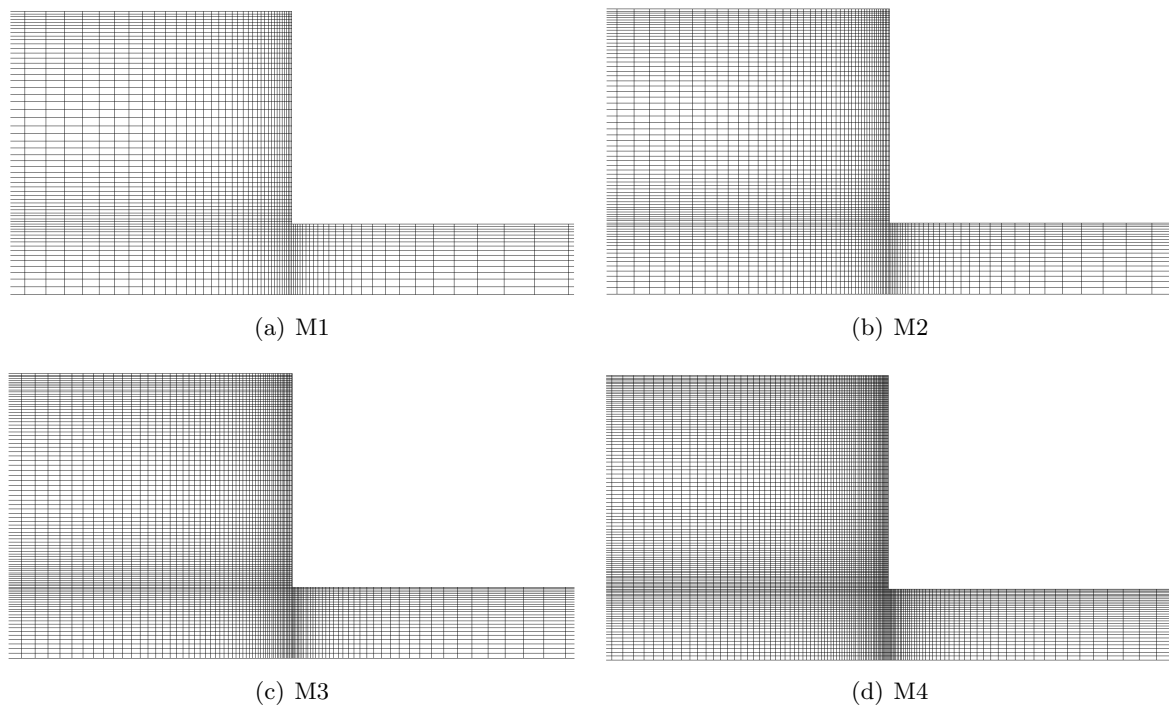


**Figure 5.7:** Detailed view of the contraction area from  $z = -R_1$  to  $z = +R_1$  for the various meshes.

The boundary conditions are similar to the Poiseuille flow, except that a rotational symmetry is used normal to the  $rz$ -plane. The Reynolds number  $Re$  for this case is in terms of the downstream section variables

$$Re = \frac{\rho R_2 \bar{U}_{z,2}}{\eta_0}$$

where  $\bar{U}_{z,2}$  is the mean velocity in axial direction in the downstream channel. A parabolic velocity profile is assigned at the inlet at  $\bar{U}_{z,1} = 0.00129$  m/s. The density is  $\rho = 921$  kg/m<sup>3</sup> and the total viscosity is  $\eta_0 = 10^4$  kg/ms. This results in a  $Re = 3.9 \cdot 10^{-6}$  corresponding to creeping flow conditions. The retardation ratio is set to  $\beta = 19/20$ , thus assuming the solvent contribution to be negligibly small, which approximately recovers an UCM model. This is in agreement with Baaijens [22], who concluded that a small portion of solvent viscosity does not



affect the asymptotical behavior near the re-entrant corner, in which we are also interested in this study.

The Deborah number  $De$

$$De = \frac{\lambda \bar{U}_{z,2}}{R_2}$$

will be varied by varying the relaxation time  $\lambda$  to give  $De = 0, 1, 2, 3, 5, 10$ . The temperature at the upstream wall ( $z < l_1$ ) is  $T_{w,1} = 462\text{K}$ , while for the downstream wall ( $z \geq l_1$ ) the temperature  $T_{w,2}$  is chosen such as to give temperature jumps of  $\Delta T = -30\text{K}, -10\text{K}, 0\text{K}, 10\text{K}, 30\text{K}$ . The Peclet number  $Pe$

$$Pe = \frac{\rho R_2 \bar{U}_{z,2} c_P}{k}$$

is kept constant in the non-isothermal simulations at  $Pe = 345$  by setting  $c_P = 1500\text{J/kgK}$  and  $k = 0.17\text{W/mK}$ . The WLF parameters are  $C_1 = 4.54$  and  $C_2 = 150.36\text{K}$ . The split coefficient is varied between pure energy elasticity and entropy elasticity  $\alpha = 0, 1$ .

Results are presented in terms of dimensionless variables. The velocities are normalized with  $\bar{U}_{z,2}$  and the stresses with  $\eta_0 \bar{U}_{z,2}/R_2$

$$\begin{aligned} \tilde{\mathbf{U}}_k &= \frac{\mathbf{U}_k}{\bar{U}_{z,2}} \\ \tilde{\tau}_{P,kl} &= \frac{\tau_{P,kl} R_2}{\eta_0 \bar{U}_{z,2}} \end{aligned}$$

where  $k$  and  $l$  denote the directions, respectively. The energy source-term in its dimensionless form is

$$\tilde{Q} = \frac{QR_2^2}{\eta_0 \bar{U}_{z,2}^2}$$

and the dimensionless vortex length is

$$\chi = \frac{L_R}{2R_1}$$

### Stability of the extrapolation method

Simulations were performed for both the extrapolation method and the zero gradient method for stress. It was found that the zero gradient method was stable and convergent for all Deborah numbers considered in this work (up to  $De = 10$ ). When using the extrapolation method, stable and convergent simulations could be performed only up to a Deborah number of  $De = 5$ . From  $De > 6$  no convergence could be achieved up to the specified tolerances

and the flow became unsteady. It is worth noting that from this point on, the positive-definiteness of the conformation tensor  $\mathbf{c}$  was also violated. This property was examined by checking  $\det(\mathbf{c}) \geq 1$ . [23] Since the positive-definiteness is necessary in view of a well-posed constitutive equation, this violation is supposedly the reason for the loss of convergence. In critical regions (here the re-entrant corner) the stress shows exponential profiles and using the extrapolation method, the exponential profiles are linearly extrapolated onto the wall. We suppose that the extrapolation sharpens these profiles leading to more pronounced profiles, which in turn cause the loss of positive-definiteness. The isolines of  $\det(\mathbf{c})$  at  $De = 6$  shown in Fig. 5.8 support this assumption. It can be seen that the minimum of  $\det(\mathbf{c})$  occurs few cells downstream of the re-entrant corner. In this region, there is also the maximum of  $\tau_{P,xx}$  and the minimum of  $\tau_{P,yy}$  as well as the largest gradients of them. On the other hand, it was found that with the zero gradient method the positive-definiteness was ensured for all Deborah numbers. The zero gradient method even does not seem to be limited by  $De = 10$  and higher Deborah number can be attained, similar as with the code of Wachs and Clermont. [6] It can be concluded that although having a higher accuracy, the extrapolation method is less stable at higher Deborah numbers. In view of that, we performed subsequent simulations up to  $De = 5$  with the extrapolation method due to its higher accuracy and from  $De = 6$  on with the zero gradient method.

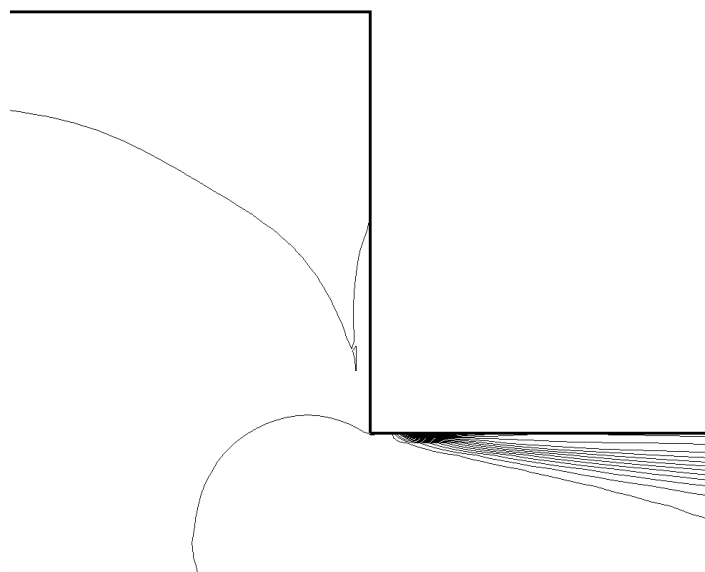


**Figure 5.8:** Isolines of  $\det(\mathbf{c})$  at  $De = 6$  using mesh M1. 20 isolines are equally distributed between  $\det(\mathbf{c})_{min} = -340$  and  $\det(\mathbf{c})_{min} = 0.999$ .

### Isothermal analysis

In Fig. 5.9 the profiles of the axial velocity and the axial normal stress at the line of symmetry are shown. For Newtonian flow ( $De = 0$ ), there is no overshoot in the velocity. The axial normal stress has its maximum at the contraction and rapidly decreases downstream. Mesh independent results are already obtained for M1. When adding elasticity, an overshoot in the

5 Development of a methodology for numerical simulation of non-isothermal viscoelastic fluid flows with application to axisymmetric 4:1 contraction flows

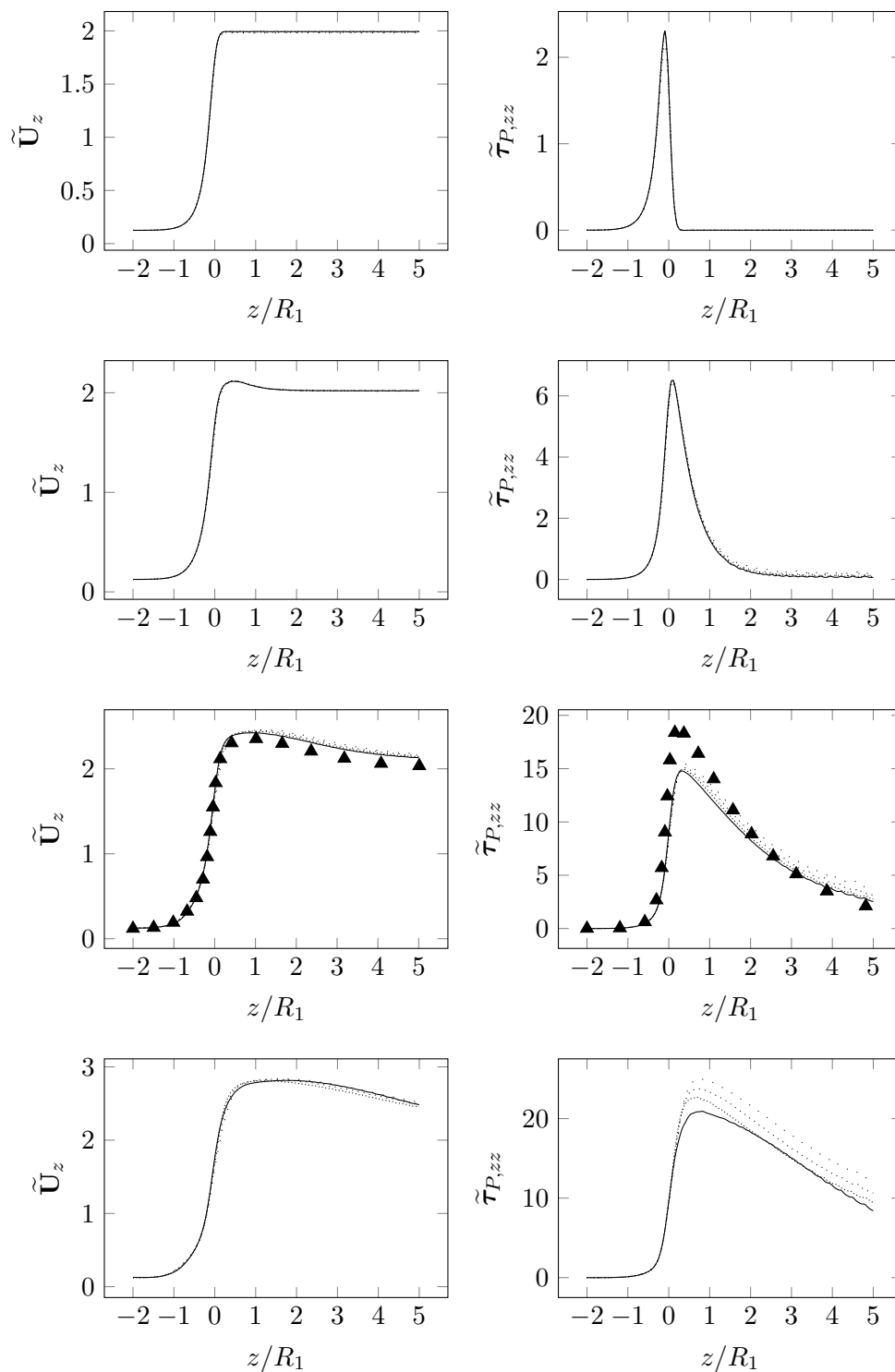


**Figure 5.9:** Axial velocity  $\tilde{U}_z$  and normal stress  $\tilde{\tau}_{P,zz}$  as a function of the axial position at the centerline  $r/R_2 = 0$  for the isothermal case for different Deborah numbers and meshes.  $De = 0, 1, 5, 10$  from top to bottom. (·····): M1, (-·-·-·): M2, (- - - -): M3, (—): M4, (▲): results of Wachs and Clermont [6] at  $De = 5$ .

velocity is found shortly after the contraction ( $De = 1$ ). The maximum axial normal stress is higher and does not decrease as rapidly as in the Newtonian case. Mesh convergence is again achieved with mesh M1. For  $De = 5$  and  $De = 10$ , these effects become more distinct. The velocity overshoot increases and decreases much slower in the downstream channel for increasing Deborah numbers. The maximum of the normal stress is increasing and shifted downstream. The decrease of the normal stress is much slower and almost becomes linear for  $De = 10$ . The results for  $De = 5$  are in agreement with the results of Wachs and Clermont [6], however, our maximum of the normal stress is somewhat smaller, while the velocity in the downstream channel is slightly larger. At  $De = 10$ , the normal stress becomes severely mesh dependent with the maximum decreasing with increasing mesh refinement. The velocity, although being not as mesh dependent as the normal stress, slightly decreases with mesh refinement.

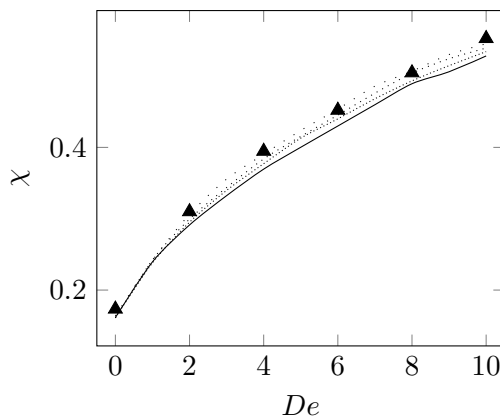


**Figure 5.10:** Dimensionless vortex length  $\chi$  as a function of the Deborah number  $De$  for the isothermal case for various meshes. (· · ·): M1, (- · - · -): M2, (- - -): M3, (—): M4, (▲): results of Wachs and Clermont [6] using their finest mesh.

The influence of the Deborah number on the dimensionless vortex length  $\chi$  is shown in Fig. 5.10. For Newtonian flow, we closely resemble a value of  $\chi_{De=0} \approx 0.17$ . The vortex length is monotonically increasing with the Deborah number. However, at higher Deborah numbers the vortex length grows slower and the increase becomes almost linear from  $De = 8$  on. When comparing our results with the results of Wachs and Clermont [6], we find that the vortex length predicted with mesh M1 closely resembles the results of Wachs and Clermont using their finest mesh. However, with increasing mesh refinement, we find the dimensionless vortex length to still decrease slightly. This effect is more pronounced at higher Deborah numbers.

Fig. 5.9 and 5.10 indicate that with increasing Deborah numbers the results become more mesh dependent. The main reason is that with increasing elasticity, the convected derivative term in the constitutive equation becomes increasingly dominant in the proximity of the re-entrant corner. Since the convection term therein is discretized with the first-order upwind scheme the accuracy decreases with increasing elasticity and thus higher-order schemes have

to be considered in order to avoid the use of too refined meshes, which would result in very high computational costs. The effect of the high-order CUBISTA scheme [24] will be discussed in a subsequent work.

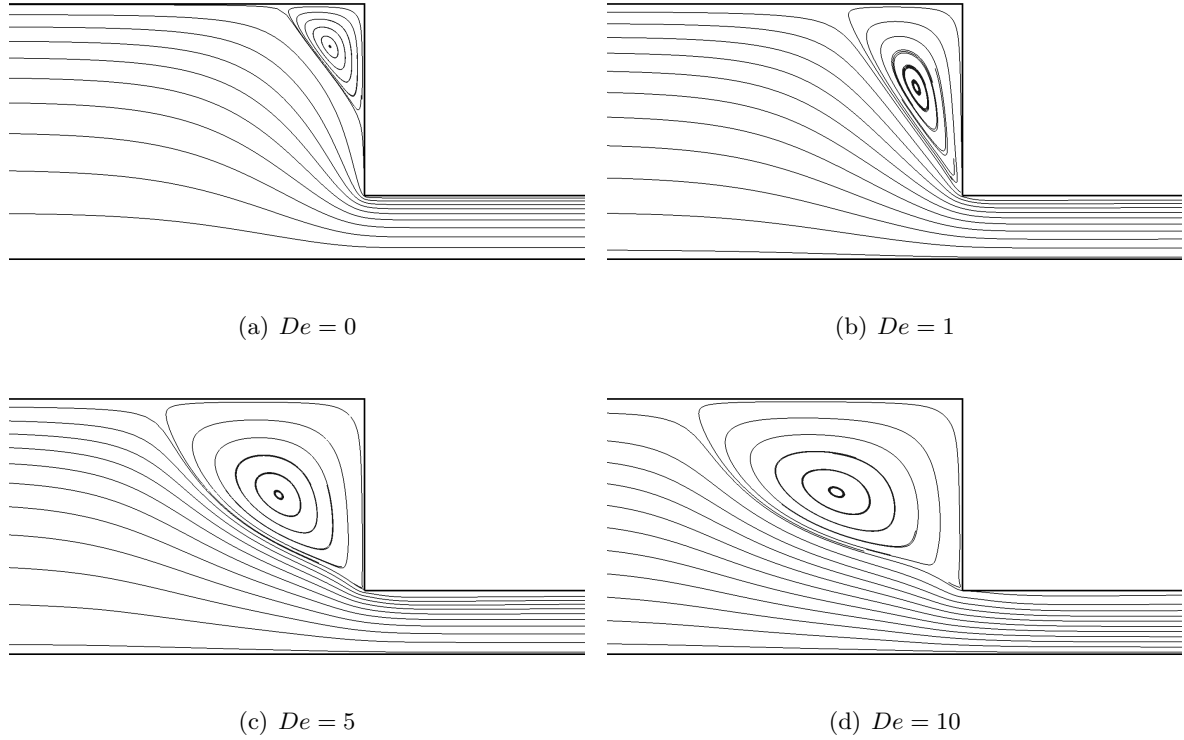


**Figure 5.11:** Streamlines for  $De = 0, 1, 5, 10$  for the isothermal case using mesh M4.

Fig. 5.11 shows the streamlines for four different Deborah numbers. Initially for  $De = 0$ , the vortex is solely at the salient corner. From  $De = 1$  on, the vortex connects with the re-entrant corner. A lip vortex cannot be observed. From  $De = 1$  on, the convexity and the length of the vortex is considerably increasing.

Dean and Montagnon [25] and Moffatt [26] provide the asymptotical flow behavior near the re-entrant corner for Newtonian fluids as

$$\begin{aligned}\tilde{\mathbf{U}}_k &\propto \xi^{0.545} \\ \tilde{\boldsymbol{\tau}}_{P,kl} &\propto \xi^{-0.455}\end{aligned}$$

Considering an Oldroyd-B fluid, Hinch [27] found different slopes than for Newtonian flows

$$\begin{aligned}\tilde{\mathbf{U}}_k &\propto \xi^{5/9} \\ \tilde{\boldsymbol{\tau}}_{P,kl} &\propto \xi^{-2/3}\end{aligned}$$

5 Development of a methodology for numerical simulation of non-isothermal viscoelastic fluid flows with application to axisymmetric 4:1 contraction flows

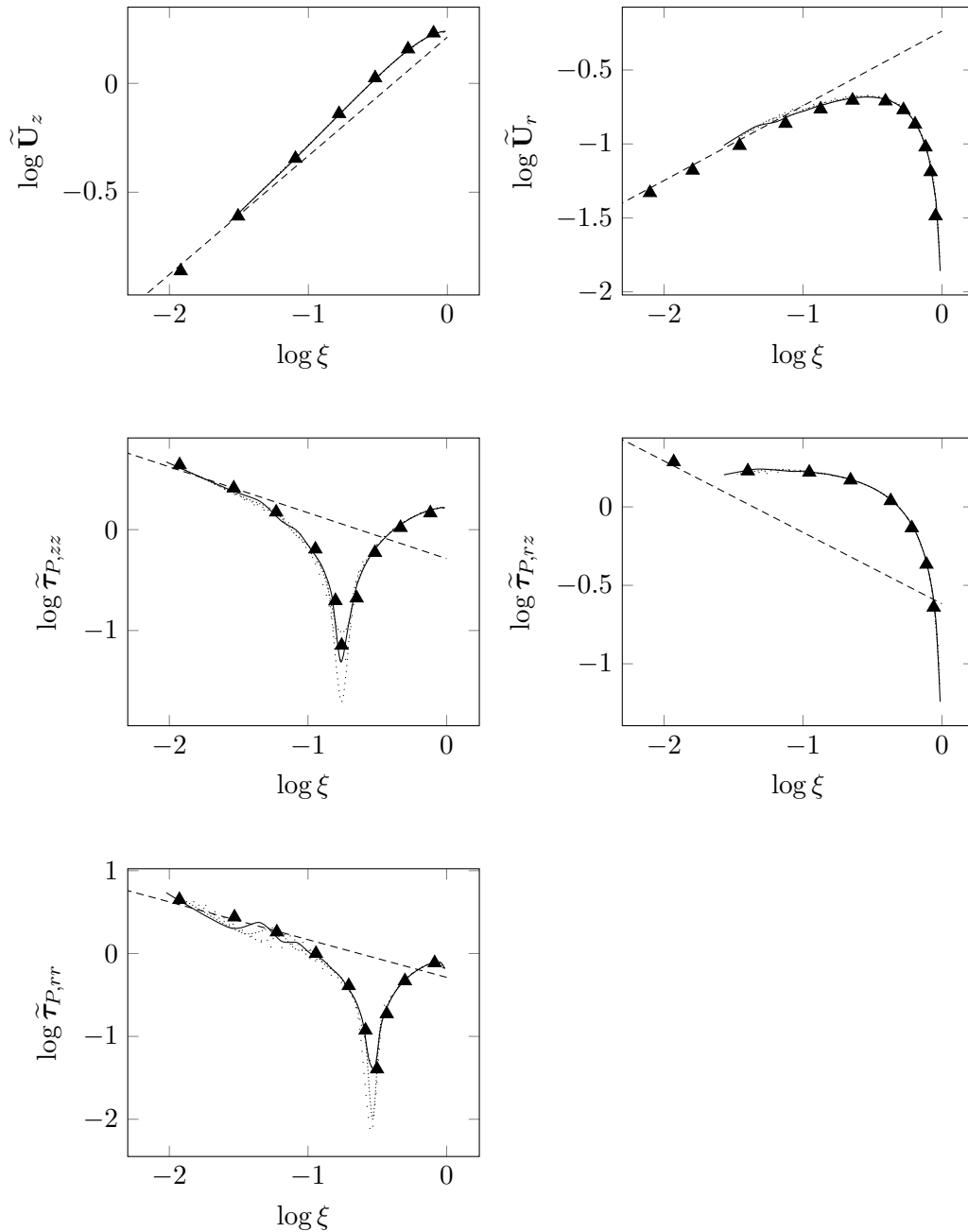


**Figure 5.12:** Normalized velocities and stresses as a function of the distance  $\xi$  for isothermal viscoelastic flow at  $De = 0$  using various meshes. (· · ·): M1, (— · — ·): M2, (— · — · — ·): M3, (—): M4, (▲): results of Wachs and Clermont [6], (----): Newtonian asymptotes [25, 26].

5 Development of a methodology for numerical simulation of non-isothermal viscoelastic fluid flows with application to axisymmetric 4:1 contraction flows

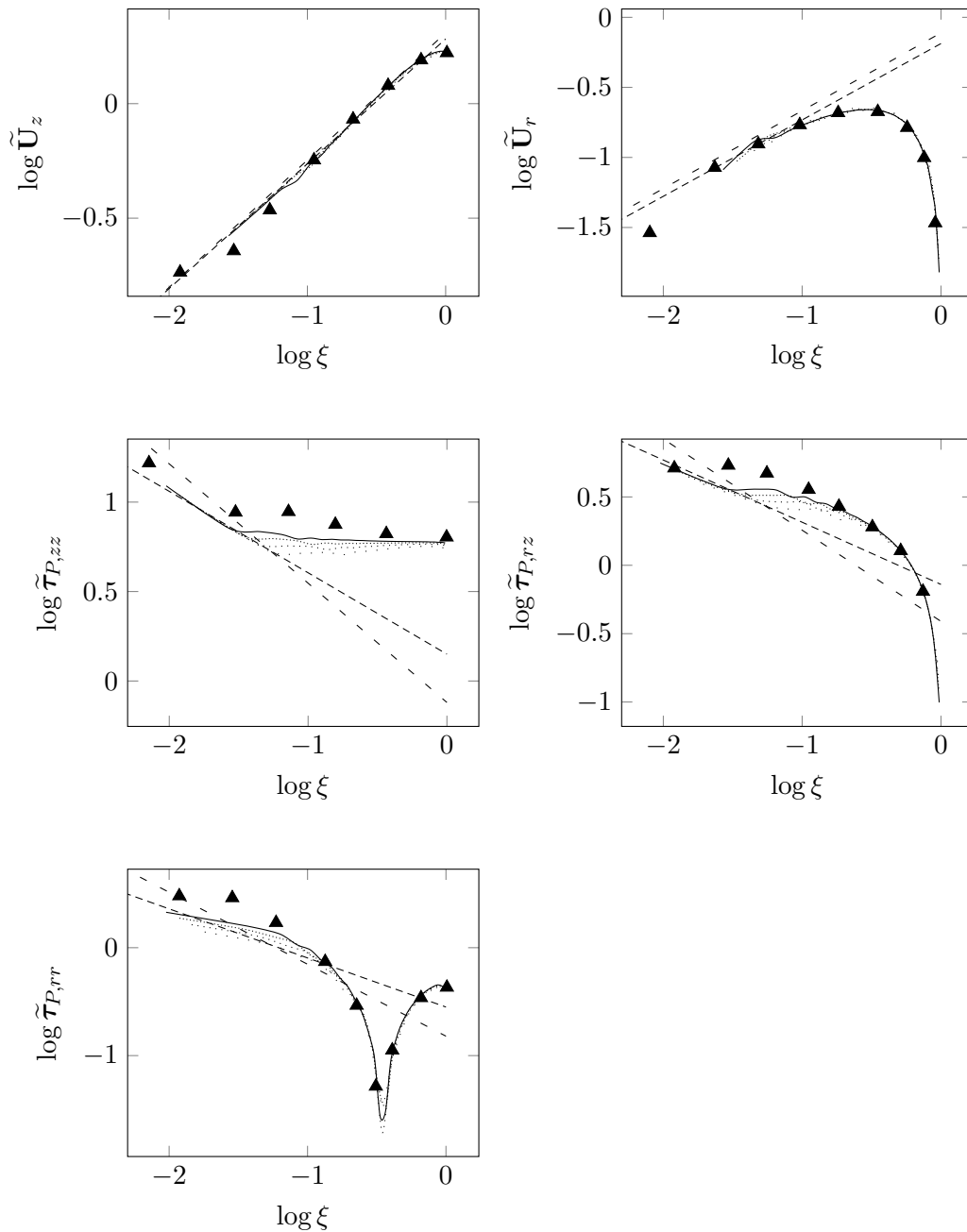


**Figure 5.13:** Normalized velocities and stresses as a function of the distance  $\xi$  for isothermal viscoelastic flow at  $De = 1$  using various meshes.

( $\cdots$ ): M1, ( $\cdots\cdots$ ): M2, ( $\cdots\cdots\cdots$ ): M3, ( $\text{---}$ ): M4, ( $\blacktriangle$ ): results of Wachs and Clermont [6], ( $\text{---}$ ): Newtonian asymptotes [25, 26], ( $\text{- -}$ ): viscoelastic asymptotes [27].

5 Development of a methodology for numerical simulation of non-isothermal viscoelastic fluid flows with application to axisymmetric 4:1 contraction flows

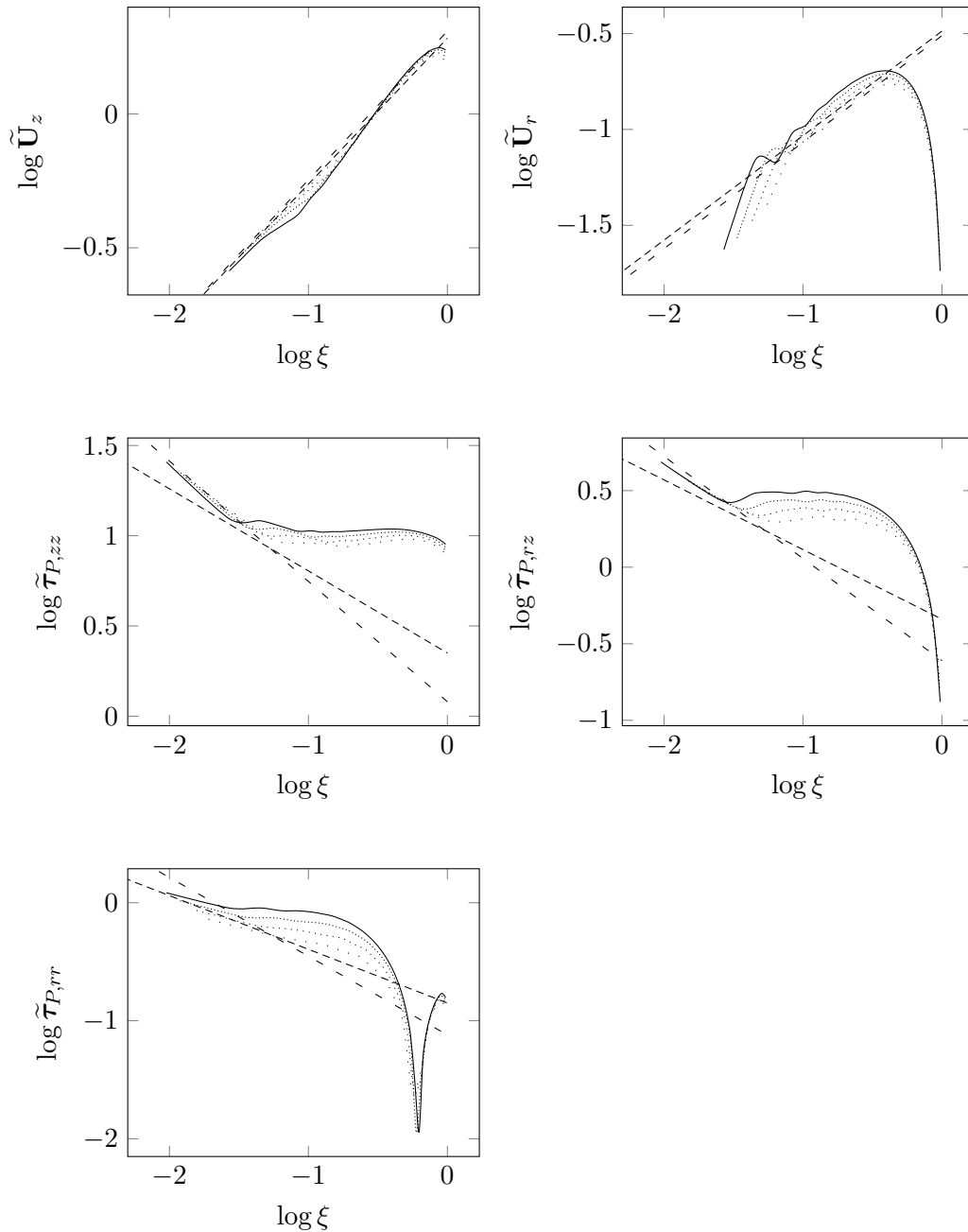


**Figure 5.14:** Normalized velocities and stresses as a function of the distance  $\xi$  for isothermal viscoelastic flow at  $De = 5$  using various meshes. (· · ·): M1, (· · · ·): M2, (· · · · ·): M3, (—): M4, (---): Newtonian asymptotes [25, 26], (- · -): viscoelastic asymptotes [27].



In Fig. 5.12 the results are shown for  $De = 0$  together with the asymptotes outlined above and the numerical results of Wachs and Clermont [6] using their finest mesh. In general an acceptable agreement is found for velocities and stresses with both the asymptotes outlined above and the results of Wachs and Clermont [6], except for the shear stress  $\tilde{\tau}_{P,rz}$ . However, the results of Wachs and Clermont [6] indicate, that for the shear stress the slope is obtained with their two cells next to the re-entrant corner. Since our smallest cell is somewhat larger, this slope cannot be reproduced. However, at larger distances from the re-entrant corner, our results almost perfectly match the results of Wachs and Clermont [6]. The results for  $De = 1$  are shown in Fig. 5.13. Our results again show an asymptotical behavior. Mesh convergence is achieved with the four meshes used in this study. The slopes, however, more likely coincide with the Newtonian asymptotes, rather than the viscoelastic asymptotes. Close to the re-entrant corner, our results perceptibly deviate from the results of Wachs and Clermont [6]. At higher levels of elasticity, here  $De = 5$ , we find the axial normal stress and shear stress to almost perfectly show the behavior of the viscoelastic asymptotes of Hinch [27], see Fig. 5.14. However, the radial normal stress still resembles the Newtonian asymptote. The axial velocity again shows an asymptotical behavior close to the Newtonian and viscoelastic asymptotes, while the radial velocity component severely deviates from that behavior. At  $De = 5$ , the results at the re-entrant corner for both velocity and stress components become more mesh dependent than for  $De = 1$ .

### Non-isothermal analysis

In this section, we present the results for the non-isothermal flow simulations. Simulations were performed for  $De = 1, 5$  and  $\alpha = 0, 1$  with all four meshes.

In Fig. 5.15, the axial profiles of the temperature, axial normal stress and velocity close to the contraction are shown. Mesh convergence is achieved for the temperature for all four meshes and in both cases of energy elasticity ( $\alpha = 0$ ) and entropy elasticity ( $\alpha = 1$ ). Shortly before the contraction, the temperature increases owing to the increased deformation close to the contraction and the resulting dissipation. In the case of entropy elasticity, where all energy is dissipated as heat, the temperature is found to be higher throughout the profile compared to the case of energy elasticity, where more amount of energy is stored. At the contraction, the fluid comes close to the wall with the specified temperature of  $T_{w,2} = 462$  K and thus the temperature rapidly decreases due to heat conduction towards the wall. The decrease is more distinct for entropy elasticity due to its higher temperature and the thereby larger heat conduction rate. Shortly after the re-entrant corner, the temperature again rapidly increases since the maxima of the normal stresses are present in this area resulting in a large amount of dissipation. The increase in temperature is not as high in the energy elasticity case as more energy is stored. Further down in the downstream channel the temperatures still increase, although with the rates decreasing. Also the difference in the temperatures becomes smaller further away from the re-entrant corner as now more energy is released for the purely energetic fluid flow ( $\alpha = 0$ ). When considering the axial normal stress profiles,

5 Development of a methodology for numerical simulation of non-isothermal viscoelastic fluid flows with application to axisymmetric 4:1 contraction flows

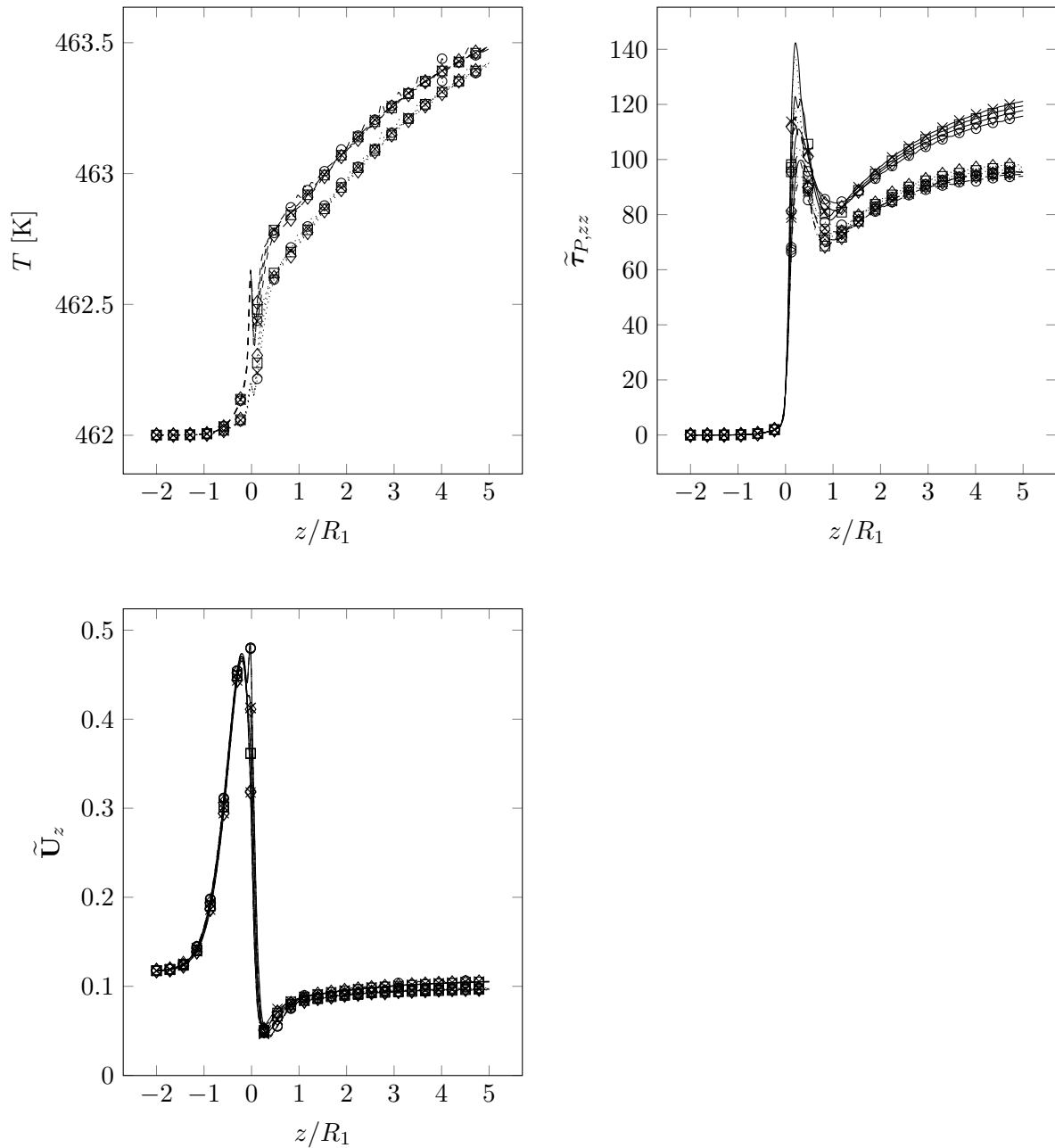


**Figure 5.15:** Temperature  $T$ , axial normal stress  $\tilde{\tau}_{P,zz}$  and velocity  $\tilde{U}_z$  as a function of the axial position on the line  $r = 0.97R_2$  for different values of  $\alpha$  at  $De = 5$  and  $\Delta T = 0K$  using various meshes. (—): isothermal case, (---):  $\alpha = 1$ , (⋯):  $\alpha = 0$ . (○): M1, (×): M2, (□): M3, (◇): M4.

we find that the stresses are smaller in the non-isothermal case compared to the isothermal case. The reason for that is the increase in temperature and the resulting smaller viscosity due to the temperature-dependent viscosity (WLF-relation). Further, the relaxation time also decreases with increasing temperature resulting in a smaller local Deborah number when comparing to the isothermal case. We find that the normal stresses are very dependent upon mesh resolution with the maxima perceivably decreasing with mesh refinement. The effect is more pronounced in the isothermal case, which can be attributed to the higher local Deborah number. We find the normal stresses of the case of  $\alpha = 0$  are more close to the isothermal case, since the temperatures in the purely energetic case are generally lower and thus the local viscosities and relaxation times come closer to the isothermal case. When considering the axial velocity, we find that there is almost no influence of the temperature on the local velocity profile and both cases of entropy elasticity and energy elasticity closely resemble the axial velocity of the isothermal case. However, differences are to be expected at higher Deborah numbers. When comparing the axial normal stress to the results of Wachs and Clermont [6], we find that the profile is qualitatively the same, however, the maxima in our simulations are smaller by approximately a factor of three.

In Fig. 5.16 the axial profiles of the dimensionless energy source term and the temperature on a line further away from the re-entrant corner are shown. The energy source term upstream of the re-entrant corner is larger for the purely entropic case ( $\alpha = 1$ ). At the contraction, the source term rapidly decreases and shortly after that increases again due to the local stress profile for  $\alpha = 1$ . These two distinct peaks are not present in the purely energetic case ( $\alpha = 0$ ), for which the energy source term monotonically increases. The energy source term is larger for  $z/R_1 \leq 1.5$  for the case of  $\alpha = 1$  showing that more energy is dissipated as heat in this region compared to the case of  $\alpha = 0$ . Further downstream, the energy sources approach a same level, although the energy source in the purely elastic case being slightly larger since more energy is released here. Mesh convergence is again achieved for all four meshes. When comparing to the results of Wachs and Clermont [6], we find that although qualitatively showing similar effects, their profile for  $\alpha = 1$  shows more pronounced peaks and the energy source terms are larger throughout the profile considered. This difference may be attributed to the use of the UCM model ( $\beta = 1$ ) in the studies of Wachs and Clermont [6]. When considering the corresponding temperature profiles, we again find the temperature to rapidly increase close to the re-entrant corner due to the high amount of dissipation owing to the high stresses in this region. The temperatures in the purely entropic case are again larger than the temperatures in the purely elastic case. However, the differences tend to decrease further downstream, since more energy is released as heat in this region for the purely elastic flow. Mesh convergence is again achieved for all meshes. The temperature profiles of Wachs and Clermont [6] show a steeper increase close to the contraction, although the temperature increase in the downstream channel being smaller and the value of the temperatures being smaller from  $z/R_1 \leq 2$ .

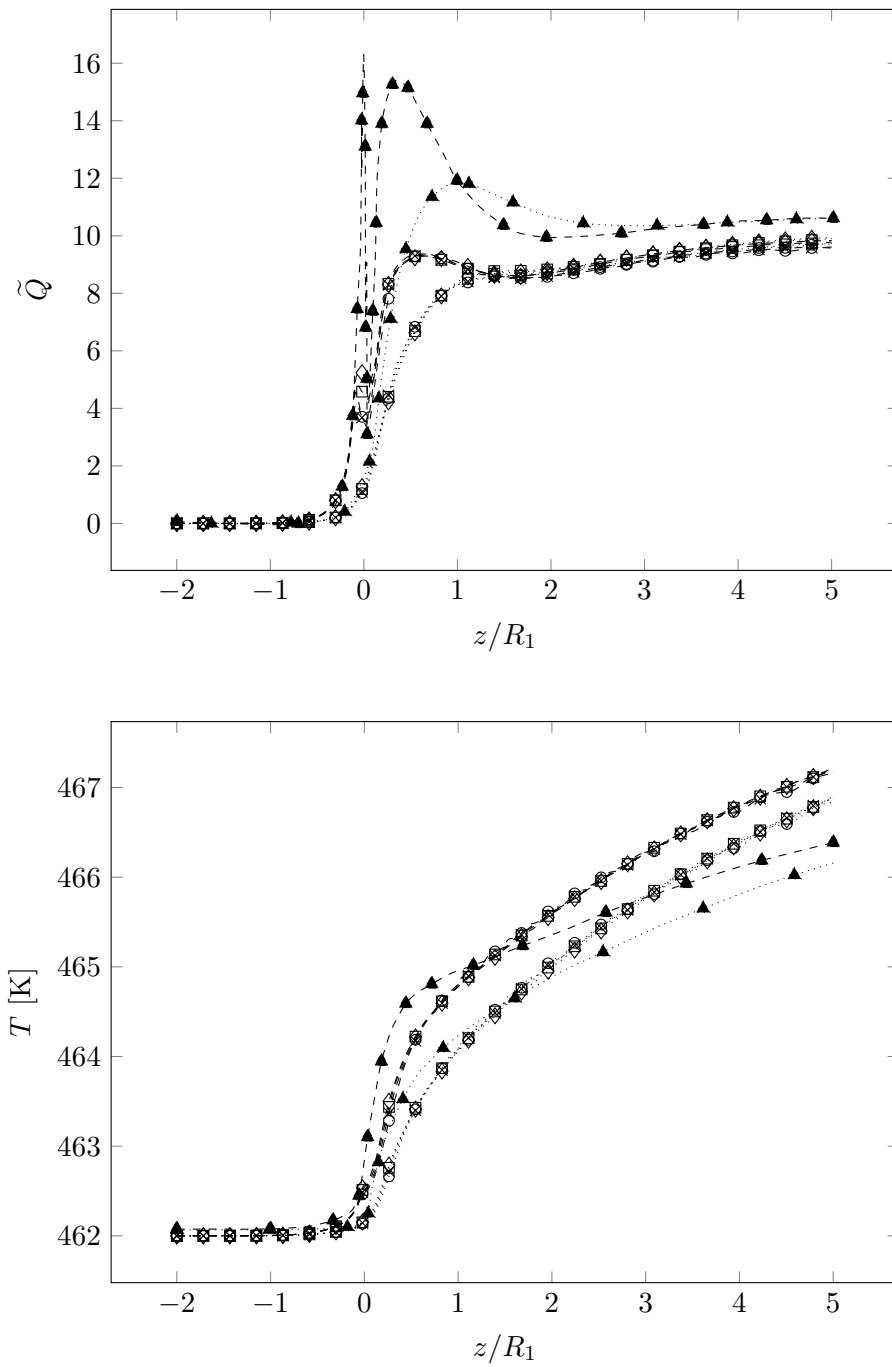


**Figure 5.16:** Dimensionless energy source term  $\tilde{Q}$  and temperature  $T$  as a function of the axial position on the line  $r = 0.87R_2$  for different values of  $\alpha$  at  $De = 5$  and  $\Delta T = 0K$  using various meshes.  
 (----):  $\alpha = 1$ , (.....):  $\alpha = 0$ .  
 (o): M1, (x): M2, (□): M3, (◇): M4, (▲): results of Wachs and Clermont [6].

Temperature differences are found to not result in a change of the kinematics at the considered level of elasticity. Therefore, simulations were also performed for temperature jumps at the contraction walls of  $\Delta T = -30$  K,  $-10$  K,  $0$  K,  $10$  K and  $30$  K. This is done also in view of considering the effect of external cooling and heating on the kinematics.

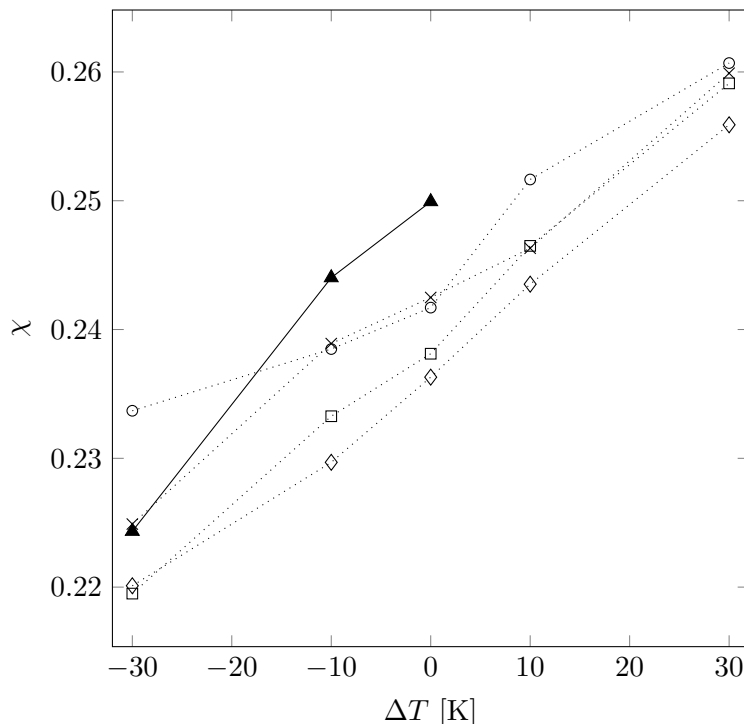


**Figure 5.17:** Dimensionless vortex length  $\chi$  as a function of the temperature jump  $\Delta T$  at  $De = 1$  and  $\alpha = 0$  for various meshes. (○): M1, (×): M2, (□): M3, (◇): M4, (▲): results of Wachs and Clermont [6] for  $\alpha = 1$ .

In Fig. 5.17 and 5.18 we present the dimensionless vortex length as a function of the temperature jump at  $De = 1$  and  $De = 5$ . In both cases we find the vortex length to almost linearly increase with increasing temperature jump. The results are still dependent upon the mesh, although the absolute values vary in the same range as in the isothermal case (c.f. Fig. 5.10). Although still mesh dependent, the tendency of increasing vortex length with increasing temperature jump is clearly present for all four meshes. The increase may be attributed to the increase in the viscosity. [6] We find that for  $De = 1$  our results quantitatively match the results of Wachs and Clermont [6], however, at  $De = 5$ , they obtained a decreasing vortex length with increasing temperature jumps (although only considering external cooling), which was attributed to the increasing elastic effects, which become stronger than the influence of the increasing viscosity. However, this effect is not present in our study, which may partly be attributed to the use of the Oldroyd-B model. Almost no differences for the vortex length are found when comparing the isothermal case (c.f. Fig. 5.10) and the non-isothermal case ( $\Delta T = 0$  K, c.f. Fig. 5.17 and 5.18) for both  $De = 1$  and  $De = 5$ , which again shows that temperature effects (without considering external heating or cooling) have no influence on the kinematics of the flow at this level of elasticity. Furthermore, for  $De = 5$  it is shown that the energy conversion mechanism ( $\alpha = 0$  or  $\alpha = 1$ ) has no influence on the

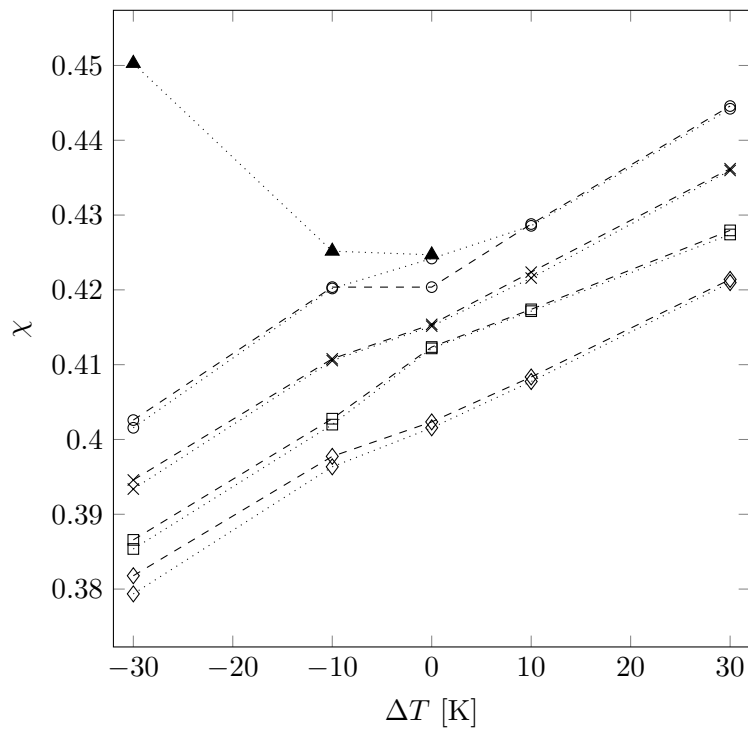


**Figure 5.18:** Dimensionless vortex length  $\chi$  as a function of the temperature jump  $\Delta T$  and  $\alpha$  at  $De = 5$  for various meshes.  
 (---):  $\alpha = 1$ , (····):  $\alpha = 0$ .  
 (○): M1, (×): M2, (□): M3, (◇): M4, (▲): results of Wachs and Clermont [6] for  $\alpha = 1$ .

dimensionless vortex length even when considering temperature jumps. Again, differences are expected only for higher Deborah numbers.

5 Development of a methodology for numerical simulation of non-isothermal viscoelastic fluid flows with application to axisymmetric 4:1 contraction flows

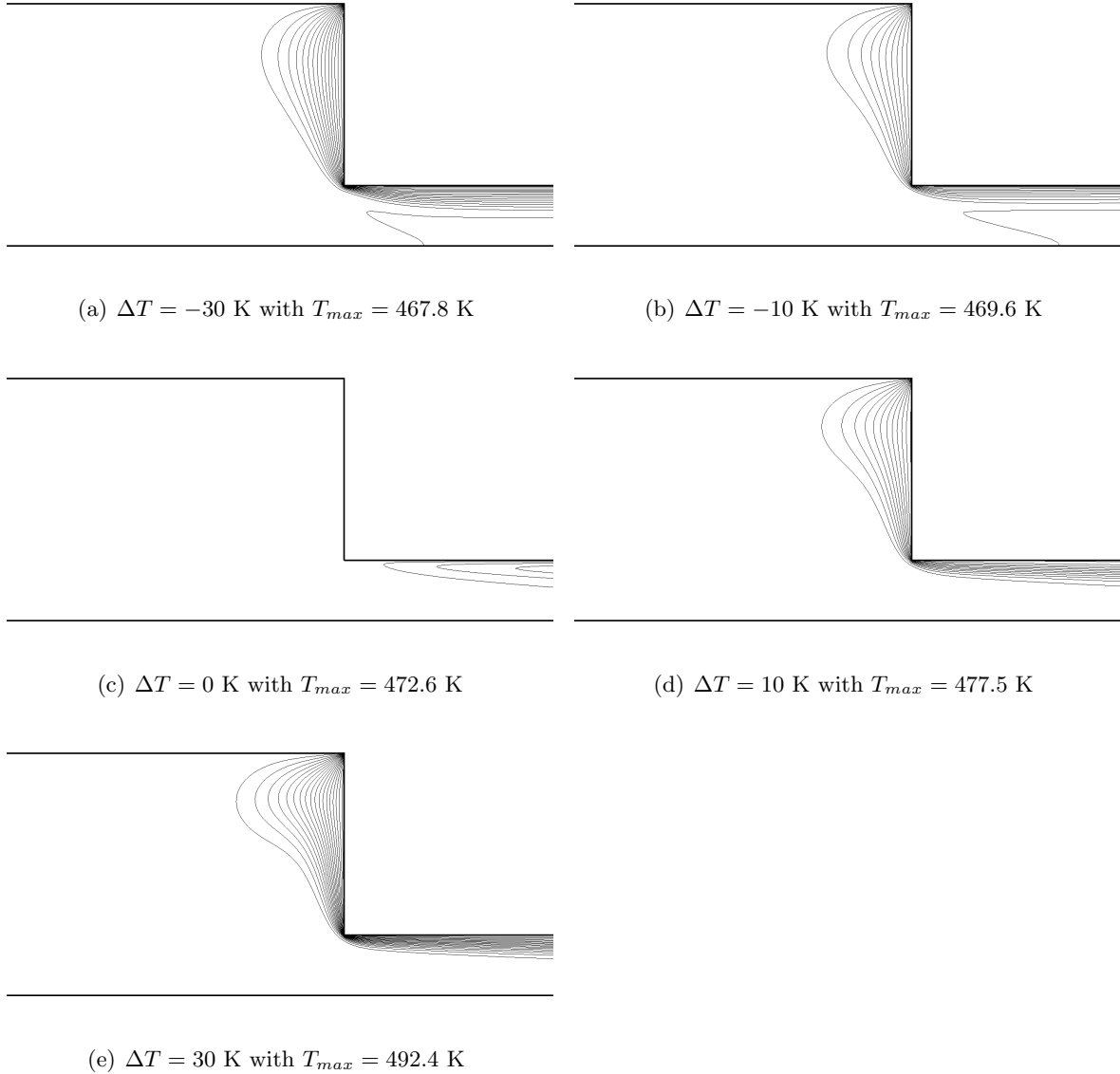


**Figure 5.19:** Temperature isolines for different temperature jumps  $\Delta T$  at  $De = 5$  and  $\alpha = 0$  using mesh M4. 20 isolines are equally distributed between  $\Delta T_{min} = 462K + \Delta T$  and  $T_{max}$ .

In Fig. 5.19 we present the temperature isolines for the five temperature jumps considered using the finest mesh at  $De = 5$ . The isolines for  $\Delta T = 0$  K show that the upstream region is not affected in the non-isothermal case, which is why no differences are found when comparing to the isothermal cases. Further, one finds that the isolines are shifted further away from the contraction wall for  $\Delta T = -30$  K and  $\Delta T = 30$  K when comparing to  $\Delta T = -10$  K and  $\Delta T = 10$  K thus affecting a larger region. The corresponding streamlines are shown in Fig. 5.20. It can be seen that the overall shape of the vortex is retained for the different temperature jumps and only the vortex length varies for different temperature jumps.

The energy source term, temperature and axial velocity profiles at the outlet of the downstream section are shown in Fig. 5.21 for  $De = 5$  and  $\alpha = 0, 1$  using the finest mesh M4.

5 Development of a methodology for numerical simulation of non-isothermal viscoelastic fluid flows with application to axisymmetric 4:1 contraction flows

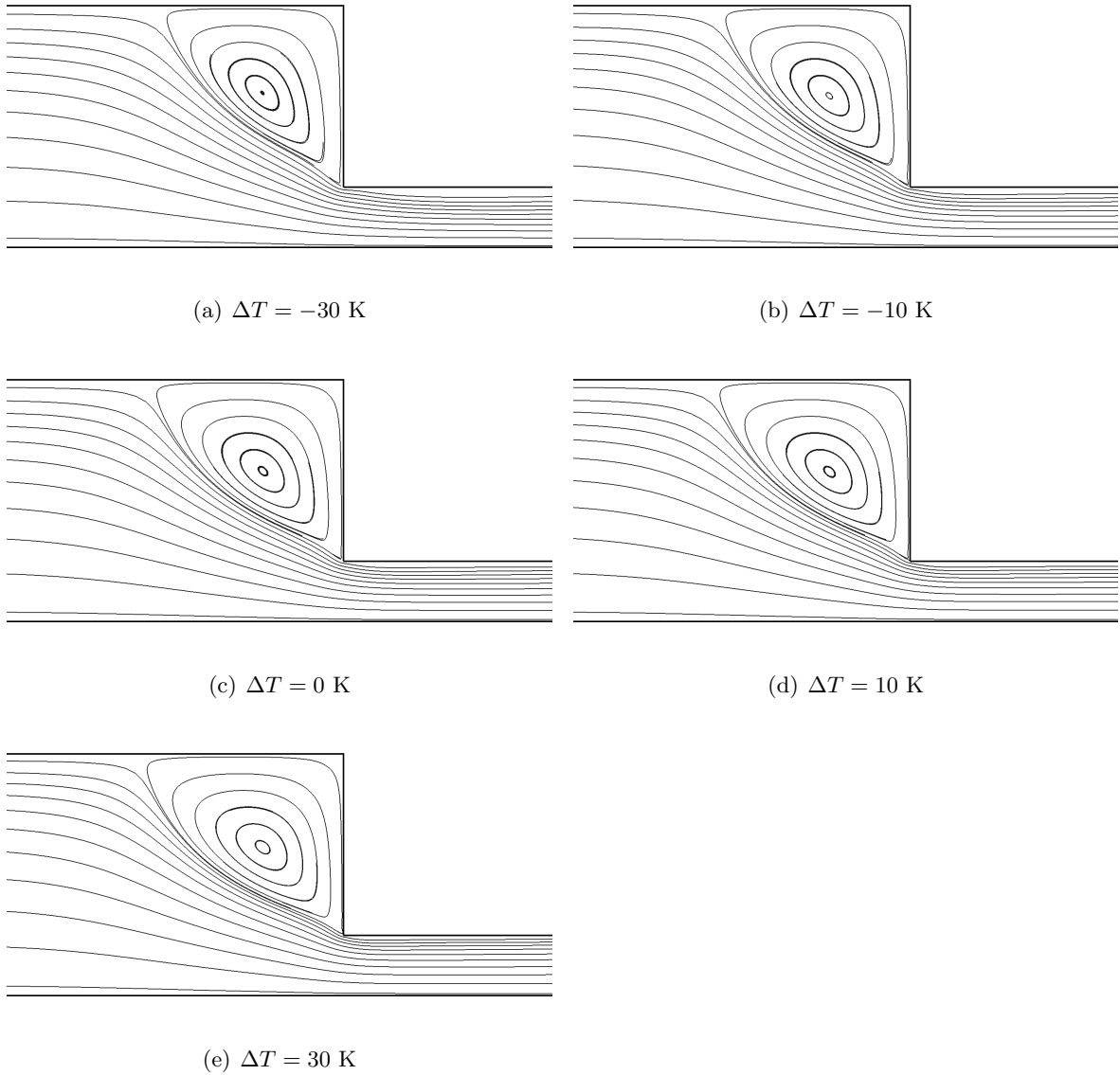


**Figure 5.20:** Streamlines for different temperature jumps  $\Delta T$  at  $De = 5$  and  $\alpha = 0$  using mesh M4.



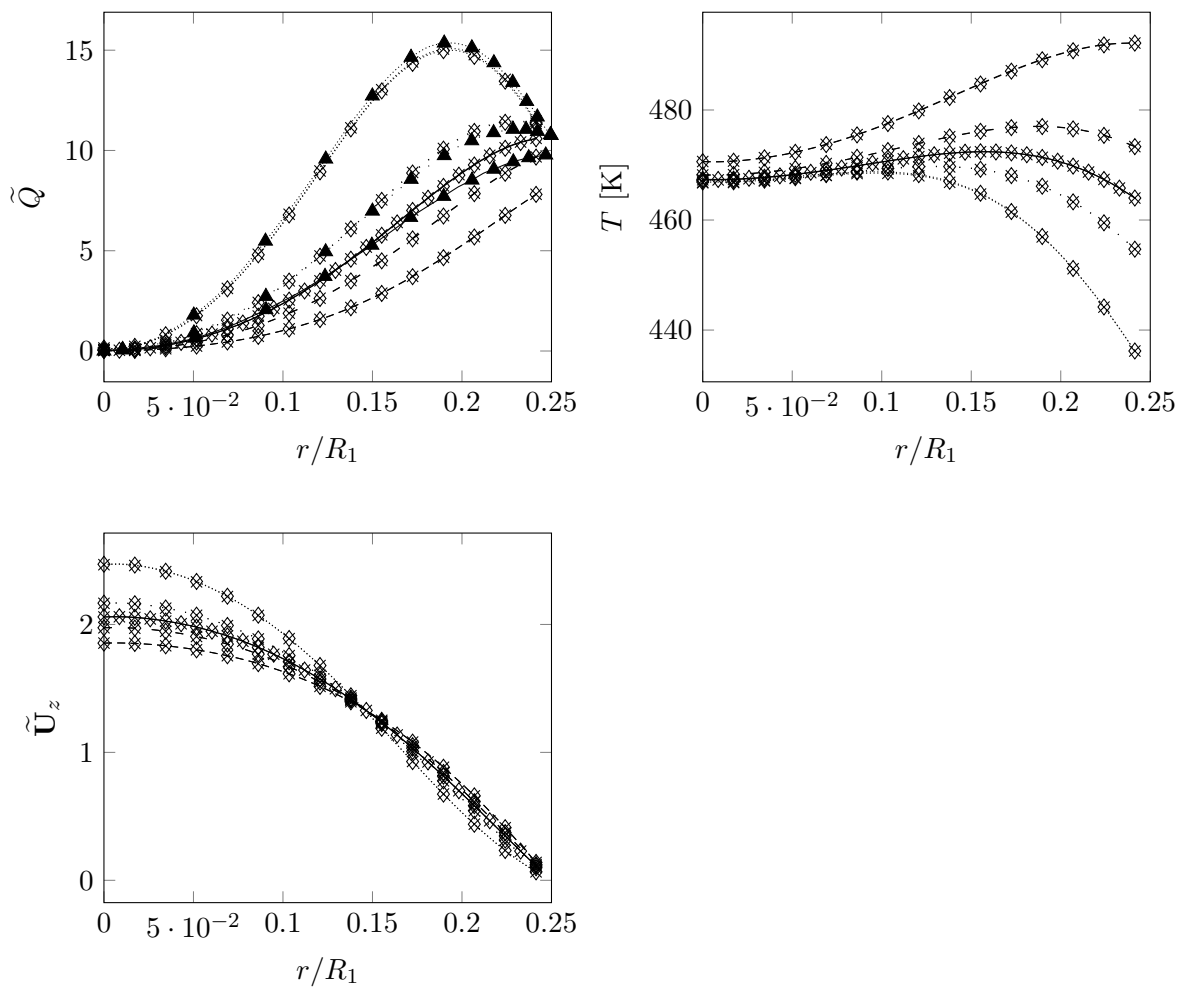


**Figure 5.21:** Axial velocity  $\tilde{U}_z$ , temperature  $T$  and dimensionless energy source term  $\tilde{Q}$  as a function of the radial distance at the outlet for different temperature jumps and values of  $\alpha$  for  $De = 5$  using mesh M4.  
 ( $\times$ ):  $\alpha = 1$ , ( $\diamond$ ):  $\alpha = 0$ , ( $\blacktriangle$ ): results of Wachs and Clermont [6] for  $\alpha = 1$ .  
 (---):  $\Delta T = 30\text{K}$ , (- -):  $\Delta T = 10\text{K}$ , (—):  $\Delta T = 0\text{K}$ , (···):  $\Delta T = -10\text{K}$ ,  
 (·····):  $\Delta T = -30\text{K}$ .

The energy source term is large for external cooling and increasing towards the wall due to the decrease of the temperature in that direction, which results in a larger viscosity in the wall-near region. With increasing temperature jumps the energy source term decreases due to the smaller viscosities, which are caused by the higher temperatures of the walls. When comparing to the results of Wachs and Clermont [6] we find the energy sources to agree with their results. Deviations are most distinct at  $\Delta T = 0$  K. However, in their studies a downstream channel of  $200 \cdot R_1$  is used in order to obtain a steady state. As can be seen from the temperatures, no steady state is obtained in our simulation ( $80 \cdot R_1$ ) and the differences in the energy source term may be caused by the differing temperature profiles. Although the wall temperature varying over 60 K at the wall, we find the temperatures at the centerline to only vary by 3.45 K from  $\Delta T = -30$  K to  $\Delta T = 30$  K, which also supports the difficulty in thermal control of the flow by external heating or cooling, which only has limited effect on the bulk of the flow. The velocity profiles show that with decreasing temperature jump the velocity at the centerline is increasing owing to the smaller viscosity in the wall near-region due to the lower temperature. Again we find that there is no difference between pure entropy elasticity and energy elasticity at the outlet of the downstream section for all temperature jumps considered (cf. Fig. 5.21).

## 5.4 Conclusion

In this work a new solution algorithm to solve non-isothermal viscoelastic fluid flows with a collocated finite volume method is developed and implemented in the freely available software *OpenFOAM*<sup>®</sup>. The thermorheological modeling technique employed in this work is based on the ideas of Peters and Baaijens [10], in which an a-priori defined split factor is used to determine the amounts of energy elasticity and entropy elasticity.

A new method for extrapolating stresses on solid walls is introduced for evaluating the stress divergence. The method is designed such as to be applicable to any nonorthogonal mesh, boundary shape and constitutive equation. A thorough validation proved its superiority regarding accuracy, however, we find the method to be less stable compared to the commonly employed zero gradient method at higher Deborah numbers.

The solution algorithm is applied to a 4:1 axisymmetric contraction for both isothermal and non-isothermal cases. Mesh convergence is attained and proved throughout the study as well as stable and convergent simulations can be performed up to a Deborah number of  $De = 10$ , although this does not seem to be the limiting value.

In the isothermal simulations the vortex is found to increase in size and is becoming more convex with increasing Deborah number. The asymptotical behavior at the re-entrant corner is compared to the asymptotical analyses of Dean and Montagnon [25], Moffatt [26] and Hinch [27] showing a generally acceptable agreement. Good agreement with the numerical

*5 Development of a methodology for numerical simulation of non-isothermal viscoelastic fluid flows with application to axisymmetric 4:1 contraction flows*

results of Wachs and Clermont [6] is mostly obtained. For non-isothermal simulations we find the temperature changes to be generally too small to result in a significant change in the kinematics at the considered level of elasticity. It is shown that the vortex length is increasing with increasing temperature jumps showing the effect of external heating or cooling on the upstream kinematics. This behavior is found for all Deborah number considered, contrary to the previous work of Wachs and Clermont [6]. The energy conversion mechanism is found to only influence local profiles of the temperature (and energy source term) close to regions of high stresses without affecting global kinematics, even for the simulations with temperature jumps.

## 5.A Literature

- [1] S.-C. Xue, N. Phan-Thien, R. I. Tanner, Three dimensional numerical simulations of viscoelastic flows through planar contractions, *J. Non-Newtonian Fluid Mech.* 74 (1998) 195–245.
- [2] J. M. Kim, C. Kim, J. H. Kim, C. Chung, K. H. Ahn, S. J. Lee, High-resolution finite element simulation of 4:1 planar contraction flow of viscoelastic fluid, *J. Non-Newtonian Fluid Mech.* 129 (2005) 23–37.
- [3] M. S. N. Oliveira, P. J. Oliveira, F. T. Pinho, M. A. Alves, Effect of contraction ratio upon viscoelastic flow in contractions: The axisymmetric case, *J. Non-Newtonian Fluid Mech.* 147 (2007) 92–108.
- [4] P. Wapperom, M. A. Hulsen, J. P. P. M. V. der Zanden, A numerical method for steady and non-isothermal viscoelastic fluid for high Deborah and Peclet numbers, *Rheol. Acta* 37 (1998) 73–88.
- [5] S. J. Park, S. J. Lee, On the use of the open boundary condition method in the numerical simulation of nonisothermal viscoelastic flow, *J. Non-Newtonian Fluid Mech.* 87 (1999) 197–214.
- [6] A. Wachs, J. R. Clermont, Non-isothermal viscoelastic flow computations in an axisymmetric contraction at high Weissenberg numbers by a finite volume method, *J. Non-Newtonian Fluid Mech.* 95 (2000) 147–184.
- [7] E. Peters, M. Hulsen, B. van den Brule, Instationary eulerian viscoelastic flow simulations using time separable rivlin-sawyers constitutive equations, *J. Non-Newtonian Fluid Mech.* 89 (2000) 209–228.
- [8] J. L. Favero, A. R. Secchi, N. S. M. Cardozo, H. Jasak, Viscoelastic flow simulation: Development of a methodology of analysis using the software openfoam and differential constitutive equations, *J. Non-Newtonian Fluid Mech.* 165 (2010) 1625–1636.
- [9] G. W. M. Peters, Thermorheological modelling of viscoelastic materials, in: *IUTAM Symposium on Non-Isothermal Flows of Viscoelastic Fluids*, Kluwer Academic Publishers, 1993.
- [10] G. W. M. Peters, F. P. T. Baaijens, Modelling of non-isothermal viscoelastic flows, *J. Non-Newtonian Fluid Mech.* 68 (1997) 205–224.
- [11] R. B. Bird, R. C. Armstrong, O. Hassager, *Dynamics of Polymeric Liquids*, Wiley, 1987.

*5 Development of a methodology for numerical simulation of non-isothermal viscoelastic fluid flows with application to axisymmetric 4:1 contraction flows*

- [12] P. Wapperom, M. A. Hulsen, Thermodynamics of viscoelastic fluids: The temperature equation, *J. Rheol.* 42 (1998) 999–1019.
- [13] M. Hütter, C. Luap, H. C. Öttinger, Energy elastic effects and the concept of temperature in flowing polymeric liquids, *Rheol. Acta* 48 (2009) 301–316.
- [14] J. D. Ferry, *Viscoelastic properties of polymers*, Wiley, New York, 1980.
- [15] R. Guénette, M. Fortin, A new mixed finite element method for computing viscoelastic flows, *J. Non-Newtonian Fluid Mech.* 60 (1995) 27–52.
- [16] S. V. Patankar, D. B. Spalding, A calculation procedure for heat, mass and momentum transfer in three-dimensional parabolic flows, *Int. Heat Mass Transf.* 115 (1972) 1787–1803.
- [17] D. Trebotich, P. Colella, G. H. Miller, A stable and convergent scheme for viscoelastic flow in contraction channels, *J. Comp. Phys.* 205 (2005) 315–342.
- [18] P. J. Oliveira, On the numerical implementation of nonlinear viscoelastic models in a finite-volume method, *Numerical Heat Transfer, Part B* 40 (2001) 283–301.
- [19] M. F. Tomé, N. Mangiavacchi, J. A. Cuminato, A. Castelo, S. McKee, A finite differencing technique for simulating unsteady viscoelastic free surface flows, *J. Non-Newtonian Fluid Mech.* 106 (2002) 61–106.
- [20] L. M. Quinzani, R. C. Armstrong, R. A. Brown, Birefringence and laser-doppler velocimetry (ldv) studies of viscoelastic flow through a planar contraction, *J. Non-Newtonian Fluid Mech.* 52 (1994) 1–36.
- [21] M. A. Alves, F. T. Pinho, P. J. Oliveira, Effect of a high resolution differencing scheme on finite-volume predictions of viscoelastic flows, *J. Non-Newtonian Fluid Mech.* 93 (2000) 287–314.
- [22] F. P. T. Baaijens, An iterative solver for the devss/dg method with application to smooth and non-smooth flows of the upper convected maxwell fluid, *J. Non-Newtonian Fluid Mech.* 75 (1998) 119–138.
- [23] M. A. Hulsen, Some properties and analytical expressions for plane flow of leonov and giesekus models, *J. Non-Newtonian Fluid Mech.* 30 (1988) 85–92.
- [24] M. A. Alves, P. J. Oliveira, F. T. Pinho, A convergent and universally bounded interpolation scheme for the treatment of advection, *Int. J. Numer. Meth. Fluids* 41 (2003) 47–75.

*5 Development of a methodology for numerical simulation of non-isothermal viscoelastic fluid flows with application to axisymmetric 4:1 contraction flows*

- [25] W. R. Dean, P. E. Montagnon, On the steady motion of viscous liquid in a corner., Proc. Camb. Phil. Soc. 45 (1949) 389–394.
- [26] H. K. Moffatt, Viscous and resistive eddies near a sharp corner, J. Fluid Mech. 18 (1964) 1–18.
- [27] E. J. Hinch, The flow of an Oldroyd fluid around a sharp corner, J. Non-Newtonian Fluid Mech. 50 (1993) 161–171.

## 5.B Nomenclature

Normal symbols represent scalar quantities and boldface symbols represent vector and tensor quantities in general.

### Roman Symbols

Symbol	Description	Unit
$a_T$	Horizontal shift factor	[–]
$\mathbf{c}$	Conformation tensor	[–]
$C_1$	Constant of Williams-Landel-Ferry model	[–]
$C_2$	Constant of Williams-Landel-Ferry model	[K]
$c_P$	Heat capacity	$[\frac{m^2}{s^2K}]$
$\mathbf{D}$	Rate of deformation tensor	$[s^{-1}]$
$e_\phi$	Error of variable $\phi$	[–]
$h$	Channel height	[m]
$i$	Index	[–]
$\mathbf{I}$	Identity matrix	[–]
$k$	Thermal conductivity	$[\frac{kgm}{s^3K}]$
	or index	[–]
$l$	Channel length	[m]
$l_1$	Upstream channel length	[m]
$l_2$	Downstream channel length	[m]
$L_R$	Vortex length	[m]
$m$	Number of modes	[–]
$n$	Number of cell faces	[–]
	or index	[–]
$p$	Pressure	$[\frac{kg}{ms^2}]$
$\mathbf{q}$	Heat flux	$[\frac{kgm^2}{s^3}]$
$Q$	Internal energy source or sink	$[\frac{kgm^2}{s^3}]$
$R_1$	Upstream channel radius	[m]
$R_2$	Downstream channel radius	[m]
$\mathbf{S}_{fi}$	Surface area normal vector at the $i$ -th cell face	$[m^2]$
$t$	Time	[s]
$T$	Temperature	[K]

*5 Development of a methodology for numerical simulation of non-isothermal viscoelastic fluid flows with application to axisymmetric 4:1 contraction flows*

<b>Symbol</b>	<b>Description</b>	<b>Unit</b>
$T_0$	Reference temperature	[K]
$T_{w,1}$	Upstream wall temperature	[K]
$T_{w,2}$	Downstream wall temperature	[K]
$u$	Specific internal energy	$[\frac{kgm^2}{s^2}]$
$\mathbf{U}$	Velocity	$[\frac{m}{s}]$
$\mathbf{U}_r$	Velocity component in radial direction	$[\frac{m}{s}]$
$\mathbf{U}_\Theta$	Velocity component in $\Theta$ -direction	$[\frac{m}{s}]$
$\mathbf{U}_x$	Velocity component in x-direction	$[\frac{m}{s}]$
$\mathbf{U}_y$	Velocity component in y-direction	$[\frac{m}{s}]$
$\mathbf{U}_z$	Velocity component in axial direction	$[\frac{m}{s}]$
$V$	Volume	$[m^3]$
$x$	Position	[m]
$y$	Position	[m]
$z$	Position	[m]

**Greek Symbols**

<b>Symbol</b>	<b>Description</b>	<b>Unit</b>
$\alpha$	Energy partitioning coefficient	[-]
$\Delta x_{cell}$	Edge length of computational cell	[m]
$\Delta T$	Temperature difference	[K]
$\nabla$	Nabla (gradient) operator	$[m^{-1}]$
$\nabla \cdot$	Divergence operator	$[m^{-1}]$
$\zeta$	Local coordinate	[m]
$\eta_0$	Zero shear-rate viscosity	$[\frac{kg}{ms}]$
$\eta_P$	Polymeric viscosity	$[\frac{kg}{ms}]$
$\eta_S$	Solvent viscosity	$[\frac{kg}{ms}]$
$\lambda$	Relaxation time	[s]
$\xi$	Local coordinate	[m]
$\rho$	Density	$[\frac{kg}{m^3}]$
$\boldsymbol{\tau}$	Deviatoric or extra-stress tensor	$[\frac{kg}{ms^2}]$
$\boldsymbol{\tau}_P$	Polymeric stress tensor	$[\frac{kg}{ms^2}]$
$\boldsymbol{\tau}_{P,fi}$	Polymeric stress tensor at the $i$ -th cell face	$[\frac{kg}{ms^2}]$



5 Development of a methodology for numerical simulation of non-isothermal viscoelastic fluid flows with application to axisymmetric 4:1 contraction flows

Symbol	Description	Unit
$\tau_{P,i}$	Polymeric stress tensor of the $i$ -th mode	$[\frac{kg}{ms^2}]$
$\tau_{P,ij}$	$ij$ -th element of polymeric stress tensor	$[\frac{kg}{ms^2}]$
$\tau_{P,P}$	Polymeric stress tensor of computational cell $P$	$[\frac{kg}{ms^2}]$
$\tau_{P,xy}$	Polymeric shear stress	$[\frac{kg}{ms^2}]$
$\tau_{P,xy,max}$	Maximum polymeric shear stress	$[\frac{kg}{ms^2}]$
$\tau_S$	Solvent stress tensor	$[\frac{kg}{ms^2}]$
$\phi$	General property	

### Subscripts, Superscripts and Oversymbols

Symbol	Description
$Q_1$	Upstream value of $Q$
$Q_2$	Downstream value of $Q$
$det(Q)$	Determinant of matrix $Q$
$Q_{exact}$	Exact value of $Q$
$Q_{max}$	Maximum value of $Q$
$tr(Q)$	Trace of matrix $Q$
$Q^T$	Transpose of matrix $Q$
$\overset{\nabla}{Q}$	Upper-convected time derivative
$\overline{Q}$	Arithmetic mean value of $Q$ or average value of $Q$
$\tilde{Q}$	Dimensionless value of $Q$

### Nondimensional Groups

Symbol	Description	Definition
$De$	Deborah number	$\frac{\lambda \overline{U}_{z,2}}{R_2}$
$Pe$	Peclet number	$\frac{\lambda R_2 \overline{U}_{z,2} c_P}{k}$
$Re$	Reynolds number	$\frac{\rho R_2 \overline{U}_{z,2}}{\eta_0}$
$\beta$	Retardation factor	$\frac{\eta_P}{\eta_0}$
$\chi$	Dimensionless vortex length	$\frac{L_R}{2R_1}$

## **Abbreviations**

<b>Abbreviation</b>	<b>Description</b>
AMG	Algebraic multigrid
BiCGstab	Bi-conjugate gradient stabilized
CFD	Computational fluid dynamics
CUBISTA	Convergent and universally bounded interpolation scheme for treatment of advection
DEVSS	Discrete elastic-viscous stress splitting
UCM	Upper-convected Maxwell
WLF	Williams-Landel-Ferry

## 5.C Summary

In this chapter a methodology for the free-to-use software *OpenFOAM*<sup>®</sup>, which is generally applicable to any mesh type and geometry, is developed to simulate non-isothermal viscoelastic flows. The methodology is validated by simulating non-isothermal viscoelastic flows in 4:1 axisymmetric contractions, in which the viscoelastic fluid is governed by the Oldroyd-B constitutive equation. The thermorheological modeling may vary between pure energy elasticity and entropy elasticity depending on a pre-determined split coefficient. The temperature-dependent viscosity and relaxation time are modeled using the WLF (Williams-Landel-Ferry) relation. The governing equations are discretized in *OpenFOAM*<sup>®</sup> using a collocated finite volume method. The DEVSS technique is employed for stabilization of the numerical algorithm at high Deborah numbers. An extrapolation method is proposed for the viscoelastic stress on solid walls, which is subsequently being evaluated regarding accuracy and stability. Next, flows in axisymmetric 4:1 contractions with a temperature jump at the contraction are simulated, similar to the studies of Wachs and Clermont [6]. The influence of the Deborah number and the temperature jump on the flow behavior, such as the vortex length, are examined. Furthermore, the asymptotic behavior at the singularity is examined for different Deborah numbers.

## 5.D Author contribution

The author of this thesis contributed to this publication by having the idea to develop a non-isothermal viscoelastic module within *OpenFOAM*<sup>®</sup>, by discovering the drawbacks from using a zero gradient boundary condition for stress on solid walls, by having the idea for an extrapolation boundary condition for stress for reasons of better accuracy, by doing the implementation of the non-isothermal module and the extrapolation boundary condition in the software package *OpenFOAM*<sup>®</sup>, by proposing the concept of the validation base to show the benefits and drawbacks of the extrapolation boundary condition, by proposing the concept to show the behavior of the non-isothermal module, by doing all simulation runs except those for Figs. 5.4 and 5.5 and by writing the whole manuscript.

## 5.E Copyright permission

This chapter is originated from the following publication:

F. Habla, A. Woitalka, S. Neuner, O. Hinrichsen, Development of a methodology for numerical simulation of non-isothermal viscoelastic fluid flows with application to axisymmetric 4:1 contraction flows, *Chemical Engineering Journal* 207-208 (2012) 772-784.

Reprinted with permission from Elsevier Ltd.



# 6 Modeling and Simulation of Conditionally Volume Averaged Viscoelastic Two-Phase Flows

## 6.1 Introduction

Viscoelastic two-phase flows can be found in a broad range of industrial applications such as injection molding [1], polymer blending [2] and coextrusion [3]. Understanding and predicting the fluid's behavior is a major research challenge. The key issue is dealing with both complex fluid behavior, including viscous and elastic effects, as well as multi-phase flows. These types of flows comprise a variety of spatial and temporal scales. The spatial scales are ranging from microscale of the molecular conformation to the mesoscale of the interfacial morphology, and up to the macroscale of the hydrodynamics of the flow. On the other hand, the temporal scales range from the time-scale of molecular conformation changes up to the duration of the experiment. These aspects complicate the requirements of the numerical treatment.

Over the years, many techniques have evolved to address the multiphase-treatment, which can be subdivided into sharp interface and diffuse interface methods.

A conceptual straightforward approach for sharp interface methods is to use a moving mesh with the nodes deforming according to the boundary motion. This approach is used for example in Cristini et al. [4]. However, the necessity of remeshing leads to huge amounts of additional computational costs and interpolation errors. Moreover, changes in the interfacial topology when facing breakup or coalescence are intractable using such a methodology.

In contrast, in diffuse interface methods, the interface possesses a finite width with the physical properties, such as density and viscosity, smoothly varying across the interface. [5] The Volume-of-Fluid (VoF) originally proposed by Hirt and Nichols [6] is one of these methods. The volume-fraction is used as an order parameter to determine, which phase is present in a particular volume. This order parameter is convected as an invariant of the flow field. However, one of the major disadvantages of the Volume-of-Fluid method is the difficulty to accurately reconstruct the interfacial morphology such as curvature and interface normal vector from the order parameter. Kim et al. [7] applied a volume-of-fluid method to viscoelastic free-surface flows in order to simulate three-dimensional jet buckling. More recently, Habla et al. [8] applied a finite-volume based Volume-of-Fluid method to a variety of complex multi-phase problems, including die extrusion, rod-climbing and droplet deformations in shear and elongational flows. The Level-Set method was also successfully applied to two-phase flows [9, 10] and more recently to viscoelastic two-phase flows [11]. In the Level-Set method the interface is defined as the zero Level-Set of a smooth auxiliary

function. Interfacial forces such as surface tension are smoothed across the interface. [9] Although the interface remains sharp in this treatment, the conservation of mass cannot be guaranteed. Some authors developed a hybrid approach making use of the advantages of both the Volume-of-Fluid and Level-Set methods. [12, 13] This approach is called coupled Level-Set Volume-of-Fluid (CLSVOF) method and was more recently applied to simulating bubble and drop motion of a FENE-CR fluid. [14] Another diffuse-interface approach was developed by Unverdi and Tryggvason [15, 16] called front-tracking. In front-tracking, an interface indicator function is artificially spread over a few computational cells from the known sharp interface position. Subsequently, this indicator function is used to convect the interface. Being thermodynamically derived, the phase-field method is another type of diffuse-interface methods, which was recently adapted by Yue et al. [17, 18] to simulate deformation and head-on collision of droplets with either phase being an Oldroyd-B type fluid.

A common aspect of the aforementioned diffuse-interface methods is that they consist of only one set of conservation equations, i.e., mass and momentum, wherein the fluid properties vary across the interface smoothly using a phase indicator function. Advantages of diffuse interface methods are, that a fixed grid can be used in an Eulerian treatment, and that large distortions of the interface, occurring for example in breakup and coalescence, are handled in a straightforward manner and will not affect the numerical simulation. However, due to the numerical necessity of artificially smearing the interface, problems may arise if the width of the smeared interface is on the order of the considered phenomena, which is the case, for example, in breakup and coalescence of droplets. Furthermore, due to the artificial smearing of the interface, the results obtained strongly depend upon the way the indicator function varies across the interface. This is particularly distinct if the fluids possess large property differences. As a result, a model, in which the results are independent of the interface width, such that the interface width can be chosen arbitrarily large, is highly needed.

The technique of averaging is commonly employed for deriving two-phase models for large-scale two-phase flows such as bubbly and particulate flows. The averaging is done on a larger-scale compared to the dispersed phase elements. Consequently, the interfacial scale is not resolved and coupling between the phases is accounted for only in an average sense. However, Beckermann recently applied ensemble-averaging on an atomic scale to the local single-phase equations to arrive at a model suitable for direct simulation of two-phase flows. [19, 20, 21] Herein, the averaging is applied on a much smaller scale compared to the interfacial averaging methods, so as to partly resolve the interfacial morphology and the flows inside the interface. In contrast to commonly used diffuse interface methods, wherein only a single velocity and pressure is present even in the interfacial region, the ensemble averaged two-phase model by Beckermann and co-workers treats both phases separately with each phase having its own velocity and pressure. As a consequence separate conservation equations for mass and momentum have to be solved, which is common for the interfacial averaged two-phase models. These equations are explicitly coupled using closure relations to account for the phase

interaction. Beckermann showed that the resulting model possesses the important property of being independent of the chosen interface width; however, this is only the case with zero surface tension. [20]

In this work, we will apply the technique of conditional volume averaging to the mass and momentum equations, but on a larger scale compared to Sun and Beckermann [20]. Our model is motivated by the desire to predict meso- and macroscale flows by underresolving microscale structures, rather than a need to resolve the scale of the fluctuating atomic structures inside the diffuse interface to allow direct numerical simulation. That is, the mean interfacial curvature is resolved and large compared to the interfacial width. The resulting model will be based on local instantaneous conservation equations, which are transformed using the mathematically well-grounded conditional volume-averaging technique. The resulting coupling terms are then physically interpreted by splitting them into resolved and unresolved portions. A drawback of treating both phases separately is that they require a model for the coupling terms, which is usually based on simple concepts. [20] In this work, we will present closure relations to couple our derived set of equations based on the above mentioned ideas. In doing so, the stress terms are treated using the well-known Oldroyd-B constitutive equation, see for example Bird et al. [22], in order to allow for either phase being viscoelastic. By solving each phase separately, no a-priori defined variation of variables across the interface has to be postulated. Moreover, both phases coexist inside the interfacial region thus avoiding rapid changes in the properties across the interface.

This work is organized as follows: In Section 6.2, we will introduce the concept of conditional volume averaging and then derive the conditionally volume averaged mass and momentum equations. Closure laws are subsequently presented for the viscoelastic stresses, interfacial morphology, interfacial force density and momentum source due to surface tension. The numerical implementation is outlined in Section 6.3. The derived equations are rearranged in view of the numerics and a numerical procedure to solve the strongly coupled set of equations is presented. In Section 6.4, we present the results for a single-phase Poiseuille flow and two basic two-phase test cases to demonstrate the correctness of the viscoelasticity treatment and the closures for momentum source and phase coupling. Finally, we pursue an error analysis using a viscoelastic two-phase Poiseuille flow.

## 6.2 Mathematical formulation

### 6.2.1 Conditional Averaging

First, we will shortly outline the concept of conditional volume averaging. For further reading, we would like to refer the reader to the literature. [23, 24, 25, 26, 27]

In order to distinguish between multiple phases, the phase indicator function  $I_\varphi(\mathbf{x}, t)$  is introduced, which equals one, if phase  $\varphi$  is present and is zero elsewhere

$$I_\varphi(\mathbf{x}, t) = \begin{cases} 1 & \text{if point } (\mathbf{x}, t) \text{ is in phase } \varphi \\ 0 & \text{otherwise.} \end{cases} \quad (6.1)$$

As a result of Eq. 6.1, the following must hold for  $N$  phases

$$\sum_{i=1}^N I_\varphi(\mathbf{x}, t) = 1 \quad (6.2)$$

Let  $\mathbf{Q}$  be any local instantaneous physical property, e.g., a scalar, vector or tensor. Multiplication of the phase indicator function  $I_\varphi(\mathbf{x}, t)$  with  $\mathbf{Q}$  gives  $\mathbf{Q}_\varphi \equiv I_\varphi(\mathbf{x}, t) \mathbf{Q}$ , where  $\mathbf{Q}_\varphi$  denotes the conditioned quantity.

Volume averaging of a local instantaneous physical property  $\mathbf{Q}$  using an arbitrary averaging volume element  $\delta V$  is defined as

$$\overline{\mathbf{Q}}^{\delta V} \equiv \frac{1}{\delta V} \int_{\delta V} \mathbf{Q}(\mathbf{x}, t) d\mathbf{y} \quad (6.3)$$

where  $\delta V$  is the averaging volume and the vector  $\mathbf{y}$  is a relative position vector pointing inside the volume  $\delta V$ . In the remainder, the index  $\delta V$  will be dropped due to brevity.

Now consider the volume average of the phase indicator function  $I_\varphi(\mathbf{x}, t)$

$$\alpha_\varphi(\mathbf{x}, t) = \overline{I_\varphi(\mathbf{x}, t)} \quad (6.4)$$

then  $\alpha_\varphi(\mathbf{x}, t)$  is the phase volume fraction, which in the case of ensemble averaging can be thought of the probability of a point  $(\mathbf{x}, t)$  pertaining to phase  $\varphi$ . Note, that  $(\mathbf{x}, t)$  will be dropped for  $I_\varphi(\mathbf{x}, t)$  and  $\alpha_\varphi(\mathbf{x}, t)$  and will solely be denoted as  $I_\varphi$  and  $\alpha_\varphi$  in the remainder.

The conditional volume average of a local instantaneous physical property  $\mathbf{Q}$  is then defined as follows [23]

$$\overline{I_\varphi \mathbf{Q}} = \alpha_\varphi \overline{\mathbf{Q}_\varphi} \quad (6.5)$$

The conditional fluctuation is the difference between the local instantaneous and conditional volume average of the property [27]

$$\mathbf{Q}'_\varphi = \mathbf{Q} - \overline{\mathbf{Q}_\varphi} \quad (6.6)$$

The conditional volume averaged product of  $\mathbf{Q}$  and another property  $\mathbf{P}$  is

$$\overline{I_\varphi \mathbf{P} \mathbf{Q}} = \alpha_\varphi \overline{\mathbf{P}_\varphi \mathbf{Q}_\varphi} + \alpha_\varphi \overline{\mathbf{P}'_\varphi \mathbf{Q}'_\varphi} \quad (6.7)$$



In order to apply conditional volume averaging to the mass and momentum equation, we additionally need to consider conditional volume averaged differential operations. It is worth noting here that differential operators and the averaging operation commute

$$\overline{\nabla(I_\varphi \mathbf{Q})} = \nabla(\overline{I_\varphi \mathbf{Q}}) = \nabla(\alpha_\varphi \overline{\mathbf{Q}}_\varphi) \quad (6.8)$$

and

$$\frac{\partial \overline{I_\varphi \mathbf{Q}}}{\partial t} = \frac{\partial \overline{I_\varphi \mathbf{Q}}}{\partial t} = \frac{\partial(\alpha_\varphi \overline{\mathbf{Q}}_\varphi)}{\partial t} \quad (6.9)$$

Now consider the conditional volume average of  $I_\varphi \nabla \mathbf{Q} = \nabla(I_\varphi \mathbf{Q}) - (\nabla I_\varphi) \mathbf{Q}$  over a control volume  $\partial V$ .  $\nabla I_\varphi$  is non-zero only at the interface where it has a value of infinity thus resembling the Dirac delta function and the direction  $\mathbf{n}_{I,\varphi}$  normal to the interface pointing inside of the volume  $\varphi$ . Then the conditional volume average of  $I_\varphi \nabla \mathbf{Q}$  is

$$\begin{aligned} \overline{I_\varphi \nabla \mathbf{Q}} &= \overline{\nabla(I_\varphi \mathbf{Q})} - \overline{(\nabla I_\varphi) \mathbf{Q}} \\ &= \nabla(\alpha_\varphi \overline{\mathbf{Q}}_\varphi) - \overline{\lim_{\delta V \rightarrow 0} \frac{1}{\delta V} \int_{S(\mathbf{x},t)} \mathbf{n}_{I,\varphi} \mathbf{Q} dS} \\ &= \nabla(\alpha_\varphi \overline{\mathbf{Q}}_\varphi) - \widehat{\mathbf{n}_{I,\varphi} \mathbf{Q}} \Sigma \end{aligned} \quad (6.10)$$

where  $S(\mathbf{x}, t) = 0$  is the equation of the interface,  $\Sigma$  is the interfacial area density

$$\Sigma \equiv \overline{\lim_{\delta V \rightarrow 0} \frac{1}{\delta V} \int_{S(\mathbf{x},t)} dS} \quad (6.11)$$

and  $\widehat{\mathbf{Q}}$  denotes the interface average of a property  $\mathbf{Q}$  [27]

$$\widehat{\mathbf{Q}} \equiv \frac{\lim_{\delta V \rightarrow 0} \overline{\frac{1}{\delta V} \int_{S(\mathbf{x},t)} \mathbf{Q} dS}}{\Sigma} \quad (6.12)$$

The conditionally volume averaged divergence of the property  $\mathbf{Q}$  can be obtained analogously

$$\begin{aligned} \overline{I_\varphi \nabla \cdot \mathbf{Q}} &= \overline{\nabla \cdot (I_\varphi \mathbf{Q})} - \overline{(\nabla I_\varphi) \cdot \mathbf{Q}} \\ &= \nabla \cdot (\alpha_\varphi \overline{\mathbf{Q}}_\varphi) - \overline{\lim_{\delta V \rightarrow 0} \frac{1}{\delta V} \int_{S(\mathbf{x},t)} \mathbf{n}_{I,\varphi} \cdot \mathbf{Q} dS} \\ &= \nabla \cdot (\alpha_\varphi \overline{\mathbf{Q}}_\varphi) - \widehat{\mathbf{n}_{I,\varphi} \cdot \mathbf{Q}} \Sigma \end{aligned} \quad (6.13)$$

For the time derivative we obtain

$$\begin{aligned}
 \overline{I_\varphi \frac{\partial \mathbf{Q}}{\partial t}} &= \overline{\frac{\partial I_\varphi \mathbf{Q}}{\partial t}} - \overline{\mathbf{Q} \frac{\partial I_\varphi}{\partial t}} \\
 &= \frac{\partial (\alpha_\varphi \overline{\mathbf{Q}_\varphi})}{\partial t} + \overline{\mathbf{Q} ((\nabla I_\varphi) \cdot \mathbf{U}_I)} \\
 &= \frac{\partial (\alpha_\varphi \overline{\mathbf{Q}_\varphi})}{\partial t} + \lim_{\delta V \rightarrow 0} \frac{1}{\delta V} \int_{S(\mathbf{x}, t)} \mathbf{Q} (\mathbf{n}_{I, \varphi} \cdot \mathbf{U}_I) dS \\
 &= \frac{\partial (\alpha_\varphi \overline{\mathbf{Q}_\varphi})}{\partial t} + \overbrace{\mathbf{Q} (\mathbf{n}_{I, \varphi} \cdot \mathbf{U}_I)}^\Sigma
 \end{aligned} \tag{6.14}$$

which follows from the fact that the phase indicator function  $I_\varphi$  is convected with the velocity of the interface  $\mathbf{U}_I$

$$\frac{\partial I_\varphi}{\partial t} + (\nabla I_\varphi) \cdot \mathbf{U}_I = 0 \tag{6.15}$$

A useful identity can be obtained from Eq. 6.10 with  $\mathbf{Q} = 1$

$$\nabla \alpha_\varphi = \overbrace{\mathbf{n}_{I, \varphi}}^\Sigma \tag{6.16}$$

Moreover, by using Eq. 6.14 with  $\mathbf{Q} = 1$ , one can derive the evolution equation for the volume fraction  $\alpha_\varphi$  of phase  $\varphi$

$$\frac{\partial \alpha_\varphi}{\partial t} + \overbrace{\mathbf{n}_{I, \varphi} \cdot \mathbf{U}_I}^\Sigma = 0 \tag{6.17}$$

Similar to decomposing the local instantaneous quantity into a volume average and a fluctuation (Eq. 6.6), an interfacial quantity  $\mathbf{Q}_I$  (a quantity defined solely on the interface) may also be decomposed into a surface average and surface fluctuation

$$\mathbf{Q}_I = \overbrace{\mathbf{Q}}^\Sigma + \mathbf{Q}^\# \tag{6.18}$$

Although the general approach is valid for any number of phases (see Eq. 6.2), we restrict the derivation in the subsequent section to the case of two phases ( $\varphi$  and  $\omega$ ).

## 6.2.2 Conservation equations

In this section, we will apply conditional volume averaging to derive a set of equations from the local instantaneous mass and momentum conservation suitable for describing multiphase flows, in which we seek to capture the interfacial morphologies on a mesoscale, while under-resolving the microscale structures. The derivation of the conditional volume averaged continuity and momentum equations in particular follows the derivation of Weller [27]. However, in Weller [27] a model for simulating interfacial averaged bubbly multiphase flows is derived, with one phase being dispersed in another phase. Throughout this work we will consider transient, isothermal two-phase flows of incompressible viscoelastic fluids.

### Conditionally Volume Averaged Mass Conservation

The local instantaneous continuity equation is

$$\frac{\partial \rho}{\partial t} + \nabla \cdot (\rho \mathbf{U}) = 0 \quad (6.19)$$

where  $\rho$  is the density and  $\mathbf{U}$  is the velocity.

Conditional volume averaging of the local instantaneous continuity equation for phase  $\varphi$  gives

$$\overline{I_\varphi \frac{\partial \rho}{\partial t}} + \overline{I_\varphi \nabla \cdot (\rho \mathbf{U})} = 0 \quad (6.20)$$

Using Eqs. 6.13 and 6.14 gives

$$\frac{\partial (\alpha_\varphi \bar{\rho}_\varphi)}{\partial t} + \overbrace{\rho (\mathbf{n}_{I,\varphi} \cdot \mathbf{U}_I) \Sigma} + \nabla \cdot (\alpha_\varphi \bar{\rho}_\varphi \bar{\mathbf{U}}_\varphi) - \overbrace{\rho (\mathbf{n}_{I,\varphi} \cdot \mathbf{U}) \Sigma} = 0 \quad (6.21)$$

Note here, that due to the assumption of incompressible fluids no density weighted averages appear. The interface contribution terms can be grouped together

$$\frac{\partial (\alpha_\varphi \bar{\rho}_\varphi)}{\partial t} + \nabla \cdot (\alpha_\varphi \bar{\rho}_\varphi \bar{\mathbf{U}}_\varphi) = \overbrace{\rho (\mathbf{n}_{I,\varphi} \cdot (\mathbf{U} - \mathbf{U}_I)) \Sigma} \quad (6.22)$$

Assuming no mass-transfer, i.e.,  $\mathbf{U} - \mathbf{U}_I = 0$ , and by dividing Eq. 6.22 by the constant density  $\bar{\rho}_\varphi$ , one obtains

$$\frac{\partial \alpha_\varphi}{\partial t} + \nabla \cdot (\alpha_\varphi \bar{\mathbf{U}}_\varphi) = 0 \quad (6.23)$$

Note that the same equation holds for the second phase  $\omega$  by simply changing the indices.

### Conditionally Volume Averaged Momentum Conservation

The local instantaneous momentum equation can be written as

$$\frac{\partial \rho \mathbf{U}}{\partial t} + \nabla \cdot (\rho \mathbf{U} \mathbf{U}) = -\nabla p + \nabla \cdot \boldsymbol{\tau} + \rho \mathbf{g} \quad (6.24)$$

where  $p$  is the pressure,  $\boldsymbol{\tau}$  is the extra-stress tensor and  $\mathbf{g}$  is the gravitational acceleration vector.

Conditional volume averaging of the momentum equation gives

$$\overline{I_\varphi \frac{\partial \rho \mathbf{U}}{\partial t}} + \overline{I_\varphi \nabla \cdot (\rho \mathbf{U} \mathbf{U})} = -\overline{I_\varphi \nabla p} + \overline{I_\varphi \nabla \cdot \boldsymbol{\tau}} + \overline{I_\varphi \rho \mathbf{g}} \quad (6.25)$$

By again making the a-priori assumption of incompressible fluids, as is the case for the continuity equation, one obtains

$$\begin{aligned}
 & \frac{\partial \alpha_\varphi \bar{\rho}_\varphi \bar{\mathbf{U}}_\varphi}{\partial t} + \overbrace{\rho \mathbf{U} (\mathbf{n}_{I,\varphi} \cdot \mathbf{U}_I) \Sigma} \\
 & + \nabla \cdot (\alpha_\varphi \bar{\rho}_\varphi \bar{\mathbf{U}}_\varphi \bar{\mathbf{U}}_\varphi) + \nabla \cdot \left( \alpha_\varphi \bar{\rho}_\varphi \overbrace{\mathbf{U}'_\varphi \mathbf{U}'_\varphi} \right) - \overbrace{\rho \mathbf{U} (\mathbf{n}_{I,\varphi} \cdot \mathbf{U}) \Sigma} \\
 & = \\
 & - \nabla (\alpha_\varphi \bar{p}_\varphi) + \overbrace{\mathbf{n}_{I,\varphi} p \Sigma} + \nabla \cdot (\alpha_\varphi \bar{\boldsymbol{\tau}}_\varphi) - \overbrace{\mathbf{n}_{I,\varphi} \cdot \boldsymbol{\tau} \Sigma} + \alpha_\varphi \bar{\rho}_\varphi \mathbf{g}
 \end{aligned} \tag{6.26}$$

In this work, the momentum dispersion term, i.e., the fourth term on the left hand side of Eq. 6.26, is neglected by assuming that the flow is slow enough, which is similarly made in Sun and Beckermann [20]. Furthermore, with the assumption of no mass-transfer between the phases, the two interfacial average terms on the left hand side of Eq. 6.26 sum to zero resulting in

$$\begin{aligned}
 & \frac{\partial \alpha_\varphi \bar{\rho}_\varphi \bar{\mathbf{U}}_\varphi}{\partial t} + \nabla \cdot (\alpha_\varphi \bar{\rho}_\varphi \bar{\mathbf{U}}_\varphi \bar{\mathbf{U}}_\varphi) \\
 & = \\
 & - \nabla (\alpha_\varphi \bar{p}_\varphi) + \overbrace{\mathbf{n}_{I,\varphi} p \Sigma} + \nabla \cdot (\alpha_\varphi \bar{\boldsymbol{\tau}}_\varphi) - \overbrace{\mathbf{n}_{I,\varphi} \cdot \boldsymbol{\tau} \Sigma} + \alpha_\varphi \bar{\rho}_\varphi \mathbf{g}
 \end{aligned} \tag{6.27}$$

Dividing Eq. 6.27 by the constant bulk density  $\bar{\rho}_\varphi$ , applying the product rule to the bulk pressure term according to  $\nabla (\alpha_\varphi \bar{p}_\varphi) = \alpha_\varphi \nabla \bar{p}_\varphi + (\nabla \alpha_\varphi) \bar{p}_\varphi$  and grouping the interface contributed terms on the right hand side into an interfacial momentum transfer term  $\mathbf{M}_\varphi$ , one obtains [27]

$$\frac{\partial \alpha_\varphi \bar{\mathbf{U}}_\varphi}{\partial t} + \nabla \cdot (\alpha_\varphi \bar{\mathbf{U}}_\varphi \bar{\mathbf{U}}_\varphi) = - \frac{\alpha_\varphi \nabla \bar{p}_\varphi}{\bar{\rho}_\varphi} + \frac{\nabla \cdot (\alpha_\varphi \bar{\boldsymbol{\tau}}_\varphi)}{\bar{\rho}_\varphi} + \alpha_\varphi \mathbf{g} + \frac{\mathbf{M}_\varphi}{\bar{\rho}_\varphi} \tag{6.28}$$

where  $\mathbf{M}_\varphi = -(\nabla \alpha_\varphi) \bar{p}_\varphi + \overbrace{\mathbf{n}_{I,\varphi} p \Sigma} - \overbrace{\mathbf{n}_{I,\varphi} \cdot \boldsymbol{\tau} \Sigma}$ . According to Eq. 6.18, we decompose the interfacial pressure into a mean and a fluctuation [26]

$$\overbrace{\mathbf{n}_{I,\varphi} p \Sigma} = \overbrace{p \mathbf{n}_{I,\varphi} \Sigma} + \overbrace{\mathbf{n}_{I,\varphi}^\# p^\# \Sigma} \tag{6.29}$$

and by using Eq. 6.16 we obtain

$$\overbrace{\mathbf{n}_{I,\varphi} p \Sigma} = \overbrace{p \nabla \alpha_\varphi} + \overbrace{\mathbf{n}_{I,\varphi}^\# p^\# \Sigma} \tag{6.30}$$

This results in

$$\mathbf{M}_\varphi = \left( \overbrace{p} - \bar{p}_\varphi \right) \nabla \alpha_\varphi + \overbrace{\mathbf{n}_{I,\varphi} p^\# \Sigma} - \overbrace{\mathbf{n}_{I,\varphi} \cdot \boldsymbol{\tau} \Sigma} \tag{6.31}$$

The first term can be thought of as a net force normal to the interface due to a pressure difference, whereas the last two terms can be thought of the momentum exerted due to unbalanced pressures and stresses. In order to obtain the correct jump conditions at the interface, the following condition must hold [20]

$$\mathbf{M}_\varphi + \mathbf{M}_\omega = \mathbf{M}_\sigma \quad (6.32)$$

where  $\mathbf{M}_\sigma$  denotes the averaged interfacial momentum source due to surface tension, which is

$$\mathbf{M}_\sigma \equiv \overbrace{\sigma \kappa_{I,\varphi} \mathbf{n}_{I,\varphi}} \Sigma \quad (6.33)$$

### 6.2.3 Viscoelastic Two-Phase Flow Closure

The two continuity equations (Eqs. 6.23) and momentum equations (Eqs. 6.28) (one for each phase  $\varphi$  and  $\omega$  in a two-phase flow) together with the volume fraction equations (Eq. 6.17) constitute our two-phase model. Note here, that only one volume fraction equation is necessary for a two-phase flow since by adding up both equations it follows that

$$\alpha_\omega = 1 - \alpha_\varphi \quad (6.34)$$

However, the model still includes two terms  $\bar{\boldsymbol{\tau}}_\varphi$  and  $\mathbf{M}_\varphi$ , which need proper closure models for the flow under consideration. In the following sections, we will derive closure relations for an incompressible, isothermal, viscoelastic two-phase flow without mass-transfer.

#### Modeling of the stress terms

We will first derive closure relations for the conditional volume averaged stress tensor  $\bar{\boldsymbol{\tau}}_\varphi$ . We start by stating the single phase stress equations and subsequently apply conditional volume averaging.

The fluids are assumed to obey the Oldroyd-B constitutive equation. Herein, the stress tensor for phase  $\varphi$  can be split into a Newtonian (solvent) contribution and a viscoelastic (polymeric) contribution as follows

$$\boldsymbol{\tau} = \boldsymbol{\tau}_S + \boldsymbol{\tau}_P \quad (6.35)$$

The Newtonian law is

$$\boldsymbol{\tau}_S = \eta_S \left( \nabla \mathbf{U} + (\nabla \mathbf{U})^T - \frac{2}{3} (\nabla \cdot \mathbf{U}) \mathbf{I} \right) \quad (6.36)$$

where  $\mathbf{I}$  denotes the identity matrix. Conditional volume averaging gives

$$\overline{I_\varphi \boldsymbol{\tau}_S} = \overline{I_\varphi \eta_S \nabla \bar{\mathbf{U}}} + \overline{I_\varphi \eta_S (\nabla \mathbf{U})^T} - \overline{I_\varphi \eta_S \frac{2}{3} (\nabla \cdot \mathbf{U}) \mathbf{I}} \quad (6.37)$$

Applying the previously derived relationships results in

$$\begin{aligned} \alpha_\varphi \overline{\boldsymbol{\tau}_{S\varphi}} &= \nabla (\alpha_\varphi \eta_{S,\varphi} \bar{\mathbf{U}}_\varphi) - \overbrace{\mathbf{n}_{I,\varphi} (\eta_S \mathbf{U}) \Sigma} \\ &\quad + (\nabla (\alpha_\varphi \eta_{S,\varphi} \bar{\mathbf{U}}_\varphi))^T - \overbrace{(\eta_S \mathbf{U}) \mathbf{n}_{I,\varphi} \Sigma} \\ &\quad - \nabla \cdot \left( \frac{2}{3} \alpha_\varphi \eta_{S,\varphi} \bar{\mathbf{U}}_\varphi \right) \mathbf{I} + \overbrace{\mathbf{n}_{I,\varphi} \cdot (\eta_S \mathbf{U}) \Sigma} \\ &= \alpha_\varphi \eta_{S,\varphi} \nabla \bar{\mathbf{U}}_\varphi + \eta_{S,\varphi} (\nabla \alpha_\varphi) \bar{\mathbf{U}}_\varphi - \eta_{S,\varphi} (\nabla \alpha_\varphi) \mathbf{U}_I \\ &\quad + \alpha_\varphi \eta_{S,\varphi} (\nabla \bar{\mathbf{U}}_\varphi)^T + \eta_{S,\varphi} \bar{\mathbf{U}}_\varphi \nabla \alpha_\varphi - \eta_{S,\varphi} \mathbf{U}_I (\nabla \alpha_\varphi) \\ &\quad - \frac{2}{3} \eta_{S,\varphi} \{ \alpha_\varphi (\nabla \cdot \bar{\mathbf{U}}_\varphi) \mathbf{I} + [(\nabla \alpha_\varphi) \cdot \bar{\mathbf{U}}_\varphi] \mathbf{I} - (\mathbf{U}_I \cdot \nabla \alpha_\varphi) \mathbf{I} \} \end{aligned} \quad (6.38)$$

Regrouping of the various terms leads to the closure for the Newtonian contribution  $\overline{\boldsymbol{\tau}_{S\varphi}}$

$$\begin{aligned} \alpha_\varphi \overline{\boldsymbol{\tau}_{S\varphi}} &= \alpha_\varphi \eta_{S,\varphi} \left[ \nabla \bar{\mathbf{U}}_\varphi + (\nabla \bar{\mathbf{U}}_\varphi)^T - \frac{2}{3} (\nabla \cdot \bar{\mathbf{U}}_\varphi) \mathbf{I} \right] \\ + \eta_{S,\varphi} &\left[ \nabla \alpha_\varphi (\bar{\mathbf{U}}_\varphi - \mathbf{U}_I) + (\bar{\mathbf{U}}_\varphi - \mathbf{U}_I) \nabla \alpha_\varphi - \frac{2}{3} \nabla \alpha_\varphi \cdot (\bar{\mathbf{U}}_\varphi - \mathbf{U}_I) \mathbf{I} \right] \end{aligned} \quad (6.39)$$

From Eq. 6.39, one can conclude that the average stress contains two contributions. The first term on the right represents the self-interaction of the single-phase to itself. The second term is due to the relative motion between the two phases. [20]

The polymeric contribution  $\boldsymbol{\tau}_P$  obeys an Upper-Convected-Maxwell equation

$$\boldsymbol{\tau}_P + \lambda \overset{\nabla}{\boldsymbol{\tau}}_P = \eta_P \left( \nabla \mathbf{U} + (\nabla \mathbf{U})^T - \frac{2}{3} (\nabla \cdot \mathbf{U}) \mathbf{I} \right) \quad (6.40)$$

where the upper-convected time derivative  $\overset{\nabla}{\boldsymbol{\tau}}_P$  is defined as

$$\overset{\nabla}{\boldsymbol{\tau}}_P \equiv \frac{\partial \boldsymbol{\tau}_P}{\partial t} + \nabla \cdot (\mathbf{U} \boldsymbol{\tau}_P) - (\nabla \mathbf{U})^T \cdot \boldsymbol{\tau}_P - \boldsymbol{\tau}_P \cdot (\nabla \mathbf{U}) \quad (6.41)$$

Applying conditional volume averaging leads to

$$\begin{aligned} \overline{I_\varphi \boldsymbol{\tau}_P} + \overline{I_\varphi \lambda \frac{\partial \boldsymbol{\tau}_P}{\partial t}} + \overline{I_\varphi \lambda \nabla \cdot (\mathbf{U} \boldsymbol{\tau}_P)} - \overline{I_\varphi \lambda (\nabla \mathbf{U})^T \cdot \boldsymbol{\tau}_P} - \overline{I_\varphi \lambda \boldsymbol{\tau}_P \cdot (\nabla \mathbf{U})} \\ = \\ \overline{I_\varphi \eta_P \nabla \bar{\mathbf{U}}} + \overline{I_\varphi \eta_P (\nabla \mathbf{U})^T} - \overline{I_\varphi \eta_P \frac{2}{3} (\nabla \cdot \mathbf{U}) \mathbf{I}} \end{aligned} \quad (6.42)$$

This results in

$$\begin{aligned}
 & \alpha_\varphi \overline{\boldsymbol{\tau}}_{P\varphi} + \lambda_\varphi \frac{\partial \alpha_\varphi \overline{\boldsymbol{\tau}}_{P\varphi}}{\partial t} + \lambda_\varphi \overbrace{\boldsymbol{\tau}_P (\mathbf{n}_{I,\varphi} \cdot \mathbf{U}_I)} \Sigma \\
 & + \lambda_\varphi \nabla \cdot (\alpha_\varphi \overline{\boldsymbol{\tau}}_{P\varphi} \overline{\mathbf{U}}_\varphi) + \nabla \cdot (\alpha_\varphi \overline{\boldsymbol{\tau}'_{P,\varphi} \mathbf{U}'_\varphi}) - \lambda_\varphi \overbrace{\boldsymbol{\tau}_P (\mathbf{n}_{I,\varphi} \cdot \mathbf{U})} \Sigma \\
 & - \alpha_\varphi \lambda_\varphi (\nabla \overline{\mathbf{U}}_\varphi)^T \cdot \overline{\boldsymbol{\tau}}_{P\varphi} - \alpha_\varphi \lambda_\varphi \overline{(\nabla \mathbf{U}_\varphi)^T} \cdot \overline{\boldsymbol{\tau}'_{P,\varphi}} \\
 & - \alpha_\varphi \lambda_\varphi \overline{\boldsymbol{\tau}}_{P\varphi} \cdot \nabla \overline{\mathbf{U}}_\varphi - \alpha_\varphi \lambda_\varphi \overline{\boldsymbol{\tau}'_{P,\varphi}} \cdot (\nabla \mathbf{U}_\varphi)' \\
 & = \\
 & \nabla (\alpha_\varphi \eta_{P,\varphi} \overline{\mathbf{U}}_\varphi) - \overbrace{\mathbf{n}_{I,\varphi} (\eta_P \mathbf{U})} \Sigma \\
 & + (\nabla (\alpha_\varphi \eta_{P,\varphi} \overline{\mathbf{U}}_\varphi))^T - \overbrace{(\eta_P \mathbf{U}) \mathbf{n}_{I,\varphi}} \Sigma \\
 & - \nabla \cdot \left( \frac{2}{3} \alpha_\varphi \eta_{P,\varphi} \overline{\mathbf{U}}_\varphi \right) \mathbf{I} + \overbrace{\mathbf{n}_{I,\varphi} \cdot (\eta_P \mathbf{U})} \mathbf{I} \Sigma
 \end{aligned} \tag{6.43}$$

The interface terms on the left hand side of Eq. 6.43 again sum up to zero, since there is no mass transfer

$$\lambda_\varphi \overbrace{\boldsymbol{\tau}_P [\mathbf{n}_{I,\varphi} \cdot (\mathbf{U}_I - \mathbf{U})]} \Sigma = 0 \tag{6.44}$$

The stress dispersion term and the fluctuation terms, i.e., the fifth, eighth and tenth term on the left hand side of Eq. 6.43, respectively, are assumed to be negligibly small, similar to the momentum dispersion term, and thus neglected. Finally, assembling the above results and regrouping the terms, we obtain the following form of the conditional volume averaged upper-convected Maxwell equation

$$\begin{aligned}
 & \alpha_\varphi \overline{\boldsymbol{\tau}}_{P\varphi} \\
 & + \lambda_\varphi \left[ \left( \frac{\partial \alpha_\varphi \overline{\boldsymbol{\tau}}_{P\varphi}}{\partial t} \right) + \nabla \cdot (\alpha_\varphi \overline{\boldsymbol{\tau}}_{P\varphi} \overline{\mathbf{U}}_\varphi) - \alpha_\varphi \overline{\boldsymbol{\tau}}_{P\varphi} \cdot \nabla \overline{\mathbf{U}}_\varphi - \alpha_\varphi (\nabla \overline{\mathbf{U}}_\varphi)^T \cdot \overline{\boldsymbol{\tau}}_{P\varphi} \right] \\
 & = \\
 & \alpha_\varphi \eta_{P,\varphi} \left[ \nabla \overline{\mathbf{U}}_\varphi + (\nabla \overline{\mathbf{U}}_\varphi)^T - \frac{2}{3} (\nabla \cdot \overline{\mathbf{U}}_\varphi) \mathbf{I} \right] \\
 & + \eta_{P,\varphi} \left[ \nabla \alpha_\varphi (\overline{\mathbf{U}}_\varphi - \mathbf{U}_I) + (\overline{\mathbf{U}}_\varphi - \mathbf{U}_I) \nabla \alpha_\varphi - \frac{2}{3} \nabla \alpha_\varphi \cdot (\overline{\mathbf{U}}_\varphi - \mathbf{U}_I) \mathbf{I} \right]
 \end{aligned} \tag{6.45}$$

Once again we see two contributions to the rate of change to the polymeric stress, a term representing the self-interaction of the phase  $\varphi$  with itself and a contribution from the relative motion of the two phases  $\varphi$  and  $\omega$ .

Modelling of the averaged velocity on the  $\varphi$ -side of the interface  $\mathbf{U}_I$  will be discussed in the next section.

### Modeling of the interface morphology

The local interface unit normal vector  $\mathbf{n}_{I,\varphi}$  and curvature  $\kappa_{I,\varphi}$  are defined via the phase indicator function as follows

$$\mathbf{n}_{I,\varphi} = \frac{\nabla I_\varphi}{|\nabla I_\varphi|} \quad (6.46)$$

$$\kappa_{I,\varphi} = -\nabla \cdot \mathbf{n}_{I,\varphi} \quad (6.47)$$

In order to obtain closure for the interfacial averaged unit normal vector  $\widehat{\mathbf{n}}_{I,\varphi}$  and curvature  $\widehat{\kappa}_{I,\varphi}$ , one could simply use volume averaging of the above equations

$$\widehat{\mathbf{n}}_{I,\varphi} = \frac{\overline{\mathbf{n}_{I,\varphi} \nabla I_\varphi}}{\overline{|\nabla I_\varphi|}} \quad (6.48)$$

$$\widehat{\kappa}_{I,\varphi} = \frac{\overline{\kappa_{I,\varphi} \nabla I_\varphi}}{\overline{|\nabla I_\varphi|}} \quad (6.49)$$

However, this would require knowledge of the exact local interfacial morphology, which is subsequently lost after using volume averaging.

In order to obtain an exploitable relationship, we use Eq. 6.16. This will be our closure for the interfacial averaged unit normal vector

$$\widehat{\mathbf{n}}_{I,\varphi} = \frac{\nabla \alpha_\varphi}{\Sigma} \quad (6.50)$$

By taking the absolute value of Eq. 6.50, we obtain

$$|\nabla \alpha_\varphi| = \left| \widehat{\mathbf{n}}_{I,\varphi} \right| \Sigma = \left| \mathbf{n}_{I,\varphi} \right| \Sigma \quad (6.51)$$

Now since  $\left| \mathbf{n}_{I,\varphi} \right| = 1$ , we obtain for the interfacial area density  $\Sigma$

$$\Sigma = |\nabla \alpha_\varphi| \quad (6.52)$$

and by using Eq. 6.52 together with Eq. 6.50, we obtain the following closure

$$\widehat{\mathbf{n}}_{I,\varphi} = \frac{\nabla \alpha_\varphi}{|\nabla \alpha_\varphi|} \quad (6.53)$$

and similar

$$\widehat{\kappa}_{I,\varphi} = -\nabla \cdot \left( \frac{\nabla \alpha_\varphi}{|\nabla \alpha_\varphi|} \right) \quad (6.54)$$

In a study on flame wrinkling Donbar et al. [28] suggest using an inverse relationship between the interfacial area density  $\Sigma$  and the thickness of the flame brush. We will adopt this concept



for our two-phase scenario to suppose that the thickness of the interfacial region is inversely proportional to the interfacial area density

$$\delta_I \approx \frac{1}{\Sigma} = \frac{1}{|\nabla\alpha_\varphi|} \quad (6.55)$$

In order to obtain a closure relation for the local interface velocity  $\mathbf{U}_I$ , we decompose the velocity into a mean and fluctuation

$$\mathbf{U}_I = \widehat{\mathbf{U}} + \mathbf{U}^\# \quad (6.56)$$

Sun and Beckermann [20] proposed a viscosity weighted linear function of the average total velocities of both phases in the case of different viscosities

$$\widehat{\mathbf{U}} = \frac{\alpha_\omega \eta_{eff,\varphi} \overline{\mathbf{U}}_\varphi + \alpha_\varphi \eta_{eff,\omega} \overline{\mathbf{U}}_\omega}{\alpha_\omega \eta_{eff,\varphi} + \alpha_\varphi \eta_{eff,\omega}} \quad (6.57)$$

This relation can be thought as an average no-slip condition at the interface. In the case of Newtonian fluids, one may use the simple expression  $\eta_{eff,\varphi} = \eta_{S,\varphi}$ . However, in the case of an Oldroyd-B fluid, the effective viscosity must account for elastic effects as well. A simple, but still good approximation would be to use  $\eta_{eff,\varphi} = \eta_{S,\varphi} + \eta_{P,\varphi}$ . This closure relation assumes the interface to behave in a viscous manner. In the course of this study, more implicit closures to explicitly account for elastic behavior of the interface were examined, such as  $\eta_{eff,\varphi} = \eta_{S,\varphi} + \frac{\|\overline{\boldsymbol{\tau}}_{P\varphi}\|}{\|\overline{\boldsymbol{\gamma}}_\varphi\|}$ , where  $\overline{\boldsymbol{\gamma}}$  is the shear-rate tensor, or  $\eta_{eff,\varphi} = \eta_{S,\varphi} + \frac{\|\overline{\boldsymbol{\tau}}_{P\varphi}^*\|}{\|\overline{\boldsymbol{\gamma}}_\varphi\|}$ , where  $\overline{\boldsymbol{\tau}}_{P\varphi}^*$  is obtained via  $\frac{\overline{\boldsymbol{\tau}}_{P\varphi}}{\partial t} + \nabla \cdot (\overline{\mathbf{U}}_\varphi \overline{\boldsymbol{\tau}}_{P\varphi}) = \frac{\overline{\boldsymbol{\tau}}_{P\varphi}^* - \overline{\boldsymbol{\tau}}_{P\varphi}}{\lambda_\varphi}$ . However, none of the implicit methods proved to be justified and so the simpler the viscous expression was chosen.

The surface fluctuation  $\mathbf{U}^\#$  is assumed to be small and neglected in the following. Using this closure for the interface velocity, one may derive for the solvent and polymeric stress

$$\begin{aligned} \alpha_\varphi \overline{\boldsymbol{\tau}}_{S\varphi} = & \\ \alpha_\varphi \eta_{S,\varphi} \left[ \nabla \overline{\mathbf{U}}_\varphi + (\nabla \overline{\mathbf{U}}_\varphi)^T - \frac{2}{3} (\nabla \cdot \overline{\mathbf{U}}_\varphi) \mathbf{I} \right] & \\ + \frac{\alpha_\varphi \eta_{S,\varphi} \eta_{eff,\omega}}{\alpha_\omega \eta_{eff,\varphi} + \alpha_\varphi \eta_{eff,\omega}} \left[ \nabla \alpha_\varphi (\overline{\mathbf{U}}_\varphi - \overline{\mathbf{U}}_\omega) + (\overline{\mathbf{U}}_\varphi - \overline{\mathbf{U}}_\omega) \nabla \alpha_\varphi - \frac{2}{3} \nabla \alpha_\varphi \cdot (\overline{\mathbf{U}}_\varphi - \overline{\mathbf{U}}_\omega) \mathbf{I} \right] & \end{aligned} \quad (6.58)$$

$$\begin{aligned}
 & \alpha_\varphi \overline{\tau_{P,\varphi}} + \lambda_\varphi \left[ \left( \frac{\partial \alpha_\varphi \overline{\tau_{P,\varphi}}}{\partial t} \right) + \nabla \cdot (\alpha_\varphi \overline{\tau_{P,\varphi}} \overline{\mathbf{U}}_\varphi) - \alpha_\varphi (\nabla \overline{\mathbf{U}}_\varphi)^T \cdot \overline{\tau_{P,\varphi}} - \alpha_\varphi \overline{\tau_{P,\varphi}} \cdot \nabla \overline{\mathbf{U}}_\varphi \right] \\
 & = \\
 & \alpha_\varphi \eta_{P,\varphi} \left[ \nabla \overline{\mathbf{U}}_\varphi + (\nabla \overline{\mathbf{U}}_\varphi)^T - \frac{2}{3} (\nabla \cdot \overline{\mathbf{U}}_\varphi) \mathbf{I} \right] \\
 & + \frac{\alpha_\varphi \eta_{P,\varphi} \eta_{eff,\omega}}{\alpha_\omega \eta_{eff,\varphi} + \alpha_\varphi \eta_{eff,\omega}} \left[ \nabla \alpha_\varphi (\overline{\mathbf{U}}_\varphi - \overline{\mathbf{U}}_\omega) + (\overline{\mathbf{U}}_\varphi - \overline{\mathbf{U}}_\omega) \nabla \alpha_\varphi - \frac{2}{3} \nabla \alpha_\varphi \cdot (\overline{\mathbf{U}}_\varphi - \overline{\mathbf{U}}_\omega) \mathbf{I} \right]
 \end{aligned} \tag{6.59}$$

### Modeling of the interfacial force density and momentum source

An important closure relation for the modeling of conditional volume averaged two-phase flows is the interfacial force density. In the course of the derivation, we will split the term into three parts, one stemming from surface tension, one from phase-slip and one from drag.

First consider a two-phase scenario without flow in the case of surface tension. Using Eq. 6.33, we split the interface term into a surface average and fluctuation as follows

$$\mathbf{M}_\sigma = \sigma \overbrace{\kappa_I \mathbf{n}_I} \Sigma = \sigma \left( \overbrace{\kappa_I} \overbrace{\mathbf{n}_I} + \overbrace{\kappa_I^\# \mathbf{n}^\#} \right) \Sigma \tag{6.60}$$

The fluctuation term is assumed to be small compared to the interface average, i.e.,  $\overbrace{\kappa_I^\# \mathbf{n}^\#} \ll \overbrace{\kappa_I} \overbrace{\mathbf{n}_I}$ . By using Eqs. 6.53 and 6.54

$$\mathbf{M}_\sigma \approx -\sigma \left( \nabla \cdot \frac{\nabla \alpha_\varphi}{|\nabla \alpha_\varphi|} \right) \nabla \alpha_\varphi \tag{6.61}$$

This will be our final closure for surface tension. Note, that this term is in accordance to the continuum surface force (CSF) model. [29]

Next, consider a flow parallel to a planar interface without gravity. In Eq. 6.31 the first term accounts for the pressure difference  $\left( \overbrace{p} - \overline{p}_\varphi \right)$  between bulk and interface. Initially, we followed Bestion [30], who suggested a relationship between the mean pressure difference and the square of the slip velocity according to

$$\overbrace{p} - \overline{p}_\varphi = \frac{\alpha_\varphi \alpha_\omega \overline{\rho}_\varphi \overline{\rho}_\omega}{\alpha_\varphi \overline{\rho}_\omega + \alpha_\omega \overline{\rho}_\varphi} |\overline{\mathbf{U}}_\varphi - \overline{\mathbf{U}}_\omega|^2 \tag{6.62}$$

However, we found in this study, that this term  $\left( \overbrace{p} - \overline{p}_\varphi \right) \approx 0$  for any flow under consideration, which is why it is subsequently neglected.

For the second part of Eq. 6.31 we have  $\overbrace{\mathbf{n}_{I,\varphi}^\# p^\# \Sigma} - \overbrace{\mathbf{n}_{I,\varphi} \cdot \boldsymbol{\tau} \Sigma}$ , which comprises the interfacial forces due to unbalanced pressures and stresses. We follow Sun and Beckermann [20], who use the following expression

$$\mathbf{M}_\varphi^d = -h \frac{\alpha_\omega \eta_{eff,\varphi} \Sigma}{\delta_I} (\bar{\mathbf{U}}_\varphi - \mathbf{U}_I) \quad (6.63)$$

That is, the interfacial Reynolds number is assumed to be small so that the drag force between the two phases is linearly proportional to the slip velocity. With the use of Eq. 6.52, Eq. 6.55 and Eq. 6.57 we obtain

$$\mathbf{M}_\varphi^d = -h \frac{\alpha_\varphi \alpha_\omega \eta_{eff,\varphi} \eta_{eff,\omega} (|\nabla \alpha_\varphi|)^2}{\alpha_\omega \eta_{eff,\varphi} + \alpha_\varphi \eta_{eff,\omega}} (\bar{\mathbf{U}}_\varphi - \bar{\mathbf{U}}_\omega) \quad (6.64)$$

Beckermann et al. [19] propose that  $h \approx 2.5 - 2.757$ , being derived for an asymptotic analysis for plane shear flow past a diffuse interface for a solid-liquid flow. The particular value depends on the profile of variation of  $\alpha_\varphi$ . The same value was used for the two-phase scenario. [20] A variational analysis over two orders of magnitude showed, that this value indeed results in the correct velocity profile even for two-phase flow. However, in this work, we use a value of  $h = 11.028 (= 4 * 2.757)$ , since after using the closure relation for  $\mathbf{U}_I$  in Eq. 6.63 the term is proportional to  $\alpha_\varphi \alpha_\omega$  having its maximum of  $\alpha_\varphi \alpha_\omega = 0.25$  (at  $\alpha_\varphi = \alpha_\omega = 0.5$ ), which is why we use a factor of four. Note, that this value results also in the correct velocity profile, as will be shown in the results, however, having beneficial stabilizing features to the solution, as the coupling between the both phases in strenghtend.

Using both Eq. 6.61 and Eq. 6.63 together with the corresponding closures results in the final closure of  $\mathbf{M}_\varphi$

$$\mathbf{M}_\varphi = -h \frac{\alpha_\varphi \alpha_\omega \eta_{eff,\varphi} \eta_{eff,\omega} (|\nabla \alpha_\varphi|)^2}{\alpha_\omega \eta_{eff,\varphi} + \alpha_\varphi \eta_{eff,\omega}} (\bar{\mathbf{U}}_\varphi - \bar{\mathbf{U}}_\omega) - \sigma \left( \nabla \cdot \frac{\nabla \alpha_\varphi}{|\nabla \alpha_\varphi|} \right) \nabla \alpha_\varphi \quad (6.65)$$

## 6.3 Numerical implementation

Our system of equations is described by the volume fraction equations (Eqs. 6.17), the continuity equations (Eqs. 6.23) and momentum equations (Eqs. 6.28), the underlying closure relations for stress (Eqs. 6.58 and 6.59) and the interfacial momentum transfer (Eq. 6.65) for both  $\varphi$  and  $\omega$ . In this section we describe the numerical procedure to solve these equations.

### 6.3.1 Pressure reformulation

A critical issue in solving the above system of equations is the need for two pressures being strongly coupled at the interface. This would require a thorough coupled solution procedure. Now, in incompressible single-phase flows, pressure is mainly used to satisfy continuity. If a

similar technique is used for a two-phase flow, then pressure will be used to guarantee overall continuity, whereas the phase fractions are obtained by the continuity equations. Therefore, we will make use of a single/mixture pressure according to

$$\bar{p} = \bar{p}_\varphi = \bar{p}_\omega \quad (6.66)$$

Since we then remove one unknown, we consequently have to remove an equation in order to stay well-posed, which will be the first volume fraction equation Eq. 6.17. The second equation will be used in its transformed form as given by Eq. 6.34.

Furthermore, in order to smooth out the pressure field, which is necessary in the numerical procedure, we will make use of a modified pressure  $\bar{p}^d$  by separating out the hydrostatic pressure,  $-\rho\mathbf{g} \cdot \mathbf{x}$ , where  $\mathbf{x}$  is the position vector and  $\rho = \alpha_\varphi\bar{\rho}_\varphi + (1 - \alpha_\varphi)\bar{\rho}_\omega$ . [31] The momentum equation for quiescent fluids and flat interfaces is

$$\frac{\nabla\bar{p}}{\bar{\rho}_\varphi} = \mathbf{g} \quad (6.67)$$

In the case of constant gravitational acceleration  $\mathbf{g}$  one may write  $\nabla(\rho\mathbf{g} \cdot \mathbf{x}) = \mathbf{g} \cdot \mathbf{x}\nabla\rho + \rho\mathbf{g}$ . This leads to

$$\frac{\nabla\bar{p}}{\bar{\rho}_\varphi} = \frac{\nabla\bar{p}^d}{\bar{\rho}_\varphi} + \frac{1}{\bar{\rho}_\varphi}(\rho\mathbf{g} + \mathbf{g} \cdot \mathbf{x}\nabla\rho) \quad (6.68)$$

Substituting Eq. 6.68 into the momentum equation, Eq. 6.28, we get

$$\begin{aligned} & \frac{\partial\alpha_\varphi\bar{\mathbf{U}}_\varphi}{\partial t} + \nabla \cdot (\alpha_\varphi\bar{\mathbf{U}}_\varphi\bar{\mathbf{U}}_\varphi) \\ & = \\ & -\frac{\alpha_\varphi\nabla\bar{p}^d}{\bar{\rho}_\varphi} + \alpha_\varphi\left(1 - \frac{\rho}{\bar{\rho}_\varphi}\right)\mathbf{g} - \alpha_\varphi\frac{\mathbf{g} \cdot \mathbf{x}\nabla\rho}{\bar{\rho}_\varphi} + \frac{\nabla \cdot (\alpha_\varphi\bar{\boldsymbol{\tau}}_\varphi)}{\bar{\rho}_\varphi} + \frac{\mathbf{M}_\varphi}{\bar{\rho}_\varphi} \end{aligned} \quad (6.69)$$

### 6.3.2 Phase fraction equation reformulation

An important aspect in two-phase flows is to keep the phase fraction  $\alpha_\varphi$  strictly bounded between zero and one. In this work, we will adopt the Weller [27] scheme by reformulating the continuity equations Eqs. 6.23. We therefore define a mixture velocity  $\bar{\mathbf{U}}$  as follows

$$\bar{\mathbf{U}} = \alpha_\varphi\bar{\mathbf{U}}_\varphi + \alpha_\omega\bar{\mathbf{U}}_\omega \quad (6.70)$$

Combining Eqs. 6.23 both for  $\varphi$  and  $\omega$  together with Eq. 6.70 yields the incompressibility constraint for the mixture velocity

$$\nabla \cdot \bar{\mathbf{U}} = 0 \quad (6.71)$$

Further, a relative velocity  $\bar{\mathbf{U}}_r$  is defined according to

$$\bar{\mathbf{U}}_r = \bar{\mathbf{U}}_\varphi - \bar{\mathbf{U}}_\omega \quad (6.72)$$

Combining Eqs. 6.23, 6.34, 6.70, and 6.72 yields the phase fraction convection equation

$$\frac{\partial \alpha_\varphi}{\partial t} + \nabla \cdot (\alpha_\varphi \bar{\mathbf{U}}) + \nabla \cdot (\bar{\mathbf{U}}_r \alpha_\varphi (1 - \alpha_\varphi)) = 0 \quad (6.73)$$

It follows from Eq. 6.71, that the first and second convection terms in Eq. 6.73 are both conservative and bounded between zero and one. However, in order to guarantee this boundedness, Eq. 6.73 has to be solved fully implicitly. Since the second convection term is nonlinear in  $\alpha_\varphi$  one has to adopt an iterative procedure.

### 6.3.3 Phase-intensive Momentum and Constitutive Equation

Another important aspect on solving the above set of equations is the difficulty for solving the momentum and constitutive equations in the case when the phase fractions become zero. We therefore derive phase intensive forms of those equations.

Considering the momentum equation (Eq. 6.69), the product rule is applied to the instationary and convective terms on the right hand side according to

$$\begin{aligned} & \frac{\partial \alpha_\varphi \bar{\mathbf{U}}_\varphi}{\partial t} + \nabla \cdot (\alpha_\varphi \bar{\mathbf{U}}_\varphi \bar{\mathbf{U}}_\varphi) \\ &= \\ & \alpha_\varphi \frac{\partial \bar{\mathbf{U}}_\varphi}{\partial t} + \bar{\mathbf{U}}_\varphi \frac{\partial \alpha_\varphi}{\partial t} + \alpha_\varphi \bar{\mathbf{U}}_\varphi \cdot \nabla \bar{\mathbf{U}}_\varphi + \bar{\mathbf{U}}_\varphi \nabla \cdot (\alpha_\varphi \bar{\mathbf{U}}_\varphi) \end{aligned} \quad (6.74)$$

Next, subtracting  $\bar{\mathbf{U}}_\varphi$ -times the continuity equation (Eq. 6.23) and dividing by  $\alpha_\varphi$  yields

$$\frac{\partial \bar{\mathbf{U}}_\varphi}{\partial t} + \bar{\mathbf{U}}_\varphi \cdot \nabla \bar{\mathbf{U}}_\varphi = -\frac{\nabla p^d}{\bar{\rho}_\varphi} + \left(1 - \frac{\rho}{\bar{\rho}_\varphi}\right) \mathbf{g} - \frac{\mathbf{g} \cdot \mathbf{x} \nabla \rho}{\bar{\rho}_\varphi} + \frac{\nabla \cdot (\alpha_\varphi \bar{\boldsymbol{\tau}}_\varphi)}{\alpha_\varphi \bar{\rho}_\varphi} + \frac{\mathbf{M}_\varphi}{\alpha_\varphi \bar{\rho}_\varphi} \quad (6.75)$$

Note here, that this equation is in non-conservative form for both the instationary and convective term. The convective term can numerically be evaluated as

$$\bar{\mathbf{U}}_\varphi \cdot \nabla \bar{\mathbf{U}}_\varphi = \nabla \cdot (\bar{\mathbf{U}}_\varphi \bar{\mathbf{U}}_\varphi) - \bar{\mathbf{U}}_\varphi (\nabla \cdot \bar{\mathbf{U}}_\varphi) \quad (6.76)$$

With respect to the numerical implementation of the stress terms, they are expanded into a pure bulk and interfacial part according to

$$\frac{\nabla \cdot (\alpha_\varphi \bar{\boldsymbol{\tau}}_\varphi)}{\alpha_\varphi \bar{\rho}_\varphi} = \frac{1}{\bar{\rho}_\varphi} \nabla \cdot \bar{\boldsymbol{\tau}}_\varphi + \frac{\nabla \alpha_\varphi}{\alpha_\varphi \bar{\rho}_\varphi} \cdot \bar{\boldsymbol{\tau}}_\varphi \quad (6.77)$$

Consequently, we will need the phase-intensive form of  $\overline{\boldsymbol{\tau}}_{S\varphi}$  and  $\overline{\boldsymbol{\tau}}_{P\varphi}$ . In order to obtain the phase intensive solvent stress contribution, we simply divide Eq. 6.39 by  $\alpha_\varphi$

$$\begin{aligned} \overline{\boldsymbol{\tau}}_{S\varphi} = & \\ & \eta_{S,\varphi} \left[ \nabla \overline{\mathbf{U}}_\varphi + (\nabla \overline{\mathbf{U}}_\varphi)^T - \frac{2}{3} (\nabla \cdot \overline{\mathbf{U}}_\varphi) \mathbf{I} \right] \\ & + \frac{\eta_{S,\varphi} \eta_{eff,\omega}}{\alpha_\omega \eta_{eff,\varphi} + \alpha_\varphi \eta_{eff,\omega}} \left[ \nabla \alpha_\varphi (\overline{\mathbf{U}}_\varphi - \overline{\mathbf{U}}_\omega) + (\overline{\mathbf{U}}_\varphi - \overline{\mathbf{U}}_\omega) \nabla \alpha_\varphi - \frac{2}{3} \nabla \alpha_\varphi \cdot (\overline{\mathbf{U}}_\varphi - \overline{\mathbf{U}}_\omega) \mathbf{I} \right] \end{aligned} \quad (6.78)$$

Furthermore, the solvent stress is split into a diffusive and correction term in view of the numerical implementation

$$\overline{\boldsymbol{\tau}}_{S\varphi} = \overline{\boldsymbol{\tau}}_{S\varphi}|_{diff.} + \overline{\boldsymbol{\tau}}_{S\varphi}|_{corr.} \quad (6.79)$$

where

$$\overline{\boldsymbol{\tau}}_{S\varphi}|_{diff.} = \eta_{S,\varphi} \nabla \overline{\mathbf{U}}_\varphi \quad (6.80)$$

and

$$\begin{aligned} \overline{\boldsymbol{\tau}}_{S\varphi}|_{corr.} = & \\ & \eta_{S,\varphi} \left[ (\nabla \overline{\mathbf{U}}_\varphi)^T - \frac{2}{3} (\nabla \cdot \overline{\mathbf{U}}_\varphi) \mathbf{I} \right] \\ & + \frac{\eta_{S,\varphi} \eta_{eff,\omega}}{\alpha_\omega \eta_{eff,\varphi} + \alpha_\varphi \eta_{eff,\omega}} \left[ \nabla \alpha_\varphi (\overline{\mathbf{U}}_\varphi - \overline{\mathbf{U}}_\omega) + (\overline{\mathbf{U}}_\varphi - \overline{\mathbf{U}}_\omega) \nabla \alpha_\varphi - \frac{2}{3} \nabla \alpha_\varphi \cdot (\overline{\mathbf{U}}_\varphi - \overline{\mathbf{U}}_\omega) \mathbf{I} \right] \end{aligned} \quad (6.81)$$

The same approach that was applied to the momentum equation is now used for the Oldroyd-B equation. We start by applying the product rule to the instationary and convective terms of Eq. 6.59 to obtain

$$\begin{aligned} & \frac{\partial \alpha_\varphi \overline{\boldsymbol{\tau}}_{P\varphi}}{\partial t} + \nabla \cdot (\alpha_\varphi \overline{\boldsymbol{\tau}}_{P\varphi} \overline{\mathbf{U}}_\varphi) \\ = & \\ & \alpha_\varphi \frac{\partial \overline{\boldsymbol{\tau}}_{P\varphi}}{\partial t} + \overline{\boldsymbol{\tau}}_{P\varphi} \frac{\partial \alpha_\varphi}{\partial t} + \alpha_\varphi \overline{\mathbf{U}}_\varphi \cdot \nabla \overline{\boldsymbol{\tau}}_{P\varphi} + \overline{\boldsymbol{\tau}}_{P\varphi} \nabla \cdot (\alpha_\varphi \overline{\mathbf{U}}_\varphi) \end{aligned} \quad (6.82)$$

Next, subtracting  $\lambda_\varphi \overline{\boldsymbol{\tau}}_{P\varphi}$  multiplied with Eq. 6.23 and dividing by  $\alpha_\varphi$  from Eq. 6.59 leads to the phase-intensive conditionally volume averaged Oldroyd-B equation

$$\begin{aligned}
 & \overline{\boldsymbol{\tau}}_{P\varphi} + \lambda_\varphi \left[ \left( \frac{\partial \overline{\boldsymbol{\tau}}_{P\varphi}}{\partial t} \right) + \overline{\mathbf{U}}_\varphi \cdot \nabla \overline{\boldsymbol{\tau}}_{P\varphi} - (\nabla \overline{\mathbf{U}}_\varphi)^T \cdot \overline{\boldsymbol{\tau}}_{P\varphi} - \overline{\boldsymbol{\tau}}_{P\varphi} \cdot \nabla \overline{\mathbf{U}}_\varphi \right] \\
 & = \\
 & \eta_{P,\varphi} \left[ \nabla \overline{\mathbf{U}}_\varphi + (\nabla \overline{\mathbf{U}}_\varphi)^T - \frac{2}{3} (\nabla \cdot \overline{\mathbf{U}}_\varphi) \mathbf{I} \right] \\
 & + \frac{\eta_{P,\varphi} \eta_{eff,\omega}}{\alpha_\omega \eta_{eff,\varphi} + \alpha_\varphi \eta_{eff,\omega}} \left[ \nabla \alpha_\varphi (\overline{\mathbf{U}}_\varphi - \overline{\mathbf{U}}_\omega) + (\overline{\mathbf{U}}_\varphi - \overline{\mathbf{U}}_\omega) \nabla \alpha_\varphi - \frac{2}{3} \nabla \alpha_\varphi \cdot (\overline{\mathbf{U}}_\varphi - \overline{\mathbf{U}}_\omega) \mathbf{I} \right]
 \end{aligned} \tag{6.83}$$

where the nonconservative convection term is treated numerically as

$$\overline{\mathbf{U}}_\varphi \cdot \nabla \overline{\boldsymbol{\tau}}_{P\varphi} = \nabla \cdot (\overline{\boldsymbol{\tau}}_{P\varphi} \overline{\mathbf{U}}_\varphi) - (\nabla \cdot \overline{\mathbf{U}}_\varphi) \overline{\boldsymbol{\tau}}_{P\varphi} \tag{6.84}$$

### 6.3.4 Stabilization using the Both Sides Diffusion

In order to stabilize the solution procedure due to the treatment of viscoelasticity, we use the both sides diffusion (BSD) technique, which introduces an elliptic operator into the momentum equation (Eq. 6.75 coupled with Eq. 6.77), see for example [32]

$$\begin{aligned}
 & \frac{\partial \overline{\mathbf{U}}_\varphi}{\partial t} + \overline{\mathbf{U}}_\varphi \cdot \nabla \overline{\mathbf{U}}_\varphi - \nabla \cdot \left( \frac{\eta_{P,\varphi}}{\bar{\rho}_\varphi} \nabla \overline{\mathbf{U}}_\varphi \right) \\
 & = \\
 & - \frac{\nabla p^d}{\bar{\rho}_\varphi} + \left( 1 - \frac{\rho}{\bar{\rho}_\varphi} \right) \mathbf{g} - \frac{\mathbf{g} \cdot \mathbf{x} \nabla \rho}{\bar{\rho}_\varphi} \\
 & + \frac{1}{\bar{\rho}_\varphi} \nabla \cdot \overline{\boldsymbol{\tau}}_\varphi + \frac{\nabla \alpha_\varphi}{\alpha_\varphi \bar{\rho}_\varphi} \cdot \overline{\boldsymbol{\tau}}_\varphi - \nabla \cdot \left( \frac{\eta_{P,\varphi}}{\bar{\rho}_\varphi} \nabla \overline{\mathbf{U}}_\varphi \right) + \frac{\mathbf{M}_\varphi}{\alpha_\varphi \bar{\rho}_\varphi}
 \end{aligned} \tag{6.85}$$

### 6.3.5 Summary of the model

Finally, assembling all of the above equations yields our final set of equations describing viscoelastic two-phase flows for both  $\varphi$  and  $\omega$ : the phase fraction convection (Eqs. 6.73 and 6.34), continuity (Eq. 6.71), momentum (Eq. 6.85 in combination with Eqs. 6.65, 6.80 and 6.81) and the Oldroyd-B equation (Eq. 6.83).

### 6.3.6 Numerical discretization

In this section, we will briefly outline the discretization practices adopted to solve the above set of equations.

The package *OpenFOAM*<sup>®</sup>, which is based on the finite volume method, is used. This package is capable of handling both regular orthogonal cells and non-orthogonal cells. A collocated grid arrangement is used storing all variables at the cell centers.

For temporal discretization we use a three-point scheme giving at least second order accuracy in time. [33]

The convective terms are discretized using the Gamma scheme with a blending factor of 0.8. [34] A study on viscoelastic single-phase flows using this scheme can be found in Favero et al. [35].

### 6.3.7 Iterative procedure

In order to solve the above strongly coupled set of equations, we use a pressure-implicit with splitting of operators algorithm (PISO). [36] The iterative procedure can be summarized as follows

- 1.) Solve the phase fraction equation Eq. 6.73 for a given number of times ( $n_\alpha = 2$ ).
- 2.) PISO-Loop:
  - 2.1.) Predict the cell fluxes.
  - 2.2.) Construct and solve a Poisson-type equation for pressure using Eq. 6.71.
  - 2.3.) Correct the fluxes and velocities.
  - 2.4.) Repeat from a) for a given number of times ( $n_{PISO} = 2$ ).
- 3.) Solve the Oldroyd-B equations Eqs. 6.83.
- 4.) If necessary, repeat from 1.) until a given accuracy is met (in this work  $n_{total} = 1$  is used throughout).

For pressure correction, a PCG solver with DIC preconditioning is used at a tolerance of  $10^{-12}$ . For the phase fraction and polymeric stress equations, a BiCGStab is used with a Cholesky preconditioner at a tolerance of  $10^{-10}$  for phase fraction and  $10^{-6}$  for stress, respectively.



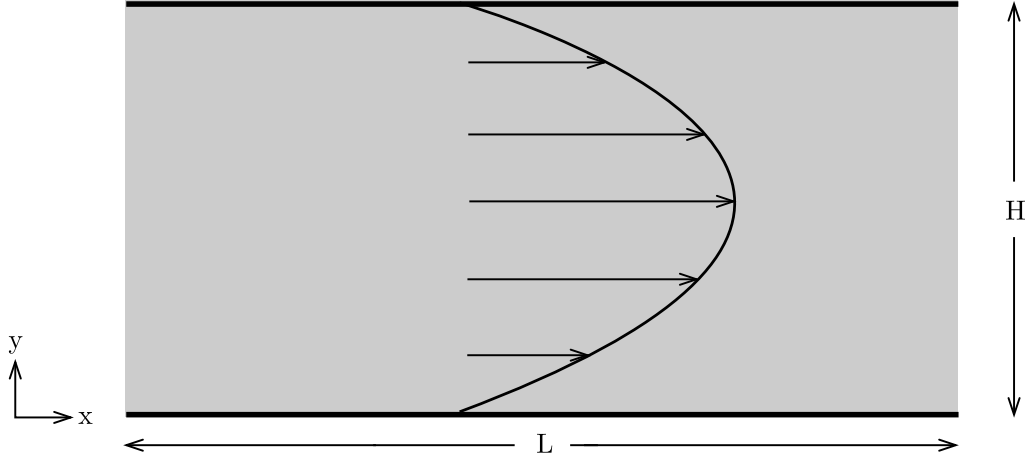


Figure 6.1: Domain and boundary conditions for a single phase Poiseuille flow.

## 6.4 Results and Discussion

### 6.4.1 Single Phase Flow

In the case of only one fluid being present, a model for multiphase-flows must behave as a single-phase model. This is, we have  $\alpha_\varphi = 1$  throughout the domain. The phase fraction equation (Eq. 6.73) reduces to  $\alpha_\varphi = const.$ , whereas the second modified continuity equation (Eq. 6.71) reduces to the single phase incompressibility constraint  $\nabla \cdot \bar{\mathbf{U}}_\varphi = 0$ . No coupling interfacial terms are present, and the momentum equation for phase  $\varphi$  (Eq. 6.85) reduces to the single-phase momentum equation. The same applies to the stress models (Eqs. 6.81 and 6.83), in which the interfacial terms disappear. In this section, we will prove this behavior numerically.

Therefore, consider a single-phase flow between two parallel plates due to a pressure gradient (Poiseuille-flow), see Fig. 6.1. The retardation ratio is set to  $\beta = \eta_S/\eta_0 = 0.5$  and the local Weissenberg number at the wall is chosen to be  $Wi_{wall} = \lambda \dot{\gamma}_{wall} = 1$ . The domain is discretized with regular hexahedra with  $\Delta x/\Delta y = 1$  with 40 cells in y-direction and 20 cells in x/flow-direction.

The results for the normalized velocity, polymeric normal and shear stress are shown in Fig. 6.2. The excellent agreement with the single-phase analytical solution proves that the above condition is satisfied and the single phase model is recovered. Defining a maximum error for the quantity  $\Phi$  according to

$$e_{L_\infty}^\Phi := \max_j^N (|\Phi_{ana,j} - \Phi_{num,j}|) \quad (6.86)$$

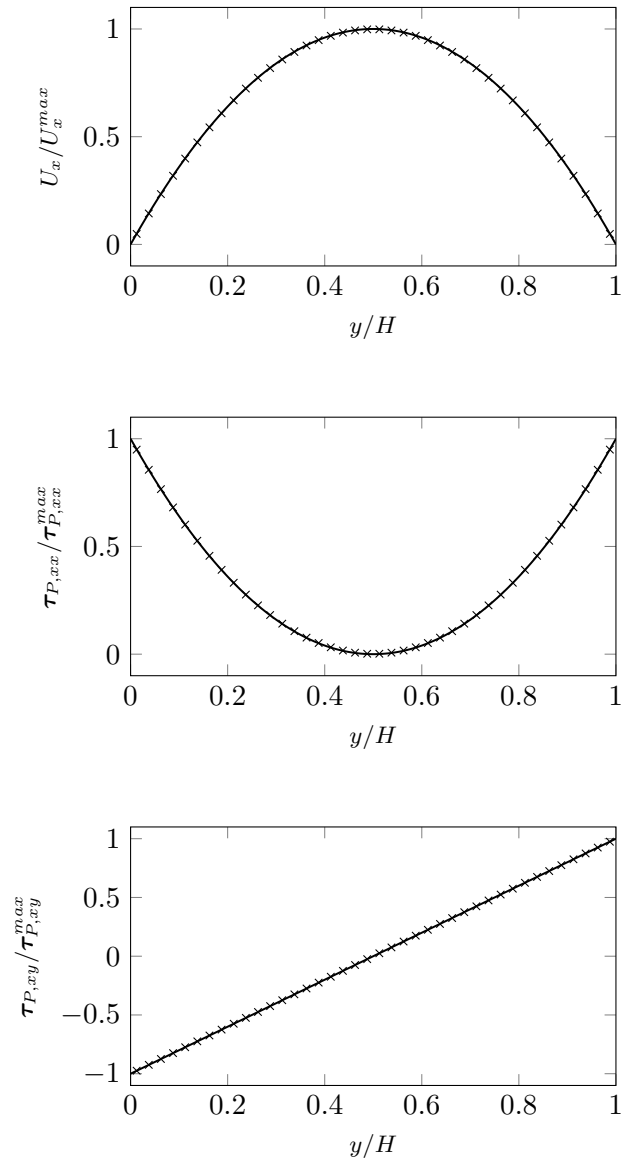


**Figure 6.2:** Single-phase flow between two parallel plates. Solid line is the analytical solution, crosses are numerical predictions.

for  $N$  values, which correspond to the cell centered values, we obtain the error for velocity of  $e_\infty^{u_x} = 1.25 \cdot 10^{-3}$ , for the polymeric normal stress of  $e_\infty^{\tau^{P,xx}} = 5.23 \cdot 10^{-5}$  and for the polymeric shear stress of  $e_\infty^{\tau^{P,xy}} = 1.14 \cdot 10^{-5}$ .

### 6.4.2 Shear-flow parallel to a planar interface

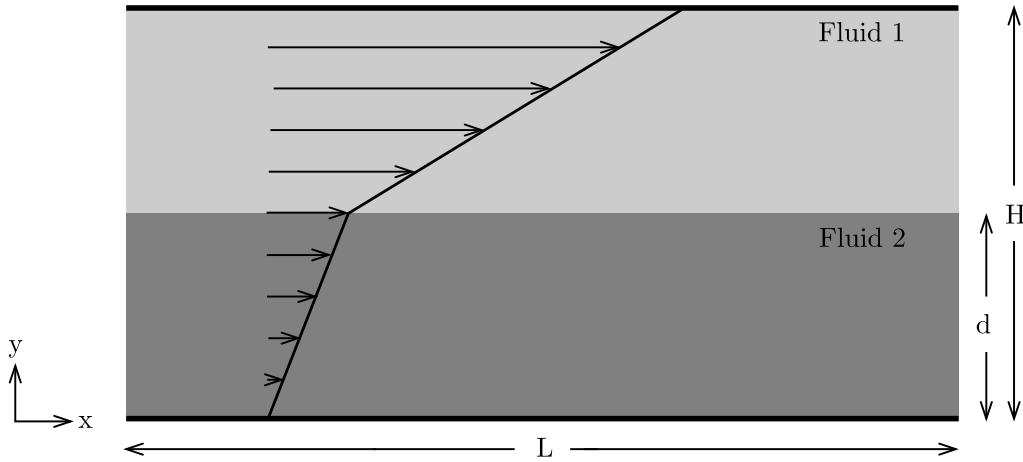


**Figure 6.3:** Domain and boundary conditions for a shear flow parallel to a flat interface at different viscosities.

In this section, a two-phase shear flow parallel to a planar interface is considered in order to examine the coupling between the two phases and the choice of  $h = 11.028$ . Furthermore, the behavior of the model with mesh refinement and varying diffuse interface width is examined.

In Fig. 6.3 the domain is shown. The fluids have a viscosity ratio of  $\eta_r = \eta_2/\eta_1 = 10$ . We set the retardation ratio to  $\beta = 0.5$  and choose a very small relaxation time, i.e.,  $\lambda_1 = \lambda_2 \rightarrow 0$ . The upper wall moves in positive  $x$ -direction and the lower wall remains stationary, such that the interface moves in  $x$ -direction with a velocity of  $(U_{I,x}/U_{wall,x} = (\eta_r + 1)^{-1})$ . The domain is discretized with regular hexahedra with  $\Delta x/\Delta y = 1$ . The diffuse interface is assigned with a tangent hyperbolic profile according to

$$\alpha_\varphi = 0.5 \left( 1 - \tanh \left( \frac{y - 0.5 \text{ m}}{2\delta} \right) \right)$$

where  $y$  is the height and  $\delta$  is the diffuse interface width, such that  $\alpha_\varphi$  varies between 0.05 and 0.95 over  $6\delta$ . [20] The ratio of  $\delta/\Delta x$  is the interfacial resolution and is proportional to the number of interface containing cells in the interface-normal direction.

The results are shown in Fig. 6.4. In the first column, we vary the interface resolution between  $\delta/\Delta x = 0.25 \dots 4$  (corresponding to  $H/\delta = 640 \dots 40$ ) at a constant cell count number of  $H/\Delta x = 160$  distributed over the height. We find that the velocities match the analytical profile almost perfectly, except for the case of the smallest interface width considered. In this case, the interface width compared to cell size is  $\delta/\Delta x = 0.25$  corresponding to approximately

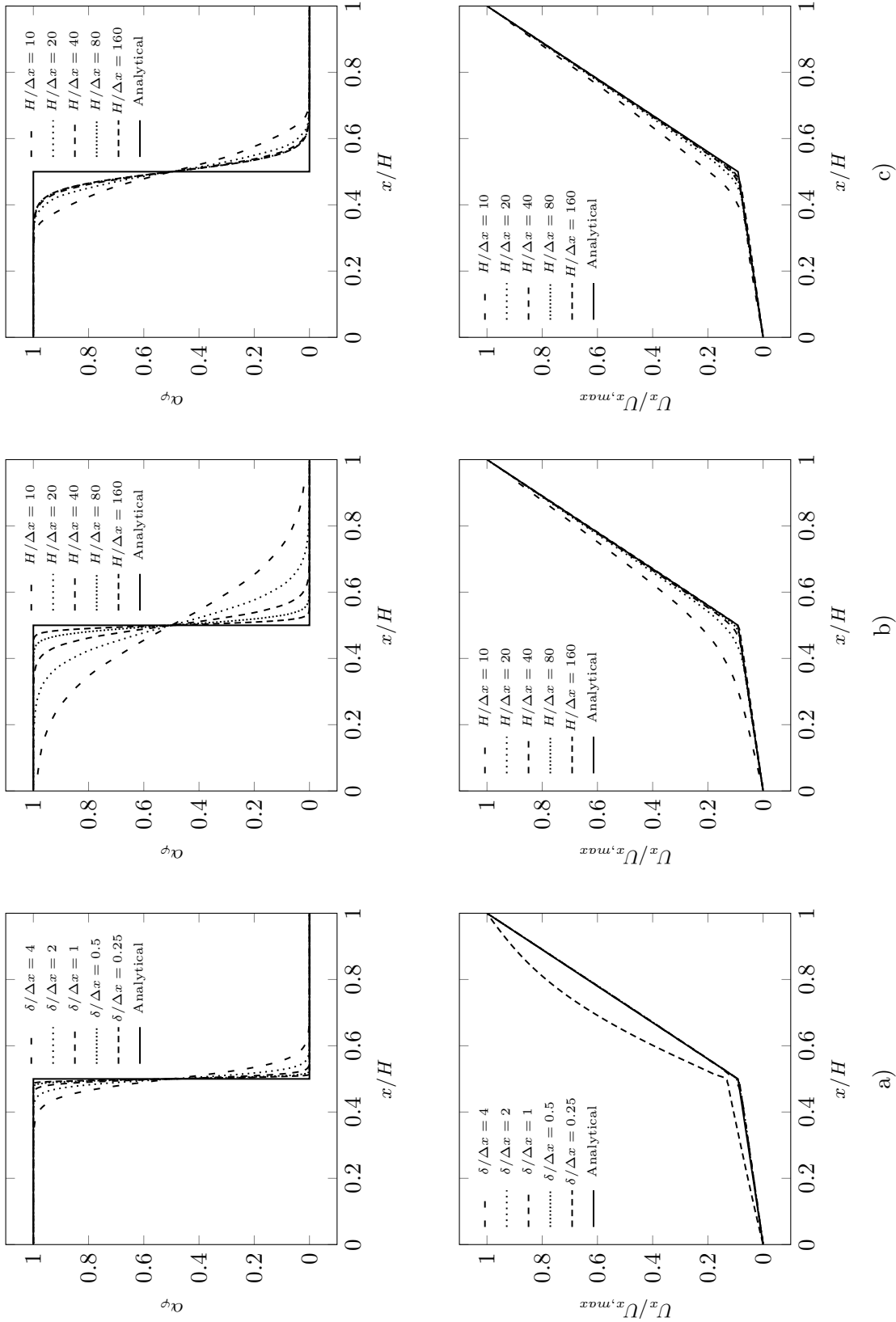


**Figure 6.4:** Volume fraction and velocity profiles across a planar interface with a shear-flow parallel to the interface at  $\eta_r = 10$ . a)  $H/\Delta x = 160$  as a function of  $\delta/\Delta x$ , b)  $\delta/\Delta x = 1$  as a function of  $H/\Delta x$ , c)  $H/\delta = 40$  as a function of  $H/\Delta x$  ( $\delta/\Delta x = 1/40 \cdot H/\Delta x$ ).

two interface containing cells in the interface-normal direction. It is our understanding that in this case the coupling between the two-phases is too small resulting in an unphysical velocity profile. Provided that the interface resolution is sufficient, which in this case is  $\delta/\Delta x \geq 0.5$ , the velocity profiles match the analytical profile regardless of the interface width. In the middle column of Fig. 6.4, we keep the interface resolution constant at  $\delta/\Delta x = 1$  (corresponding to approximately nine interface containing cells in the interface-normal direction), which was found to be a sufficient resolution, and vary the cell number from  $H/\Delta x = 10 \dots 160$  in the y-direction. Here we find that the velocities vary smoothly inside of the diffuse interface, whereas outside of the diffuse interface they are found to exactly match the analytical velocity profile. This is in accordance with the results of Sun and Beckermann [20]. It has to be pointed out that for the smallest cell size, the interface is distributed over the entire height of the domain, while still having nearly the correct slope at the walls. In the results shown in the third column of Fig. 6.4, we have a constant interface width compared to the height of the domain of  $H/\delta = 40$  corresponding to an interface height of approximately 0.2 m. Herein, we vary the cell count number in y-direction from 10 to 160, which corresponds to interfacial resolutions of  $\delta/\Delta x = 0.25 \dots 4$ . For  $\delta/\Delta x = 0.25$  the profile deviates from the analytical solution. However, for finer interface resolutions, we again find that the velocities match the analytical solution very well, while smoothly varying inside of the diffuse interface.

Overall, we find that a value of  $h = 11.028$  is a reasonable choice, since the above results show that the analytical profile is reproduced almost perfectly. Furthermore, as a result of the above examined behavior of the model, one may in fact choose an arbitrary interface width, which, if being sufficiently resolved, does not bias the velocity outside of it. Considering a flow of interest, the upper limit of the interface width is solely determined by the length scales of interest, i.e., the characteristic curvature of the interface. This is a remarkable advantage compared to common diffuse interface methods.

### 6.4.3 Pressure jump across a cylindrical interface due to surface tension

In this section, the behavior of the surface tension closure is examined by considering a case without flow having a two-dimensional cylindrical interface with surface tension.

Consider a quadrant of length and height  $L = H$ , in which a cylindrical interface of  $D = 2R = L$  is imposed with its center on the left bottom. Symmetry boundary conditions are imposed at the bottom and left hand side.

The far-field pressure is set to  $p_\infty = 0 \text{ kg/ms}^2$ . Again, regular hexahedra, i.e.,  $\Delta x/\Delta y = 1$ , are used for discretization. The diffuse interface is set up using a tangent hyperbolic profile similar to the last case.

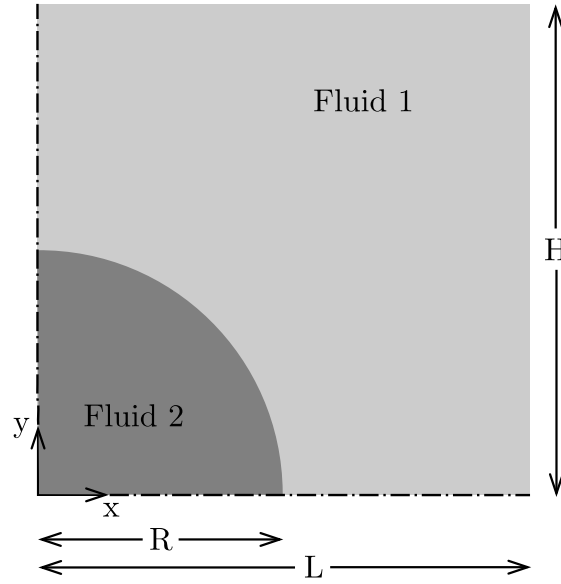


**Figure 6.5:** Domain and boundary conditions for a pressure difference due to a cylindrical interface with surface tension.

At first, we set a constant discretization of  $D/\Delta x (= L/\Delta x = H/\Delta x) = 160$  and vary the interface width such as to obtain resolutions of  $\delta/\Delta x = 0.25 \dots 4$ , which is shown in the left column of Fig. 6.6. Here we find, that for the coarsest interface resolution, i.e.,  $\delta/\Delta x = 0.25$ , the pressure profile possesses overshoots and undershoots resulting in a profile with two kinks. Furthermore, the Young-Laplace equation is not satisfied, as can be seen from the total pressure difference. This effect attenuates with finer interface resolution, i.e.,  $\delta/\Delta x = 0.5$ , and totally disappears when  $\delta/\Delta x = 1$ . Furthermore, we find that for  $\delta/\Delta x \geq 1$  the Young-Laplace relation is sufficiently reproduced. In the middle column of Fig. 6.6, the interface resolution is kept at a constant  $\delta/\Delta x = 1$ , which, as can be seen in the left column, is a sufficient resolution. We vary the cell count number in y-direction from  $D/\Delta x = 10$  to  $H/\Delta x = 160$ . For the coarsest resolution  $D/\Delta x = 10$ , the interface is distributed over the total radius of the cylindrical interface resulting in a smoothed pressure profile over the whole cylinder. Furthermore, the Young-Laplace relation is not satisfied. By doubling the resolution to  $D/\Delta x = 20$ , the pressure profile almost matches the analytical pressure profile outside of the diffuse interface while smoothly varying inside of the diffuse interface. From  $H/\Delta x \geq 40$ , we find, that the pressure profile is almost perfectly reproduced outside of the diffuse interface. Further, the volume fraction and pressure profile sharpen with further mesh refinement due to the constant interface resolution of  $\delta/\Delta x = 1$ . In the third column of Fig. 6.6, we impose a constant diffuse interface width of  $D/\delta = 40$  corresponding to an interface width of approximately 0.2 m (with the diameter of the cylindrical interface being 1 m), while successively refining the mesh from  $D/\Delta x = 10$  to  $D/\Delta x = 160$  corresponding to interface resolutions from  $\delta/\Delta x = 0.25$  to  $\delta/\Delta x = 4$ , respectively. Again, we find, that the Young-Laplace relation is satisfactorily reproduced from  $\delta/\Delta x \geq 1$ .

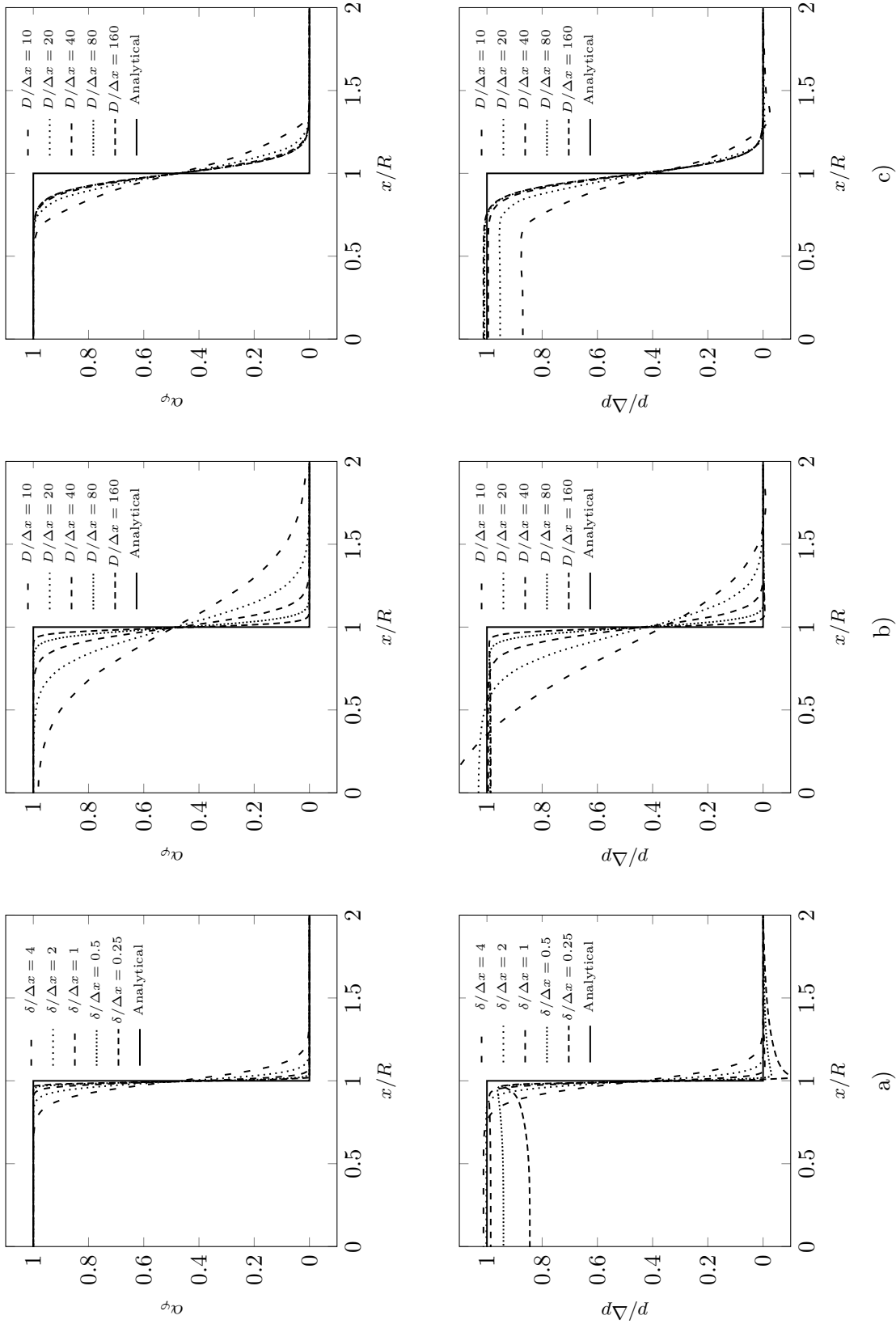


**Figure 6.6:** Volume fraction and pressure profiles across a cylindrical interface with surface tension. a)  $D/\Delta x = 160$  as a function of  $\delta/\Delta x$ , b)  $\delta/\Delta x = 1$  as a function of  $D/\Delta x$ , c)  $D/\delta = 40$  as a function of  $D/\Delta x$  ( $\delta/\Delta x = 1/40 \cdot D/\Delta x$ ).

To summarize, we find that in order to numerically model two-phase flows with surface tension using the closure relation in Eq. 6.61 one needs a sufficient resolution of the diffuse interface width, i.e.,  $\delta/\Delta x \geq 1$  corresponding to the interface being distributed over approximately nine cells. Furthermore, using an interface resolution of  $\delta/\Delta x = 1$ , the characteristic radius must be at least  $R/\delta = 20$  (see the results of the middle column of Fig. 6.6). However, due to the model behavior shown in the last case, one can in fact provide a sufficiently resolved interface distributed over an arbitrary number of cells, without biasing the flow outside of the interface. These results prove the capability of the model to predict large scale flows by numerically motivated diffusion of the interfacial region without falsifying the results, which is an exceptional behavior.

**Table 6.1:** Fluid properties.

$\eta_r$	$\beta_1$	$\beta_2$	$Wi_1$	$Wi_2$
27.03	0.5	0.5	0.2059	0.2059

#### 6.4.4 Mesh convergence study: Poiseuille Two-Phase Flow

In this section, we will examine the convergence properties of the model with respect to the spatial discretization using a stratified two-phase flow due to a pressure gradient (two-phase Poiseuille flow). Note here, that this is not a convection dominated flow.

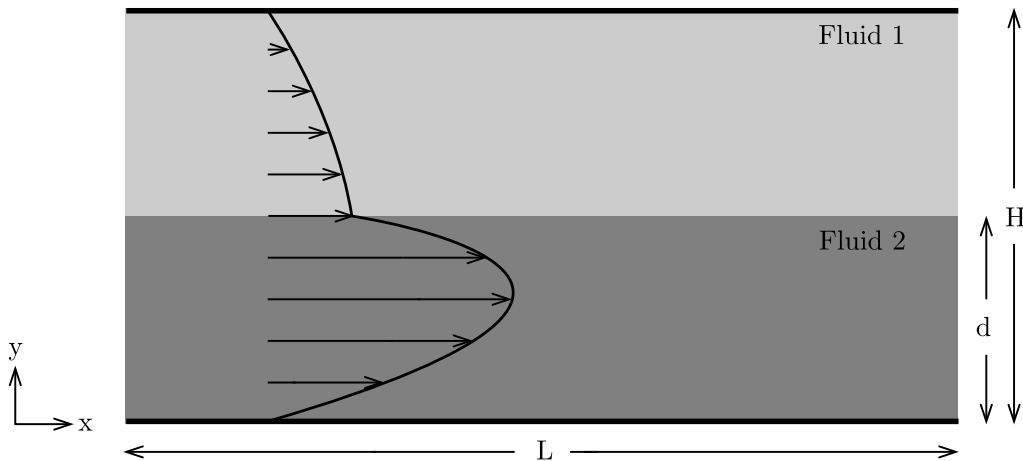


**Figure 6.7:** Domain and boundary conditions for a stratified two-phase Poiseuille flow between two parallel plates.

The domain and boundary conditions are shown in Fig. 6.7 with  $L = 2H$  and the interface being located at  $d = H/2$ . The fluid properties are tabulated in Table 6.1 with the



Weissenberg number defined as  $Wi = \lambda U_{x,max}/H$ . The meshes used for mesh convergence analysis are listed in Table 6.2.

**Table 6.2:** Meshes used for mesh convergence analysis.

Mesh	$N_x$	$N_y$	$H/\Delta x$	Number of control volumes
M1	10	10	0.1	100
M2	20	20	0.05	400
M3	40	40	0.025	1600
M4	80	80	0.0125	6400

The analytical expressions for the velocity, normal and shear stresses are given as follows

$$\mathbf{U}_x(y) = \begin{cases} \frac{1}{2\eta_1} \frac{\partial p}{\partial x} \left( y^2 - \frac{H^2+d^2(\eta_2/\eta_1-1)}{H+d(\eta_2/\eta_1-1)} y \right), & \text{for } 0 \leq y < h \\ \frac{1}{2\eta_2} \frac{\partial p}{\partial x} \left( y^2 - \frac{H^2+d^2(\eta_2/\eta_1-1)}{H+d(\eta_2/\eta_1-1)} y + \frac{(\eta_2/\eta_1-1)(Hd^2-H^2d)}{H+d(\eta_2/\eta_1-1)} \right), & \text{for } h < y \leq H \end{cases}$$

$$\tau_{P,xx}(y) = \begin{cases} 2\eta_{P,1}\lambda_1 \left[ \frac{1}{\eta_1} \frac{\partial p}{\partial x} \left( y - \frac{1}{2} \frac{H^2+d^2(\eta_2/\eta_1-1)}{H+d(\eta_2/\eta_1-1)} \right) \right]^2, & \text{for } 0 \leq y < h \\ 2\eta_{P,2}\lambda_2 \left[ \frac{1}{\eta_2} \frac{\partial p}{\partial x} \left( y - \frac{1}{2} \frac{H^2+d^2(\eta_2/\eta_1-1)}{H+d(\eta_2/\eta_1-1)} \right) \right]^2, & \text{for } h < y \leq H \end{cases}$$

$$\tau_{P,xy}(y) = \begin{cases} \frac{\eta_{P,1}}{\eta_1} \frac{\partial p}{\partial x} \left( y - \frac{1}{2} \frac{H^2+d^2(\eta_2/\eta_1-1)}{H+d(\eta_2/\eta_1-1)} \right), & \text{for } 0 \leq y < h \\ \frac{\eta_{P,2}}{\eta_2} \frac{\partial p}{\partial x} \left( y - \frac{1}{2} \frac{H^2+d^2(\eta_2/\eta_1-1)}{H+d(\eta_2/\eta_1-1)} \right), & \text{for } h < y \leq H \end{cases}$$

Using these expressions, we calculate the error using the  $L_1$ - and  $L_2$ -norms of the quantity  $\Phi$  according to

$$e_{L_1}^\Phi := \frac{1}{N} \sum_j^N |\Phi_{ana,j} - \Phi_{num,j}|$$

$$e_{L_2}^\Phi := \sqrt{\frac{1}{N} \sum_j^N (\Phi_{ana,j} - \Phi_{num,j})^2}$$

as well as the  $L_\infty$ -error (see Eq. 6.86).

The rate of convergence  $p$  is calculated using the errors of two successive meshes  $e_1$  and  $e_2$  (with the characteristic cell length being halved).

$$p = \log_2 \left( \frac{e_1}{e_2} \right)$$

The diffuse interface is assigned with a tangent hyperbolic profile. For the convergence analysis, we use the approach of having a constant  $\delta/\Delta x = 1$ , when refining the mesh. Note, that this was shown to give good results both for flows at different viscosities and flows involving surface tension, as shown in the above two cases.

The resulting volume fraction, velocity, normal and shear stress profiles are shown in Fig. 6.8 for the four different meshes. The diffuse interface is sharpened with mesh refinement due to the condition  $\delta/\Delta x = 1$ . The velocity profile is reproduced quite well, except for the coarsest mesh, in which the interface is distributed over almost the total height of the channel. With mesh refinement, we again find that the velocity smoothly varies inside of the diffuse interface, while not falsifying the solution outside of the diffuse interface. However, for the coarse mesh we find the velocity to perceptibly deviate from the analytical solution, which is due to the small spatial resolution. When considering the normal stress, we find the same behavior as we saw for the velocity, i.e. the deviation reduces with mesh refinement and the profiles match the analytical solution, outside of the diffuse interface, except for the coarse mesh. The jump in the normal stress is smoothed over the diffuse interface. The transition region is becoming smaller and the smoothed profile becoming steeper with mesh refinement. The necessary condition, that the jump is reproduced for  $\delta \rightarrow 0$ , is met. The linear shear stress profile is almost exactly predicted for all meshes.

In Table 6.3, the errors for velocity, normal and shear stress are tabulated according to the above error definitions and analytical solutions. In Table 6.4, the rate of convergence using the errors of Table 6.3 are listed. No monotonic convergence can be found for the meshes under consideration, with the rates varying from approximately  $p = 0.5 \dots 1.8$ . Two rates are negative, indicating that the error increases with mesh refinement. For the mesh transition  $M1 - M2$ , the  $L_\infty$ -error for the normal stress increases. Both maxima can be found in the cell next to the interface in the less viscous phase. The negativeness in  $p$  is due to the center of the cell of mesh  $M2$  being closer to the interface and thus being compared to a larger value of the normal stress resulting in a larger error. The reason for the negativeness in  $p$  calculated from

**Table 6.3:** Error calculation for Poiseuille two-phase flow simulation.

Mesh	$L_1$ -Norm			$L_2$ -Norm			$L_\infty$ -Norm		
	U [m/s]	$\tau_{xx}$ [N/m <sup>2</sup> ]	$\tau_{xy}$ [N/m <sup>2</sup> ]	U [m/s]	$\tau_{xx}$ [N/m <sup>2</sup> ]	$\tau_{xy}$ [N/m <sup>2</sup> ]	U [m/s]	$\tau_{xx}$ [N/m <sup>2</sup> ]	$\tau_{xy}$ [N/m <sup>2</sup> ]
1	$2.849e^{-3}$	$3.568e^{-5}$	$7.719e^{-6}$	$3.884e^{-3}$	$6.134e^{-5}$	$8.443e^{-6}$	$8.904e^{-3}$	$1.819e^{-4}$	$1.701e^{-5}$
2	$8.551e^{-4}$	$2.412e^{-5}$	$1.972e^{-6}$	$1.379e^{-3}$	$4.944e^{-5}$	$2.364e^{-6}$	$3.943e^{-3}$	$1.953e^{-4}$	$4.945e^{-6}$
3	$3.736e^{-4}$	$1.333e^{-5}$	$1.522e^{-6}$	$6.234e^{-4}$	$3.642e^{-5}$	$1.699e^{-6}$	$2.306e^{-3}$	$1.910e^{-4}$	$3.954e^{-6}$
4	$2.453e^{-4}$	$7.378e^{-6}$	$1.234e^{-6}$	$3.538e^{-4}$	$2.432e^{-5}$	$8.794e^{-7}$	$1.075e^{-3}$	$1.737e^{-4}$	$6.307e^{-6}$

**Table 6.4:** Rate of convergence for Poiseuille two-phase flow simulation.

Meshes	$L_1$ -Norm		$L_2$ -Norm		$L_\infty$ -Norm				
	U	$\tau_{xx}$	U	$\tau_{xy}$	U	$\tau_{xx}$	U	$\tau_{xy}$	
M1-M2	1.736	0.565	1.969	1.494	0.311	1.836	1.175	-0.102	1.782
M2-M3	1.195	0.856	0.374	1.145	0.441	0.477	0.774	0.032	0.323
M3-M4	0.607	0.854	0.303	0.817	0.583	0.950	1.101	0.137	-0.673

the  $L_\infty$ -error of the shear stress for mesh transition  $M3 - M4$  is that the solution tolerance for the constitutive equation is of the same order as the errors of the stress.

## 6.5 Conclusions

In this work we developed a model for simulating viscoelastic two-phase flows derived from conditional volume averaging of the single-phase conservation equations. This procedure results in a set of conservation equations, one for each phase, having unclosed term. Subsequently, closure modeling is done. For the first time, we apply the aforementioned technique to a viscoelastic constitutive equation - the Oldroyd-B model - in order to obtain a closure for the stress. Furthermore, closures for the interfacial morphology, the momentum source due to surface tension and interfacial force density, which accounts for the viscous coupling between the two phases, are presented. This is done by splitting averaged terms into a mean part and a fluctuation part. Next, a numerical methodology was presented to solve the strongly coupled system of equations. Due to numerical issues, the equations are first reformulated.

We showed, that the developed model is capable of predicting several basic test cases. Moreover, the model possesses outstanding properties. That is, the interface width may be chosen arbitrary large without falsifying the solution outside of the diffuse interface, as long as it is sufficiently resolved. This is especially necessary, if surface tension is present, for which a certain width is needed to numerically evaluate the curvature of the interface. Having that in mind, we pursued a convergence analysis for a viscoelastic two-phase Poiseuille flow by keeping the interface resolution constant while refining the mesh. Consistency and convergence were proved.

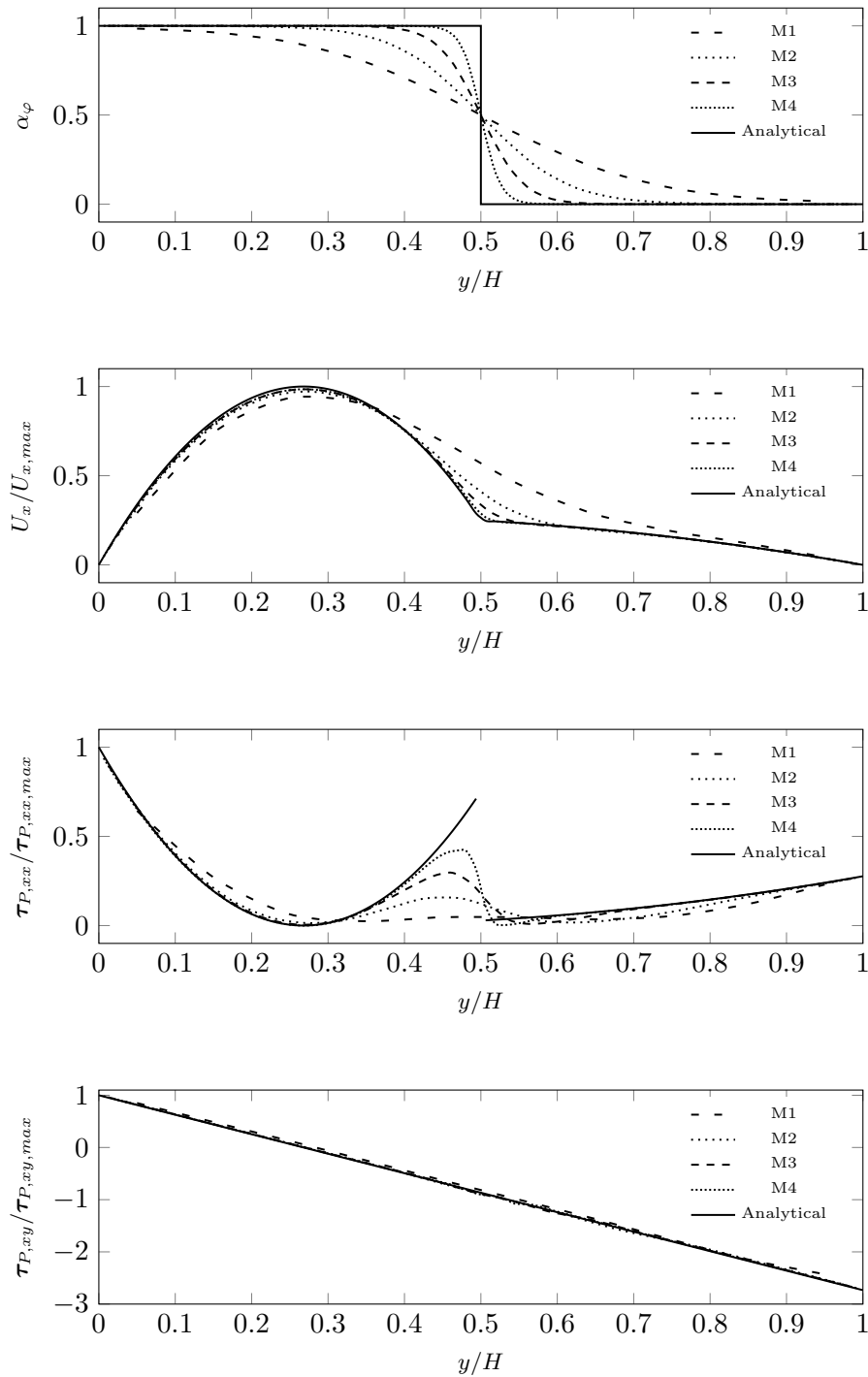


**Figure 6.8:** Volume fraction, velocity and stress profiles of the Poiseuille two-phase flow simulation at a constant  $\delta/\Delta x = 1$ .

## 6.A Literature

- [1] D. M. Bryce, *Plastic Injection Molding: Manufacturing Process Fundamentals*, Society of Manufacturing Engineers, 1996.
- [2] L. A. Utracki, *Polymer Alloys and Blends*, Munich: Hanser, 1989.
- [3] C. Rauwendaal, *Polymer Extrusion*, Hanser Fachbuch, 2001.
- [4] V. Cristini, J. Blawdziewicz, M. Loewenberg, Drop breakup in three-dimensional viscous flows, *Physics Fluids* 10 (1998) 1781–1783.
- [5] D. M. Anderson, G. B. McFadden, A. A. Wheeler, Diffuse-interface methods in fluid mechanics, *Annual Review of Fluid Mechanics* 30 (1998) 139–65.
- [6] C. W. Hirt, B. D. Nichols, Volume of fluid (VOF) method for the dynamics of free boundaries, *Journal of Computational Physics* 39 (1981) 201–225.
- [7] J. M. Kim, K. H. Ahn, S. J. Lee, S. J. Lee, Numerical simulation of moving free surface problems in polymer processing using volume-of-fluid method, *Polymer Engineering & Science* 41 (2001) 858–866.
- [8] F. Habla, H. Marschall, O. Hinrichsen, L. Dietsche, H. Jasak, J. L. Favero, Numerical simulation of viscoelastic two-phase flows using OpenFOAM, *Chemical Engineering Science* 66 (2011) 5487–5496.
- [9] M. Sussman, P. Smereka, S. Osher, A level set approach for computing solutions to incompressible two-phase flow, *Journal of Computational Physics* 114 (1994) 146–159.
- [10] Y. C. Chang, T. Y. Hou, B. Merriman, S. Osher, A level set formulation of Eulerian interface capturing methods for incompressible fluid flows, *Journal of Computational Physics* 124 (1996) 449–464.
- [11] S. B. Pillapakam, P. Singh, A level-set method for computing solutions to viscoelastic two-phase flow, *Journal of Computational Physics* 174 (2001) 552–578.
- [12] M. Sussman, E. G. Puckett, A coupled level set and volume-of-fluid method for computing 3D and axisymmetric incompressible two-phase flows, *Journal of Computational Physics* 162 (2000) 301–337.
- [13] M. Sussman, A second order coupled level set and volume-of-fluid method for computing growth and collapse of vapor bubbles, *Journal of Computational Physics* 187 (2003) 110–136.

- [14] P. A. Stewart, N. Lay, M. Sussman, M. Ohta, An improved sharp interface method for viscoelastic and viscous two-phase flows, *Journal of Scientific Computing* 35 (2008) 43–61.
- [15] S. O. Unverdi, G. Tryggvason, Computations of multi-fluid flows, *Physica D* 60 (1992a) 70–83.
- [16] S. O. Unverdi, G. Tryggvason, A front-tracking method for viscous, incompressible, multi-fluid flows, *Journal of Computational Physics* 100 (1992b) 25–37.
- [17] P. Yue, J. J. Feng, C. Liu, J. Shen, A diffuse-interface method for simulating two-phase flows of complex fluids, *Journal of Fluid Mechanics* 515 (2004) 293–317.
- [18] P. Yue, J. J. Feng, C. Liu, J. Shen, Transient drop deformation upon startup of shear in viscoelastic fluids, *Physics of Fluids* 17 (2005) 123101.
- [19] C. Beckermann, H.-J. Diepers, I. Steinbach, A. Karma, X. Tong, Modeling melt convection in phase-field simulations of solidification, *Journal of Computational Physics* 154 (1999) 468–496.
- [20] Y. Sun, C. Beckermann, Diffuse interface modeling of two-phase flows based on averaging: mass and momentum equations, *Physica D* 198 (2004) 281–308.
- [21] Y. Sun, C. Beckermann, A two-phase diffuse-interface model for hele-shaw flows with large property contrasts, *Physica D* 237 (2008) 3089–3098.
- [22] R. B. Bird, R. C. Armstrong, O. Hassager, *Dynamics of Polymeric Liquids, Volume 1* (2nd edition), New York: John Wiley & Sons, 1987.
- [23] C. Dopazo, On conditioned averages for intermittent turbulent flows, *Journal of Fluid Mechanics* 81 (1977) 433–438.
- [24] D. A. Drew, Mathematical modeling of two-phase flow, *Annual Review of Fluid Mechanics* 15 (1983) 261–291.
- [25] D. A. Drew, S. L. Passman, *Theory of Multicomponent Fluids*, New York: Springer, 1999.
- [26] H. G. Weller, The development of a new flame area combustion model using conditional averaging, Tech. rep., Thermo-Fluids Section Report TF 9307, Imperial College of Science, Technology and Medicine (1993).



- [27] H. G. Weller, Derivation, modelling and solution of the conditionally averaged two-phase flow equations, Tech. rep., OpenCFD Limited (2005).
- [28] J. M. Donbar, J. F. Driscoll, C. D. Carter, Reaction zone structure in turbulent non-premixed jet flames from CH-OH PLIF images, *Combustion and Flame* 122 (2000) 1–19.
- [29] J. U. Brackbill, D. B. Kothe, C. Zemach, A continuum method for modeling surface tension, *Journal of Computational Physics* 100 (1992) 335–354.
- [30] D. Bestion, The physical closure laws in the CATHARE code, *Nuclear Engineering and Design* 124 (1990) 229–245.
- [31] S. Zhang, X. Zhao, General formulation for Rhie-Chow interpolation, in: *Proceeding of HT-FED04. ASME Heat Transfer/Fluids Engineering Summer Conf.* 123, 131, 2004.
- [32] R. Guénette, M. Fortin, A new mixed finite element method for computing viscoelastic flows, *Journal of Non-Newtonian Fluid Mechanics* 60 (1995) 27–52.
- [33] S.-C. Xue, R. I. Tanner, N. Phan-Thien, Numerical modelling of transient viscoelastic flows, *Journal of Non-Newtonian Fluid Mechanics* 123 (2004) 33–58.
- [34] H. Jasak, Error analysis and estimation for the finite volume method with applications to fluid flows, Ph.D. thesis, Imperial College University of London (1996).
- [35] J. L. Favero, A. R. Secchi, N. S. M. Cardozo, H. Jasak, Viscoelastic flow simulation: Development of a methodology of analysis using the software OpenFOAM and differential constitutive equations, *Computer Aided Chemical Engineering* 27 (2009) 915–920.
- [36] R. I. Issa, Solution of implicitly discretised fluid flow equations by operator-splitting, *Journal of Computational Physics* 62 (1986) 40–65.

## 6.B Nomenclature

Normal symbols represent scalar quantities and boldface symbols represent vector and tensor quantities in general.

### Roman Symbols

Symbol	Description	Unit
$d$	Interface height	$[m]$
$D$	Cylinder diameter	$[m]$
$e_1$	Error on mesh 1	
$e_2$	Error on mesh 2	
$e_{L_1}^\Phi$	Absolute error of quantity $\Phi$ in the $L_1$ -norm	
$e_{L_2}^\Phi$	Absolute error of quantity $\Phi$ in the $L_2$ -norm	
$e_{L_\infty}^\Phi$	Absolute error of quantity $\Phi$ in the $L_\infty$ -norm	
$\mathbf{g}$	Gravitational acceleration vector	$[\frac{m}{s^2}]$
$h$	Drag coefficient	$[-]$
$H$	Channel height	$[m]$
	or domain height	$[m]$
$i$	Index	$[-]$
$\mathbf{I}$	Identity matrix	$[-]$
$I_\varphi$	Indicator function of phase $\varphi$	$[-]$
$j$	Index	$[-]$
$L$	Channel length	$[m]$
	or domain length	$[m]$
$\mathbf{M}_\varphi$	Interfacial momentum transfer of phase $\varphi$	$[\frac{kg}{m^2s^2}]$
$\mathbf{M}_\varphi^d$	Interfacial momentum transfer of phase $\varphi$ stemming from drag	$[\frac{kg}{m^2s^2}]$
$\mathbf{M}_\sigma$	Interfacial momentum source	$[\frac{kg}{m^2s^2}]$
$\mathbf{M}_\omega$	Interfacial momentum transfer of phase $\omega$	$[\frac{kg}{m^2s^2}]$
$\mathbf{n}_{I,\varphi}$	Interface normal vector pointing inside volume of phase $\varphi$	$[-]$
$N$	Number of phases	$[-]$
$p$	Pressure	$[\frac{kg}{ms^2}]$
	or rate of convergence	$[-]$
$\bar{p}$	Mixture pressure	$[\frac{kg}{ms^2}]$

Symbol	Description	Unit
$\overline{p^d}$	Modified mixture pressure	$[\frac{kg}{ms^2}]$
$\overline{p}_\varphi$	Conditional volume averaged pressure of phase $\varphi$	$[\frac{kg}{ms^2}]$
$\overline{p}_\omega$	Conditional volume averaged pressure of phase $\omega$	$[\frac{kg}{ms^2}]$
$p_\infty$	Far-field pressure	$[\frac{kg}{ms^2}]$
<b>P</b>	Arbitrary local instantaneous physical property	
<b>Q</b>	Arbitrary local instantaneous physical property	
<b>Q<sub>φ</sub></b>	Conditioned arbitrary local instantaneous physical property	
$R$	Cylinder radius	$[m]$
$S$	Surface area	$[m^2]$
$t$	Time	$[s]$
<b>U</b>	Local instantaneous velocity	$[\frac{m}{s}]$
$\overline{U}$	Mixture velocity	$[\frac{m}{s}]$
$U_I$	Interface velocity	$[\frac{m}{s}]$
$U_{I,x}$	Interface velocity in x-direction	$[\frac{m}{s}]$
$U_r$	Relative velocity	$[\frac{m}{s}]$
$U_{wall,x}$	Wall velocity in x-direction	$[\frac{m}{s}]$
$U_x$	Velocity in x-direction	$[\frac{m}{s}]$
$\overline{U}_\varphi$	Conditional volume averaged velocity of phase $\varphi$	$[\frac{m}{s}]$
$\overline{U}_\omega$	Conditional volume averaged velocity of phase $\omega$	$[\frac{m}{s}]$
<b>U<sup>#</sup></b>	Surface fluctuation of velocity	$[\frac{m}{s}]$
$x$	Position	$[m]$
<b>x</b>	Position vector	$[m]$
$y$	Position	$[m]$
<b>y</b>	Relative position vector	$[m]$

### Greek Symbols

Symbol	Description	Unit
$\alpha_\varphi$	Volume fraction of phase $\varphi$	$[-]$
$\alpha_\omega$	Volume fraction of phase $\omega$	$[-]$
$\dot{\gamma}_{wall}$	Shear-rate at the wall	$[s^{-1}]$
$\overline{\dot{\gamma}}_\varphi$	Conditioned volume-averaged shear-rate tensor of phase $\varphi$	$[s^{-1}]$
$\delta$	Interface thickness	$[m]$

Symbol	Description	Unit
$\delta_I$	Interface thickness	[m]
$\delta V$	Volume element	[m <sup>3</sup> ]
$\Delta x$	Horizontal edge length of computational cell	[m]
$\Delta y$	Vertical edge length of computational cell	[m]
$\nabla$	Nabla (gradient) operator	[m <sup>-1</sup> ]
$\nabla \cdot$	Divergence operator	[m <sup>-1</sup> ]
$\eta_1$	Viscosity of phase 1	[ $\frac{kg}{ms}$ ]
$\eta_2$	Viscosity of phase 2	[ $\frac{kg}{ms}$ ]
$\eta_{eff,\varphi}$	Effective viscosity of phase $\varphi$	[ $\frac{kg}{ms}$ ]
$\eta_{eff,\omega}$	Effective viscosity of phase $\omega$	[ $\frac{kg}{ms}$ ]
$\eta_P$	Polymeric viscosity	[ $\frac{kg}{ms}$ ]
$\eta_{P,\varphi}$	Polymeric viscosity of phase $\varphi$	[ $\frac{kg}{ms}$ ]
$\eta_r$	Viscosity ratio	[-]
$\eta_S$	Solvent viscosity	[ $\frac{kg}{ms}$ ]
$\eta_{S,\varphi}$	Solvent viscosity of phase $\varphi$	[ $\frac{kg}{ms}$ ]
$\kappa_{I,\varphi}$	Curvature of interface with respect to phase $\varphi$	[m <sup>-1</sup> ]
$\lambda$	Relaxation time	[s]
$\lambda_\varphi$	Relaxation time of phase $\varphi$	[s]
$\rho$	Local instantaneous density	[ $\frac{kg}{m^3}$ ]
$\bar{\rho}_\varphi$	Conditional volume averaged density	[ $\frac{kg}{m^3}$ ]
$\Sigma$	Interfacial area density	[m <sup>2</sup> ]
$\sigma$	Surface tension	[ $\frac{kg}{s^2}$ ]
$\boldsymbol{\tau}$	Deviatoric or extra-stress tensor	[ $\frac{kg}{ms^2}$ ]
$\boldsymbol{\tau}_P$	Polymeric stress tensor	[ $\frac{kg}{ms^2}$ ]
$\boldsymbol{\tau}_S$	Solvent stress tensor	[ $\frac{kg}{ms^2}$ ]
$\overline{\boldsymbol{\tau}}_P_\varphi$	Conditional volume averaged polymeric stress tensor	[ $\frac{kg}{ms^2}$ ]
$\tau_{P,xx}$	Polymeric normal stress in x-direction	[ $\frac{kg}{ms^2}$ ]
$\tau_{P,xy}$	Polymeric shear stress	[ $\frac{kg}{ms^2}$ ]
$\overline{\boldsymbol{\tau}}_P^*_\varphi$	Conditional volume averaged polymeric equilibrium stress tensor	[ $\frac{kg}{ms^2}$ ]
$\overline{\boldsymbol{\tau}}_S_\varphi$	Conditional volume averaged solvent stress tensor	[ $\frac{kg}{ms^2}$ ]
$\Phi$	Arbitrary quantity	
$\Phi_{ana,j}$	Analytical value of quantity $\Phi$ at position $j$	
$\Phi_{num,j}$	Numerically calculated value of quantity $\Phi$ at position $j$	

## Subscripts, Superscripts and Oversymbols

Symbol	Description
$Q_1$	Property $Q$ of phase 1
$Q_2$	Property $Q$ of phase 2
$Q^d$	Drag or modified
$Q_{eff}$	Effective
$Q_I$	$Q$ at the interface
$Q^{max}$	Maximum value of $Q$
$Q_r$	Relative
$Q^T$	Transpose of matrix $Q$
$Q_{wall}$	Value of $Q$ at the wall
$Q_\varphi$	Conditioned $Q$ , belonging to phase $\varphi$
$Q_\omega$	Conditioned $Q$ , belonging to phase $\omega$
$Q'_\varphi$	Conditional fluctuation of $Q$ in phase $\varphi$
$Q^\#$	Surface fluctuation of $Q$
$\overline{Q}$	Volume averaged $Q$ or mixture value of $Q$
$\overline{Q}_\varphi$	Conditional volume averaged $Q$ , belonging to phase $\varphi$
$\overbrace{Q}$	Interface average of $Q$
$\overset{\nabla}{Q}$	Upper-convected time derivative
$ Q $	Magnitude of vector $Q$
$\ Q\ $	Magnitude of tensor $Q$
$Q _{corr.}$	Correction to $Q$
$Q _{diff.}$	Diffusion contribution of $Q$

## Nondimensional Groups

Symbol	Description	Definition
$Wi$	Weissenberg number	$\frac{\lambda U_{x,max}}{H}$
$Wi_{wall}$	Weissenberg number at the wall	$\lambda \dot{\gamma}_{wall}$
$\beta$	Retardation ratio	$\frac{\eta_S}{\eta_0}$
$\eta_r$	Viscosity ratio	$\frac{\eta_1}{\eta_2}$

## Abbreviations

Abbreviation	Description
BiCGstab	Bi-conjugate gradient stabilized
BSD	Both-side-diffusion
CLSVOF	Coupled Level-Set Volume-of-Fluid
CSF	Continuum surface force
DIC	Discrete incomplete Cholesky
FENE-CR	Finite extensible non-linear elastic - Chilcott and Rallison
PCG	Preconditioned conjugate gradient
PISO	Pressure implicit with splitting of operator
VoF	Volume-of-Fluid

## 6.C Summary

In this chapter conditional volume averaging is applied to develop a model capable for simulation of two-phase flows of viscoelastic fluids with surface tension effects.

The chapter starts with the single-phase mass and momentum balances, which are subsequently conditionally volume averaged. In doing so, a set of equations having unclosed interfacial terms is obtained, for which closure relations for viscoelastic fluids are presented. The resulting equations possess a structure similar to the single-phase equations; however, separate conservation equations are solved for each phase. As a result, each phase has its own pressure and velocity over the entire domain. Next, the numerical implementation is briefly outlined.

It is found that a Poiseuille single-phase flow is predicted correctly with this model. The closure terms are examined and successfully validated by considering a two-phase shearing flow and a quiescent cylinder with surface tension. A convergence analysis is performed for a steady stratified two-phase flow with both phases being viscoelastic.

## 6.D Author contribution

The author of this thesis contributed to this publication by doing the whole derivation to finally obtain the conditionally volume-averaged viscoelastic two-phase model, by finding a reformulation to make the model numerically solvable, by implementing this model in the software package *OpenFOAM*<sup>®</sup>, by proposing the concept for the validation to show the behavior of the conditionally volume-averaged viscoelastic two-phase model, by doing all simulations and by writing the whole manuscript.

## 6.E Copyright permission

This chapter is originated from the following publication:

F. Habla, L. Dietsche, O. Hinrichsen, Modeling and simulation of conditionally volume averaged viscoelastic two-phase flows, *AIChE Journal* 59 (2013) 3914-3927.

Reprinted with permission from Wiley-VCH GmbH.





# 7 An Improved Conditionally Volume Averaged Viscoelastic Two-Phase Model for Simulation of Transient Droplet Deformations under Simple Shear

## 7.1 Introduction

Predicting droplet deformations under defined flow conditions is demanding if either or both phases are viscoelastic. The main issue is that one has to deal both with moving interfaces as well as the complex viscoelastic flow behavior.

There are several approaches to the moving interface problem, such as front-tracking, Volume-of-Fluid (VoF) and Level-Set methods. In front-tracking the position of the interface is determined by markers located on the interface, which are advected with the flow. The accuracy of the interface morphology is directly linked to the number of markers. If the interface stretches or contracts a redistribution of the markers is necessary. Special care has to be taken when considering topological changes of the interface. [1] The volume-of-fluid method is used widespread as it is comparatively easy to implement and shows good mass conservation properties. Besides that, topological changes are treated inherently and no special care has to be taken. The interface position is geometrically reconstructed from a color function, which describes the volume fraction in a cell. A known drawback is that higher-order accuracy is hard to achieve due to the step-like color function. Level-Set methods are becoming more popular recently. In Level-Set the interface is generally described by the zero level-set of a smooth signed distance function. To keep the color function a signed distance function, reinitialization steps are necessary when advecting the interface. Topological changes are also treated inherently and higher order schemes such as essentially non-oscillatory (ENO) methods are commonly in use. A drawback of Level-Set methods is the poor mass conservation. However, Olsson and Kreiss [1] recently proposed the so-called 'conservative Level-Set method', which shows superior mass conservation properties compared to other level-set methods. In this method the interface is described by the 0.5 level-set of a color function  $\Phi$  with  $0 \leq \Phi \leq 1$ . The method is conservative and more specifically also preserves the thickness and the profile of the transition region from 0 to 1.

In a recent work we derived a new model for viscoelastic two-phase flows, which is up to second-order accurate. [2] The model was derived by conditional volume averaging of the standard single-phase mass and momentum balance equations. Subsequent closure modeling for viscoelastic fluids governed by the Oldroyd-B constitutive equation [3] led to a closed set of equations, which was afterwards reformulated in order to become numerically solvable.

The interface position in this model can be described by the 0.5 level-set of a color function  $\alpha_\varphi$  ( $0 \leq \alpha_\varphi \leq 1$ ), which describes the volume fraction. It was shown that the thickness of the transition region from 0 to 1 can be chosen arbitrarily without falsifying the flow outside of this transition region as long as the transition region is sufficiently spatially resolved.  $\delta/\Delta x \geq 1$ , where  $\delta$  is the characteristic length parameter of a specific tangent hyperbolic function, was shown to be a proper condition for several basic validation cases including the pressure jump across a circular interface with surface tension as well as a pressure-driven and a shear-induced two-phase flow. [2] However, the model described in Habla et al. [2] uses standard volume-of-fluid advection methods to propagate  $\alpha_\varphi$ . Thus, we could not guarantee to preserve the condition  $\delta/\Delta x = 1$  for problems involving moving interfaces, which is why we restricted our validation to very basic cases with steady interfaces.

Fortunately, the 'conservative level-set method' of Olsson and Kreiss [1] exactly suits our needs: the area/volume within the  $\Phi = 0.5$  contour is conserved for divergence free velocity fields; the method is second-order accurate; and above all the thickness of the transition region is preserved. The aim of this work is to adapt our model to the interface model of Olsson and Kreiss [1] for the advection of our color function  $\alpha_\varphi$ .

This paper is organized as follows: in Section 7.2 the model derived in Habla et al. [2] as well as the numerically motivated reformulation is shortly revisited. The intermediate step proposed by Olsson and Kreiss [1] is outlined and our final numerical algorithm is presented. In Section 7.3 the interface model is first validated using a test case depicted from Olsson and Kreiss [1]. Next, simulations of a Newtonian droplet deforming in a viscoelastic matrix under simple shear as it was experimentally analyzed by Sibillo et al. [4] are presented in 2D and 3D. Finally, in Section 7.4 the main results are summarized.

## 7.2 Theory

### 7.2.1 Conditional volume averaged viscoelastic two-phase model

In Habla et al. [2] we derive a conditional volume-averaged viscoelastic two-phase model. With the assumption of no mass-transfer and a constant density in each phase the conditionally volume averaged mass balance for phase  $\varphi$  is

$$\frac{\partial \alpha_\varphi}{\partial t} + \nabla \cdot (\alpha_\varphi \bar{\mathbf{U}}_\varphi) = 0 \quad (7.1)$$

The equation is applicable to both phases by simply changing the index  $\varphi$  to  $\omega$ . Similarly, one obtains the conditional volume averaged momentum balance

$$\frac{\partial \alpha_\varphi \bar{\mathbf{U}}_\varphi}{\partial t} + \nabla \cdot (\alpha_\varphi \bar{\mathbf{U}}_\varphi \bar{\mathbf{U}}_\varphi) = -\frac{\alpha_\varphi \nabla \bar{p}_\varphi}{\bar{\rho}_\varphi} + \frac{\nabla \cdot (\alpha_\varphi \bar{\boldsymbol{\tau}}_\varphi)}{\bar{\rho}_\varphi} + \alpha_\varphi \mathbf{g} + \frac{\mathbf{M}_\varphi}{\bar{\rho}_\varphi} \quad (7.2)$$

where  $\alpha_\varphi \overline{\boldsymbol{\tau}}_\varphi$  represents the phasic stress and  $\mathbf{M}_\varphi$  is a term to describe the interfacial momentum transfer. Considering a generalized Maxwell fluid the phasic stress can be written as the sum of a solvent and a polymeric contribution according to  $\alpha_\varphi \overline{\boldsymbol{\tau}}_\varphi = \alpha_\varphi (\overline{\boldsymbol{\tau}}_{S,\varphi} + \overline{\boldsymbol{\tau}}_{P,\varphi})$ . Applying conditional volume averaging to the Newtonian law leads to the following expression for the solvent contribution

$$\begin{aligned} \alpha_\varphi \overline{\boldsymbol{\tau}}_{S,\varphi} &= \alpha_\varphi \eta_{S,\varphi} \left[ \nabla \overline{\mathbf{U}}_\varphi + (\nabla \overline{\mathbf{U}}_\varphi)^T - \frac{2}{3} (\nabla \cdot \overline{\mathbf{U}}_\varphi) \mathbf{I} \right] \\ &+ \eta_{S,\varphi} \left[ \nabla \alpha_\varphi (\overline{\mathbf{U}}_\varphi - \mathbf{U}_I) + (\overline{\mathbf{U}}_\varphi - \mathbf{U}_I) \nabla \alpha_\varphi - \frac{2}{3} \nabla \alpha_\varphi \cdot (\overline{\mathbf{U}}_\varphi - \mathbf{U}_I) \mathbf{I} \right] \end{aligned} \quad (7.3)$$

while the same procedure applied to the Oldroyd-B constitutive equation leads to the closure expression for the polymeric contribution

$$\begin{aligned} &\alpha_\varphi \overline{\boldsymbol{\tau}}_{P,\varphi} \\ &+ \lambda_\varphi \left[ \left( \frac{\partial \alpha_\varphi \overline{\boldsymbol{\tau}}_{P,\varphi}}{\partial t} \right) + \nabla \cdot (\alpha_\varphi \overline{\boldsymbol{\tau}}_{P,\varphi} \overline{\mathbf{U}}_\varphi) - \alpha_\varphi \overline{\boldsymbol{\tau}}_{P,\varphi} \cdot \nabla \overline{\mathbf{U}}_\varphi - \alpha_\varphi (\nabla \overline{\mathbf{U}}_\varphi)^T \cdot \overline{\boldsymbol{\tau}}_{P,\varphi} \right] \\ &= \\ &\alpha_\varphi \eta_{P,\varphi} \left[ \nabla \overline{\mathbf{U}}_\varphi + (\nabla \overline{\mathbf{U}}_\varphi)^T - \frac{2}{3} (\nabla \cdot \overline{\mathbf{U}}_\varphi) \mathbf{I} \right] \\ &+ \eta_{P,\varphi} \left[ \nabla \alpha_\varphi (\overline{\mathbf{U}}_\varphi - \mathbf{U}_I) + (\overline{\mathbf{U}}_\varphi - \mathbf{U}_I) \nabla \alpha_\varphi - \frac{2}{3} \nabla \alpha_\varphi \cdot (\overline{\mathbf{U}}_\varphi - \mathbf{U}_I) \mathbf{I} \right] \end{aligned} \quad (7.4)$$

The local interface velocity  $\mathbf{U}_I$  appearing in the above equations can be modeled by a viscosity weighted linear function of the average total velocities, similar as it was proposed by Sun and Beckermann [5]

$$\mathbf{U}_I = \frac{\alpha_\omega \eta_{eff,\varphi} \overline{\mathbf{U}}_\varphi + \alpha_\varphi \eta_{eff,\omega} \overline{\mathbf{U}}_\omega}{\alpha_\omega \eta_{eff,\varphi} + \alpha_\varphi \eta_{eff,\omega}} \quad (7.5)$$

where the sum of  $\eta_{S,\varphi}$  and  $\eta_{P,\varphi}$  is denoted as the effective viscosity  $\eta_{eff,\varphi}$ . Eq. 7.5 obeys the condition of phase symmetry and can be considered as an average no-slip condition at the interface. The interfacial momentum transfer term  $\mathbf{M}_\varphi$  in the presence of surface tension  $\sigma$  is modeled as

$$\mathbf{M}_\varphi = -h \frac{\alpha_\varphi \alpha_\omega \eta_{eff,\varphi} \eta_{eff,\omega} (|\nabla \alpha_\varphi|)^2}{\alpha_\omega \eta_{eff,\varphi} + \alpha_\varphi \eta_{eff,\omega}} (\overline{\mathbf{U}}_\varphi - \overline{\mathbf{U}}_\omega) - \sigma \left( \nabla \cdot \frac{\nabla \alpha_\varphi}{|\nabla \alpha_\varphi|} \right) \nabla \alpha_\varphi \quad (7.6)$$

where  $h$  is an empirical coupling coefficient. Specifically,  $h = 11.028$  was found to be a proper choice in Habla et al. [2]. The interface morphology is expressed by the unit normal vector  $\widehat{\mathbf{n}}_{I,\varphi}$  and the curvature  $\widehat{\kappa}_{I,\varphi}$ , for which closure modeling resulted in

$$\widehat{\mathbf{n}}_{I,\varphi} = \frac{\nabla \alpha_\varphi}{|\nabla \alpha_\varphi|} \quad (7.7)$$

$$\widehat{\kappa_{I,\varphi}} = -\nabla \cdot \left( \frac{\nabla \alpha_\varphi}{|\nabla \alpha_\varphi|} \right) \quad (7.8)$$

## 7.2.2 Numerical reformulation

To be able to use the above model in a numerical algorithm, the equations have to be reformulated for some reasons. [2] The detailed procedure of the reformulation can be found in that article. The reformulations include the assumption of a modified mixture pressure  $\bar{p}^d$ , which is equal in both phases. The pressure is further modified by extracting the hydrostatic pressure to smooth out the pressure field. Furthermore, phase-intensive equations are formulated for the momentum and constitutive equation because this removes the difficulty for solving these equations in the case when  $\alpha_\varphi$  becomes zero. Additionally, the both sides diffusion is used in the momentum equation to stabilize the algorithm for flows, which behave highly elastic. For convenience, we summarize the final set of equations here

$$\frac{\partial \alpha_\varphi}{\partial t} + \nabla \cdot (\alpha_\varphi \bar{\mathbf{U}}) + \nabla \cdot (\bar{\mathbf{U}}_r \alpha_\varphi (1 - \alpha_\varphi)) = 0 \quad (7.9)$$

$$\alpha_\omega = 1 - \alpha_\varphi \quad (7.10)$$

$$\nabla \cdot \bar{\mathbf{U}} = 0 \quad (7.11)$$

$$\begin{aligned} & \frac{\partial \bar{\mathbf{U}}_\varphi}{\partial t} + \nabla \cdot (\bar{\mathbf{U}}_\varphi \bar{\mathbf{U}}_\varphi) - \bar{\mathbf{U}}_\varphi (\nabla \cdot \bar{\mathbf{U}}_\varphi) - \nabla \cdot \left( \frac{\eta_{S,\varphi} + \eta_{P,\varphi}}{\bar{\rho}_\varphi} \nabla \bar{\mathbf{U}}_\varphi \right) = \\ & - \frac{\nabla \bar{p}^d}{\bar{\rho}_\varphi} + \left( 1 - \frac{\rho}{\bar{\rho}_\varphi} \right) \mathbf{g} - \frac{\mathbf{g} \cdot \mathbf{x}}{\bar{\rho}_\varphi} + \frac{1}{\bar{\rho}_\varphi} (\rho \mathbf{g} + \mathbf{g} \cdot \mathbf{x} \nabla \rho) + \frac{1}{\bar{\rho}_\varphi} \nabla \cdot \bar{\boldsymbol{\tau}}_{S\varphi}|_{corr.} \\ & + \frac{\nabla \alpha_\varphi}{\alpha_\varphi \bar{\rho}_\varphi} \cdot \bar{\boldsymbol{\tau}}_{S\varphi} + \frac{1}{\bar{\rho}_\varphi} \nabla \cdot \bar{\boldsymbol{\tau}}_{P\varphi} + \frac{\nabla \alpha_\varphi}{\alpha_\varphi \bar{\rho}_\varphi} \cdot \bar{\boldsymbol{\tau}}_{P\varphi} - \nabla \cdot (\eta_{P,\varphi} \nabla \bar{\mathbf{U}}_\varphi) \\ & + \alpha_\varphi \mathbf{g} - 11.028 \frac{1}{\bar{\rho}_\varphi} \frac{\eta_\varphi \eta_\omega (|\nabla \alpha_\varphi|)^2}{\eta_\varphi \alpha_\omega + \eta_\omega \alpha_\varphi} (\bar{\mathbf{U}}_\varphi - \bar{\mathbf{U}}_\omega) - \frac{\sigma}{\bar{\rho}_\varphi} \left( \nabla \cdot \frac{\nabla \alpha_\varphi}{|\nabla \alpha_\varphi|} \right) \frac{\nabla \alpha_\varphi}{\alpha_\varphi} \end{aligned} \quad (7.12)$$

$$\begin{aligned} \bar{\boldsymbol{\tau}}_{S\varphi} &= \eta_{S,\varphi} \left( \nabla \bar{\mathbf{U}}_\varphi + (\nabla \bar{\mathbf{U}}_\varphi)^T - \frac{2}{3} (\nabla \cdot \bar{\mathbf{U}}_\varphi) \mathbf{I} \right) \\ &+ \frac{\eta_{S,\varphi} (\eta_{S,\omega} + \eta_{P,\omega})}{\eta_\varphi \alpha_\omega + \eta_\omega \alpha_\varphi} \left[ \nabla \alpha_\varphi (\bar{\mathbf{U}}_\varphi - \bar{\mathbf{U}}_\omega) + (\bar{\mathbf{U}}_\varphi - \bar{\mathbf{U}}_\omega) \nabla \alpha_\varphi \right. \\ &\left. - \frac{2}{3} \nabla \alpha_\varphi \cdot (\bar{\mathbf{U}}_\varphi - \bar{\mathbf{U}}_\omega) \mathbf{I} \right] \end{aligned} \quad (7.13)$$

$$\begin{aligned}
\overline{\tau}_S^\varphi|_{corr.} &= \eta_{S,\varphi} \left( (\nabla \overline{\mathbf{U}}_\varphi)^T - \frac{2}{3} (\nabla \cdot \overline{\mathbf{U}}_\varphi) \mathbf{I} \right) \\
&+ \frac{\eta_{S,\varphi} (\eta_{S,\omega} + \eta_{P,\omega})}{\eta_\varphi \alpha_\omega + \eta_\omega \alpha_\varphi} \left[ \nabla \alpha_\varphi (\overline{\mathbf{U}}_\varphi - \overline{\mathbf{U}}_\omega) + (\overline{\mathbf{U}}_\varphi - \overline{\mathbf{U}}_\omega) \nabla \alpha_\varphi \right. \\
&\left. - \frac{2}{3} \nabla \alpha_\varphi \cdot (\overline{\mathbf{U}}_\varphi - \overline{\mathbf{U}}_\omega) \mathbf{I} \right]
\end{aligned} \tag{7.14}$$

$$\begin{aligned}
\overline{\tau}_P^\varphi + \lambda_\varphi \left[ \left( \frac{\partial \overline{\tau}_P^\varphi}{\partial t} \right) + \nabla \cdot (\overline{\tau}_P^\varphi \overline{\mathbf{U}}_\varphi) - \overline{\tau}_P^\varphi (\nabla \cdot \overline{\mathbf{U}}_\varphi) - \overline{\tau}_P^\varphi \cdot \nabla \overline{\mathbf{U}}_\varphi \right. \\
\left. - (\nabla \overline{\mathbf{U}}_\varphi)^T \cdot \overline{\tau}_P^\varphi \right] = \\
\eta_{P,\varphi} \left( \nabla \overline{\mathbf{U}}_\varphi + (\nabla \overline{\mathbf{U}}_\varphi)^T - \frac{2}{3} (\nabla \cdot \overline{\mathbf{U}}_\varphi) \mathbf{I} \right) \\
+ \frac{\eta_{P,\varphi} (\eta_{S,\omega} + \eta_{P,\omega})}{\eta_\varphi \alpha_\omega + \eta_\omega \alpha_\varphi} \left[ \nabla \alpha_\varphi (\overline{\mathbf{U}}_\varphi - \overline{\mathbf{U}}_\omega) + (\overline{\mathbf{U}}_\varphi - \overline{\mathbf{U}}_\omega) \nabla \alpha_\varphi \right. \\
\left. - \frac{2}{3} \nabla \alpha_\varphi \cdot (\overline{\mathbf{U}}_\varphi - \overline{\mathbf{U}}_\omega) \mathbf{I} \right]
\end{aligned} \tag{7.15}$$

where  $\overline{\mathbf{U}}_r$  is the relative velocity,  $\overline{\mathbf{U}}_r = \overline{\mathbf{U}}_\varphi - \overline{\mathbf{U}}_\omega$ .

In the basic validation study performed in Habla et al. [2] it was found that the interface transition region of  $\alpha_\varphi$  from 0 to 1 can be chosen arbitrarily without falsifying the flow outside of this transition region, however, a minimum spatial resolution is required.  $\delta/\Delta x \geq 1$ , where  $\delta$  is the characteristic length parameter of a specific tangent hyperbolic function, was found a proper choice. [2] Unfortunately, when solving the interface advection equation Eq. 7.9 numerically using standard methods, none of the methods available - not even TVD (total variation diminishing) methods in conjunction with specific limiters such as the van Leer or Superbee limiter - can guarantee to preserve the thickness and profile of the interface transition region, but will diffuse and smear the interface to a certain degree. [1] Thus, a special technique is required, which will be outlined in the following.

### 7.2.3 Intermediate Step

Based on the idea of Harten [6] to add artificial compression to Eq. 7.9 in order to maintain the resolution of contact discontinuities, Olsson and Kreiss [1] suggest to additionally add an artificial diffusion term in order to avoid an unsteadiness at the interface. Thus, the basic idea is to solve the following equation in an intermediate step

$$\frac{\partial \alpha_\varphi}{\partial \tau} + \nabla \cdot \mathbf{f}(\alpha_\varphi) = \nabla \cdot \epsilon \nabla \alpha_\varphi \tag{7.16}$$

where  $\mathbf{f}$  is the compressive flux and  $\epsilon$  is the artificial diffusion coefficient. The time variable is designated as  $\tau$  to clarify that this is an artificial time and not the actual time  $t$ . The requirements for  $\mathbf{f}(\alpha_\varphi)$  are to act in the area of the interface ( $0 < \alpha_\varphi < 1$ ) and in normal direction to the interface. Therefore,  $\mathbf{f}$  is chosen to be  $\mathbf{f}(\alpha_\varphi) = \alpha_\varphi(1 - \alpha_\varphi) \widehat{\mathbf{n}}_{I,\varphi}$ . [1]

Solving Eq. 7.16 in an intermediate step until convergence is reached ensures that the thickness and the profile of the interface is kept constant even if the interface is moving. The thickness of the interfacial region is proportional to the artificial diffusion coefficient  $\epsilon$ . We find that this diffusion coefficient is identical to the characteristic length parameter  $\delta$  of the tangent hyperbolic function used in Habla et al. [2]

$$\alpha_\varphi(x) = 0.5 \left( 1 - \tanh \left( \frac{x}{2\delta} \right) \right) \quad (7.17)$$

such that  $\epsilon \equiv \delta$ . Since our model behaves best with  $\delta/\Delta x = 1$  an adequate choice for  $\epsilon$  would be  $\epsilon = \Delta x$ . This is illustrated in Fig. 7.1.

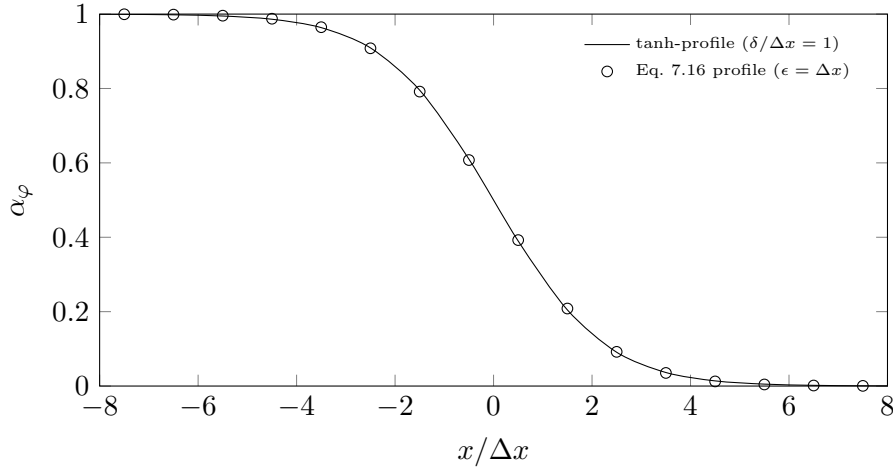


**Figure 7.1:** Comparison of the hyperbolic tangent profile (Eq. 7.17) and the converged solution of Eq. 7.16.

Similar to Olsson and Kreiss [1] we solve Eq. 7.16 with an explicit Euler scheme in conservative form

$$\alpha_\varphi^{**} = \alpha_\varphi^* + \Delta\tau \left\{ \nabla \cdot \left[ -\alpha_\varphi^* (1 - \alpha_\varphi^*) \widehat{\mathbf{n}}_{I,\varphi}^* + \epsilon \nabla \alpha_\varphi^* \right] \right\} \quad (7.18)$$

where  $\alpha_\varphi^{**}$  and  $\alpha_\varphi^*$  denote the new guess and the current guess of alpha  $\alpha_\varphi$ , respectively. Eq. 7.18 is solved after the solution of Eq. 7.9 for multiple times until convergence is reached. After each solution of Eq. 7.16, the interface normal vector  $\widehat{\mathbf{n}}_{I,\varphi}$  needs to be updated by use of Eq. 7.7 with the most recent guess of  $\alpha_\varphi$ , i.e.  $\alpha_\varphi^*$ .

## 7.2.4 Numerical Discretization and Algorithm

The time derivatives are discretized with a three-point Gear scheme, which is second-order accurate. [7] The convective terms of the momentum balance Eq. 7.12 and of the constitutive

equation Eq. 7.15 are discretized with the Gamma scheme with a blending factor of 0.8 for the 2D droplet deformation simulations [8], while the upwind scheme is used for the 3D simulations for stability reasons. The impact of this choice on simulation results will be evaluated in the next section. The convection term of the interface equation Eq. 7.9 is discretized with a standard second-order linear scheme. Diffusive terms are discretized with second-order linear interpolation and the source terms with a second-order volume integration scheme. Pressure-velocity coupling is addressed with the PISO algorithm. [9] The final numerical algorithm can be summarized as follows:

- 1.) Solve the phase fraction equation Eq. 7.9 for a given number of times ( $n_\alpha = 2$ ).
- 2.) Solve the intermediate step Eq. 7.18 for a given number of times ( $n_{interm.} = 2$ ).
- 3.) PISO-Loop:
  - 3.1.) Predict the cell fluxes.
  - 3.2.) Construct and solve a Poisson-type equation for pressure using Eq. 7.11.
  - 3.3.) Correct the fluxes and velocities.
  - 3.4.) Repeat from a) for a given number of times ( $n_{PISO} = 2$ ).
- 4.) Solve the Oldroyd-B equation Eq. 7.15 for each phase.

The first pressure equation is solved with a GAMG solver in conjunction with a GAMG preconditioner until either the absolute tolerance is below  $10^{-8}$  or the relative tolerance is below 0.01, while a PCG solver is used for solution of the second pressure equation, wherein solely the absolute tolerance of  $10^{-8}$  is used as convergence criteria. The reason for using the GAMG solver in the first pressure equation is because it is fast in initially decreasing the residual, while the PCG solver is faster when a strict absolute tolerance is used. The constitutive equations and the phase fraction equation are solved with a PBiCG solver in conjunction with a DILU preconditioner at a tolerance of  $10^{-9}$  for  $\alpha_\varphi$  and a tolerance of  $10^{-7}$  for  $\overline{\tau}_{P\varphi}$ .

Eq. 7.9 is solved twice ( $n_\alpha = 2$ ), because, although the transient and first convection term in Eq. 7.9 are fully implicit in  $\alpha_\varphi$ , the second convection term is not fully implicit in  $\alpha_\varphi$ . This is because the flux  $\overline{\mathbf{U}}_r (1 - \alpha_\varphi)$  is not independent of  $\alpha_\varphi$ . Eq. 7.9 is thus solved twice because after the first solution the new guess  $\alpha_\varphi^{**}$  is then used to update the flux  $\overline{\mathbf{U}}_r (1 - \alpha_\varphi^{**})$  and with this updated flux the equation is solved another time resulting in a much better guess  $\alpha_\varphi^{***}$  compared to if Eq. 7.9 is only solved once. Furthermore, boundedness of  $\alpha_\varphi$  between 0 and 1 is better guaranteed by iteratively solving Eq. 7.9. The choice of  $n_{interm.} = 2$  is because

of the explicit time-stepping in conjunction with the viscous term in Eq. 7.18, which results in a stability restriction in the sense that there is an upper limit for the value of  $\Delta\tau$ . [1] In order to guarantee a sufficient reinitialization of the  $\alpha_\varphi$ -field Eq. 7.18 has to be solved multiple times. In this work  $n_{interm.} = 2$  was found to be a proper choice.

## 7.3 Results and Discussion

### 7.3.1 Validation of Advection Scheme

To validate the interface model a test case depicted from Olsson and Kreiss [1] is used. A cylinder is rotated in a constant velocity field  $(u, v) = (y, -x)$  about the center of the domain for one full revolution as illustrated in Fig. 7.2. The cylinder has a diameter of  $D = 0.5$  and is initialized with  $\delta/\Delta x = 1$  (c.f. Eq. 7.17). The cylinder is initially located at  $(x, y) = (0.3, 0.3)$ . Five different grids having normalized cell sizes of  $\Delta x = 0.08, 0.04, 0.02, 0.01$  and  $0.005$  are used. The simulation parameters are set to  $\Delta t = \Delta x/2$ ,  $\epsilon = \Delta x$  and  $\Delta\tau = 1/4\Delta x$ . The results are compared after  $t = 2\pi$ , which is equivalent to one full rotation. At  $t = 2\pi$  the interface profile should be congruent with that of the initial state.

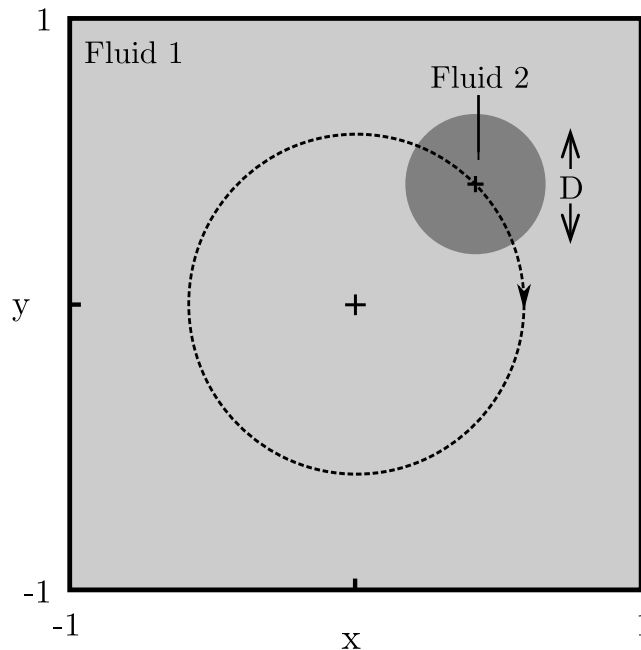


**Figure 7.2:** Domain of the validation case.

In Fig. 7.3 the  $\alpha_\varphi = 0.5$  isolines for the five grids as well as the initial state are pictured. It can be seen that the resolution  $\Delta x = 0.08$  is not sufficient and the interface profile is not smooth, while the second coarsest grid already gives comparatively good results. The isolines of the different grids clearly converge to that of the initial state with decreasing cell size. Fig. 7.4 shows the results for the isolines of  $\alpha_\varphi = 0.05, 0.5$  and  $0.95$  for the simulation with the grid  $\Delta x = 0.01$  if the intermediate step is solved twice ( $n_\alpha = 2$ ) and without the intermediate step



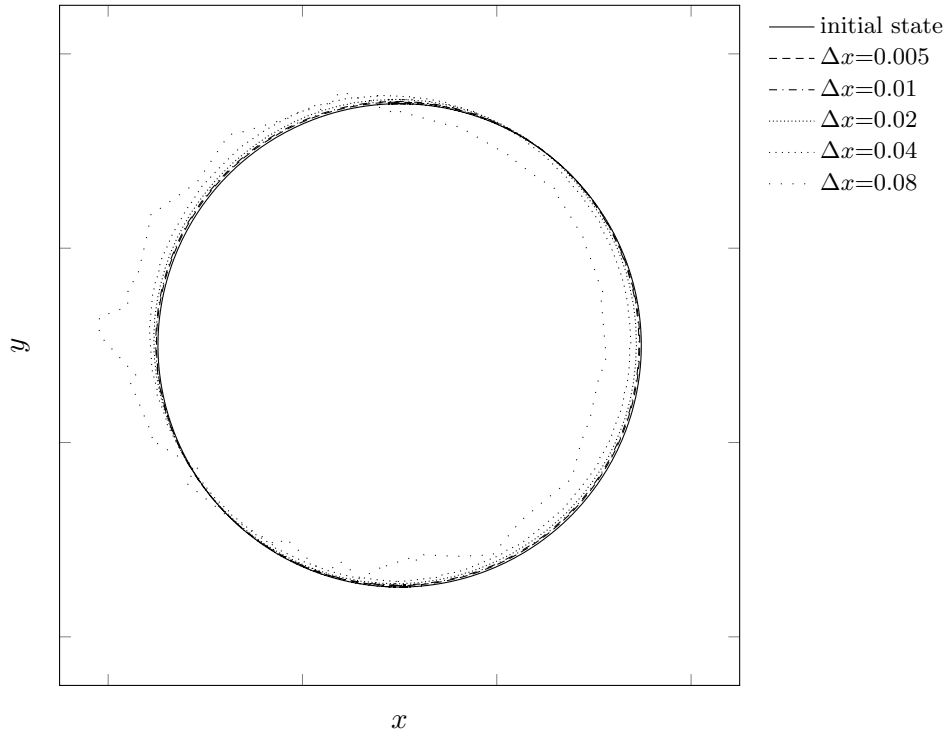


**Figure 7.3:** Isolines of  $\alpha_\varphi = 0.5$  at  $t = 2\pi$  for different grids compared to the initial state.

( $n_\alpha = 0$ ). Even if the cylinder seems to be a bit displaced in the top left direction, as can also be seen in Fig. 7.3, one can clearly deduce that the interface thickness remains constant during the rotation for the case of  $n_\alpha = 2$ , since the isolines of  $\alpha = 0.05$  and  $\alpha = 0.95$  also coincide with the initial state. However, this is not the case without the intermediate step. The isoline  $\alpha = 0.5$  is further displaced in top left direction compared to if the intermediate step is used. Furthermore, the isolines of  $\alpha = 0.05$  and  $\alpha = 0.95$  differ perceptibly from the initial state. In particular, the distance of the isolines of  $\alpha = 0.05$  and  $\alpha = 0.95$  increases and thus the interface gets diffused resulting in an increase of the interface thickness throughout simulation. In Tab. 7.1 the initial area within the  $\alpha_\varphi = 0.5$  isoline and the respective area at  $t = 2\pi$  is listed. The relative difference referring to the initial area of the  $\alpha_\varphi = 0.5$  isoline on the respective grid,  $\Delta_{num}$ , and referring to the area of a perfect circle with  $D = 0.5$ ,  $\Delta_{real}$ , become smaller with finer grids, while even on the second coarsest grid the deviation  $\Delta_{num}$  is below 0.1 %. Overall, the model shows sufficient mass conservation within the  $\alpha_\varphi = 0.5$  isoline and the interface thickness is kept constant even for moving interfaces.

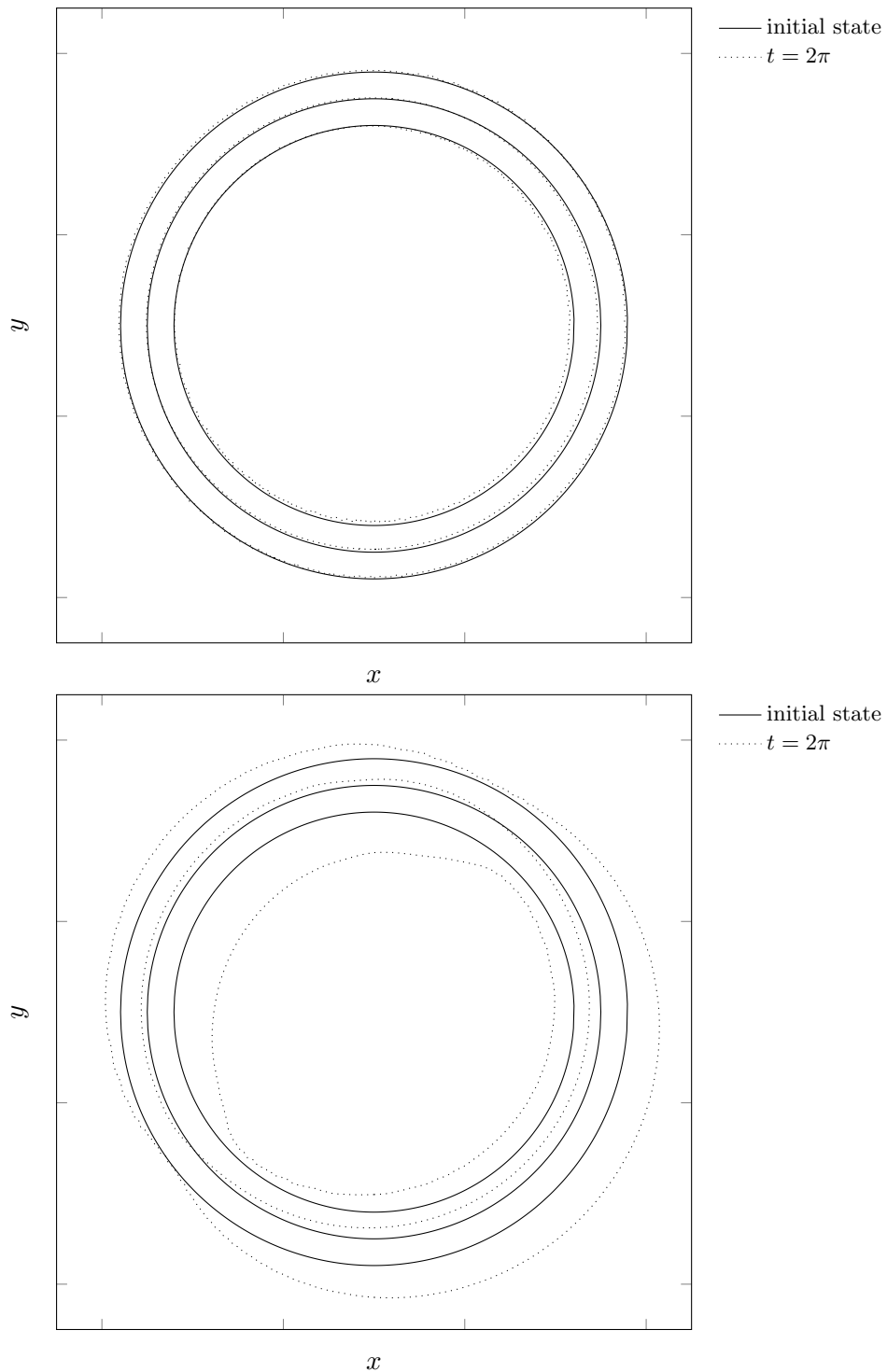


**Figure 7.4:** Isolines of  $\alpha_\varphi = 0.05, 0.5$  and  $0.95$  at  $t = 2\pi$  for  $\Delta x = 0.01$  compared to the initial state. Top: Conservative level-set method ( $n_\alpha = 2$ ); bottom: No reinitialization ( $n_\alpha = 0$ ).

**Table 7.1:** Area within the 0.5 isoline before and after the rotation and the relative deviation referred to the initial state's area and the area of a perfect circle.

$\Delta x$	$A_{t=0}$	$A_{t=2\pi}$	$\Delta_{num} = \frac{ A_{t=0}-A_{t=2\pi} }{A_{t=0}}$	$\Delta_{real} = \frac{ A_{real}-A_{t=2\pi} }{A_{real}}$
0.08	0.188310	0.185127	1.691E-02	4.095E-02
0.04	0.192980	0.192768	1.098E-03	1.716E-02
0.02	0.194022	0.193973	2.530E-04	1.186E-02
0.01	0.194298	0.194282	8.042E-05	1.045E-02
0.005	0.194365	0.194360	2.901E-05	1.011E-02

---

$A_{real} = 0.19635$

In Fig. 7.5 the relative deviation of the area  $\Delta_{num}$  is plotted against the normalized cell size  $\Delta x$ . If the coarsest grid is neglected, which is done due to the strong deviations pictured in Figs. 7.3 and 7.5, the order of the error decrease is found to be 1.74. Thus, the method is up to second-order accurate.

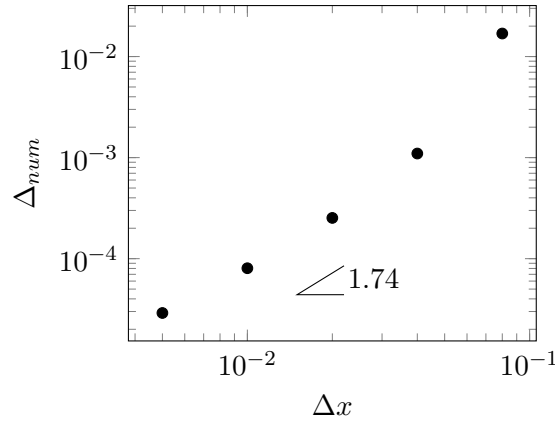


**Figure 7.5:** Determination of the order of the error decrease for the area conservation.

### 7.3.2 Droplet deformation

The adapted viscoelastic two-phase model is now applied to the simulation of transient droplet deformations of a Newtonian droplet in a viscoelastic matrix subjected to a steady planar shear-flow as depicted in Fig. 7.6. Simulations will be performed for different Capillary numbers  $Ca = \frac{\eta_m \dot{\gamma} R_0}{\sigma}$  both in 2D and 3D with adaptive mesh refinement of the interface region.

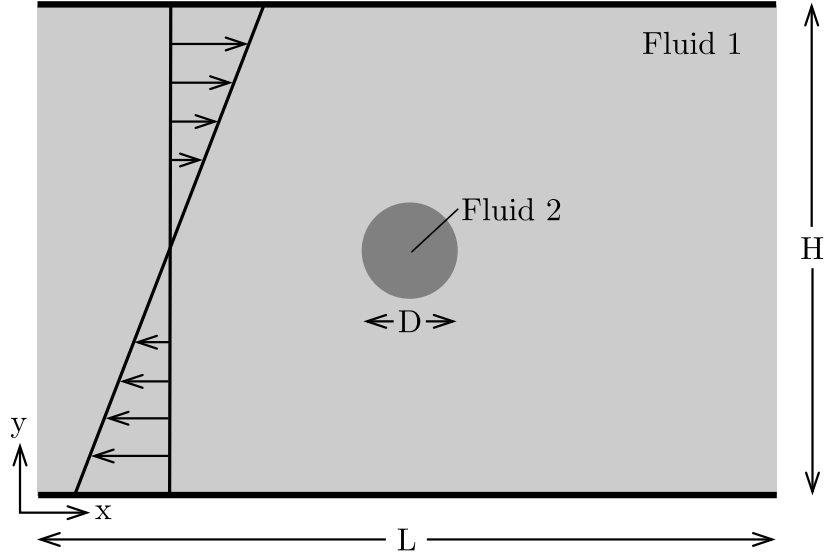


**Figure 7.6:** Domain of the droplet deformation simulations, see Habla et al. [2].

The rheology of the experimental system D4 at a viscosity ratio  $\eta_r = \eta_d/\eta_m = 2$  of Sibillo et al. [4] is used, whose results also serve as reference values.  $\eta_r$  is the viscosity ratio and  $\eta_d$  and  $\eta_m$  are the droplet and matrix viscosities, respectively. Boger fluids are used as matrix phase in the experiments of Sibillo et al. [4], although the matrix viscosity is not perfectly constant and varies from  $\eta_m = 43.1 \dots 34.8$  Pa s in the measured range ( $\dot{\gamma} \approx 0.1 \dots 10 \text{ s}^{-1}$ ). We therefore use the mean value ( $\eta_m = 38.95$  Pa s). Since simulations without a solvent contribution in the matrix phase were not stable, we use a small amount of solvent contribution. The retardation parameter in our simulations is  $\beta_m = \frac{\eta_{S,m}}{\eta_m} = \frac{\eta_{S,m}}{\eta_{S,m} + \eta_{P,m}} = 1/9$ . The relaxation time of the matrix then is  $\lambda_m = \frac{\Psi_{1,m}}{2\eta_{P,m}} = 1.34$  s, where  $\Psi_{1,m}$  is the first normal stress coefficient of the matrix phase. The weight coefficient of matrix elasticity is  $p = \lambda/\tau_{em} = 1.5$ , where  $\tau_{em} = \eta_m R_0/\sigma$  is the emulsion time. The numerical results of Yue et al. [10] determined with a phase-field model and our simulations with a VoF-model [11, 12] give additional indications for the verification of the simulation. It is noted here that the study of Yue et al. [10] uses a retardation parameter of  $\beta_m = 0.5$ , which is why we will additionally perform simulation results at  $\beta_m = 0.5$  for comparison.

The Newtonian droplet having a diameter of  $D = 100 \mu\text{m}$  and initialized with a tangent hyperbolic profile with  $\delta/\Delta x = 1$  is placed in the center of a rectangular box with  $H = 5D$  and  $L = 7.5D$ . At  $t = 0$  s a fully developed shear flow is imposed. The meshes used for the 2D and 3D simulations are summarized in Tab. 7.2.  $\epsilon$  is set to  $\Delta x$  in order to preserve  $\delta/\Delta x = 1$ . The following restrictions apply for the choice of  $\Delta\tau$ : if  $\Delta\tau$  is chosen too small the reinitialization is too weak and the interface thickness cannot be guaranteed to be kept constant anymore; on the other hand, if  $\Delta\tau$  is chosen too large the simulation aborts due to stability issues related to the explicit time-stepping. [1] The shear rate  $\dot{\gamma}$  is varied to obtain

**Table 7.2:** Meshes used for the transient droplet deformation simulations.

Meshes	$N_x$	$N_y$	$N_z$	$D/\Delta x$	Cell count
M1	150	100	-	20	15000
M2	225	150	-	30	33750
M3	300	200	-	40	60000
M4	375	250	-	50	93750
M5-3D	60	40	40	8	96000 <sup>1</sup>
M6-3D	75	50	50	10	187500 <sup>1</sup>

<sup>1</sup>Initial cell number without refinement.

Capillary numbers of  $Ca = 0.06, 0.43$  and  $0.47$ .  $Ca = 0.47$  is the experimentally found critical Capillary number above which no steady state can be reached. [4] To have a dimensionless time,  $t$  is divided by the emulsion time  $\tau_{em}$ . The droplet deformation is determined via the Taylor deformation parameter,  $D^* = (L - W)/(L + W)$ , where  $L$  is the length of the major axis and  $W$  is the length of the minor axis of the droplet in the  $xy$ -plane (in  $z$ -normal view, vorticity direction). [13, 14] Furthermore, in the three-dimensional simulations another Taylor deformation parameter  $D' = (L' - W')/(L' + W')$  is considered, where  $L'$  is the length of the major axis and  $W'$  is the length of the minor axis of the droplet in the  $xz$ -plane (in  $y$ -normal view, velocity gradient direction). The value is then normalized with the steady-state value  $D'_{ss}$  according to  $D'/D'_{ss}$ .

## 2D Simulations

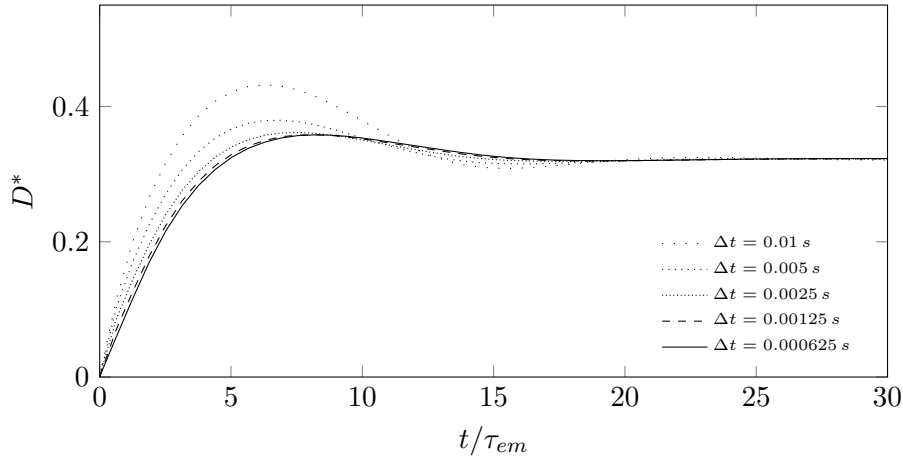


**Figure 7.7:** Deformation parameter  $D^*$  against the dimensionless time  $t/\tau_{em}$  for different time-steps at  $Ca = 0.43$  for M3.

First, the convergence with respect to the time-step size is analyzed. In Fig. 7.7 the deformation parameter  $D^*$  is plotted against the dimensionless time  $t/\tau_{em}$  for different time-steps  $\Delta t$  (0.01 s, 0.005 s, 0.0025 s, 0.00125 s and 0.000625 s) for mesh M3 and  $Ca = 0.43$ . After an almost linear increase of the deformation parameter in the beginning an overshoot occurs

between  $t/\tau_{em} = 5$  to 10. Finally, the deformation reaches a steady-state for large  $t/\tau_{em}$ . While there are deviations between the different time-steps in the initial transient region, the steady-state values are equal for all time-steps as was to be expected. It can be clearly seen that the results converge. For the remaining simulations we find that a time-step of 0.00125 s gives sufficiently time-step independent results.

Next, the convergence of the deformation parameter with respect to the mesh size is analyzed. The results for the different grids listed in Tab. 7.2 are illustrated in Fig. 7.8 for the three Capillary numbers considered. For the lowest Capillary number,  $Ca = 0.06$ , there is no overshoot before reaching a steady-state deformation. The plots for the other two Capillary numbers hardly show differences, except the slightly larger overshoot and generally larger values of  $D^*$  for  $Ca = 0.47$  compared to  $Ca = 0.43$ . The results for the different grids clearly converge, which is the case for all three Capillary numbers. Another simulation using mesh M3 in conjunction with the upwind scheme is performed for the case  $Ca = 0.43$ . In Fig. 7.8 one can see that the result with the upwind scheme is almost as good as the simulation on the same grid with the higher accurate Gamma scheme and thus one can expect that the choice of using the upwind scheme in the 3D simulations in the next subsection hardly has an impact.

To evaluate the ability of the new model to keep a constant interface thickness, the isolines for  $\alpha_\varphi = 0.05$ , 0.5 and 0.95 are pictured in Fig. 7.9. Obviously, the distance between the three isolines remains the same throughout the simulation. Thus, the new model is capable of keeping the interface thickness constant even in the droplet deformation simulations.

As the choice of  $\Delta\tau$  seems arbitrary in a certain range and is more or less assigned by trial and error, a comparison of simulations conducted with halve and double the value of the chosen  $\Delta\tau^*$  is plotted in Fig. 7.10. The results are equal, indicating that this parameter can in fact be chosen almost arbitrarily in a certain range as explained above. The particular choice does not affect the results.

Fig. 7.11 shows the result at  $Ca = 0.43$  with mesh M3 and  $\Delta t = 0.00125$  s performed at a retardation ratio of  $\beta_m = 1/9$  together with two additional simulations with  $\beta_m = 1/2$  and  $\beta_m = 1$ . The latter of which corresponds to pure Newtonian behavior of the matrix. Comparison is made with the simulation results of Yue et al. [10] ( $\beta_m = 1/2$ ) and our earlier simulations conducted with a VoF-model [11, 12] ( $\beta_m = 1/9$ ). It is found that with increasing matrix retardation parameter the initial slope decreases and thus the droplet deforms slower. Furthermore, the final steady-state deformation is larger if the matrix is Newtonian ( $\beta_m = 1$ ) compared to if a viscoelastic matrix is considered ( $\beta_m = 1/2$  and  $\beta_m = 1/9$ ). This supports the conclusion of Sibillo et al. [4] that droplet breakup is hindered by matrix elasticity. Differences between the two simulations with  $\beta_m = 1/2$  and  $\beta_m = 1/9$  are small indicating that results are hardly influenced by the choice of retardation parameter as long as the value

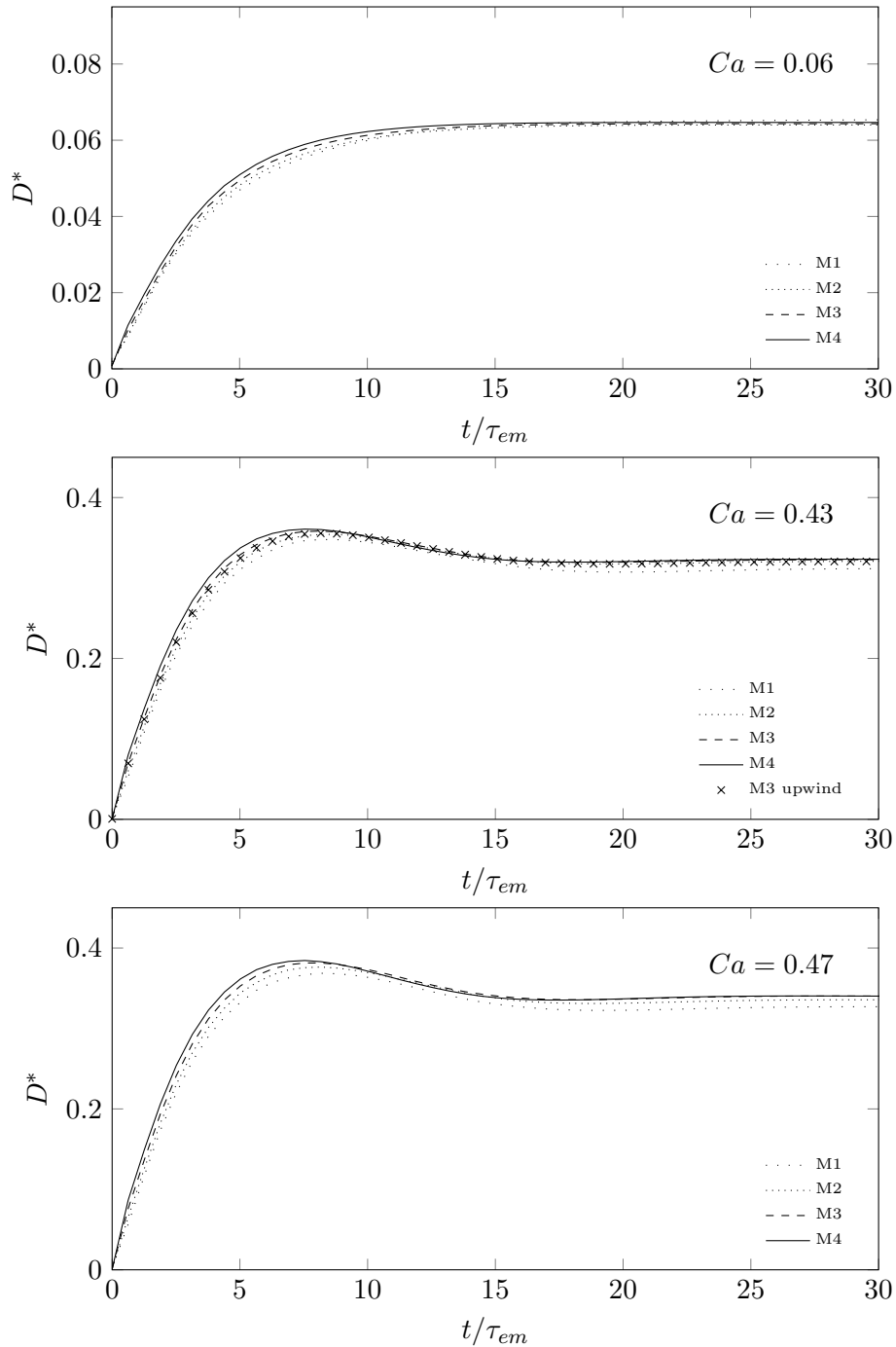


**Figure 7.8:** Deformation parameter  $D^*$  against the dimensionless time  $t/\tau_{em}$  for the different meshes and Capillary numbers at  $\Delta t = 0.00125$  s.

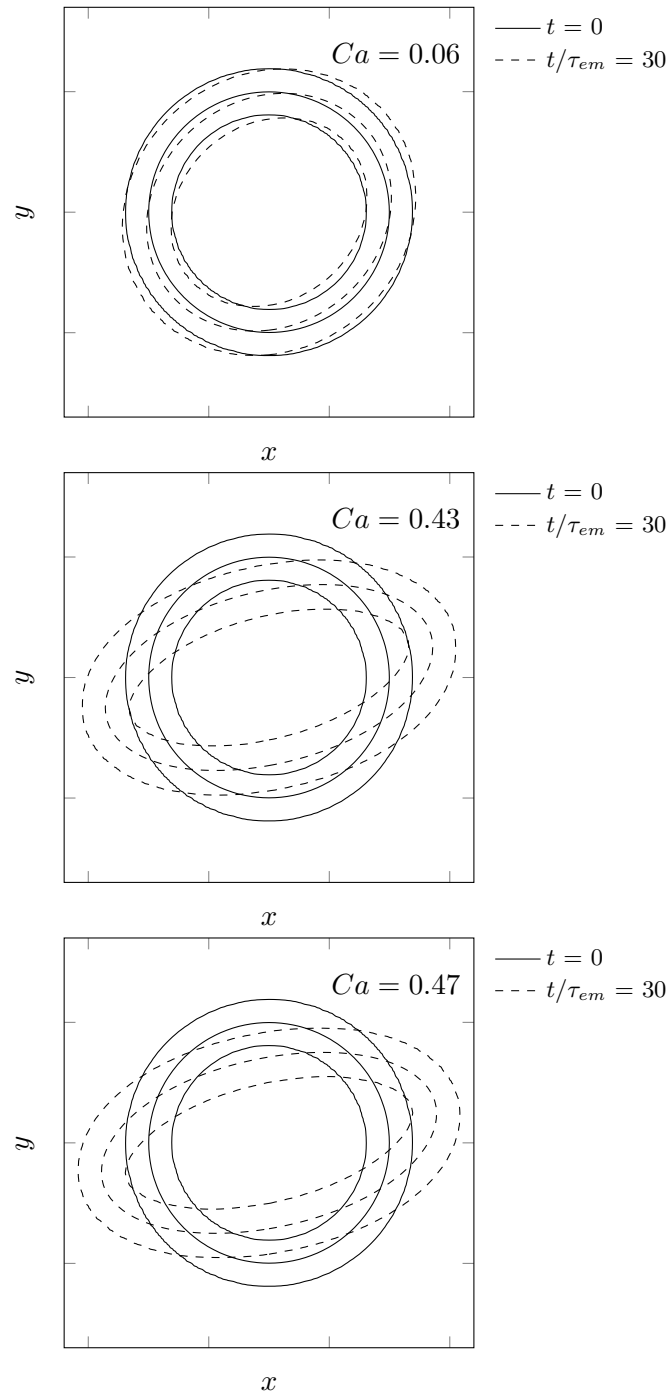


**Figure 7.9:** Isolines of  $\alpha_\varphi = 0.05, 0.5$  and  $0.95$  for  $t/\tau_{em} = 0$  and  $t/\tau_{em} = 30$  for mesh M3.



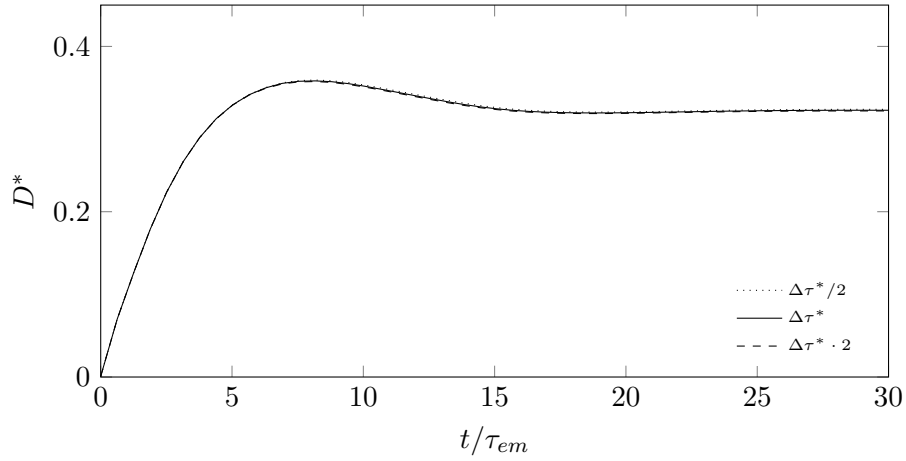


**Figure 7.10:**  $D^*$  against  $t/\tau_{em}$  for different values of  $\Delta\tau$  for mesh M3 and  $Ca = 0.43$ .

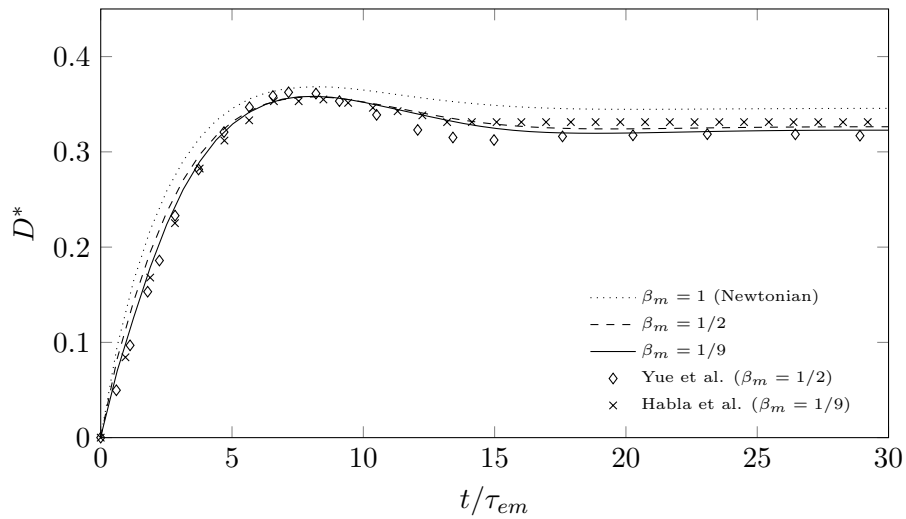


**Figure 7.11:**  $D^*$  against  $t/\tau_{em}$  compared to the simulations of Yue et al. [10] and Habla et al. [11, 12] for different values of  $\beta_m$  for mesh M3 and  $Ca = 0.43$ .

is not chosen too large. Nevertheless, the simulation result with  $\beta_m = 1/2$  corresponding to the simulation of Yue et al. [10] and the simulation result with  $\beta_m = 1/9$  corresponding to the simulation of Habla et al. [11, 12] show perceivable differences from the two literature results. A well-grounded explanation for these differences cannot be made at this point. Since our simulation results are clearly converged in time and space and thus non-convergence can be excluded, we believe that the various closure assumptions made in the derivation of our model might be the reason. Particularly, we believe that the modeling of the interfacial momentum transfer term  $\mathbf{M}_\varphi$  (cf. Eq. 7.6) influences the simulation results. The interfacial momentum transfer term was solely tested with basic scenarios involving only steady interfaces and flows parallel to the interface. The current modeling of this term might be less appropriate for more complex flows, such as is the case in droplet deformations. This will be the subject of further research.

### 3D Simulations

In this section the results of the 3D simulations are presented. The depth of the domain is chosen to  $5D$ .

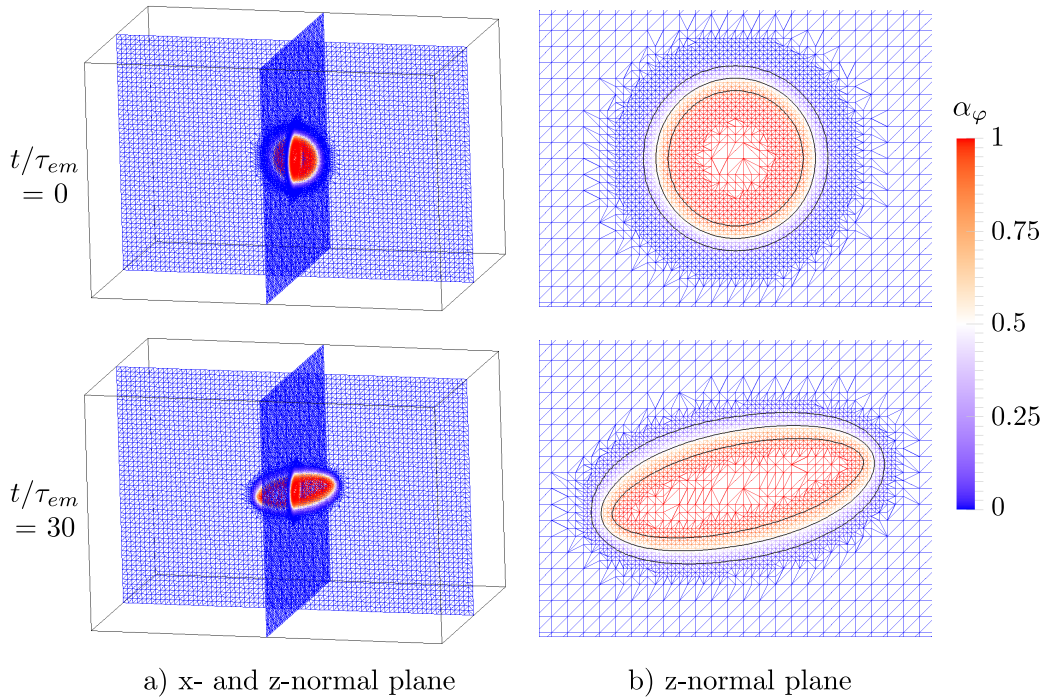


**Figure 7.12:** Illustration of the adaptive mesh refinement on mesh M6-3D for  $Ca = 0.43$ .

Top is the initial mesh and bottom is the final steady-state mesh. In the right picture the isolines of  $\alpha_\varphi = 0.05$ ,  $0.5$  and  $0.95$  are shown.

An adaptive mesh refinement technique is used in order to achieve a sufficient resolution of the interfacial region while keeping the overall cell count in the domain and consequently the computational costs small. Cells neighboring cells of  $0.01 \leq \alpha_\varphi \leq 0.99$  are split up to a level

of two. This is illustrated in Fig. 7.12, in which the initial and the final mesh is shown for  $Ca = 0.43$ . This way the initial resolution of the droplet of  $D/\Delta x = 10$  for mesh M6-3D is increased to  $D/\Delta x = 40$  around the interface, which is equivalent to the resolution of the 2D mesh M3, for which we already obtained proper mesh converged results.

**Table 7.3:** Steady-state values of  $D^*$  for meshes M4 and M6-3D, the simulations of Yue et al. [10] and Habla et al. [11] as well as the measurements of Sibillo et al. [4].

$Ca$	M4	M6-3D	Yue et al.	Habla et al.	Sibillo et al.
0.06	0.0647	0.0725	0.0660	0.0652	0.0716
0.43	0.323	0.431	0.317	0.327	0.359
0.47	0.340	0.460	0.336	<sup>2</sup>	<sup>3</sup>

<sup>2</sup>Not simulated.

<sup>3</sup>No steady-state reached.

In Fig. 7.13 the deformation parameter  $D^*$  of the three-dimensional simulations is plotted and compared to the two-dimensional simulations as well as the numerical predictions of Yue et al. [10] and Habla et al. [11, 12] and the measurements of Sibillo et al. [4]. It can be seen that the two three-dimensional grids give similar results, indicating a proper mesh convergence of our 3D simulations.

The initial slope of  $D^*$  against time  $t/\tau_{em}$  is almost the same in the 2D and 3D simulations with the slope being slightly larger in the 2D simulations in the beginning for all three Capillary numbers. From  $t/\tau_{em} > 5$  the 3D simulations predict larger deformations than the 2D simulations. An overshoot of  $D^*$  around  $t/\tau_{em} \approx 5$  predicted with the 2D simulations for the two larger Capillary numbers  $Ca = 0.43$  and  $0.47$  is not visible in the 3D simulations confirming that these overshoots are artifacts of the 2D simplification. The reason for that is the treatment of the droplet as a cylinder in the two-dimensional approximation. Deformations are not predicted to full extent this way. This aspect was already addressed in Verhulst et al. [15]. For the lowest Capillary number  $Ca = 0.06$  our 3D results are in good agreement with the measurements of Sibillo et al. [4]. The steady-state values of  $D^*$  predicted with mesh M4 and M6-3D are compared with those of Sibillo et al. [4], Yue et al. [10] and Habla et al. [11, 12] in Tab. 7.3. Here it can also be seen that for  $Ca = 0.06$  our 2D simulation is in better agreement with the simulations of Yue et al. [10] and Habla et al. [11, 12], while our 3D simulations predict the experimentally measured steady-state deformation parameter quite well. For the two larger Capillary numbers of  $0.43$  and  $0.47$  it

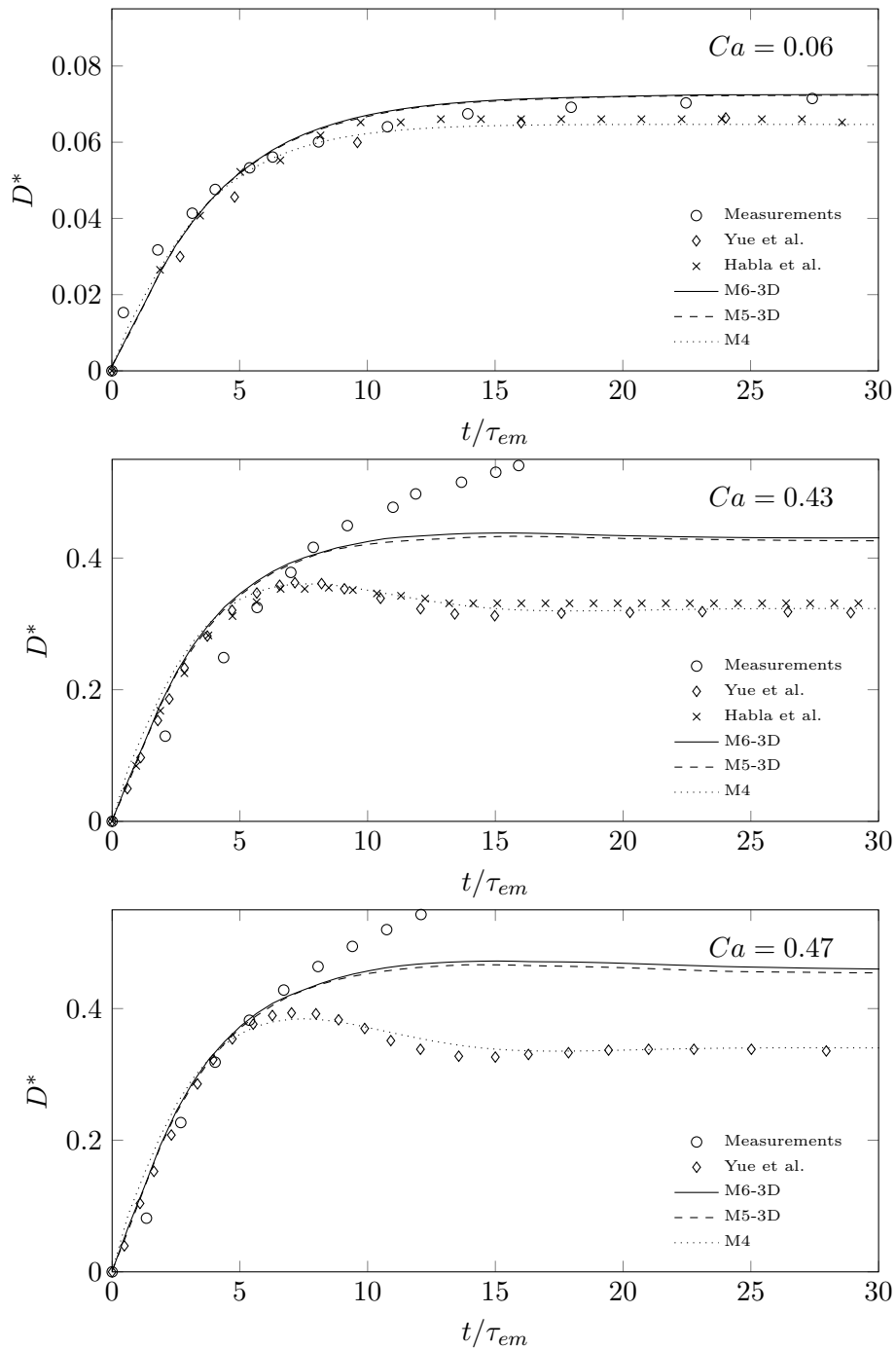


**Figure 7.13:** Deformation parameter  $D^*$  against the dimensionless time  $t/\tau_{em}$  compared to the measurements of Sibillo et al. [4] and the simulations of Yue et al. [10] and Habla et al. [11, 12].

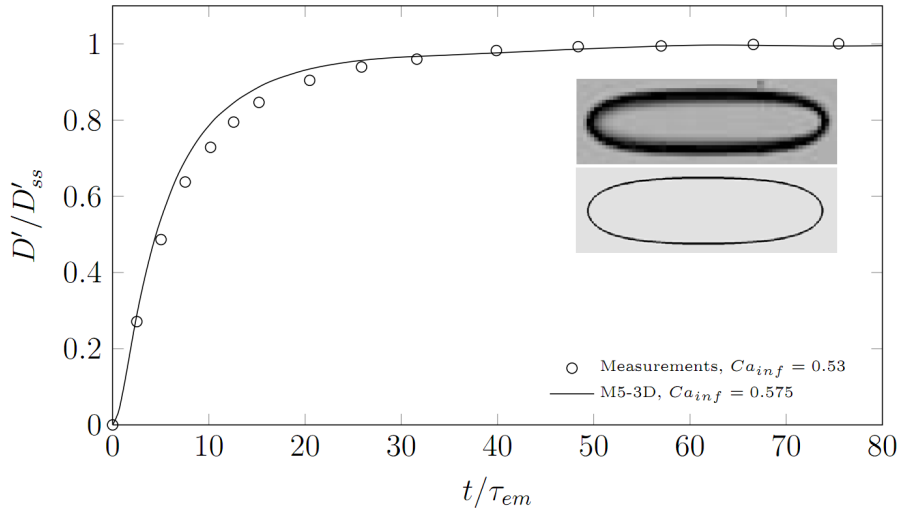


**Figure 7.14:**  $D'/D'_{ss}$  against  $t/\tau_{em}$  compared to the measurements of Sibillo et al. [4] for the highest subcritical Capillary number  $Ca_{inf}$  explored. Images are steady-state droplet shapes of the experiments (top) and the simulation (bottom) in  $y$ -normal view.

can be seen that for  $t/\tau_{em} > 5$  both the 2D and 3D simulations deviate perceptibly from the measurements. It is emphasized here that the experimentally measured deformation parameter exceed the  $y$ -axis for both Capillary numbers. For  $Ca = 0.43$  the experimentally measured deformation parameter shows a pronounced overshoot around  $t/\tau_{em} \approx 35$  and ends up in a steady-state around  $t/\tau_{em} \approx 140$ . The approximate value is listed in Tab. 7.3. Contrary to that, the experimentally measured deformation parameter ever increases for  $Ca = 0.47$  and the droplet ends up in break-up around  $t/\tau_{em} \approx 120$ . [4] The following aspects have to be taken into account as possible reasons for the deviations of our simulation results from the measurements: the Oldroyd-B model is used to fit the rheological data, which is not the most elaborate one to describe viscoelastic flows: the Oldroyd-B model predicts an infinite extensional viscosity at finite extensional rates, which is unphysical, and no second normal stress difference in steady shear flow. Furthermore, the range of viscosities given by Sibillo et al. [4] indicates that the fluids are in fact not ideal Boger fluids, but there is a shear-thinning behavior, which is not captured by this rheological modeling. However, fitting the rheological data given in Sibillo et al. [4] with a more sophisticated viscoelastic model is hardly possible. Besides that, only one relaxation time is used to describe the fluid, however, as for example stated in Verhulst et al. [15], the agreement with experimental data generally gets better if more relaxation times are considered.

In order to examine and clarify whether the rheological modeling is the reason for the differences found the deformation of a Newtonian droplet in a Newtonian matrix is simulated, for which the rheological modeling is straightforward and Sibillo et al. [4] also provide experimental measurements. This is shown in Fig. 7.14, in which  $D'/D'_{ss}$  is plotted against time  $t/\tau_{em}$  at the maximum Capillary number at which steady-state deformation was achieved ( $Ca_{inf}$ ). In our simulations we increased the Capillary number in steps of 0.025 and found break-up

at  $Ca_{cr} = 0.6$ . In the experiments the largest value found was  $Ca_{inf} = 0.53$ , which is smaller compared to our prediction of  $Ca_{inf} = 0.575$ , although we find this difference to be comparatively small. The predicted transient behavior is in acceptable agreement with the measurements with deviations particularly in the range  $5 < t/\tau_{em} < 20$ , see Fig. 7.14. The photograph of the droplet at steady-state, which is the upper picture in Fig. 7.14, is well resembled by the numerically predicted steady-state droplet shape. Thus, although there are slight differences in the pure Newtonian case, we conclude that the large differences in the viscoelastic simulations are presumably caused by the rheological modeling.

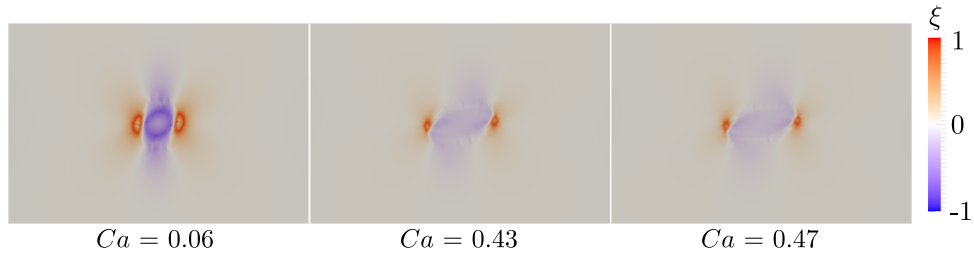


**Figure 7.15:** Z-normal plane colored by the local flow-type parameter  $\xi$  at  $t/\tau_{em} = 30$  using mesh M6-3D.

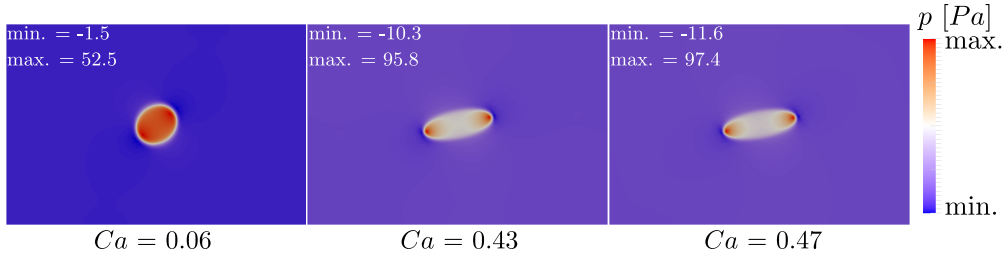


**Figure 7.16:** Z-normal plane colored by the pressure at  $t/\tau_{em} = 30$  using mesh M6-3D.

Finally, we present the local flow-type parameter  $\xi$  [16], the pressure and the stress components in and around the droplet in the z-normal plane in Figs. 7.15, 7.16 and 7.17 for our 3D simulations. The local flow-type parameter  $\xi$  has a value between 1 and -1. A value of -1 represents solid-like rotation, 0 is pure shear flow and 1 corresponds to pure extensional flow. For all three Capillary numbers considered the local flow-type parameter is between 0 and -1 within the droplet. For  $Ca = 0.06$  the droplet is almost solely rotated. With increasing Capillary number the flow inside the droplet changes from rotation and to getting sheared. At the tips of the droplet there is an area of strong extensional flow in the matrix phase. However, the center of extensional flow is not exactly aligned with the major axis of the droplet, but shifted slightly in y-direction to the x-axis. The area of extensional flow decreases with increasing Capillary number. At some distance away from the droplet the flow of the matrix is dominated by pure shear flow, as was to be expected due to the imposed flow type. The pressure inside the droplet is higher than in the matrix phase due to surface tension, see Fig. 7.16. The maxima are located at the tip of the drop on the inside and the minima are located on the outside of the tip with the values increasing with increasing Capillary numbers and the area of the extrema shrinking. The components of the stress  $\tau$  are pictured

7 An Improved Conditionally Volume Averaged Viscoelastic Two-Phase Model for Simulation of Transient Droplet Deformations under Simple Shear

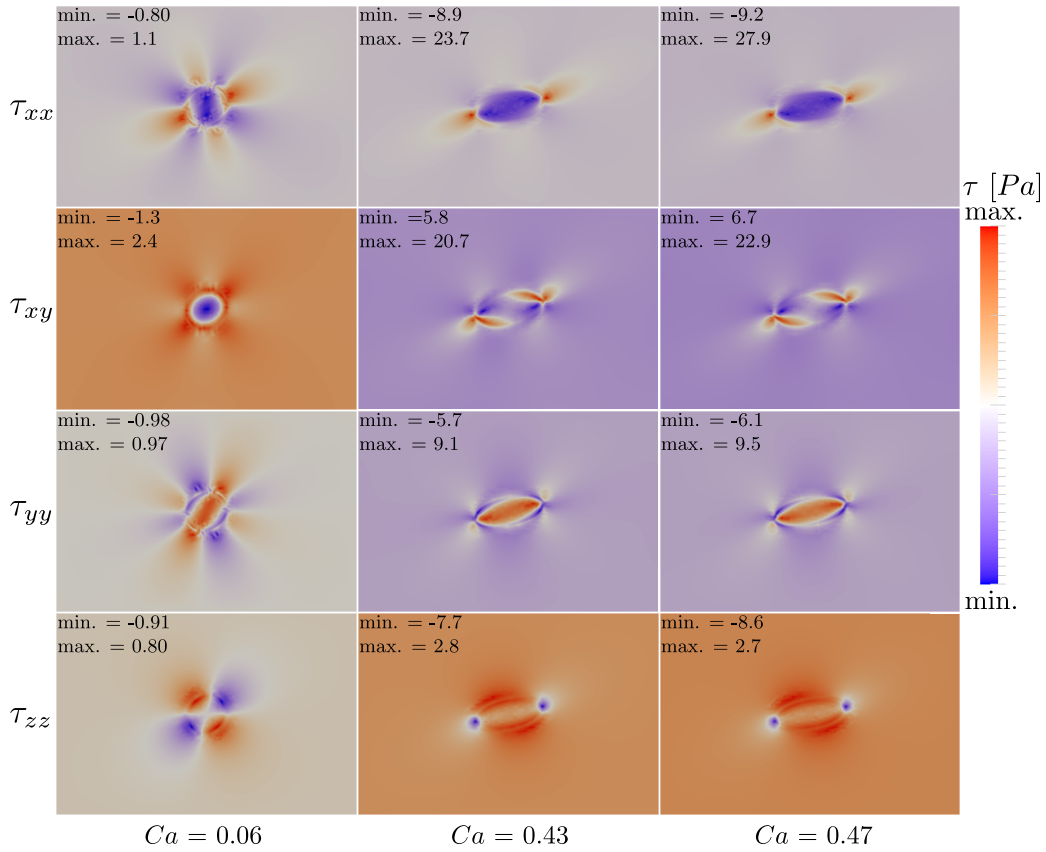


**Figure 7.17:** Z-normal plane colored by the respective stress components at  $t/\tau_{em} = 30$  using mesh M6-3D.

in Fig. 7.17. Again we find the maxima to increase and the minima to decrease as well as the areas of the extrema to shrink with increasing  $Ca$ , which is also found by Verhulst et al. [17]. An important aspect is that the stress field is not symmetric about the major axis of the droplet. Consequently, the deformation is asymmetric and the droplet is not exactly shaped like an ellipse. [18] Experiments of Liu et al. [19] showed that the shape of deformed droplets in viscoelastic matrices can only be symmetric if the flow is symmetric. But even if the flow is symmetric the deformation may be asymmetric, which implies that a three-dimensional approach is necessary to analyze the deformation. [18] In all three Figs. 7.15, 7.16 and 7.17 the differences between  $Ca = 0.43$  and  $Ca = 0.47$  are hardly visible. Apparently, this is caused by the fact that the critical Capillary number found by Sibillo et al. [4] doesn't accord with that of the simulations.

## 7.4 Summary

This work has been concerned with the adaption and validation of a conditionally volume averaged viscoelastic two-phase model and its application to the transient simulation of a Newtonian droplet deforming in a viscoelastic matrix under shear flow.

As the former model presented in Habla et al. [2] was not capable of keeping the interface thickness constant for moving interface problems, which, however, was a necessary condition in order to give proper results, an intermediate step proposed by Olsson and Kreiss [1], which preserves the width and profile of the interfacial transition region, was adopted.

A validation case proved that this intermediate step can in fact fix this issue for moving interface problems in our code. The adapted model was then applied to the two- and three-dimensional simulation of the deformation of a Newtonian droplet in a viscoelastic matrix under steady planar shear flow. The convergence with respect to the time-step and grid size was demonstrated. Furthermore, it was shown that the interface thickness is kept constant even in such a complex flow problem and the results are in reasonable agreement with the experiments of Sibillo et al. [4] and in good agreement with the phase-field simulations of Yue et al. [10] and our VoF simulations [11, 12].



## 7.A Literature

- [1] E. Olsson, G. Kreiss, A conservative level set method for two phase flow, *J. Comput. Phys.* 210 (2005) 225–246.
- [2] F. Habla, L. Dietsche, O. Hinrichsen, Modeling and simulation of conditionally volume averaged viscoelastic two-phase flows, *AIChE J.* 59 (2013) 3914–3927.
- [3] R. B. Bird, R. C. Armstrong, O. Hassager, Dynamics of polymeric liquids, 2nd ed., vol. 1, Wiley, New York, 1987.
- [4] V. Sibillo, M. Simeone, S. Guido, Break-up of a Newtonian drop in a viscoelastic matrix under simple shear flow, *Rheol. Acta* 43 (2004) 449–456.
- [5] Y. Sun, C. Beckermann, Diffuse interface modeling of two-phase flows based on averaging: mass and momentum equations, *Physica D* 198 (2004) 281–308.
- [6] A. Harten, The artificial compression method for computation of shocks and contact discontinuities: III. Self-adjusting hybrid schemes, *Math. Comput.* 32 (1978) 363–389.
- [7] S.-C. Xue, R. I. Tanner, N. Phan-Thien, Numerical modelling of transient viscoelastic flows, *J. Non-Newtonian Fluid Mech.* 123 (2004) 33–58.
- [8] J. Jasak, H. G. Weller, A. D. Gosman, High resolution NVD differencing scheme for arbitrarily unstructured meshes, *Int. J. Numer. Meth. Fluids* 31 (1999) 431–449.
- [9] R. I. Issa, Solution of implicitly discretised fluid flow equations by operator-splitting, *J. Comput. Phys.* 62 (1986) 40–65.
- [10] P. Yue, J. Feng, C. Liu, J. Shen, Transient drop deformation upon startup of shear in viscoelastic fluids, *Phys. Fluids* 17 (2005) 1–6.
- [11] F. Habla, H. Marschall, O. Hinrichsen, L. Dietsche, H. Jasak, J. L. Favero, Numerical simulation of viscoelastic two-phase flows using OpenFOAM®, *Chem. Eng. Sci.* 66 (2011) 5487–5496.
- [12] F. Habla, H. Marschall, O. Hinrichsen, L. Dietsche, H. Jasak, J. L. Favero, Corrigendum to "Numerical simulation of viscoelastic two-phase flows using OpenFOAM®" [*Chem. Eng. Sci.* 66 (2011) 5487-5496], submitted to *Chem. Eng. Sci.*
- [13] G. Taylor, The viscosity of a fluid containing small drops of another fluid, *Proc. Roy. Soc. London* 146 (1932) 501–523.

- [14] G. Taylor, The formation of emulsions in definable fields of flow., Proc. Roy. Soc. London 146 (1934) 61–106.
- [15] K. Verhulst, R. Cardinaels, P. Moldenaers, S. Afkhamib, Y. Renardy, Influence of viscoelasticity on drop deformation and orientation in shear flow. Part 2: Dynamics, J. Non-Newtonian Fluid Mech. 156 (2008) 44–57.
- [16] J. S. Lee, R. Dylla-Spears, N.-P. Tecler, S. J. Muller, Microfluidic four-roll mill for all flow types, Appl. Phys. Lett. 90 (2007) 074103.
- [17] K. Verhulst, R. Cardinaels, P. Moldenaers, S. Afkhamib, Y. Renardy, Influence of viscoelasticity on drop deformation and orientation in shear flow. Part 1: Stationary states, J. Non-Newtonian Fluid Mech. 156 (2008) 29–43.
- [18] S. Pillappakkam, P. Singh, A level-set method for computing solutions to viscoelastic two-phase flow, J. Comput. Phys. 174 (2001) 552–578.
- [19] Y. J. Liu, T. Y. Liao, D. D. Joseph, A two-dimensional cusp at the trailing edge of an air bubble rising in a viscoelastic liquid, J. Fluid Mech. 304 (1995) 321–342.

## 7.B Nomenclature

Normal symbols represent scalar quantities and boldface symbols represent vector and tensor quantities in general.

### Roman Symbols

Symbol	Description	Unit
$A$	Area	$[m^2]$
$D$	Cylinder or droplet diameter	$[m]$
$\mathbf{f}$	Compressive flux	$[\frac{m}{s}]$
$\mathbf{g}$	Gravitational acceleration vector	$[\frac{m}{s^2}]$
$h$	Drag coefficient	$[-]$
$H$	Domain height	$[m]$
$\mathbf{I}$	Identity matrix	$[-]$
$L$	Domain length	$[m]$
	or length of major axis in the xy-plane	$[m]$
$L'$	Length of major axis in the xz-plane	$[m]$
$\mathbf{M}_\varphi$	Interfacial momentum transfer of phase $\varphi$	$[\frac{kg}{m^2s^2}]$
$\mathbf{n}_{I,\varphi}$	Interface normal vector pointing inside volume of phase $\varphi$	$[-]$
$N_x$	Cell number in x-direction	$[-]$
$N_y$	Cell number in y-direction	$[-]$
$N_z$	Cell number in z-direction	$[-]$
$p$	Pressure	$[\frac{kg}{ms^2}]$
$\overline{p^d}$	Modified mixture pressure	$[\frac{kg}{ms^2}]$
$\overline{p}_\varphi$	Conditional volume averaged pressure of phase $\varphi$	$[\frac{kg}{ms^2}]$
$R$	Droplet radius	$[m]$
$t$	Time	$[s]$
$\mathbf{U}$	Local instantaneous velocity	$[\frac{m}{s}]$
$\overline{\mathbf{U}}$	Mixture velocity	$[\frac{m}{s}]$
$\mathbf{U}_I$	Interface velocity	$[\frac{m}{s}]$
$\mathbf{U}_r$	Relative velocity	$[\frac{m}{s}]$
$\overline{\mathbf{U}}_\varphi$	Conditional volume averaged velocity of phase $\varphi$	$[\frac{m}{s}]$
$\overline{\mathbf{U}}_\omega$	Conditional volume averaged velocity of phase $\omega$	$[\frac{m}{s}]$
$W$	Length of minor axis in the xy-plane	$[m]$

*7 An Improved Conditionally Volume Averaged Viscoelastic Two-Phase Model for Simulation of Transient Droplet Deformations under Simple Shear*

<b>Symbol</b>	<b>Description</b>	<b>Unit</b>
$W'$	Length of minor axis in the xz-plane	$[m]$
$x$	Position	$[m]$
$\mathbf{x}$	Position vector	$[m]$
$y$	Position	$[m]$

**Greek Symbols**

<b>Symbol</b>	<b>Description</b>	<b>Unit</b>
$\alpha_\varphi$	Volume fraction of phase $\varphi$	$[-]$
$\alpha_\omega$	Volume fraction of phase $\omega$	$[-]$
$\dot{\gamma}$	Shear-rate	$[s^{-1}]$
$\delta$	Interface thickness	$[m]$
$\Delta$	Relative deviation	$[-]$
$\Delta t$	Time-step size	$[s]$
$\Delta x$	Horizontal edge length of computational cell	$[m]$
$\Delta \tau$	Artificial time-step size	$[s]$
$\nabla$	Nabla (gradient) operator	$[m^{-1}]$
$\nabla \cdot$	Divergence operator	$[m^{-1}]$
$\epsilon$	Artificial diffusion coefficient	$[\frac{m^2}{s}]$
$\eta_d$	Droplet viscosity	$[\frac{kg}{ms}]$
$\eta_{eff,\varphi}$	Effective viscosity of phase $\varphi$	$[\frac{kg}{ms}]$
$\eta_{eff,\omega}$	Effective viscosity of phase $\omega$	$[\frac{kg}{ms}]$
$\eta_m$	Matrix viscosity	$[\frac{kg}{ms}]$
$\eta_P$	Polymeric viscosity	$[\frac{kg}{ms}]$
$\eta_{P,m}$	Polymeric viscosity of matrix phase	$[\frac{kg}{ms}]$
$\eta_{P,\varphi}$	Polymeric viscosity of phase $\varphi$	$[\frac{kg}{ms}]$
$\eta_r$	Viscosity ratio	$[-]$
$\eta_S$	Solvent viscosity	$[\frac{kg}{ms}]$
$\eta_{S,m}$	Solvent viscosity of matrix phase	$[\frac{kg}{ms}]$
$\eta_{S,\varphi}$	Solvent viscosity of phase $\varphi$	$[\frac{kg}{ms}]$
$\eta_\varphi$	Viscosity of phase $\varphi$	$[\frac{kg}{ms}]$
$\eta_\omega$	Viscosity of phase $\omega$	$[\frac{kg}{ms}]$
$\kappa_{I,\varphi}$	Curvature of interface with respect to phase $\varphi$	$[m^{-1}]$

*7 An Improved Conditionally Volume Averaged Viscoelastic Two-Phase Model for Simulation of Transient Droplet Deformations under Simple Shear*

<b>Symbol</b>	<b>Description</b>	<b>Unit</b>
$\lambda$	Relaxation time	[s]
$\lambda_m$	Relaxation time of matrix phase	[s]
$\lambda_\varphi$	Relaxation time of phase $\varphi$	[s]
$\xi$	Flow-type parameter	[-]
$\rho$	Local instantaneous density	$[\frac{kg}{m^3}]$
$\bar{\rho}_\varphi$	Conditional volume averaged density	$[\frac{kg}{m^3}]$
$\sigma$	Surface tension	$[\frac{kg}{s^2}]$
$\tau$	Deviatoric or extra-stress tensor	$[\frac{kg}{ms^2}]$
$\tau_P$	Polymeric stress tensor	$[\frac{kg}{ms^2}]$
$\tau_S$	Solvent stress tensor	$[\frac{kg}{ms^2}]$
$\overline{\tau_P}_\varphi$	Conditional volume averaged polymeric stress tensor	$[\frac{kg}{ms^2}]$
$\overline{\tau_S}_\varphi$	Conditional volume averaged solvent stress tensor	$[\frac{kg}{ms^2}]$
$\tau$	Artificial time	[s]
$\tau_{em}$	Emulsion time	[s]
$\Phi$	Arbitrary quantity	
$\Psi_{1,m}$	First normal stress coefficient of matrix phase	$[\frac{kg}{ms}]$

**Subscripts, Superscripts and Oversymbols**

<b>Symbol</b>	<b>Description</b>
$\mathbf{Q}_0$	Initial value of $\mathbf{Q}$
$\mathbf{Q}_d$	Droplet
$\mathbf{Q}^d$	Modified
$\mathbf{Q}_{eff}$	Effective
$\mathbf{Q}_{em}$	Emulsion
$\mathbf{Q}_I$	$\mathbf{Q}$ at the interface
$\mathbf{Q}_{inf}$	Maximum attainable number of $\mathbf{Q}$ under steady-state conditions
$\mathbf{Q}_m$	Matrix
$\mathbf{Q}_{num}$	Numerical
$\mathbf{Q}_r$	Relative
$\mathbf{Q}_{real}$	Real
$\mathbf{Q}_{ss}$	Steady-state value of $\mathbf{Q}$
$\mathbf{Q}^T$	Transpose of matrix $\mathbf{Q}$

Symbol	Description
$\mathbf{Q}_\varphi$	Conditioned $\mathbf{Q}$ , belonging to phase $\varphi$
$\mathbf{Q}^*$	Estimate of variable $\mathbf{Q}$
$\mathbf{Q}^{**}$	Estimate of variable $\mathbf{Q}$
$\overline{\mathbf{Q}}$	Volume averaged $\mathbf{Q}$ or mixture value of $\mathbf{Q}$
$\overline{\mathbf{Q}}_\varphi$	Conditional volume averaged $\mathbf{Q}$ , belonging to phase $\varphi$
$\underbrace{\mathbf{Q}}$	Interface average of $\mathbf{Q}$
$ \mathbf{Q} $	Magnitude of $\mathbf{Q}$
$\mathbf{Q} _{corr.}$	Correction to $\mathbf{Q}$
$\mathbf{Q} _{diff.}$	Diffusion contribution of $\mathbf{Q}$

### Nondimensional Groups

Symbol	Description	Definition
$Ca$	Capillary number	$\frac{\eta_m \dot{\gamma} R_0}{\sigma}$
$D^*$	Taylor deformation parameter in the xy-plane	$\frac{L-W}{L+W}$
$D'$	Taylor deformation parameter in the xz-plane	$\frac{L'-W'}{L'+W'}$
$p$	Weight coefficient of elasticity	$\frac{\lambda}{\tau_{em}}$
$\beta_m$	Retardation ratio of matrix phase	$\frac{\eta_{S,m}}{\eta_m}$
$\eta_r$	Viscosity ratio	$\frac{\eta_d}{\eta_m}$

### Abbreviations

Abbreviation	Description
DILU	Discrete incomplete lower-upper
GAMG	Generic algebraic multigrid
PCG	Preconditioned conjugate gradient
PISO	Pressure implicit with splitting of operator
TVD	Total variation diminishing
VOF	Volume-of-Fluid

## 7.C Summary

In this chapter the transient deformation of a Newtonian droplet in a viscoelastic matrix subject to a simple shear flow is simulated. The viscoelastic two-phase model was derived in a former work by applying the technique of conditionally volume averaging and subsequent closure modeling. [2] It was shown that the model requires a sufficient spatial resolution of the interfacial transition region in order to give proper results. As the original model was not capable of keeping the interface thickness constant when simulating problems involving moving interfaces, an intermediate step originally proposed by Olsson and Kreiss [1] is adopted in order to remedy this shortcoming. The intermediate step is validated by the simulation of a rotating cylinder and it is shown that this step can in fact fix this issue. The adapted model is then used to simulate transient droplet deformations carried out in 2D and 3D. In the 3D simulations an adaptive mesh refinement technique is used in order to guarantee a sufficient interface resolution while keeping the computational costs low. It is shown that the intermediate step keeps the interface thickness constant even in such a complex flow. The evolution of the Taylor deformation parameter is compared to the measurements of Sibillo et al. [4] and the simulations of Yue et al. [10] and Habla et al. [11] for three different Capillary numbers and finally the steady-state stress and pressure fields as well as the local flow-type parameter  $\xi$  are presented.

## 7.D Author contribution

The author of this thesis contributed to this publication by having the idea to provide a constant interface thickness even for moving and deforming interfaces by adapting the conservative level-set method, by implementing the method in the software *OpenFOAM*<sup>®</sup>, by proposing the concept of the validation base to show the benefits of using this technique, by doing the purely inelastic droplet deformation simulations and by writing the whole manuscript.

## 7.E Copyright permission

This chapter is originated from the following publication:

F. Habla, C. Waas, L. Dietsche, O. Hinrichsen, An Improved Conditionally Volume Averaged Viscoelastic Two-Phase Model for Simulation of Transient Droplet Deformations under Simple Shear, submitted to Chemical Engineering Science.

Reprinted with permission from Elsevier Ltd.





# 8 CFD Analysis of the Frame Invariance of the Melt Temperature Rise in a Single-Screw Extruder

## 8.1 Introduction

The metering channel of single-screw extruders (SSE) is the subject of many studies, both theoretical and experimental. [1, 2] In analytical approaches two different ways of creating the screw-motion are used: either by rotating the screw and keeping the barrel stationary or by fixing the screw and rotating the barrel. The latter uses a rotating coordinate system and is usually preferred in theoretical approaches due to its simplified analysis, although the former approach having a fixed coordinate system corresponds to the physical extrusion process used in practice. In the 90's the implicit assumption that both approaches result in the same flow field and throughput was disputed (see Campbell et al. [3, 4]); however, the question of frame independence of the flow field was sufficiently proved both experimentally and theoretically, with the theoretical differences being attributed to the neglect of the curvature in the unwound channel, see for example Rauwendaal et al. [5].

More recently, the group of Campbell (see Campbell et al. [6, 7]) claims that screw- and barrel-rotation result in different melt temperature rises. Their conclusion was underlined both theoretically by an analysis for an unwound channel and experimentally by using a device in which the barrel and the screw can be rotated independently of each other. The melt temperature rise was found to be perceivably higher in case of barrel rotation with the effect being more pronounced for Newtonian-like fluids than for shear-thinning fluids. Differences were attributed to the frame difference of the viscous dissipation term.

In this work we aim at examining this issue by first giving a simple proof for frame indifference of the viscous dissipation function and subsequently using a CFD analysis to further support this fact with simulation results. The simulations are performed for screw-rotation, barrel-rotation and a setup which we name real-barrel-rotation corresponding to the experimental setup, in which the centrifugal and Coriolis forces are obviously not considered. The results obtained are subsequently compared to each other. The analysis includes a two-dimensional cross-section and a three-dimensional model of the single-screw extruder. The two-dimensional simulations are performed both with and without the presence of a flight clearance. The fluid considered is a Newtonian-like polymer with a temperature-dependent viscosity. This work is organized as follows: In Section 8.2 a straightforward proof for objectivity of the viscous dissipation term is given and subsequently the theory of our model to describe the temperature rise in a screw pump is developed, which will help to further clarify this fact. The model is based on the conservation equations for mass, momentum and energy.

Differences between screw-rotation, barrel-rotation and real-barrel-rotation in our modeling approach are clarified. The numerical method is shortly outlined and the fluid rheology is described. In Section 8.3 the results are presented for a two-dimensional cross-section of a single-screw extruder and a fully three-dimensional extruder with two full turns. Finally, in Section 8.4 the main conclusions are drawn.

## 8.2 Theory

### 8.2.1 Viscous dissipation

The viscous dissipation or so-called dissipation function  $Q$  is

$$Q = \boldsymbol{\tau} : \mathbf{D} \text{ or } Q = \boldsymbol{\tau} : \mathbf{L} \quad (8.1)$$

where  $\boldsymbol{\tau}$  is the (symmetric) stress tensor and  $\mathbf{D}$  is the rate of deformation tensor

$$\mathbf{D} = \frac{1}{2} [\mathbf{L} + \mathbf{L}^T] \quad (8.2)$$

which is the symmetrical part of the velocity gradient  $\mathbf{L} = \nabla \mathbf{U}$ , i.e.  $\mathbf{D} = (\mathbf{L})_{symm.}$ . The two formulations in Eq. 8.1 are essentially equal due to the fact that  $\boldsymbol{\tau} : \mathbf{W} = \mathbf{0}$  ( $\mathbf{W}$  is per definition antisymmetric according to  $\mathbf{L} = (\mathbf{L})_{symm.} + (\mathbf{L})_{antisymm.} = \mathbf{D} + \mathbf{W}$ ).

The viscous stress  $\boldsymbol{\tau}$  for a Newtonian-like fluid with a temperature-dependent viscosity  $\eta(T)$  can be written as

$$\boldsymbol{\tau} = 2\eta(T) \mathbf{D} \quad (8.3)$$

The following proof for frame indifference of the viscous dissipation of a Newtonian-like fluid described by Eq. 8.1 in combination with Eq. 8.3 is straightforward and the procedure can be found in any standard textbook, see for example Holzapfel [8].

Let  $\mathbf{R}(t)$  (denoted as  $\mathbf{R}$  in the remainder) be a rotation matrix corresponding to a time-dependent rotational speed vector  $\boldsymbol{\omega}(t)$  and let  $\mathbf{A}$  be a second order tensor field.  $\mathbf{A}$  is objective if it transforms like  $\mathbf{A}^* = \mathbf{R}\mathbf{A}\mathbf{R}^T$ . With use of the deformation gradient  $\mathbf{F}$ , for which  $\mathbf{F}^* = \mathbf{R}\mathbf{F}$  holds, the rate of deformation tensor can be rewritten as  $\mathbf{D} = \left( \dot{\mathbf{F}}\mathbf{F}^{-1} \right)_{symm.}$ . Objectivity of the rate of deformation tensor can be shown by  $\mathbf{D}^* = \left( \dot{\mathbf{F}}^*\mathbf{F}^{*-1} \right)_{symm.} = \left( \dot{\mathbf{R}}\mathbf{R}^T + \mathbf{R}\dot{\mathbf{F}}\mathbf{F}^{-1}\mathbf{R}^T \right)_{symm.} = \mathbf{R}\mathbf{D}\mathbf{R}^T$ .

Frame indifference of the viscous dissipation term, Eq. 8.1, with use of the Newtonian Law, Eq. 8.3, is shown by  $Q^* = 2\eta(T) \mathbf{D}^* : \mathbf{D}^* = 2\eta(T) \mathbf{R}\mathbf{D}\mathbf{R}^T : \mathbf{R}\mathbf{D}\mathbf{R}^T = 2\eta(T) \mathbf{D} : \mathbf{D} = Q$ .

In consequence of the viscous dissipation being frame invariant,  $Q$  is identical when calculating it in different reference frames (here in particular when calculating  $Q$  with the velocities or similarly deformation gradients obtained in the stationary and the rotating reference frames).

## 8.2.2 Conservation laws

The frame invariance of viscous dissipation will be underlined by showing simulation results. Therefore, we will develop a CFD model, which is capable of calculating the kinematics and temperature rise in the two reference frames. Finally, by comparison of the temperature rise we will show that the results for screw- and barrel-rotation are indeed equal.

When deriving conservation laws one generally starts by using control masses ( $CM$ ) over which the conservation of a general intensive property  $\phi$  must hold. However, the treatment of control masses is difficult in fluid mechanical analyses due to the need to track the  $CM$ 's. Thus, conservation laws are commonly reformulated in terms of

$$\frac{d}{dt} \int_{V_{CM}} \rho \phi dV = \frac{d}{dt} \int_{V_{CV}} \rho \phi dV + \int_{S_{CV}} \rho \phi (\mathbf{U} - \mathbf{U}_b) \cdot \mathbf{n} dS \quad (8.4)$$

$\mathbf{U}$  is the velocity at which the fluid enters the control volume at a particular point of the surface  $S$ ,  $\mathbf{U}_b$  is the velocity of the control surface itself and  $\mathbf{n}$  denotes the unit normal vector to the control surface at that point.  $\mathbf{U}$  is referred to as the absolute velocity and the difference  $(\mathbf{U} - \mathbf{U}_b)$  as the relative velocity, i.e. the relative velocity of the fluid to the control volume motion. Mass, momentum and energy conservation can now be formulated

$$\frac{\partial}{\partial t} \int_{V_{CV}} \rho dV + \int_{S_{CV}} \rho (\mathbf{U} - \mathbf{U}_b) \cdot \mathbf{n} dS = 0 \quad (8.5)$$

$$\frac{\partial}{\partial t} \int_{V_{CV}} \rho \mathbf{U} dV + \int_{S_{CV}} \rho \mathbf{U} (\mathbf{U} - \mathbf{U}_b) \cdot \mathbf{n} dS = \int_{S_{CV}} \mathbf{T} \cdot \mathbf{n} dS + \int_{V_{CV}} \rho \mathbf{f} dV \quad (8.6)$$

$$\frac{\partial}{\partial t} \int_{V_{CV}} \rho U dV + \int_{S_{CV}} \rho U (\mathbf{U} - \mathbf{U}_b) \cdot \mathbf{n} dS = \int_{S_{CV}} \mathbf{q} \cdot \mathbf{n} dS + \int_{V_{CV}} Q dV \quad (8.7)$$

In Eq. 8.6  $\mathbf{f}$  represent the body forces, which in our case are the fictitious forces due to the rotating reference frame; and  $\mathbf{T}$  is the extra stress tensor  $\mathbf{T} = -p\mathbf{I} + \boldsymbol{\tau}$ , where  $p$  is pressure and  $\mathbf{I}$  is the identity tensor. In Eq. 8.7  $U$ , is the internal energy, which may be written in terms of the heat capacity at constant pressure  $c_P$  according to  $U = c_P T$ ;  $\mathbf{q}$  is the heat flux obeying Fourier's Law  $\mathbf{q} = -\lambda \nabla T$ , where  $\lambda$  is the heat conductivity; and  $Q$  is the energy source term due to viscous dissipation as described above (see Eq. 8.7).

### 8.2.3 Single-screw extruder modeling

When considering single-screw extruders, one may either make use of a stationary reference frame, in which the barrel is stationary and the screw is rotated. This is commonly referred to as *screw-rotation*. On the other hand, one can also make use of a rotating reference frame, in which the screw is stationary while the barrel rotates. This is called *barrel-rotation*, see Fig. 8.1.

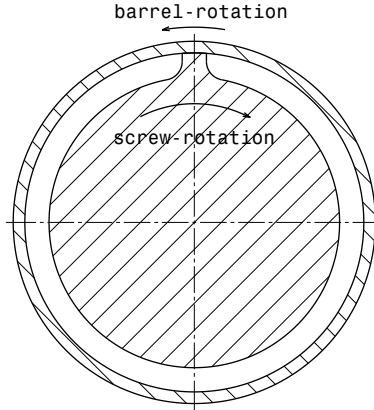


**Figure 8.1:** *Screw- and barrel-rotation.*

In case of *barrel-rotation* the fluid cavity is stationary and we may consider stationary (non-moving) control volumes. In this case  $\mathbf{U}_b = \mathbf{0}$ . Centrifugal and Coriolis acceleration arises due to the rotating coordinate system:  $\mathbf{f} = -\boldsymbol{\omega} \times (\boldsymbol{\omega} \times \mathbf{r}) + 2(\boldsymbol{\omega} \times \mathbf{U})$ , where the rotational speed  $\boldsymbol{\omega}$  is a vector normal to the plane shown in Fig. 8.1 with its origin located in the center.  $\mathbf{r}$  is the radial distance from the center. If the rotational speed is varying with time, the Euler acceleration has to also be considered:  $\mathbf{f} = -\boldsymbol{\omega} \times (\boldsymbol{\omega} \times \mathbf{r}) + 2(\boldsymbol{\omega} \times \mathbf{U}) + \frac{\delta\boldsymbol{\omega}}{\delta t} \times \mathbf{r}$ . In case of *screw-rotation* the fluid cavity rotates about the center and control volumes are rotated with the cavity about the center. In this case, we have  $\mathbf{f} = \mathbf{0}$  due to the fixed coordinate system, however,  $\mathbf{U}_b = \boldsymbol{\omega} \times \mathbf{r}$  due to the motion of the control volumes. In this study we are also interested in finding out what the differences are if one would indeed rotate the barrel as is being done in the experiments of Campbell et al. [6]. In this case again  $\mathbf{U}_b = \mathbf{0}$ , but the centrifugal, Coriolis and Euler acceleration is obviously neglected:  $\mathbf{f} = \mathbf{0}$ . This simplifying assumption is often used in theoretical approaches. We will refer to this setup as *real-barrel-rotation*. Differences between *barrel-rotation* and *real-barrel-rotation* can be attributed to the influence of the centrifugal and Coriolis forces. However, it should be noted that these forces are expected to be negligible. [9] In order to compare the velocity fields between *barrel-rotation*, *real-barrel-rotation* and *screw-rotation*, the velocity fields obtained for *barrel-rotation* and *real-barrel-rotation* are transformed to a stationary reference frame - as is the case in *screw-rotation* - according to

$$\mathbf{U}_{screw-rot.} = \mathbf{U}_{barrel-rot.} - \boldsymbol{\omega} \times \mathbf{r} \quad (8.8)$$

## 8.2.4 Fluid rheology

The fluid considered in this work is a Newtonian-like polycarbonate. Its temperature dependence can be modeled with the Vogel equation [10]

$$\ln(\eta(T)) = \frac{A + B}{T - T_0} \quad (8.9)$$

where  $A$ ,  $B$  and  $T_0$  are the model constants. In this work  $A + B = 1300K$  and  $T_0 = 365K$ . The thermal conductivity is  $k = \frac{\lambda}{\rho c_P} = 9.80 \cdot 10^{-7} \frac{m^2}{s}$ , the heat capacity at constant pressure is  $c_P = 1941.7 \frac{J}{kgK}$  and the density is  $\rho = 1070 \frac{kg}{m^3}$ , which are assumed to be independent of the temperature.

## 8.2.5 Numerical methodology

The above set of equations is discretized using the finite-volume method (FVM). A collocated arrangement is used storing all variables in cell centers. Linear interpolation is used to obtain values on cell faces, except for the convective term, where the Gamma-scheme [11] is used for the 2D simulations and the first-order upwind scheme is applied to the 3D simulations. A first-order two-point scheme is used to approximate time derivatives. The PISO-loop is used to handle pressure-velocity coupling. After the PISO-loop, the viscous dissipation term is calculated from the velocities and subsequently the energy equation is solved. Once the new temperature field has been determined, the viscosity is updated for the next time step. Time step independence was ensured for all simulations by varying the time-step size and comparing the results. Tolerances of the linear solvers are set very small ( $10^{-12}$ ) to avoid errors from the iterative solution process. In order to avoid a singularity at the first time step, the angular velocity is not immediately assigned at time  $t = 0s$ , but a smooth linear startup of the angular velocity over the first half rotation is used.

In case of *screw-rotation* the position of each node is updated according to the current angular velocity. The velocity of each cell face  $U_b$  is subsequently computed and the relative velocity needed for the convective terms is then calculated.

Body forces appearing in *barrel-rotation* are explicitly included using second-order Gaussian integration.

# 8.3 Results and discussion

## 8.3.1 Two-dimensional cross-section

In Fig. 8.2 the geometry, which is based on the extruder used in Campbell et al. [7], is shown (Fig. 8.2 (a)) together with the two sample lines  $A - B$  and  $C - D$  (Fig. 8.2 (b)) used for comparison of the results. The rotational speed is  $\omega_{max} = 100 \text{ rpm}$ . The influence of the

8 CFD Analysis of the Frame Invariance of the Melt Temperature Rise in a Single-Screw Extruder

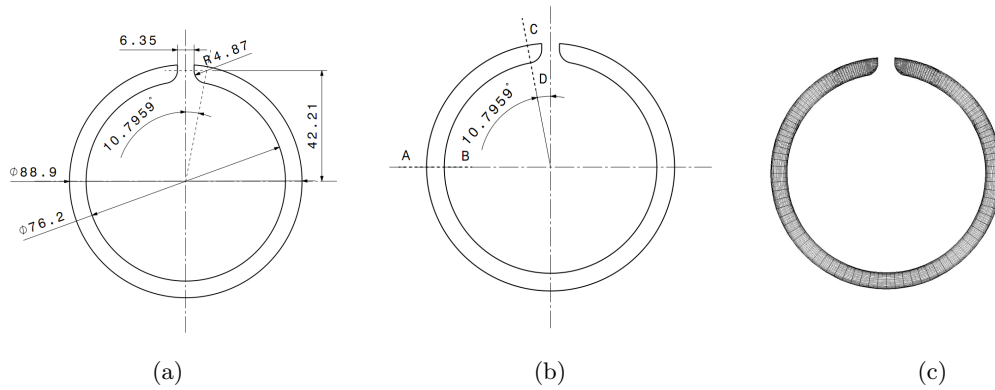


**Figure 8.2:** Geometry of the extruder (a), sample lines (b), mesh M1 (c), length are in *mm*.

leakage flow was initially assumed to be small and thus neglected. A discussion concerning this influence will be given at the end of this section.

Three meshes of different size are used to analyze the mesh independence of the results. Mesh M1 is shown in Fig. 8.2 (c). Mesh M1 has a cell count of 2,938, M2 has 11,150 and M3 has 44,600 cells. All meshes are graded towards the screw- and barrel-wall, where the largest gradients in the velocity are expected, see Fig. 8.2 (c).

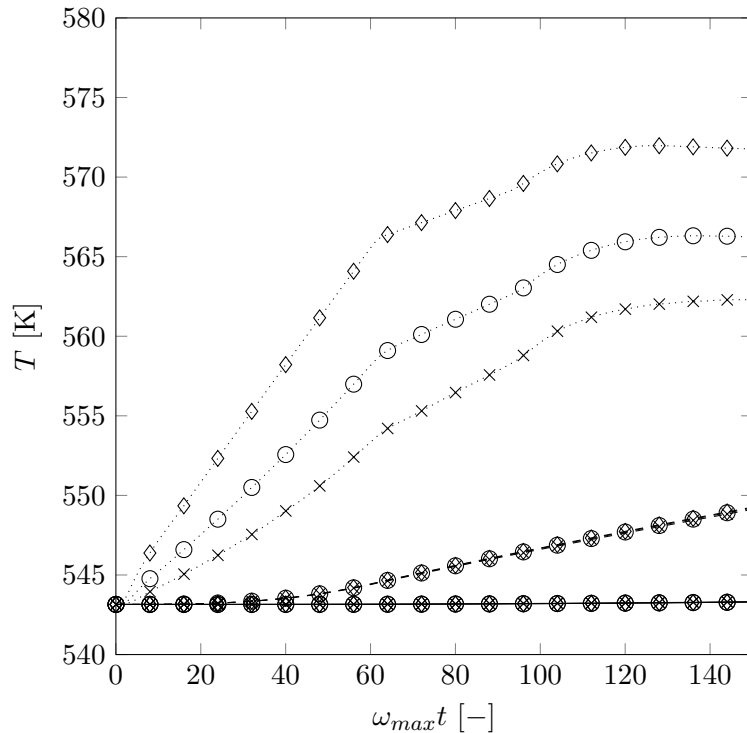


**Figure 8.3:**  $T_{min}$  (solid lines),  $T_{max}$  (dotted lines) and  $T_{av}$  (dashed lines) as a function of the dimensionless time for the three different meshes using *screw-rotation*. (x): M1, (o): M2 and (diamond): M3.

In Fig. 8.3 we present the minimum temperature  $T_{min}$  and the maximum temperature  $T_{max}$  in the cross-section as well as the area-averaged temperature  $T_{av}$  for *screw-rotation* using the three different meshes. The three temperature measures are subsequently used for comparison of the results. It can be seen that the results for  $T_{min}$  and  $T_{av}$  are spatially converged and mesh-independent, however, this is not the case for  $T_{max}$ . This lets us conclude that still finer meshes are needed to accurately predict  $T_{max}$  and the sharp temperature gradients, which are largest at the right hand side of the flight.

**Table 8.1:** Minimum, maximum and area-averaged temperature for the two-dimensional cross-section simulations at  $\omega_{max}t = 150$ .

		$T_{min}$ [K]	$T_{max}$ [K]	$T_{av}$ [K]
M1	screw	543.32	562.29	549.12
	barrel	543.32	562.41	549.10
	real-barrel	543.32	562.41	549.10
M2	screw	543.30	566.23	549.21
	barrel	543.29	566.34	549.20
	real-barrel	543.29	566.34	549.20
M3	screw	543.30	571.76	549.26
	barrel	543.29	571.82	549.26
	real-barrel	543.29	571.82	549.26

In Table 8.1 the final values of the three temperature measures at the end of the simulation time  $\omega_{max}t = 150$  are shown for the three meshes. We find that the results obtained for *barrel-rotation* and *real-barrel-rotation* are identical proving that the fictitious forces are so small that they have absolutely no influence on the temperature rise. When comparing *screw-rotation* and *barrel-rotation*, we find all three temperature measures to only differ on the second decimal for the finest mesh, which we assume is caused by remaining discretization errors. This is in particular interesting for  $T_{max}$ , which is not yet spatially converged. Despite that, the final value of  $T_{max}$  is still independent of the reference frame.

Comparison between *screw-rotation* and *barrel-rotation* is shown in Fig. 8.4 for mesh M3 (*real-barrel-rotation* is omitted since there is no difference from *barrel-rotation*). We find all three temperature measures to be in accordance with only small deviations. Even if the rotational speed is not constant, which is the case in the linear startup of the rotational speed ( $\omega_{max}t \leq 60$ ), we find the temperature measures to be equal suggesting that frame independence must also hold for non-constant rotational speeds.

In Fig. 8.5 the local velocity and temperature profiles at the sample lines  $A - B$  and  $C - D$  are shown. Velocity profiles for *barrel-rotation* are shown together with the transformed

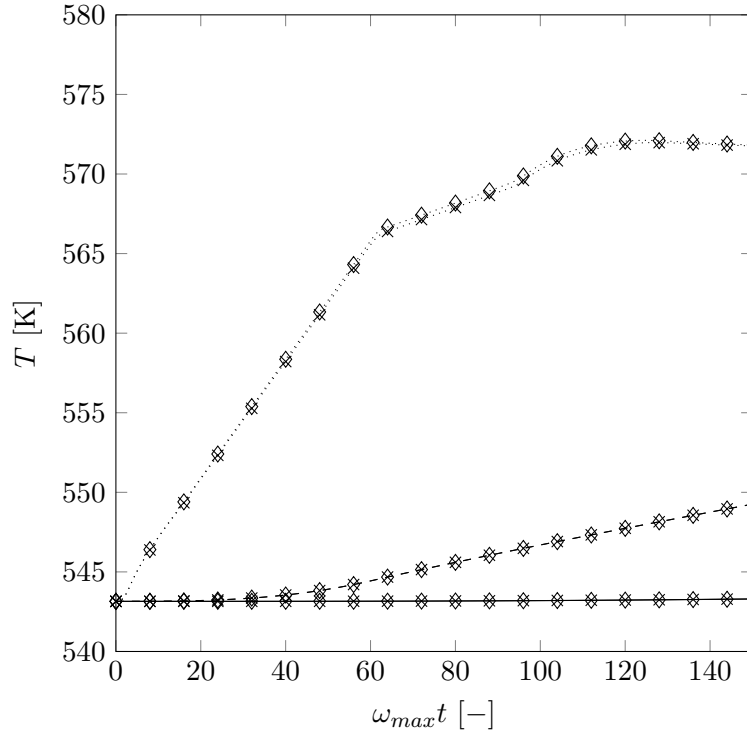


**Figure 8.4:**  $T_{min}$  (solid lines),  $T_{max}$  (dotted lines) and  $T_{av}$  (dashed lines) as a function of the dimensionless time for *screw-* and *barrel-rotation* using mesh M3; (×): screw-rotation and (◇): barrel-rotation.

velocity according to Eq. 8.8 (*real-barrel-rotation* is again omitted since there is no difference from *barrel-rotation*, which is in agreement with the findings in Spalding et al. [9]). The transformed velocity and the velocity obtained for *screw-rotation* are identical for both velocity components  $U_x$  and  $U_y$ . The temperature profiles are also identical for both reference frames showing that not only are the three global temperature measures  $T_{min}$ ,  $T_{max}$  and  $T_{av}$  frame independent, but local profiles are also frame independent.

Next, the influence of the presence of a flight clearance was examined. The flight clearance was assumed to be 1/1000 of the barrel diameter. To account for a sufficient resolution of the steep gradients appearing in the clearance, a very fine mesh of 193,979 cells is used. Again, frame invariance of the kinematics and the temperature rise as well as negligible centrifugal, Coriolis and Euler forces were initially verified by comparing the results of *screw-*, *barrel-* and *real-barrel-rotation*. This proves that these properties are not affected by the presence of a clearance. In Fig. 8.6, a comparison of the three temperature measures between the simulations with and without a flight clearance is shown. There is almost no difference in  $T_{min}$  and the difference in  $T_{av}$  is also very small with a relative deviation of  $\epsilon = \frac{T_{with\ fl.} - T_{without\ fl.}}{T_{without\ fl.} - T_0} < 0.05$  between the two simulations at final dimensionless time  $\omega_{max} t = 150$ . This owes to the fact that although high temperatures are present inside the clearance, the effect on the average temperature is small due to the small ratio of the area of the clearance to the overall area of the cross-section. This is supported by Figs. 8.7 (a) and 8.7 (b), in which it can be seen that only in a small area on the right side of the flight



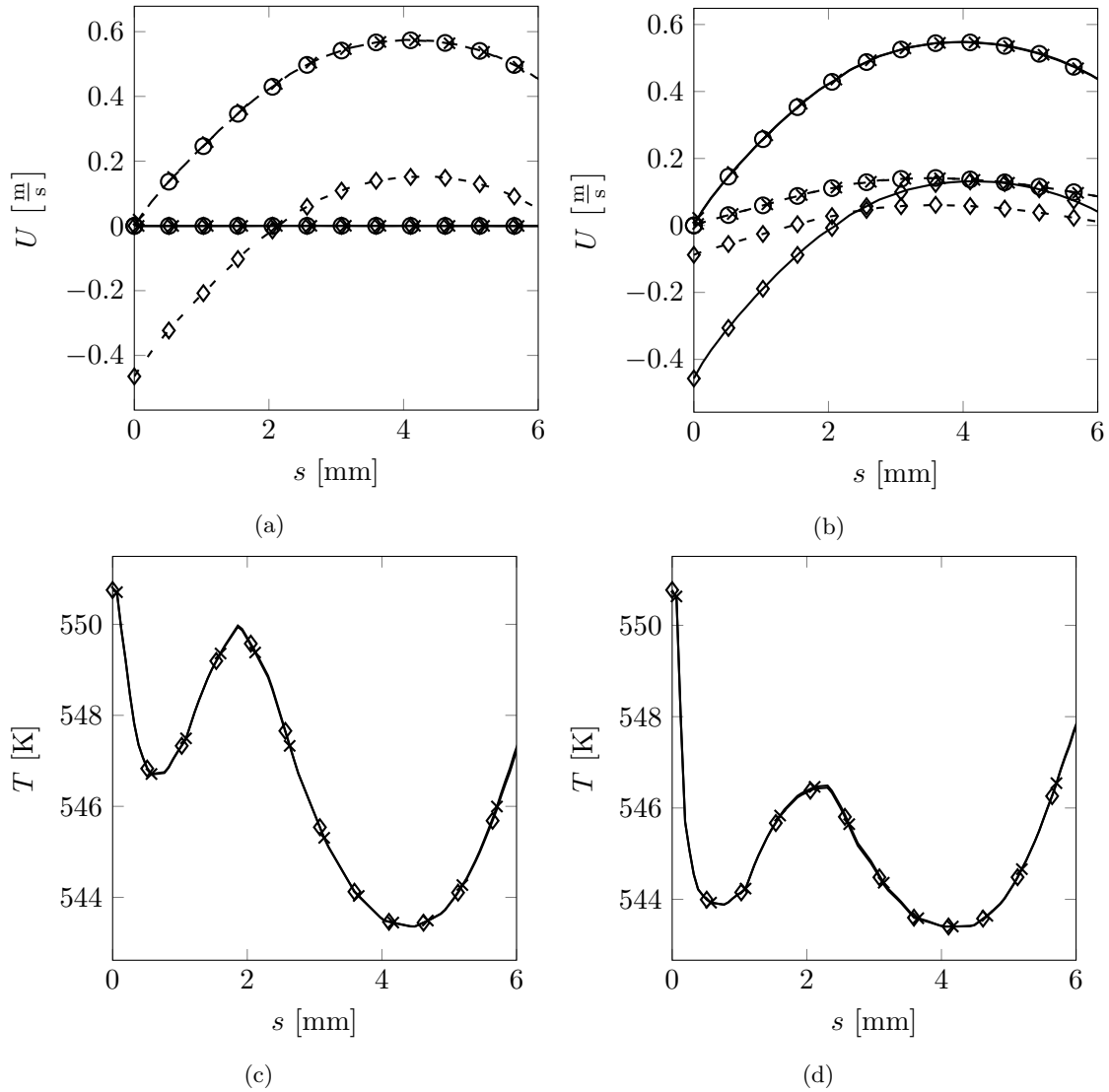


**Figure 8.5:** Local velocity ((a) and (b)) and temperature profiles ((c) and (d)) at the sampling lines A – B ((a) and (c)) and C – D ((b) and (d)) at  $\omega_{max}t = 150$  using mesh M1. Solid lines are  $U_x$  and dashed lines are  $U_y$ ; (×): screw-rotation, (◇): barrel-rotation and (○): the transformed velocity according to Eq. 8.8.

(Fig. 8.7 (b)) can a larger temperature be found, as compared to the simulation without the flight (Fig. 8.7 (a)). However, there is a significant deviation in  $T_{max}$ , which is due to the very high temperatures appearing in the clearing, see Fig. 8.6. A detailed view of the clearance is shown in Fig. 8.7 (c). The largest temperatures can be found in the left part of the flight (with the screw rotating in clockwise direction).

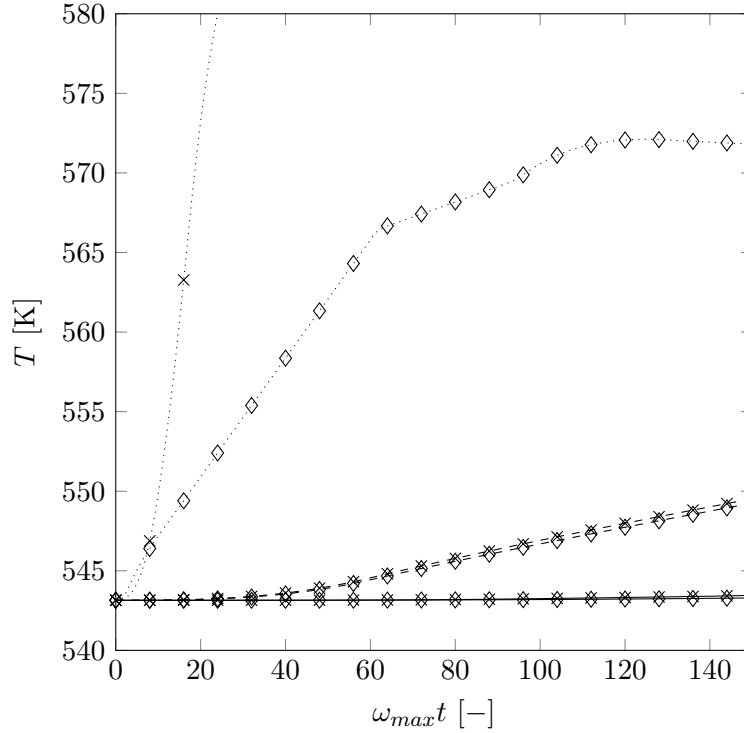


**Figure 8.6:**  $T_{min}$  (solid lines),  $T_{max}$  (dotted lines) and  $T_{av}$  (dashed lines) as a function of the dimensionless time for *barrel-rotation*.

( $\diamond$ ): simulation without flight clearance (mesh M3) ( $\times$ ): simulation with flight clearance.

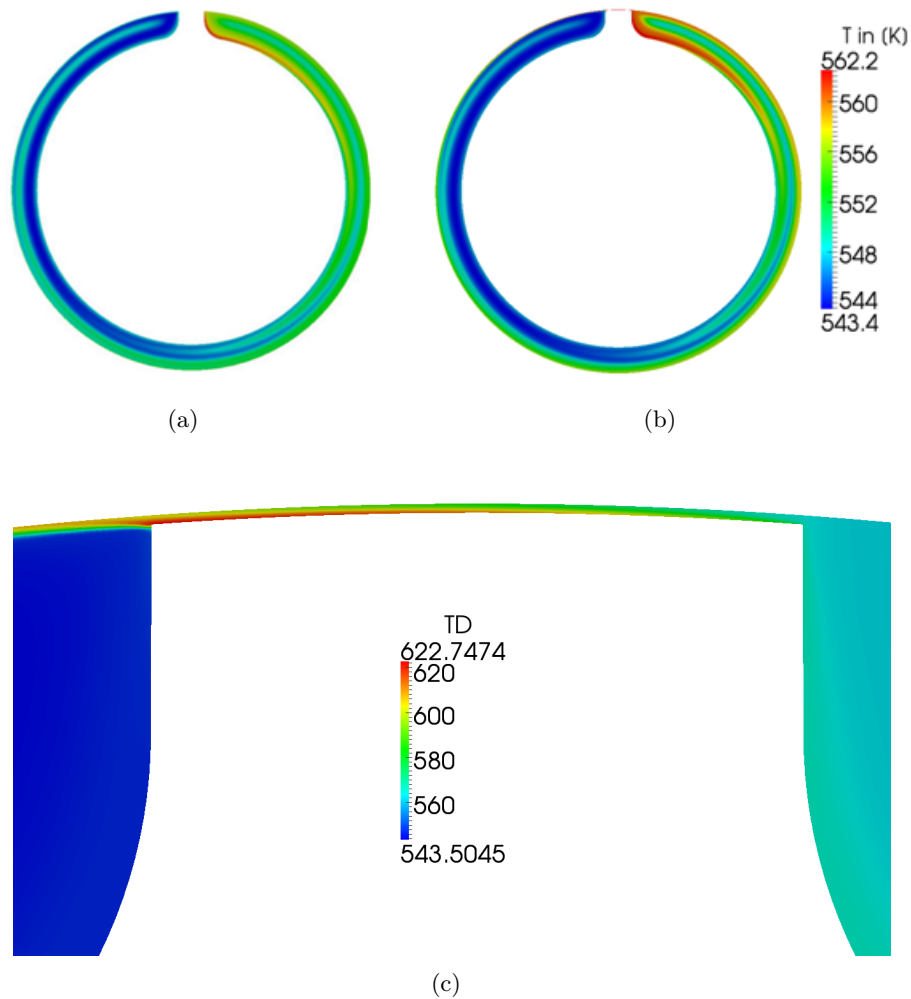


**Figure 8.7:** Temperature field for the two-dimensional cross-section at  $\omega_{max}t = 150$  using *screw-rotation*. (a) simulation without flight clearance (mesh M3), (b): simulation with flight clearance (temperature field scaled to the legend on the right), (c) enlarged view of the flight clearance (temperature field scaled to the maximum temperature of the simulation).

### 8.3.2 Three-dimensional simulations

In this section we present the results for a three-dimensional single-screw extruder with two full turns. The geometry is a three-dimensional extension to the two-dimensional cross-section used in the preceding section. No flight clearance is considered due to the findings in the previous section. Results and comparisons are presented in the cross-sectional plane after one turn of the screw in order to avoid end-effects. A tetrahedral mesh is used with a cell count of 141,389. The cross-sectional cell density is such as to reflect mesh M1, which was shown to give sufficiently converged results. Simulations are performed for 10 %, 60 % and 90 % of the maximum pumping capacity of the screw (drag rates  $Fr = 0.9, 0.4, 0.1$ , respectively), similar to the work of Campbell et al. [7]. This is done as follows: initially, a simulation was performed with an open boundary condition at the inlet. The averaged inlet velocity was then determined at steady-state and the corresponding fraction of that maximum velocity is assigned as a plug flow at the inlet.

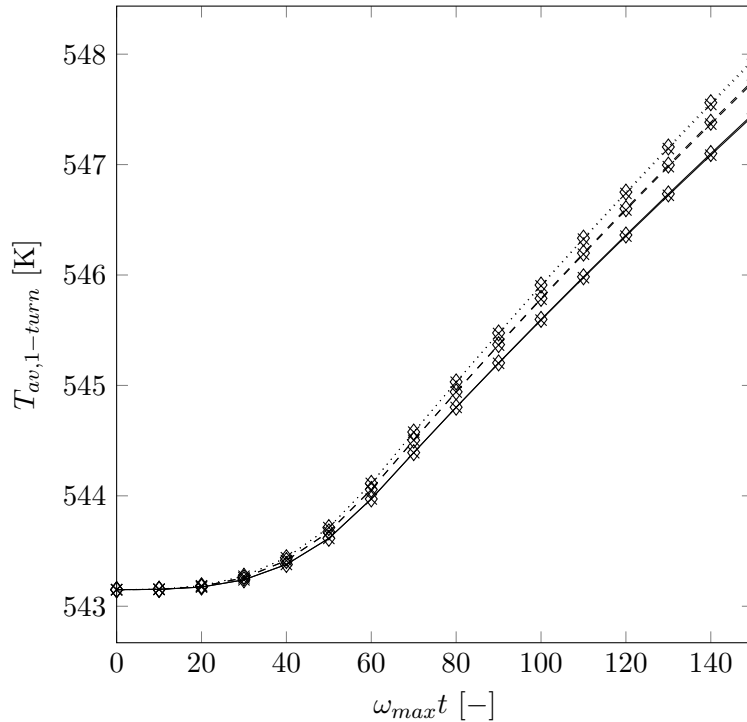


**Figure 8.8:** Area-averaged temperature in the cross-sectional plane after one full turn of the screw as a function of the dimensionless time for different discharge rates. Solid lines are  $Fr = 0.1$ , dashed lines are  $Fr = 0.4$  and dotted lines are  $Fr = 0.9$ ; ( $\times$ ): screw-rotation and ( $\diamond$ ): barrel-rotation.

The results for the area-averaged temperature over the cross-section after one turn are shown in Fig. 8.8 for the three drag rates. Temperatures for *screw-rotation* and *barrel-rotation* coincide (*real-barrel-rotation* also coincides and is omitted here for clarity). At smaller pumping rates the temperature is larger, as expected. Local profiles are shown in Fig. 8.9 for velocity and Fig. 8.10 for temperature. Velocities are in perfect agreement for *screw-rotation* and *barrel-rotation*. Temperature profiles are also in agreement, although showing small

differences, which may be attributed to discretization errors caused by the use of tetrahedral cells in conjunction with a diffusive first-order convection scheme. Again, no differences are perceivable between *barrel-rotation* and *real-barrel-rotation*, showing the negligible influence of the fictitious forces (results are omitted due to readability).

## 8.4 Conclusions

In this paper, a numerical analysis of a single-screw extruder filled with a Newtonian-like fluid was performed. Three different operating setups were considered, namely a *screw-rotation*, a *barrel-rotation* and a *real-barrel-rotation* setup. The numerical simulations include a two-dimensional cross-section and a fully three-dimensional single-screw extruder. The *real-barrel-rotation* setup was introduced to prove the irrelevance of inertial forces acting on the fluid, an assumption which is widely used in analytical extrusion modeling (see e.g. Spalding et al. [9]). By comparing the numerical results between the *screw-rotation* and the *barrel-rotation* setup, the frame indifference of a mechanical system with respect to a relative motion can be proved. No difference in the melt temperature rise between *screw-rotation* and *barrel-rotation* could be observed, which is in contradiction with some important statements made in literature (see e.g. Campbell et al. [6]). In our view, the experimentally found difference in the temperature rise cannot be caused by kinematical effects, a conclusion which can be drawn from our numerical computations. In contrast, in literature, frame difference of the dissipation function was proposed as a possible reason for the different outcomes observed in experiments (see e.g. Campbell et al. [6]). To underline our point of view, an analytical proof of frame indifference of the dissipation function was given in the beginning of our paper. A comparison between numerical simulations with and without a flight clearance suggests that the temperature rise is only minorly influenced by the presence of the flight clearance. This finding is also in disagreement with Campbell et al. [6], who suggests that a large amount of viscous dissipation arises from the clearance flow. Hence, the reason for this peculiar behavior seems not to be settled yet and should be subject of further experimental research.

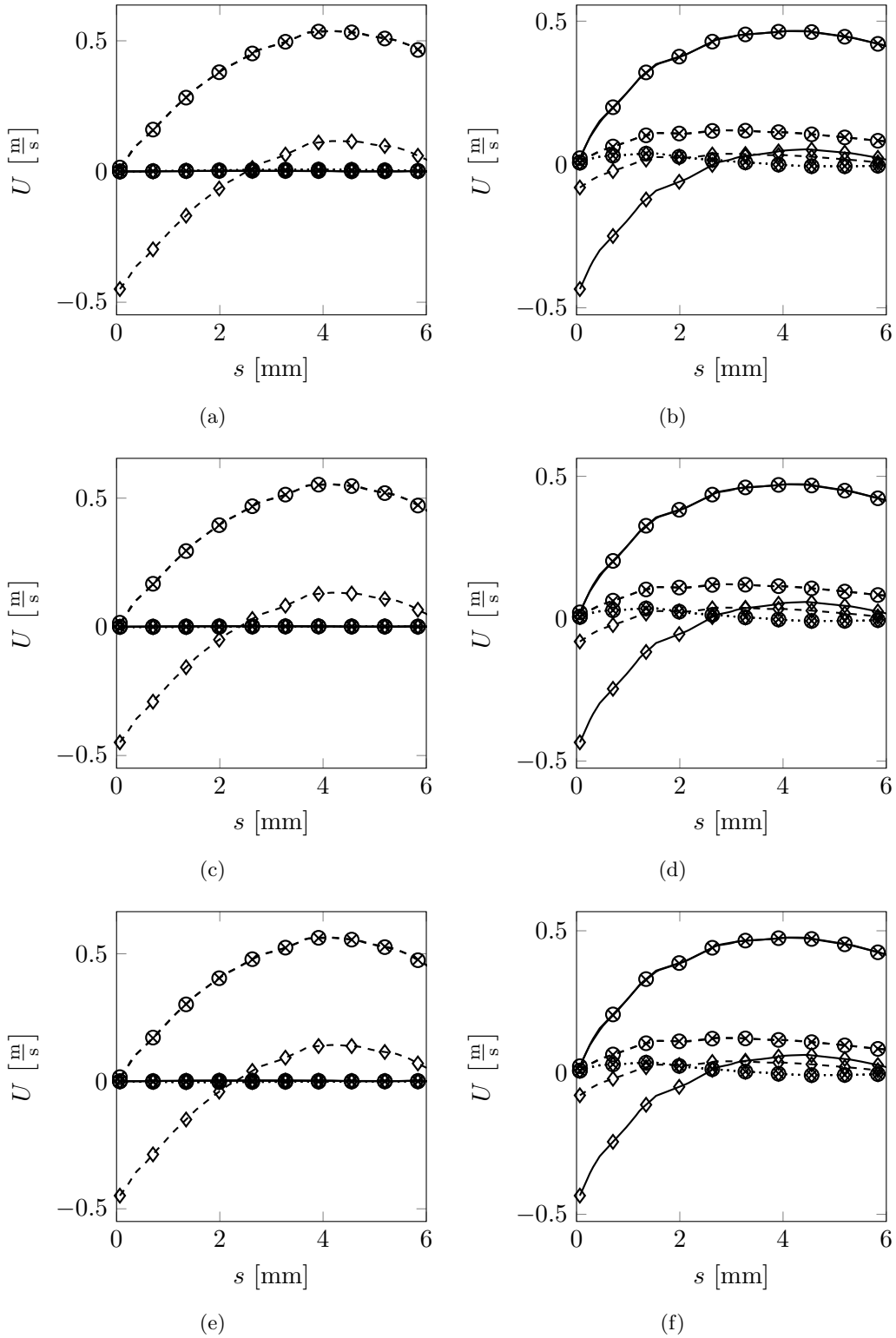


**Figure 8.9:** Local velocity profiles at the sampling lines  $A - B$  (a)  $F_r = 0.1$ , (c)  $F_r = 0.4$ , (e)  $F_r = 0.9$  and  $C - D$  (a)  $F_r = 0.1$ , (d)  $F_r = 0.4$ , (f)  $F_r = 0.9$  in the cross-sectional plane after one full turn of the screw at  $\omega_{max}t = 150$ . Solid lines are  $U_x$ , dashed lines are  $U_y$  and dotted lines are  $U_z$ ; ( $\times$ ): screw-rotation, ( $\diamond$ ): barrel-rotation and ( $\circ$ ): transformed velocity according to Eq. 8.8.

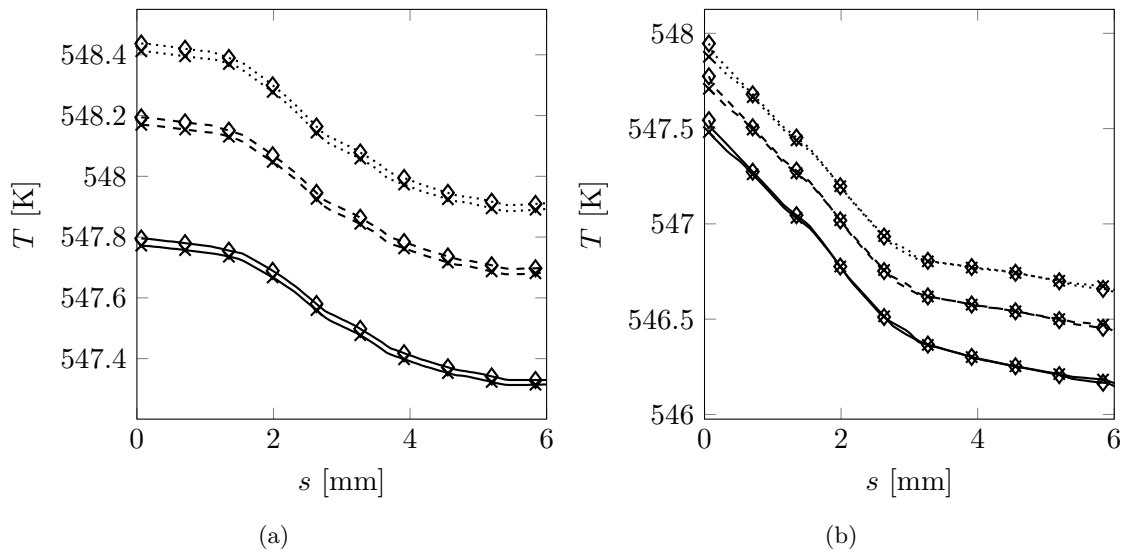


**Figure 8.10:** Local temperature profiles at the sampling lines  $A - B$  (a) and  $C - D$  (b) in the cross-sectional plane after one full turn of the screw at  $\omega_{max}t = 150$ . Solid lines are  $F_r = 0.1$ , dashed lines are  $F_r = 0.4$  and dotted lines are  $F_r = 0.9$ ; (x): screw-rotation and (◇): barrel-rotation.

## 8.A Literature

- [1] J. F. Carley, R. S. Mallouk, J. M. McKelvey, Simplified flow theory for screw extruders, *Ind. Eng. Chem.* 45 (1953) 974–978.
- [2] W. D. Mohr, R. L. Saxton, C. H. Jepson, Mixing in laminar-flow systems, *Ind. Eng. Chem.* 49 (1957) 1855–1856.
- [3] G. A. Campbell, P. A. Sweeney, J. N. Felton, Experimental investigation of the drag flow assumption in extruder analysis, *SPE ANTEC Tech. Papers* 37 (1991) 219–223.
- [4] G. A. Campbell, P. A. Sweeney, N. Dontula, C. H. Wang, Frame indifferences: Fluid flow in single pumps and extruders, *Int. Polym. Proc.* 11 (1996) 199–207.
- [5] C. Rauwendaal, T. A. O. G. Tellez, P. J. Gramann, Flow analysis in screw extruders - effect of kinematic conditions, *Int. Polym. Proc.* 8 (1998) 327–333.
- [6] G. A. Campbell, H. Cheng, C. Wang, M. Bullwinkel, M. A. te Riele, Temperature rise in single screw pump-extruders, *SPE ANTEC Tech. Papers* 47 (2001) 152–156.
- [7] G. A. Campbell, M. A. Spalding, F. Carlson, Prediction of melt temperature rise in single-screw pump extruders, *SPE ANTEC Tech. Papers* 54 (2008) 267–271.
- [8] G. A. Holzapfel, *Nonlinear solid mechanics: A continuum approach for engineering*, 1st Edition, Wiley, New York, 2000.
- [9] M. A. Spalding, J. Dooley, K. S. Hyun, S. R. Strand, Three dimensional analysis of the metering section of a single-screw extruder, *SPE ANTEC Tech. Papers* 39 (1993) 1533–1541.
- [10] G. C. Berry, T. G. Fox, The viscosity of polymers and their concentrated solutions, *Adv. Polymer Sci.* 5 (1968) 261–357.
- [11] H. Jasak, H. G. Weller, A. D. Gosman, High resolution NVD differencing scheme for arbitrarily unstructured meshes, *Int. J. Numer. Meth. Fluids* 31 (1999) 431–449.



## 8.B Nomenclature

Normal symbols represent scalar quantities and boldface symbols represent vector and tensor quantities in general.

### Roman Symbols

Symbol	Description	Unit
$\mathbf{0}$	Vector with only zeros	
$A$	Constant of Vogel model	$[K]$
$\mathbf{A}$	Second order tensor field	
$\mathbf{A}^*$	Transformed second order tensor field	
$B$	Constant of Vogel model	$[K]$
$c_p$	Heat capacity	$[\frac{m^2}{s^2 K}]$
$\mathbf{D}$	Rate of deformation tensor	$[s^{-1}]$
$\mathbf{D}^*$	Rotated rate of deformation tensor	$[s^{-1}]$
$\mathbf{f}$	Acceleration vector	$[\frac{m}{s^2}]$
$\mathbf{F}$	Deformation gradient	$[-]$
$\mathbf{F}^*$	Rotated deformation gradient	$[-]$
$Fr$	Drag rate	$[-]$
$\mathbf{I}$	Identity matrix	$[-]$
$\mathbf{L}$	Velocity gradient	$[s^{-1}]$
$\mathbf{n}$	Unit normal vector to control surface	$[-]$
$p$	Pressure	$[\frac{kg}{ms^2}]$
$\mathbf{q}$	Heat flux	$[\frac{kgm^2}{s^3}]$
$Q$	Energy source due to dissipation	$[\frac{kgm^2}{s^3}]$
$\mathbf{r}$	Radial position vector	$[m]$
$\mathbf{R}$	Rotation matrix	$[s^{-1}]$
$S$	Surface area	$[m^2]$
$S_{CV}$	Surface area of control volume	$[m^2]$
$t$	Time	$[s]$
$T$	Temperature	$[K]$
$\mathbf{T}$	Cauchy stress tensor	$[\frac{kg}{ms^2}]$
$T_0$	Reference temperature	$[K]$
$U$	Specific internal energy	$[\frac{kgm^2}{s^2}]$

Symbol	Description	Unit
$\mathbf{U}$	Velocity	$[\frac{m}{s}]$
$\mathbf{U}_b$	Velocity of control surface	$[\frac{m}{s}]$
$U_x$	Velocity component in x-direction	$[\frac{m}{s}]$
$U_y$	Velocity component in y-direction	$[\frac{m}{s}]$
$\mathbf{U}_{barrel-rot.}$	Velocity obtained with barrel-rotation	$[\frac{m}{s}]$
$\mathbf{U}_{screw-rot.}$	Velocity obtained with screw-rotation	$[\frac{m}{s}]$
$V$	Volume	$[m^3]$
$V_{CM}$	Volume of control mass	$[m^3]$
$V_{CV}$	Volume of control volume	$[m^3]$
$\mathbf{W}$	Antisymmetric component of velocity gradient	$[s^{-1}]$

### Greek Symbols

Symbol	Description	Unit
$\nabla$	Nabla (gradient) operator	$[m^{-1}]$
$\eta$	Dynamic viscosity	$[\frac{kg}{ms}]$
$\lambda$	Thermal conductivity	$[\frac{kgm}{s^3K}]$
$\rho$	Density	$[\frac{kg}{m^3}]$
$\tau$	Deviatoric or extra-stress tensor	$[\frac{kg}{ms^2}]$
$\omega$	Rotational speed	$[s^{-1}]$
$\boldsymbol{\omega}$	Rotational speed vector	$[s^{-1}]$
$\phi$	General intensive variable	

### Subscripts, Superscripts and Oversymbols

Symbol	Description
$\mathbf{Q}_0$	Value of $\mathbf{Q}$ at the beginning of simulation
$\mathbf{Q}^{-1}$	Inverse of matrix $\mathbf{Q}$
$\mathbf{Q}_{antisymm.}$	Antisymmetric part of matrix $\mathbf{Q}$
$\mathbf{Q}_{av}$	Average value of $\mathbf{Q}$
$\mathbf{Q}_{withfl.}$	Value of $\mathbf{Q}$ obtained with flight clearance
$\mathbf{Q}_{withoutfl.}$	Value of $\mathbf{Q}$ obtained without flight clearance
$\mathbf{Q}_{max}$	Maximum value of $\mathbf{Q}$
$\mathbf{Q}_{min}$	Minimum value of $\mathbf{Q}$
$\mathbf{Q}_{symm.}$	Symmetric part of matrix $\mathbf{Q}$

*8 CFD Analysis of the Frame Invariance of the Melt Temperature Rise in a Single-Screw Extruder*

<b>Symbol</b>	<b>Description</b>
$\mathbf{Q}^T$	Transpose of matrix $\mathbf{Q}$
$\mathbf{Q}^*$	Rotated matrix $\mathbf{Q}$
$\dot{\mathbf{Q}}$	Time-derivative of matrix $\mathbf{Q}$

**Nondimensional Groups**

<b>Symbol</b>	<b>Description</b>	<b>Definition</b>
$\epsilon$	Relative deviation	$\frac{T_{withfl.} - T_{withoutfl.}}{T_{withoutfl.} - T_0}$

**Abbreviations**

<b>Abbreviation</b>	<b>Description</b>
CFD	Computational fluid dynamics
CM	Control mass
CV	Control volume
FVM	Finite volume method
PISO	Pressure implicit with splitting of operator
SSE	Single-screw extruder

## 8.C Summary

In analytical analyses for single-screw extruders the simplified approach of rotating the barrel and keeping the screw fixed is often used instead of rotating the screw and fixing the barrel. Although the flow field is independent of the reference frame, as has already been shown to a satisfactory degree [5], the question of the dependence of the melt temperature rise on the reference frame is still being challenged, e.g. Campbell et al. [6, 7]. In this chapter a finite-volume CFD code is developed allowing for the three-dimensional simulation of the flow and temperature rise in both reference frames. The question of frame invariance is addressed by simulating the flow of a Newtonian-like polycarbonate both in a two-dimensional cross-section of a single-screw extruder and in a three-dimensional model with two full turns of the screw. The results show that the kinematics and the melt temperature rise are equal for screw- and barrel-rotation and thus independent of the reference frame. Furthermore, it is found that the presence of a clearance flow has a negligible influence on the temperature rise.

## 8.D Author contribution

The author of this thesis contributed to this publication by proposing the idea to do simulations for *screw-rotation*, *barrel-rotation* and *real-barrel-rotation* to show the frame invariance and the irrelevance of inertial forces, by doing the implementation in the software package *OpenFOAM*<sup>®</sup>, by proposing the idea to do simulations such as to have the results be most general, which is by doing transient and three-dimensional simulations, by generating the mesh and doing the simulations for the single-screw extruder with a flight clearance and by writing all parts of this manuscript except the conclusions (Section 8.4) and minor amendments from Olaf Kintzel to Section 8.2.1.

## 8.E Copyright permission

This chapter is originated from the following publication:

F. Habla, S. Obermeier, L. Dietsche, O. Kintzel, O. Hinrichsen, CFD Analysis of the frame invariance of the melt temperature rise in a single-screw extruder, *International Polymer Processing* (2013) 463-469.

Reprinted with permission from Carl Hanser Verlag GmbH & Co KG.

# 9 Summary and Outlook

## 9.1 Summary

In this work numerical modeling of polymeric flows is studied with focus on model development, implementation in the open-source CFD software *OpenFOAM*<sup>®</sup>, improvement of the underlying numerical techniques for solution of the partial differential equations as well as validation and verification of the developed solvers by comparison with analytical solutions, simulation of benchmark problems and comparison with other numerical studies and experimental measurements.

Numerical simulation of viscoelastic flows with a collocated finite-volume method can lead to checkerboarding effects of velocity due to a decoupling of velocity and stress. To overcome this issue, a new formulation for the divergence of the viscoelastic stress is developed, which even allows for a semi-implicit handling of the viscoelastic constitutive equation. The latter promotes numerical stability. The method is tested by simulation of three-dimensional steady contraction flows in a 4:1 planar contraction and a 4:1 square-square contraction with a simplified Phan-Thien-Tanner model. Mesh convergence and time-step independence of the results are shown and accurate and stable simulations can be performed over a wide range of Deborah numbers. Results are generally in good agreement with experimental results with deviations only found for large Deborah number flows in the square-square contraction, which were attributed to a deficiency of the viscoelastic model to describe such type of flow.

All numerical methods break down if the Weissenberg or Deborah number is increased beyond a critical value. This fundamental instability is called the High Weissenberg Number Problem (HWNP). The reason is a failure in balancing exponential growth in close to singular points with polynomial-based convection schemes. A remedy to this problem is the log-conformation reformulation, in which the viscoelastic constitutive equation is logarithmized. [1] This technique is implemented in *OpenFOAM*<sup>®</sup> in this thesis together with the CUBISTA convection scheme, which is formally of order three on uniform meshes and smooth flows. [2] The developed solver is first thoroughly validated by comparing simulation results with the analytical solution for the startup of a viscoelastic Poiseuille flow and subsequently used to simulate transient and three-dimensional viscoelastic flows in a lid-driven cavity, in which the material is governed by the Oldroyd-B constitutive equation. Mesh and time-step convergence is analyzed and the applicability of the code to unstructured meshes is shown. The effect of elasticity is investigated by comparing flows at different Weissenberg numbers. Simulations can be performed at arbitrary large values of the Weissenberg number as no upper-limit can be identified, although accuracy of such simulations is questionable as one would need very fine meshes and small time-steps for convergence.

## 9 Summary and Outlook

In this thesis a module for handling non-isothermal viscoelastic flows is implemented in the software *OpenFOAM*<sup>®</sup>. This is relevant since in industrial polymer processing temperatures commonly vary over a wide range and temperature effects become important. Thus, dependency of physical properties on temperature must be considered for obtaining accurate simulation results. Additionally, a new boundary condition for stress on solid walls is developed and implemented. Although a boundary condition for stress on solid walls is not needed for solution of the constitutive equation due to the hyperbolic nature, a boundary value must be specified to calculate the divergence of stress with use of the Gauss theorem. Commonly, a zero gradient is assumed, which is only first-order accurate. The boundary condition developed in this work is second-order accurate by linear extrapolation of interior values to the walls which is done with a linear regression technique in order to be applicable even to unstructured meshes. Simulation of a steady viscoelastic Poiseuille flow verifies the higher accuracy of the extrapolation boundary condition. The code is then applied to the simulation of non-isothermal axisymmetric 4:1 contraction flows. The influence of the elasticity and the temperature jump at the wall is investigated and compared to a similar numerical study.

A new model to describe segregated two-phase flows of viscoelastic fluids is derived with use of conditional volume-averaging and subsequent closure modeling, in which the two phases are described with the Oldroyd-B equation. The resulting set of partial differential equations is then reformulated in order to be solvable numerically. The reformulated model is implemented in *OpenFOAM*<sup>®</sup>. Basic validation of the model is performed to investigate the behavior of the model. This is done with a single-phase viscoelastic Poiseuille flow and three two-phase flows with steady interfaces. The two-phase flows include a shear-flow parallel to a planar interface to test the interfacial momentum transfer term, a cylindrical interface for testing the surface tension closure and a stratified Poiseuille flow for analyzing convergence properties of the model.

As in the latter study it was found that this viscoelastic two-phase model requires a sufficient spatial resolution of the interface, the conservative level-set method [3] is employed since this method is able to remedy this shortcoming. This is done by an additional intermediate step subsequent to the advection of the interface by compressing and diffusing the interface, which, when solved until convergence, leads to an interface indicator field with defined interface thickness. The method is first validated by simulation of a rotating cylinder and it is found that this intermediate step can in fact fix this issue. Subsequently, the model is used to simulate transient droplet deformations subject to a steady planar shear flow, in which the droplet is Newtonian and the matrix is governed by the Oldroyd-B equation. Simulations are performed in two and three dimensions. Convergence with cell size and time-step size is verified. The simulation results compare generally well to other numerical studies and experimental results, except for Capillary numbers close to break-up. It is assumed that this deficiency is caused by the poor rheological modeling of the matrix phase.

When analyzing single-screw extruder analytically the problem is often simplified by rotating the barrel and keeping the screw fixed. Although long being a controversial subject, it was yet been shown that the kinematics are not influenced by this simplification. However, there is still doubt whether this simplification is valid when analyzing the temperature rise. The reason is attributed to the viscous dissipation not being frame indifferent. This issue is investigated in this thesis by simulation of the temperature rise in screw-rotation and barrel-rotation mode. This is done in the most general way by considering the transient startup of rotation and a three-dimensional single-screw extruder. Comparison of the results obtained in both reference frames suggests that both kinematics and temperature rise are identical in both approaches and thus viscous dissipation is frame indifferent.

## 9.2 Outlook

The work presented in this thesis underlines the vast possibilities of numerical modeling of polymer processing and specifically also the advantages of using the software *OpenFOAM*<sup>®</sup> for this field of research. Further research in this regard may be directed towards the following:

- Simulation of integral viscoelastic constitutive equations

Viscoelastic constitutive equations can be sub-divided into differential and integral equations. Differential equations are comparatively easy to handle numerically and are widely used. Equations derived from molecular theory are usually of integral type and are often more sophisticated than differential equations, which can mostly be used only for polymeric solutions and mildly elastic materials. However, numerical simulation of integral type equations is very challenging and demanding. Preliminary work has been done during completion of this thesis by developing a module for handling integral viscoelastic constitutive equations in *OpenFOAM*<sup>®</sup>. The model is based on the deformation fields method as described in Hulsen et al. [4], in which the integral equation is of time-separable Rivlin-Sawyers type

$$\boldsymbol{\tau}(t) = \int_{\tau=0}^{\infty} M(\tau) f[\mathbf{F}_{\tau}(t)] d\tau \quad (9.1)$$

$\tau$  is an age-coordinate,  $M(\tau)$  is the memory function and  $\mathbf{F}_{\tau}(t)$  is the Finger tensor at age  $\tau$ . The interval  $\tau \in [0, \infty[$  is split into two sub-intervals  $\tau \in [0, \tau_c]$  and  $\tau \in ]\tau_c, \infty[$ . The Finger tensor is assumed to be constant within the interval  $\tau \in ]\tau_c, \infty[$ . As a result, this integral can be solved analytically. The first interval, on the other hand, is solved numerically by discretizing  $\tau \in [0, \tau_c]$  into a finite number of integration nodes. For each integration node a partial differential equation for the Finger tensor has to be solved

$$\frac{\partial \mathbf{F}}{\partial t} + \frac{\partial \mathbf{F}}{\partial \tau} + \nabla \cdot (\mathbf{U}\mathbf{F}) - (\nabla \mathbf{U})^T \cdot \mathbf{F} - \mathbf{F} \cdot \nabla \mathbf{U} = 0 \quad (9.2)$$

## 9 Summary and Outlook

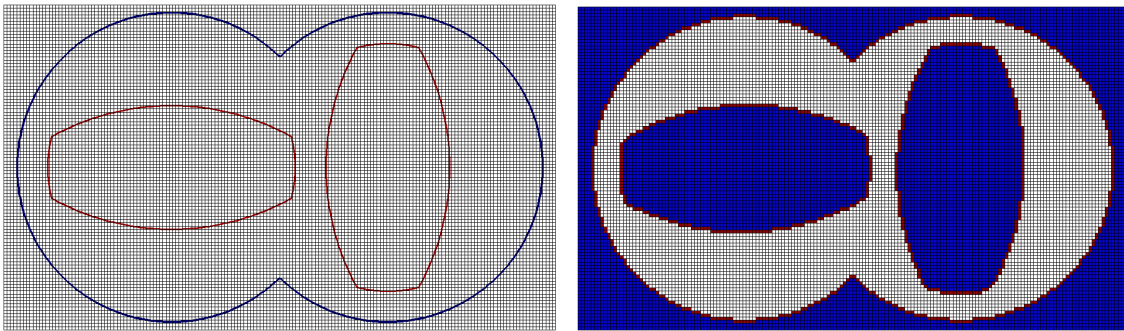
Both time-derivatives are calculated with a second-order Gear scheme. Subsequent integration is done with a Simpson technique for non-constant node spacing. Further research in this regard should be directed towards an optimization of the integration node spacing and proper choice of the cut-off time  $\tau_c$  since the overall accuracy of simulation results is very sensitive to this. A thorough validation is needed by comparison of the simulation results with appropriate analytical solutions such as the startup viscoelastic Poiseuille flow. Furthermore, the developed code should be tested with more complex flow types such as cavity or contraction flows.

- Logarithmic transformation of integral viscoelastic constitutive equations

It is known that use of a logarithmic transformation can overcome the High Weissenberg Number Problem for differential viscoelastic constitutive equations. Interestingly, such a logarithmic transformation can also be done for integral viscoelastic constitutive equations. The logarithmized variable is  $\Psi = \log(\mathbf{F})$ . The evolution equation for the Finger tensor then becomes

$$\frac{\partial \Psi}{\partial t} + \frac{\partial \Psi}{\partial \tau} + \nabla \cdot (\mathbf{U} \Psi) - (\boldsymbol{\Omega} \cdot \Psi - \Psi \cdot \boldsymbol{\Omega}) - 2\mathbf{B} = 0 \quad (9.3)$$

In this work it was found that this transformation can indeed give acceptable simulation results. However, at integration nodes close to present time ( $\tau \rightarrow 0$ ) it holds that  $\lim_{\tau \rightarrow 0} \mathbf{F} = \mathbf{I} \Leftrightarrow \lim_{\tau \rightarrow 0} \Psi = \mathbf{0}$ . In this case the logarithmic transformation becomes inaccurate. Resulting errors in the calculation affect all other Finger tensors due to the time-derivative in  $\tau$ . This issue must be further examined. A possible remedy is to do a logarithmic transformation only for Finger tensors  $\mathbf{F}$  at integration nodes  $\tau > \tau_{crit.}$ , where  $\tau_{crit.}$  is a sufficiently large time such that the eigenvalue and eigenvector computation is accurate enough.



(a) Background mesh and stl-geometry of the barrel (blue) and the screws (red).

(b) Solid cells (blue) and IB cells (red).

**Figure 9.1:** Immersed Boundary Method (IBM) for twin-screw extruder simulation.



- Twin-screw extruder modeling

Twin-screw extruder are widely used in polymer processing due to their good mixing capabilities, high flexibility and high productivity. Unfortunately, numerical modeling of twin-screw extruder is extremely difficult due to the complex screw movement. This is further complicated by the presence of viscoelastic material behavior and two-phase flow in case of partially filled twin-screw extruder. Based on the developments in this work an effort was made to capture the screw movement with the Immersed Boundary Method (IBM). In the Immersed Boundary Method a background mesh is used, which does not need to conform with the geometry considered. The geometry is described by a surface-file, see Fig. 9.1a. Cells overlapping with the geometry are identified (cf. the Immersed Boundary cells in red in Fig. 9.1b) and subsequently source terms are introduced into the governing equations in order to enforce either the Dirichlet or Neumann boundary condition of the dependent variable at the geometry surface. This is done with the discrete forcing approach in *OpenFOAM*<sup>®</sup>.

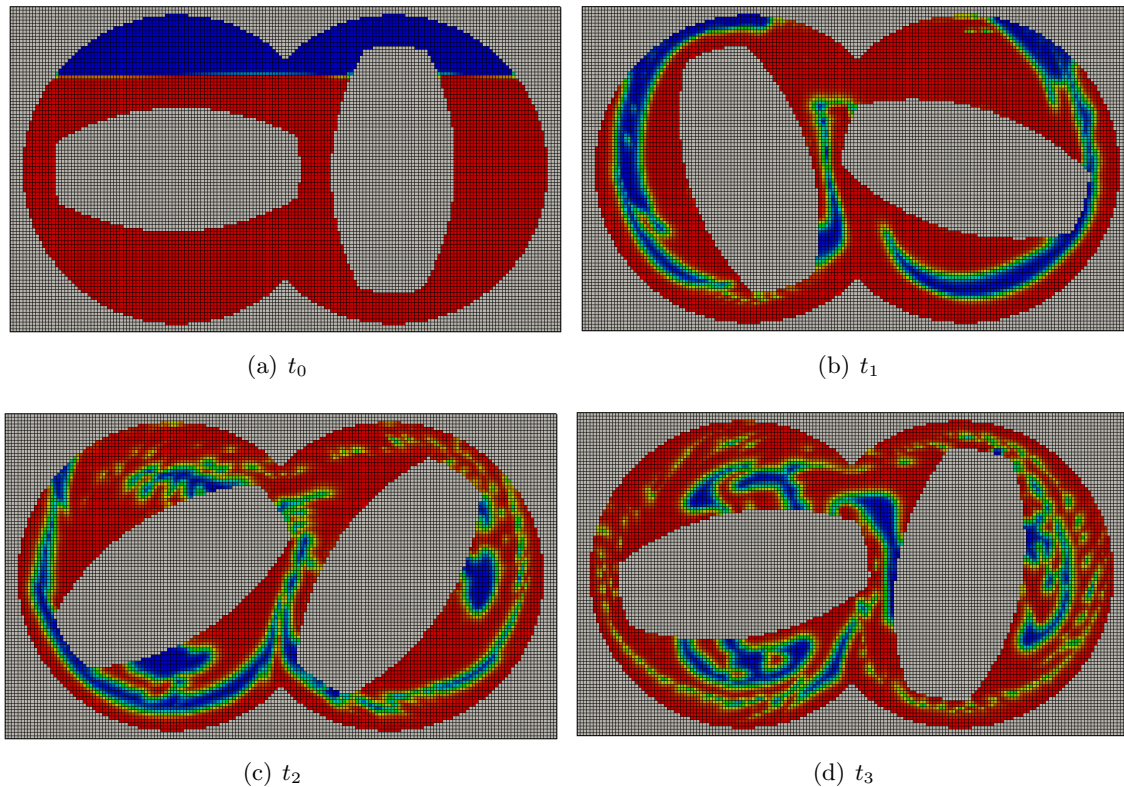


**Figure 9.2:** Simulation of the flow of a viscoelastic fluid in a partially filled twin-screw extruder ( $t_0 < t_1 < t_2 < t_3$ ).

A first step towards simulation of a partially filled twin-screw extruder with consideration of viscoelastic effects in the polymeric phase was done during this thesis, see Fig. 9.2, in which a Volume-Of-Fluid (VOF) method is used to describe the two-phase flow, while the polymer is governed by the Oldroyd-B equation. In order to finalize this study further research must be directed towards guaranteeing mass conservation, particularly over the screw boundaries.

## *9 Summary and Outlook*

Furthermore, for reasons of stability the log-conformation reformulation should be considered and the conservative level-set method may be a more appropriate choice over VOF due to the higher accuracy. Dynamic remeshing of the interface and wall-near regions would also be helpful to decrease computation time. Finally, a thorough validation of this method is necessary.

## 9.A Literature

- [1] R. Fattal, R. Kupferman, Constitutive laws for the matrix-logarithm of the conformation tensor, *J. Non-Newton. Fluid Mech.* 123 (2004) 281–285.
- [2] M. A. Alves, P. J. Oliveira, F. T. Pinho, A convergent and universally bounded interpolation scheme for the treatment of advection, *Int. J. Numer. Meth. Fl.* 41 (2003) 47–75.
- [3] E. Olsson, G. Kreiss, A conservative level set method for two phase flow, *J. Comput. Phys.* 210 (2005) 225–246.
- [4] M. A. Hulsen, E. A. J. F. Peters, B. H. A. A. van den Brule, A new approach to the deformation fields method for solving complex flows using integral constitutive equations, *J. Non-Newtonian Fluid Mech.* 98 (2001) 201–221.

## 9.B Nomenclature

Normal symbols represent scalar quantities and boldface symbols represent vector and tensor quantities in general.

### Roman Symbols

Symbol	Description	Unit
$\mathbf{0}$	Matrix with only zeros	
$\mathbf{B}$	Extensional matrix	$[s^{-1}]$
$\mathbf{F}$	Finger tensor	$[-]$
$\mathbf{I}$	Identity matrix	$[-]$
$M$	Memory function	$[-]$
$t$	Time	$[s]$
$\mathbf{U}$	Velocity	$[\frac{m}{s}]$

### Greek Symbols

Symbol	Description	Unit
$\nabla$	Nabla (gradient) operator	$[m^{-1}]$
$\nabla \cdot$	Divergence operator	$[m^{-1}]$
$\tau$	Age-coordinate	$[s]$
$\tau_c$	Cut-off time	$[s]$
$\tau_{crit.}$	Critical time	$[s]$
$\boldsymbol{\tau}$	Deviatoric or extra-stress tensor	$[\frac{kg}{ms^2}]$
$\Psi$	Logarithmic variable	$[-]$
$\boldsymbol{\Omega}$	Rotational matrix	$[s^{-1}]$

### Subscripts, Superscripts and Oversymbols

Symbol	Description
$\mathbf{Q}^T$	Transpose of matrix $\mathbf{Q}$

## **Abbreviations**

<b>Abbreviation</b>	<b>Description</b>
CFD	Computational fluid dynamics
CUBISTA	Convergent and universally bounded interpolation scheme for treatment of advection
HWNP	High Weissenberg Number Problem
IBM	Immersed boundary method
VOF	Volume-Of-Fluid



# A List of Publications

## Publications in Journals

- F. Habla, H. Marschall, O. Hinrichsen, L. Dietsche, H. Jasak, J. L. Favero, Numerical simulation of viscoelastic two-phase flows using OpenFOAM<sup>®</sup>, *Chemical Engineering Science* 66 (2011) 5487-5496.
- F. Habla, A. Woitalka, S. Neuner, O. Hinrichsen, Development of a methodology for numerical simulation of non-isothermal viscoelastic fluid flows with application to axisymmetric 4:1 contraction flows, *Chemical Engineering Journal* 207-208 (2012) 772-784.
- F. Habla, A. Obermeier, O. Hinrichsen, Semi-implicit stress formulation for viscoelastic models: Application to three-dimensional contraction flows, *Journal of Non-Newtonian Fluid Mechanics* 199 (2013) 70-79.
- F. Habla, L. Dietsche, O. Hinrichsen, Modeling and simulation of conditionally volume averaged viscoelastic two-phase flows, *AIChE Journal* 59 (2013) 3914-3927.
- F. Habla, S. Obermeier, L. Dietsche, O. Kintzel, O. Hinrichsen, CFD Analysis of the frame invariance of the melt temperature rise in a single-screw extruder, *International Polymer Processing* (2013) 463-469.
- F. Habla, M. W. Tan, J. Haßberger, O. Hinrichsen, Numerical simulation of the viscoelastic flow in a three-dimensional lid-driven cavity using the log-conformation reformulation in OpenFOAM<sup>®</sup>, *Journal of Non-Newtonian Fluid Mechanics* 212 (2014) 47-62.
- F. Habla, C. Waas, L. Dietsche, O. Hinrichsen, An Improved Conditionally Volume Averaged Viscoelastic Two-Phase Model for Simulation of Transient Droplet Deformations under Simple Shear, *Chemical Engineering Science* 126 (2015) 32-41.

## Oral Presentations on Conferences

- F. Habla, O. Hinrichsen, Numerical simulation of viscoelastic two-phase flows, 8<sup>th</sup> European Congress of Chemical Engineering, 2011, Berlin, Germany.

## *A List of Publications*

- F. Habla, J. Hable, S. Neuner, A. Woitalka, O. Hinrichsen, Accuracy and stability issues in the simulation of viscoelastic fluid flows using finite volume methods, ProcessNet Jahrestreffen der Fachgruppen Computational Fluid Dynamics und Fluidverfahrenstechnik, 2012, Weimar, Germany.
- F. Habla, A. Woitalka, O. Hinrichsen, Numerical simulation of non-isothermal viscoelastic fluid flows in 4:1 contraction flows, 22<sup>nd</sup> International Symposium on Chemical Reaction Engineering, 2012, Maastricht, The Netherlands.
- F. Habla, S. Obermeier, M. Steib, O. Hinrichsen, Frame invariance in the simulation of single screw extruder, AIChE Annual Meeting, 2012, Pittsburgh, USA.
- F. Habla, F. Haseidl, F. Ren, O. Hinrichsen, CFD-aided characterization of a spinning disc reactor (SDR), 9<sup>th</sup> European Congress of Chemical Engineering, 2013, The Hague, The Netherlands.
- F. Habla, S. Obermeier, O. Hinrichsen, CFD analysis of the frame invariance of the melt temperature rise in a single-screw extruder, 9<sup>th</sup> European Congress of Chemical Engineering, 2013, The Hague, The Netherlands.
- F. Habla, M. W. Tan, J. Haßlberger, O. Hinrichsen, Implementation of the log-conformation reformulation for viscoelastic flows in the CFD software OpenFOAM<sup>®</sup>, 23<sup>rd</sup> International Symposium on Chemical Reaction Engineering, 2014, Bangkok, Thailand.

## Poster Presentations on Conferences

- F. Habla, M. Steib, O. Hinrichsen, Two- and three-dimensional CFD simulation of polymer extrusion, ProcessNet Jahrestreffen Reaktionstechnik, 2012, Würzburg, Germany.
- F. Habla, A. Woitalka, O. Hinrichsen, Numerical simulation of non-isothermal viscoelastic fluid flows in 4:1 contraction flows, ProcessNet Jahrestreffen Reaktionstechnik, 2012, Würzburg, Germany.
- F. Habla, M. Steib, O. Hinrichsen, Two- and three-dimensional CFD simulation of polymer extrusion, 22<sup>nd</sup> International Symposium on Chemical Reaction Engineering, 2012, Maastricht, The Netherlands.



*A List of Publications*

- F. Habla, A. Weitalka, A. Obermeier, O. Hinrichsen, CFD simulation of non-isothermal flows of viscoelastic fluids in 4:1 contraction, AIChE Annual Meeting, 2012, Pittsburgh, USA.
- L. Dietsche, F. Habla, O. Hinrichsen, Development of a viscoelastic two-phase CFD model in OpenFOAM, AIChE Annual Meeting, 2012, Pittsburgh, USA.
- F. Habla, F. Haseidl, F. Ren, O. Hinrichsen, CFD-aided characterization of a spinning disc reactor (SDR), ProcessNet Jahrestreffen Reaktionstechnik, 2013, Würzburg, Germany.
- F. Habla, S. Obermeier, O. Hinrichsen, CFD analysis of the frame invariance of the melt temperature rise in a single-screw extruder, ProcessNet Jahrestreffen Reaktionstechnik, 2013, Würzburg, Germany.
- F. Habla, F. Ren, F. Haseidl, O. Hinrichsen, CFD-aided characterization of a spinning disc reactor (SDR), AIChE Annual Meeting, 2013, San Francisco, USA.
- F. Habla, J. Haßberger, L. J. Dietsche, O. Hinrichsen, Simulation of viscoelastic flows in complex geometries at high elasticities, AIChE Annual Meeting, 2013, San Francisco, USA.
- F. Habla, J. Haßberger, O. Hinrichsen, Simulation of viscoelastic flows in complex geometries at high elasticities, ProcessNet Jahrestreffen Reaktionstechnik, 2014, Würzburg, Germany.
- F. Habla, C. Waas, L. J. Dietsche, O. Hinrichsen, Simulation of transient droplet deformations under simple shear flow with a conditionally volume averaged viscoelastic two-phase model, 2<sup>nd</sup> International Symposium on Multiscale Multiphase Process Engineering, 2014, Hamburg, Germany.



# B Curriculum Vitae

## Personal data

Name	Florian Habla
Date of birth	September 7 <sup>th</sup> 1984
Place of birth	Munich, Germany
Marital status	Unmarried
Nationality	German

## Secondary education

Oct. 2010 - present	<b>Phd student</b> , Lehrstuhl I für Technische Chemie, Technische Universität München, Head: Professor Kai-Olaf Hinrichsen
Apr. 2006 - Sep. 2013	<b>Study of Business Administration</b> , FernUniversität Hagen, Germany <ul style="list-style-type: none"><li>• University degree: Dipl.-Kfm. (Univ.)</li><li>• Final grade: 2.2</li><li>• Diploma thesis: <i>Die Zusammenführung konnektionistischer Netze mit sozialen Verhaltensnetzen in der Expertensystem-Shell SPIRIT</i></li></ul>
Oct. 2004 - May 2010	<b>Study of Chemical Engineering</b> , Technische Universität München, Germany <ul style="list-style-type: none"><li>• University degree: Dipl.-Ing. (Univ.)</li><li>• Final grade: 1.2</li><li>• Diploma thesis: <i>Numerical Simulation of Viscoelastic Free-Surface Flows using Computational Fluid Dynamics</i></li></ul>
Oct. 2008 - Mar. 2009	<b>Stay abroad at the Department of Chemical and Biological Engineering</b> , University of California, Los Angeles, USA

## Primary education

Sep. 1995 - Jul. 2004      **Werner-von-Siemens Gymnasium**, Munich, Germany  
Sep. 1991 - Jul. 1995      **Grundschule an der Feldbergstraße**, Munich, Germany

## Internships

Jun. 2010 - Jul. 2010      **Grünecker, Kinkeldey, Stockmair, Schwanhäuser**, Munich, Germany  
Nov. 2007 - Dec. 2007      **EOS GmbH**, Planegg, Germany  
Oct. 2007 - Nov. 2007      **VTA GmbH**, Deggendorf, Germany  
Mar. 2006 - Apr. 2006      **Linde AG**, Munich, Germany

# C Declaration

I hereby certify that I am the sole author of this thesis.

I certify that, to the best of my knowledge, my thesis does not infringe upon anyone's copyright nor violate any proprietary rights and that any ideas, techniques, quotations, or any other material from the work of other people included in my thesis, published or otherwise, are fully acknowledged in accordance with the standard referencing practices. Furthermore, I certify that I have obtained a written permission from copyright owner(s) to include copyrighted material(s) in my thesis and have included copies of such copyright clearances right after first appearance of the material.

I declare that this is a true copy of my thesis, including any final revisions, and that this thesis has not been submitted for a higher degree to any other University or Institution.

I am familiar with the relevant course of examination for doctoral candidates at the Technische Universität München (Promotionsordnung).

Garching, June 16, 2015

Florian Habla